UNIVERSITAT AUTÒNOMA DE BARCELONA

DEPARTAMENT DE BIOQUÍMICA I BIOLOGIA MOLECULAR, FACULTAT DE BIOCIÈNCIES

DOCTORAT EN BIOQUÍMICA, BIOLOGIA MOLECULAR I BIOMEDICINA

TARGETED DRUG DELIVERY FOR THE SELECTIVE ELIMINATION OF CXCR4+ CANCER CELLS IN METASTATIC COLORECTAL CANCER MODELS

Memòria presentada per la Rita Sala Faig per optar al títol de doctora en Bioquímica, Biologia Molecular i Biomedicina per la Universitat Autònoma de Barcelona

Directors:
Ramon Mangues Bafalluy   **MªVirtudes Céspedes Navarro**

Doctoranda: Tutor:
Rita Sala Faig   **Francisco Blanco Vaca**

RITA SALA FAIG
2020

CONTENTS

ABBREVIATIONS

5-FU: 5-fluorouracil

ADA: anti-drug antibody

ADC: antibody-drug conjugate

AML: acute myeloid leukemia

APC: adenomatous polyposis coli

APC: antigen presenting cell

ATCC: American type culture collection

AUC: area under the curve

Aur: Auristatin E

CAF: cancer associated fibroblasts

CIMP: CpG island methylator phenotype

CRC: colorectal cancer

CSC: cancer stem cell

CTC: circulating tumor cell

CXCR4: C-X-C chemokine receptor 4

DISC: death-inducing signalling complex

DLBCL: diffuse large B-cell lymphoma

DMEM: Dulbeco's modified eagle medium

DNA: deoxyribonucleic acid

DTC: disseminated tumor cell

ECM: extracellular matrix

EGFR: endothelial growth factor receptor

ELISA: enzyme-linked immunoassay

EMT: epithelial-to-mesenchymal transition

EPR: enhanced permeability and retention

FAP: familial adenomatous polyposis

FDA: food and drug administration

FdU: floxuridine

G-CSF: granulocyte colony-stimulating factor

GEMM: genetically engineered mouse models

GFP: green fluorescent protein

GPCR: G protein-coupled receptor

GSDMD: gasdermin D

H&E: haematoxylin and eosin

HDI: human development index

HIF-1: hypoxia-inducible factor-1

HIV: human immunodeficiency virus

HSC: hematopoietic stem cell

HSPC: hematopoietic stem and progenitor cell

i.p.: intraperitoneal

i.v.: intravenous

ICC: immunocytochemistry

IHC: immunohistochemistry

LV: leucovorin

MIF: migration inhibitory factor

MMAE: monomethyl Auristatin E

MMR: mismatch repair

MOMP: mitochondrial outer membrane permeabilization

MPS: mononuclear phagocytic system

MSI: microsatellite instability

NK: natural killer

OCMI: orthotopic cell microinjection

ORT: orthotopic

PBS: phosphate-buffered saline

PDX: patient-derived xenograft

PEG: polyethylene glycol

PIGF: placental growth factor

RES: reticuloendothelial system

ROS: reactive oxygen species

SC: subcutaneous

SDF-1 or CXCL12: stromal cell-derived factor-1

SEC: size exclusion chromatography

SSP: sessile serrated polyp

TBS: tris-buffered saline

TIL: tumor-infiltrating lymphocyte

UAB: Univeristat Autònoma de Barcelona

VAT: visceral adipose tissue

VEGF: vascular endothelial growth factor

LIST OF FIGURES

LIST OF TABLES

ABSTRACT

Colorectal cancer (CRC) remains the third cause of cancer-related mortality in Western countries, being metastases the main cause of death. Despite progress in prevention strategies that decreased CRC incidence and mortality, still nearly a quarter of patients are diagnosed at an advanced metastatic stage, with only a 15% five-year survival rate. Thus, inhibition of metastasis development by targeting cancer stem cells, which are associated with cancer dissemination, will significantly increase the benefits of current cancer therapies. In collaboration with the Nanobiotechnology group from de UAB, we developed self-assembling protein-based nanoparticles targeting the CXCR4 receptor whose overexpression correlates with tumor dissemination, poor survival, and recurrence in CRC patients. Preclinical evaluation of the efficacy and toxicity of the T22-GFP-H6 nanocarrier and its therapeutic derivatives requires the use of adequate *in vivo* disseminated CRC models. For that purpose, we generated subcutaneous and highly metastatic models of CRC that overexpress CXCR4, derived from the SW1417 CRC cell line or the SP5 patient sample. In order to increase the metastatic efficiency of previous CXCR4$^+$ CRC models, we orthotopically implanted luciferase expressing SW1417 cells in the cecum of severe immunodeficient mice. NOD/SCID mice (deficient in T and B cells) presented a low metastatic rate. In contrast, orthotopic microinjection in NSG mice (deficient in T, B and NK cells) replicated the dissemination pattern observed in patients, causing mice death and resulting in a higher number and size of hepatic and pulmonary metastases as compared to NOD/SCID mice.

In the assessment of nanoparticles' biodistribution, T22-GFP-H6 achieved a highly selective tumor uptake in a CXCR4$^+$ CRC subcutaneous model, as detected by fluorescent emission (around 70% of the total), while displaying only transient accumulation in non-tumor organs. We demonstrated that the nanocarrier tumor accumulation was CXCR4-dependent because pre-treatment with AMD3100, a CXCR4 antagonist, reduced tumor uptake. Furthermore, tumor accumulation was increased by the functionalization of the nanocarrier with the fusogenic HA2 peptide, which promotes endosomal escape. On the one hand, we observed that the therapeutic nanoconjugate T22-GFP-H6-Aur maintained the nanocarrier's biodistribution but its antitumoral effect was surprisingly poor. T22-GFP-H6-Aur inhibited only tanscelomic metastasis in a highly metastatic CRC model,

while activating a lethal immunogenic response when repeatedly administered in low immunosuppressed mice. As an alternative therapeutic option, we replaced the GFP protein in the nanoparticle by the de-immunized PE24 toxin, to reduce its immunogenicity while promoting a potent and intrinsic cytotoxic activity. The administration of low doses of the T22-PE24-H6 nanotoxin prevented the development of lymphatic and hematogenous metastasis in the highly metastatic CRC model without toxicity. We demonstrated that the T22-PE24-H6 nanotoxin induced cancer cell death through the non-apoptotic pathway, pyroptosis. In conclusion, the use of the T22-PE24-H6 nanotoxin could be a promising strategy to selectively eliminate CXCR4^{+} CRC stem cells in the absence of systemic toxicity, applicable to chemotherapy-resistant and disseminated CRC associated with the upregulation of CXCR4 and antiapoptotic mechanisms.

RESUM

El càncer colorectal (CCR) representa la tercera causa de mortalitat per càncer en països occidentals, essent les metàstasis la principal causa de mort. Tot i el progrés en les estratègies de prevenció que han disminuït la incidència i mortalitat del CCR, prop d'un quart dels pacients encara són diagnosticats en estadis metastàtics avançats, amb una taxa de supervivència a cinc anys de només el 15%. És per això que la inhibició del desenvolupament de metàstasis actuant sobre cèl·lules mare canceroses incrementarà significativament els beneficis de les teràpies actuals. En col·laboració amb el grup de recerca en Nanobiotecnologia de la UAB, hem desenvolupat nanopartícules proteiques autoensamblables dirigides al receptor CXCR4, la sobreexpressió del qual es correlaciona amb la disseminació tumoral, baixa supervivència, i recurrència en pacients de CCR. L'avaluació preclínica de l'eficàcia i toxicitat del nanoportador T22-GFP-H6 i els seus derivats terapèutics requereix l'ús de models *in vivo* de CCR disseminats. Amb aquest objectiu, hem desenvolupat models de CCR subcutanis i altament metastàtics que sobreexpressen CXCR4, derivats de la línia cel·lular de CCR SW1417 o de la mostra de pacient SP5. Per tal d'incrementar l'eficiència metastàtica dels models CXCR4$^+$ anteriors, vam implantar ortotòpicament cèl·lules SW1417 amb expressió de luciferasa en el cec de ratolins amb immunodeficiència severa. Els ratolins NOD/SCID (deficients en cèl·lules T i B), presentaren taxes metastàtiques baixes. Per contra, la microinjecció ortotòpica en ratolins NSG (deficients en cèl·lules T, B i NK), replicà el patró de disseminació observat en pacients, provocant la mort dels ratolins i un nombre i mida més gran de metàstasis hepàtiques i pulmonars en comparació als ratolins NOD/SCID.

En l'avaluació de la biodistribució de les nanopartícules, tal i com indica l'emissió de fluorescència (al voltant del 70% del total), la T22-GFP-H6 va assolir una alta acumulació selectiva en tumors del model subcutani CXCR4$^+$, mentre que l'acumulació en òrgans no tumorals fou només transitòria. Vam demostrar que l'acumulació al tumor del nanoportador és CXCR4-dependent, perquè el pretractament amb AMD3100, un antagonista de CXCR4, va reduir l'acumulació tumoral. A més, aquesta va incrementar amb la funcionalització del nanoportador amb el pèptid fusogènic HA2, que afavoreix l'escapament endosomal. Per altra banda, vam observar que el nanoconjugat terapèutic T22-GFP-H6-Aur era capaç de mantenir la biodistribució del nanoportador, però el seu

efecte antitumoral fou sorprenentment baix. El T22-GFP-H6-Aur només va inhibir metàstasis transcel·lòmiques en un model de CCR altament metastàtic i a més, va activar una resposta immunogènica letal en la seva administració repetida en ratolins poc immunodeprimits. Com a opció terapèutica alternativa, vam substituir la proteïna GFP de la nanopartícula per la toxina PE24 desimmunitzada, per tal de reduir la seva immunogenicitat afegint al mateix temps una potent activitat citotòxica intrínseca. L'administració de dosis baixes de la nanotoxina T22-PE24-H6, va prevenir el desenvolupament de metàstasis limfàtiques i hematògenes en el model de CCR altament metastàtic sense toxicitat. Vam demostrar que la nanotoxina T22-PE24-H6 indueix la mort de cèl·lules tumorals per la via no apoptòtica de la piroptosi. En resum, l'ús de la nanotoxina T22-PE24-H6 podria ser una estratègia prometedora per a l'eliminació selectiva de cèl·lules mare de CCR CXCR4^{+} en absència de toxicitat sistèmica, aplicable a CCR metastàtics i resistents a la quimioteràpia que s'associïn a la sobreexpressió de CXCR4 i a mecanismes antiapoptòtics.

I. INTRODUCTION

I. INTRODUCTION

1) COLORECTAL CANCER

1.1. General aspects

Colorectal cancer (CRC), also known as colorectal adenocarcinoma, is the abnormal growth of epithelial cells from the colon or rectum (large intestine). The main function of the colon is the reabsorption of water and remaining nutrients, and preparation of waste products from the body for their elimination. The colon is held in place by peritoneum, a thin layer of tissue that supports the abdominal organs. In order to help the absorption, the gastrointestinal epithelium is formed by invaginations called colonic crypts. Colon stem cells are located in the bottom of the crypts. These pluripotent cells function in self-renewal. When the progenitor cells differentiate into specialised epithelium cells, they migrate from the base to the surface in about 3-5 days. Normal cells die at the surface and are replaced by the continuous stream of new cells from below. All these processes are controlled by a protein signalling gradient, in which the most common proteins are Wnt, TGF-B and BMP [1].

Most of CRC tumors (96%) typically arise from pre-existing benign polyps. The dividing cells in these polyps may accumulate sufficient genetic and epigenetic changes by which they acquire the ability to invade the bowel wall, a hallmark of CRC, and eventually spread to local lymph nodes and finally to distant metastatic sites [2]. Only 10% of all the polyps progress to invasive cancer, although the risk of cancer increases as the polyp grows larger [3].

1.2. Epidemiology

1.2.1. Incidence

Colorectal cancer (CRC) is the third most commonly diagnosed malignancy and the fourth leading cause of cancer death in the world, accounting for about 1.8 million new cases and almost 881,000 deaths in 2018 [4]. CRC has a higher incidence in men than in women, being 3–4 times more common in developed nations whereas the risk of the disease increases with age, with most patients aged over 50 years at diagnosis.
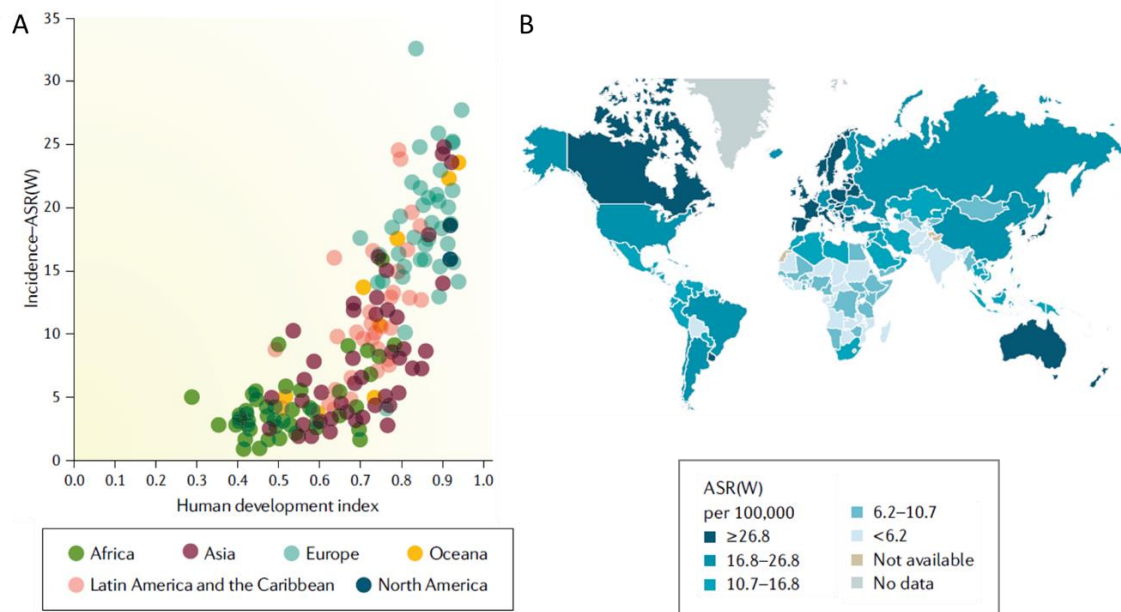
Figure 1. Epidemiology of colorectal cancer A) Correlation between a country's human development index (HDI) and colorectal cancer (CRC) incidence rates worldwide in 2018. HDI is a composite score of life expectancy, education and income, reflecting the economic development of a country. Higher incidence rates of CRC are observed in countries with higher values of HDI. B) Estimated incidence rates of CRC by country worldwide in 2018, showing wide geographical variations. Adapted from (5).

Two-thirds of all CRC cases and about 60% of all deaths are occurring in countries with a high human development index (HDI). But nowadays, CRC is considered one of the clearest markers of the cancer transition. Countries undergoing rapid social and economic evolution show fast increases in both incidence and mortality rates of cancers more frequent in high-income countries **(Figure 1)**. On the other hand, in high indexed HDI countries (USA, Australia and Western Europe) CRC incidence and mortality rates have been stabilised or decreasing, partially due to the increase in early detection and prevention through colonoscopy and polyp removal.

1.2.2. Survival

Cancer overall survival is highly dependent on the cancer stage and the type of cancer involved. Survival rates for early stage detected cancers are about five times higher than that for late stage cancers. As CRC only becomes symptomatic at an advanced stage, worldwide screening programmes are being implemented, which aim to increase early detection and reduce morbidity and mortality. The 5-year survival rate of people with

localized CRC is 90%. However, only 39% of patients are diagnosed at this early stage. If the cancer has spread to regional tissues or regional lymph nodes, the 5-year survival rate is 71%. For metastatic CRC patients, where the cancer has spread to distant parts of the body, the 5-year survival rate decreases to only 14%. In CRC the most common sites of metastasis are the liver (70%), lungs (32%), and peritoneum (21%) (6). Distant lymph node metastases are less frequent (15%), occur independently of the hematogenous spread and represents a major prognostic factor in CRC (7).

1.2.3. Etiology and risk factors

Both genetic and environmental factors play an important role in CRC development. The majority of CRC tumors are sporadic and only 15-20% of CRC patients have a positive family history. Sporadic CRC are caused by point mutations in specific genes, altering important cell signalling pathways. In contrast, inherited CRC are caused by inherited mutations that affect one of the alleles of the gene and a spontaneous point mutation in the other allele, triggers the occurrence of a cancer cell and the adenocarcinoma.

There are different genetic syndromes associated to the development of hereditary CRC. The most common is the Lynch syndrome, which is caused by a mutation in one of the DNA mismatch-repair genes such as MLH1, MSH2, MSH6, PSM2 or EPCAM. Impaired mismatch repair during replication produces an accumulation of DNA mutations, which increase the probability of developing CRC. Another syndrome strongly associated with CRC is familial adenomatous polyposis (FAP) which is caused by mutations in the adenomatous polyposis coli (APC) gene, which controls activity of the Wnt signalling pathway (8).

Many environmental lifestyle factors influence the risk of developing polyps and CRC. The main risk factors of CRC are older age, male sex, smoking, alcohol intake and obesity. In the case of alcohol consumption, the main metabolite of ethanol, acetaldehyde, has been described as carcinogenic, being high alcohol consumption associated to an increase in the risk of the 50% (9). Moreover, smoking can increase CRC affectation by up to 10% because of the content of carcinogens such as nicotine that can easily reach the intestine (10). Obesity is another important risk factor for CRC and can be related to sedentary lifestyles or type 2 diabetes mellitus (11). Both, food intake and

increased levels of visceral adipose tissue (VAT), can promote the development of CRC through the secretion of proinflammatory cytokines in the intestine. So, diet is strongly associated to CRC risk, increasing the chances up to 70% because of unhealthy nutritional habits. Moreover, red meat releases heme groups in the intestine, which enhance the formation of carcinogenic compounds (12).

1.3. Molecular pathways involved in tumor progression

The histological progression from polyp to cancer is the result of an accumulation of several genetic and epigenetic changes in the colonic epithelial cells that deregulate conserved signalling pathways involved in cellular proliferation, differentiation, survival, and apoptosis. Mutations in the DNA can be sporadic or inherited, and the order of occurrence seems to play an important role in CRC carcinogenesis. There are two different types of polyps from which CRC develops, adenomas and sessile serrated polyps (SSPs), and they normally originate by two main genetic pathways.

On the one hand, traditional adenomas, are associated with the chromosomal instability pathway, which is observed in 85% of all sporadic cancers (13). It is characterized by a cascade of accumulating mutations and imbalances in the number of chromosomes, commonly being the mutation in the APC gene the first to occur. This alteration in the APC gene affects chromosome segregation during cell division and causes the translocation of β-catenin to the nucleus, promoting cell division and invasion. Next, genetic events of progression frequently consist in mutations in the KRAS oncogene, leading to a constitutive activation of MAP kinase, thus increasing cell proliferation. Finally, over time, these mutations can cause a loss of function of the p53 gene, that controls the main cell-cycle checkpoint, causing an uncontrolled entry in the cell cycle and resulting in carcinogenesis **(Figure 2).**
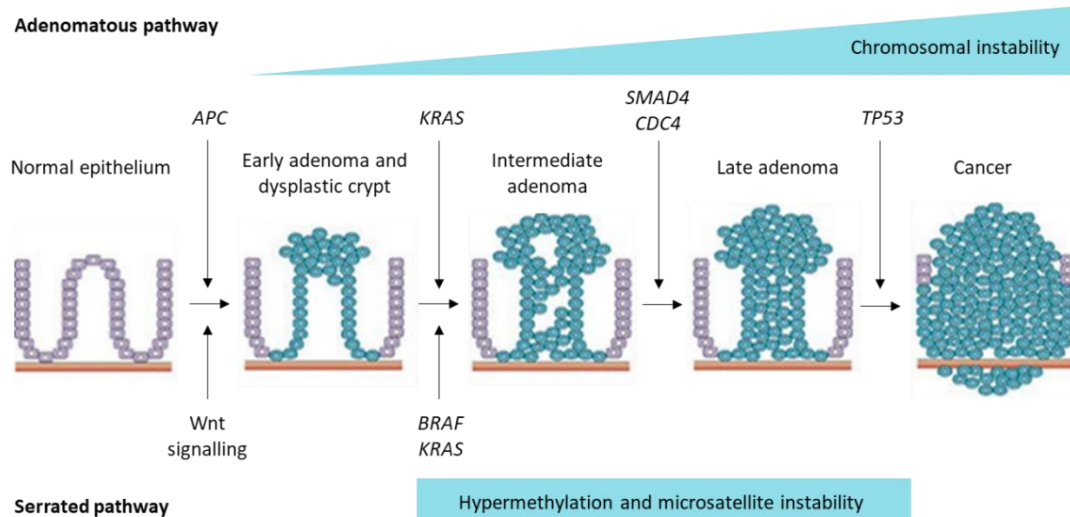
Figure 2. Schematic diagram of the polyp to CRC progression. Two different activated signalling pathways in the normal colon to CRC development have been identified. Both sequential events involve the progression of normal colon epithelial cells to aberrant crypt foci, followed by early and advanced polyps with subsequent progression to early cancer and finally advanced cancer. The traditional route is the pathway that involves the development of tubular adenomas that can progress to adenocarcinomas. An alternate pathway is that involving serrated polyps and their progression to serrated CRC. The genes mutated or epigenetically altered are indicated for each pathway. Some genes are shared between the two pathways whereas others are pathway specific (i.e. BRAF mutations and CpG Island Methylator Phenotype (CIMP) only in the serrated pathway). Adapted from (14).

On the other hand, SSPs tend to develop from mutations in the BRAF gene, which results in altered cell growth and loss of apoptosis. Moreover, epigenetic instability, which is responsible for the CpG island methylator phenotype (CIMP), is another common feature in CRC originated from SSPs. The main characteristic of CIMP tumors is the hypermethylation of oncogene promoters, which leads to gene silencing and a loss of protein expression.

Another mechanism leading to genetic diversity in CRC, that can occur in both adenomatous and serrated polyps, is microsatellite instability (MSI). MSI can result from a hypermutable phenotype due to loss of expression of mismatch repair genes (MMR). Therefore, mutations tend to accumulate leading to tumor progression. This loss of DNA repair mechanisms can be caused by spontaneous events (promoter hypermethylation) or germinal mutations such as those found in Lynch syndrome. In general, MSI tumors have a better prognosis than sporadic tumors.

1.4. CRC treatment

The choice of the first-line treatment for CRC patients is currently based in different aspects of the disease and depending on the tumor stage, chemotherapy may be used in addition to surgery. Tumor-related characteristics (localized or metastatic, number and localization of metastases or the presence or absence of biochemical markers) and patient-related factors (co-morbidity and prognosis) are used to classify patients in stages and to select the right treatment strategy. The current classification of CRC patients depends on the extent of local invasion, the degree of lymph node involvement and the presence of distant metastasis (TNM staging system), creating four different risk groups.

In stage I tumors, cells have grown through the mucosa and have invaded the muscular layer of the colon or rectum, whereas in stage II tumors, cells have already invaded nearby tissues such as the peritoneum but have not spread into lymph nodes or distant organs. In these patients the recommended management consists on complete surgical resection of the tumor with adequate margins and without chemotherapy since it has no benefits to the overall survival of these stages. The standard procedure is a partial colectomy where the affected part of the colon or rectum is resected together with its mesocolon and blood supply to facilitate removal of draining lymph nodes.

Stage 0	Stage I	Stage II	Stage III	Stage IV
		Chemotherapy		
	Surgery (colectomy)			
Polyp removal				
			Targeted therapies	
	Radiation therapy			
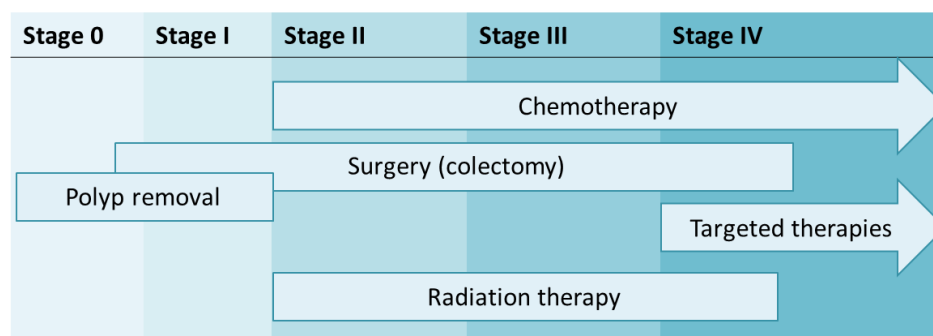
Figure 3. CRC treatment approach depending on the CRC stage. Early-stage CRC patients are normally treated with surgery, resecting only the polyps or the affected part of the colon (colectomy). Patients at advanced stages are treated with a combination of surgery, chemotherapy and targeted therapies. Chemotherapy consists of different regimes that combine drugs such as 5-fluorouracil, oxaliplatin, leucovorin and irinotecan. Currently used targeted therapies include monoclonal antibodies targeting VEGF (bevacizumab) or the EGFR (cetuximab and panitumumab).

If cancer has spread to the lymph nodes or distant organs such as liver, lung or peritoneum, which is the case in stage III and stage IV CRC respectively, chemotherapy is an integral part of the treatment. Approximately two-thirds of patients with stage III CRC (as well as some patients with stage II disease) receive adjuvant chemotherapy to lower their risk of recurrence. For stage IV CRCs, when there are limited metastases, the surgical treatment is usually combined with chemotherapy and/or radiation therapy **(Figure 3)**. Currently, several targeted drug therapies are also available to treat metastatic disease, and in some cases, depending on the tumor's molecular characteristics immunotherapy may also be appropriate.

1.4.1. Chemotherapy

As mentioned before, most metastatic CRC patients are treated with classic cytotoxic agents in combination with molecularly targeted therapies. Chemotherapy can be used as neoadjuvant therapy to shrink the tumor before surgery, facilitating its resection, and for the depletion of the remaining cancer cells after surgery. First-line chemotherapy includes drugs as fluoropyrimidines (5-fluorouracil (5-FU) or capecitabine), leucovorin (LV), oxaliplatin or irinotecan. The drugs capecitabine and fluorouracil are interchangeable, being respectively oral or intravenous fluoropyrimidine agents. Currently, some specific regimens which combine these chemotherapeutic agents are used in metastatic CRC to avoid the emergence of resistances. In FOLFOX and CAPOX regimens oxaliplatin is combined with LV and 5-FU or capecitabine respectively. In contrast, in FOLFIRI regimen, irinotecan is combined with 5-FU and LV. Moreover, all these cytotoxic drugs (5-FU, LV, oxaliplatin and irinotecan) are combined in the FOLFOXIRI regime. The use of LV reduces the toxicity of the treatment, whereas the use of the other cytotoxic agents has been shown to increase the progression-free survival despite worsening the toxic effects of the treatment.

Although all these chemotherapeutic agents have shown efficacy, toxicity remains the main limitation of cancer treatment. All these agents are biodistributed within the body by passive diffusion, affecting both normal and cancer cells. Common side effects produced by chemotherapy are anaemia, fatigue, hair loss, nauseas, diarrhea, muscle disorders and neuropathy.

1.4.2. Molecularly targeted therapies

In order to increase antitumor activity while reducing toxicity and side effects of cancer treatments, new targeted therapies were designed to halt the growth and spread of cancer cells by targeting or interfering with important and specific molecules of tumor progression and growth. These targeted therapies can interfere with pathways causing apoptosis of cancer cells or stopping the growth of abnormal blood vessels that feed tumors (antiangiogenesis). Nowadays, in first-line treatment of metastatic CRC, traditional chemotherapy is combined with antiangiogenic drugs, improving patient overall survival (15). For that, monoclonal antibodies or proteins against different effectors of the angiogenic pathway can be used. On the one hand, strategies targeting the vascular endothelial growth factor (VEGF) have been developed, being the most common the monoclonal antibody Bevacizumab and the recombinant fusion protein Aflibercept. Bevacizumab targets circulating VEGF-A, therefore inhibiting signalling from the VEGF receptor, while Aflibercept blocks multiple angiogenic growth factors such as VEGF-A, VEGF-B and placental growth factor (PIGF). These compounds might act by normalizing the dysregulated tumor vasculature, which would lead to improved tumor oxygenation and delivery of chemotherapy (16).

On the other hand, anti-EGFR targeting therapies are used in metastatic CRC treatment. Approximately 80% of all CRC express EGFR and overexpression correlates with reduced survival and increased risk of metastases. There are two anti-EGFR targeted agents approved for CRC: Cetuximab which is a recombinant chimeric monoclonal IgG1 antibody (17) and Panitumumab which is a human EGFR-specific antibody. Anti-EGFR therapies are only used in the absence of *RAS* mutations because they have been proven ineffective in *KRAS* or *NRAS* mutated gene tumors (18). *RAS* is mutated in about half of all CRC. Thus, the *RAS* status of the tumor must be examined before making decisions to treat with EGFR targeted therapies.

1.5. Cell death mechanisms induced by anticancer drugs

Cell death was believed to be the result of only two different processes in mammalian tissues: apoptosis, also known as programmed cell death, or necrosis, the uncontrolled cell death. However, in recent years, several other forms of cell death have been

discovered, demonstrating that cells can die via distinct pathways. It has also been noticed that classic chemotherapeutic agents kill cancer cells not only activating apoptosis but other forms of non-apoptotic cell death such as necrosis, autophagy, pyroptosis and mitotic catastrophe or inhibiting growth by entering senescence. The new cell death classification is based on many biochemical and morphological characteristics present in dying cells. Thus, the development of more efficient and safer chemotherapeutics might succeed by understanding these novel cell death mechanisms. The activation or inhibition of their mediators could lead to the design of new anticancer agents. Moreover, the discovery of these cell death pathways can also help to address the issue of drug resistance, by understanding the mechanisms used by cancer cells to inhibit cell death, and directly influencing in their susceptibility to chemotherapeutic agents.

1.5.1. Apoptosis

Apoptosis is the best known form of programmed cell death in multicellular organisms and is responsible for maintaining tissue homeostasis by regulating the equilibrium between cell proliferation and death. Furthermore, it has been considered the major mechanism of chemotherapy-induced cell death. Apoptosis leads to morphological cell changes and death induction. These morphological characteristics include cell membrane blebbing, cell shrinkage, chromatin condensation and nucleosomal fragmentation. So, apoptosis produces cell fragments called apoptotic bodies that phagocytic cells engulf and remove from tissues.

The induction of apoptosis is highly regulated by activating mechanisms, existing two main signalling pathways: the intrinsic, or mitochondria-mediated pathway, and the extrinsic, or extracellular activated pathway. The intrinsic pathway is usually activated in response to intracellular stress signals and depends on protein release from the intermembrane space of mitochondria. These signals include DNA damage, high levels of reactive oxygen species (ROS), viral infection and exposure to cytotoxic agents. The BCL-2 protein family senses these signals resulting in the initiation of mitochondrial apoptosis. The BCL-2 family is formed by the anti-apoptotic (BCL-2, MCL-1 and BCL-xL) and the pro-apoptotic (PUMA, NOXA and BAD) proteins as well as the effector proteins

(BAK and BAX). The balance among the different family members determines the activation of BAK and/or BAX causing mitochondrial outer membrane permeabilization (MOMP) and release of pro-apoptotic proteins such as cytochrome *c*, facilitating apoptosome formation and the activation of caspases 9 and 3. The extrinsic pathway is initiated by the binding of an extracellular ligand to cell-surface receptors, leading to the formation of the death-inducing signalling complex (DISC), which activates caspases 8 and 10. Activated caspase 8 can then cleave the effector caspases 3 and 7 to amplify the death signal **(Figure 4)**. In both pathways the proteolytic enzymes caspases are triggered to mediate a rapid disorganization of cellular organelles and architecture, as well as enabling a crosstalk between the two apoptotic pathways, resulting in death signal amplification.

1.5.2. Pyroptosis

Pyroptosis is a highly inflammatory form of non-apoptotic programmed cell death that is most frequently activated upon microbial infection (19). This form of cell death displays many morphological differences as compared to apoptosis. Classical apoptosis is characterised by the compartmentalisation of intracellular components and removal of cellular debris without any damage for the surrounding tissues. In contrast, during pyroptosis the nucleus remains undamaged, but the plasma membrane is disrupted, resulting in the leakage of intracellular components into the extracellular milieu.

Once the pyroptotic pathway is activated by a pathogen or some anticancer drugs, procaspase-1 is cleaved to active caspase-1 through the formation of the inflammasome (NLRP3/ASC/Procaspase-1). Then, active caspase-1 processes the proforms of the inflammatory cytokines interleukin 1β (IL-1β) and IL-18 into their active forms, resulting in cell death, that associates with the release of inflammatory cytokines into the surrounding environment. Moreover, caspase-1 also cleaves gasdermin D (GSDMD) generating the N-terminal and C-terminal fragments. The N-terminus of GSDMD translocates to the membrane and undergoes pore formation by oligomerization, which leads to extracellular content infiltration, cell swelling and then cell lysis **(Figure 4)**.

Recent studies indicate that chemotherapeutic drugs and targeted therapy drugs could activate pyroptosis in different cancer types. Molecular analysis of *in vitro* and *in vivo*

studies with HT29 and HCT116 CRC cell lines, revealed that lobaplatin reduced their viability exhibiting microscopic features of cell swelling and large bubbles emerging from the plasma membrane, as well as multiple pores in the membrane. In this lobaplatin-induced pyroptosis, GSDME, rather than GSDMD, was cleaved due to caspase-3 activation (20). Thus, the pyroptotic cell death could be a new target in cancer therapy.
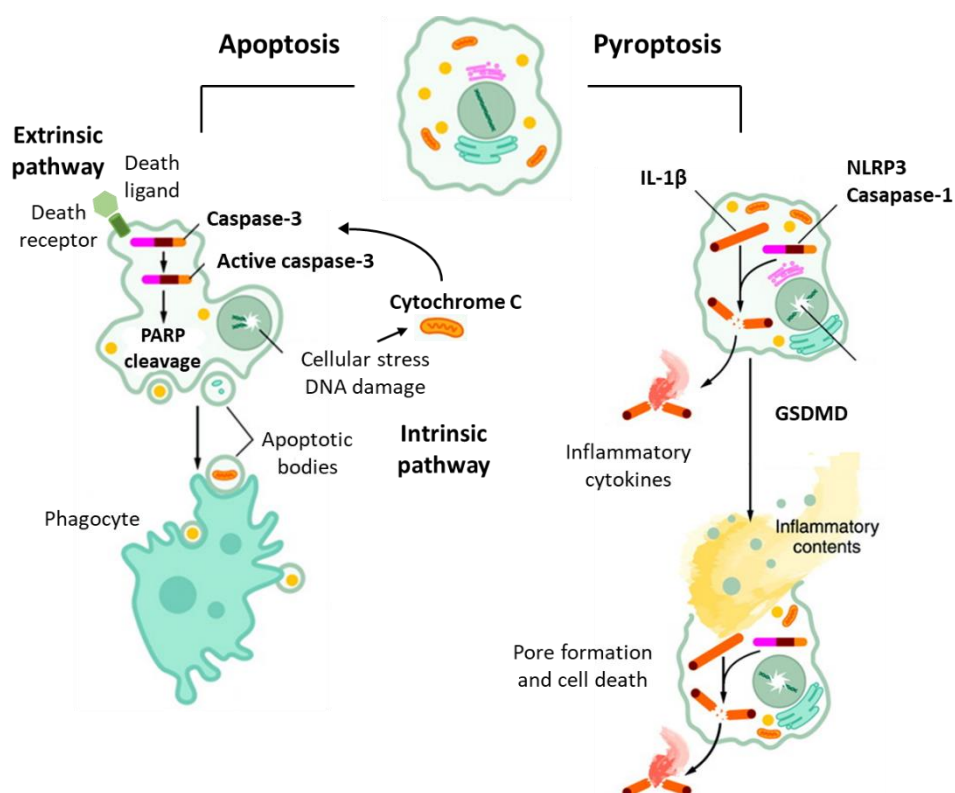
Figure 4. Apoptosis vs pyroptosis cell death pathways. Cells respond to death-inducing stimuli such as anticancer agents by initiating a variety of molecular pathways leading to cell death. Recently, non-apoptotic cell death mechanisms, such as pyroptosis, have been described. Apoptosis leads to cell death by activation of initiator caspases which in turn activate effector caspases to cleave cellular substrates. Pyroptosis is a cell death pathway mediated by the activation of caspase-1, a protease that also activates the inflammatory cytokines, IL-1β, and IL-18. This pathway is therefore inherently proinflammatory.

1.5.3. Mitotic catastrophe

Mitotic catastrophe is a process involving abnormal mitosis resulting from improper segregation of chromosomes during sister chromatid separation. Generally, it is not considered itself a form of cell death, but rather an irreversible trigger for death (21). Mitotic catastrophe results in the formation of giant, multinucleated cells with

condensed chromosomes, distinguishing them morphologically from other mechanisms of cell death. There are some biochemical hallmarks shared with apoptosis, in particular mitochondrial permeabilization and caspase activation (22). It is the most common mechanism of cell death in cancer cells exposed to ionizing radiation and other cytotoxic agents affecting DNA or microtubule assembly. Some of the anticancer agents affecting cancer cells by mitotic catastrophe are etoposide, taxol, cisplatin or bleomycin (23). Taxanes drive cancer cells to mitotic catastrophe through the hyperpolymerization of the microtubules (24). Moreover, since cancer cells are frequently deficient in cell cycle checkpoints, tumor cells may be particularly susceptible to the induction of mitotic catastrophe by these drugs.

2) METASTASIS AND CXCR4 RECEPTOR

2.1. Metastasis

One of the major hallmarks of cancer is the spread of primary tumor cells to adjacent organs or to distal sites. This process is referred to as metastasis and is associated with poor patient prognosis, being the foremost cause of cancer-related death. Metastasis causes 90% of all deaths from cancer and exhibits specific clinical characteristics. The metastatic progression is a dynamic process in which cancer cells undergo a series of sequential and complex steps **(Figure 5)**.

i) **Dissociation and local invasion:** to leave the primary tumor and infiltrate to the surrounding stroma, is required the activation of cellular mechanisms enabling cell movement, weakening cell–cell adhesions or degradation of the extracellular matrix (ECM). These processes are similar in normal cells during embryonic development and are known as epithelial-to-mesenchymal transition (EMT). Cells can migrate individually or collectively as multicellular groups, when cell–cell adhesions are retained. Molecularly, tumor cell dissociation requires loss of cell–cell adhesion, which is mediated by molecules such as cadherins, selectins and integrins, while mesenchymal cell invasion depends on protease activities.

ii) **Intravasation:** In the first step, tumor cells invade the endothelial basal lamina and migrate between the endothelial cells of the capillaries, and then enter the

circulation. During entry into the vascular system, tumor cells exhibit changes in shape which enable them to penetrate into endothelial cell–cell junctions. What governs cancer cell intravasation is still not fully elucidated, but evidence points toward intrinsic cancer cell signals, the activity of stromal cells such as macrophages and neutrophils, and organization of the ECM. Cell–cell communication and chemotaxis are also key elements in the intravasation process that can occur via paracrine signals mediated by cytokines or chemokines or by direct contact between different cell types such as macrophages and neutrophils, during tumor cell invasion.

iii) **Survival in the circulation:** only a small fraction of circulating tumor cells (CTCs) are capable to survive and extravasate in distant sites. Studies have shown that CTCs travel either as individual cells or, more often, as clusters (25). These clusters appear to maintain a partial EMT program which facilitate resistance to anoikis and an increased probability to seed and survive at secondary sites. This resistance to anoikis (apoptosis induced by inadequate cell–cell or cell–ECM interactions) in CTCs is driven through various mechanisms, including expression of the tyrosine kinase receptor TrkB192 or activation of non-canonical Wnt signalling. Moreover, during circulation, there is an important crosstalk among tumor cells and accompanying cancer-associated fibroblasts (CAFs), platelets, leukocytes, and endothelial cells.

iv) **Extravasation:** cells migrate from the blood or lymphatic system into the target metastatic organ. In this process, cancer cells first adhere to the vascular endothelium and then migrate across the endothelial cell lining, entering the surrounding tissue. Both the motility and vascular endothelium permeability of cancer cells are important for extravasation. In the seed and soil hypothesis, primary tumors in different organs show unique patterns of metastatic colonization to specific organs through site-selective adhesion (27). Several molecules such as the CXCR4 receptor, play a pivotal role in organ-specific metastasis. Another hypothesis supports that tumor cells are trapped in small vessels due to their size limit, since they tend to be larger than other circulating cells when they aggregate with platelets. Cancer cells start to proliferate in the lumen of vessels and destroy their walls and finally penetrate into the surrounding tissues.
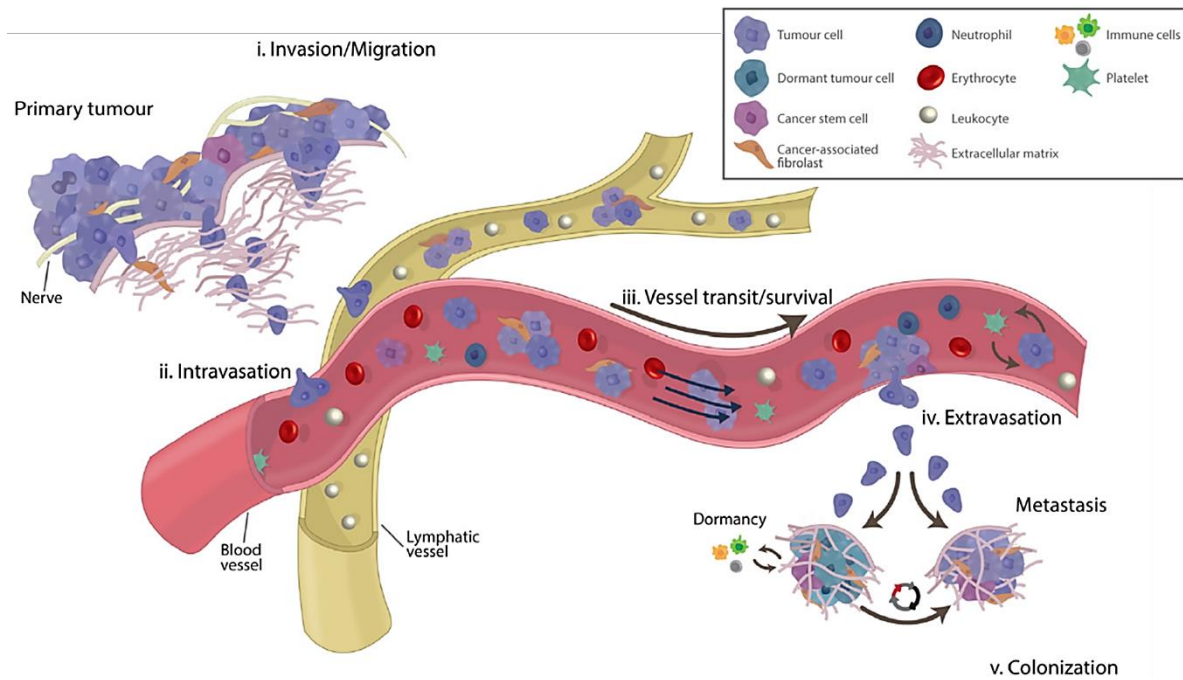
Figure 5. Schematic representation of spatial and temporal metastasis events. The process can be broadly divided into the following stages: **i**) invasion/migration at/near the primary tumor, **ii**) intravasation into the local blood and lymphatic vessels, **iii**) survival and transit of cancer cells in the circulation, **iv**) arrest and extravasation at secondary sites, and **v**) overt colonization of secondary sites. Adapted from (26).

v) Colonization of the secondary site: despite a high number of cancer cells enter the bloodstream daily, only a very small proportion survive, escape, and progress toward established metastases. It is known that the microenvironment plays an important role in sustaining their survival, regulating their growth, and conferring resistance to therapy.

These events are both influenced by the intrinsic cellular mutational burden of cancer cells and the crosstalk between malignant and tumor microenvironment cells. To colonize distant organs, metastatic cells must overcome many obstacles such as evading immune defences, adapting to supportive niches and surviving as latent tumor initiating cells. That is why, metastasis is a highly inefficient process, but once metastatic foci have been established, current treatments are failing in controlling their growth.

Conventional drugs for cancer treatment are mainly cytostatic agents designed to target the intrinsic cancer cell mechanisms such as cell cycle progression and further induction

of apoptosis. In many cases they are successful in reducing primary tumor size, however, they have poor effect on disseminated tumor cells since these cells have increased their heterogeneity and mutational burden, evading cell death. Thus, current research is focused in designing drugs which interfere with cell motility and targeting the different phases of the metastatic spread.

2.1.1. Metastatic routes

Primary tumor cells can spread to distant organs by activating different pathways which may vary among the different target organs. Cancer cells can travel along the body through the lymphatic system or the blood circulation.

Lymphatic spread consists in the transport of tumor cells to surrounding lymph nodes of the primary tumor and then, to distant lymph nodes. It is also the initial and the most common route of metastasis in carcinomas, whereas it is uncommon in sarcoma's progression. Localized spread to regional lymph nodes is not normally described as metastasis, but as secondary tumor, although is also correlated with poor outcome. Since the lymphatic system drains from the thoracic duct and right lymphatic duct into the systemic venous system, the metastatic cells can also eventually spread through the haematogenous route.

Intravasated tumor cells into the blood circulation are travelling through the haematogenous route. This is the most common route of sarcomas' metastasis, but also for certain types of carcinoma, like renal cell carcinoma. Because of their thinner walls, veins are more frequently invaded than arteries. Moreover, metastasis tends to follow the pattern of venous flow, with particular features depending on the location of the primary tumor. CRC spreads primarily through this route invading the portal vein and colonizing the liver.

In addition, there are other metastatic spreading routes such as the transcelomic in which tumor cells invade the serosal wall of the coelomic cavity to spread through the coelomic fluid. The peritoneal cavity is normally involved in CRC metastasis, but only occasionally pleural and pericardial cavities are affected.

2.1.2. Chemokines and chemokine receptors

Chemokines and their receptors are involved in the cancer metastasis process. Chemokines are a family of small (8-10 kDa) cytokines or signalling proteins secreted by cells. Their name is derived from their ability to induce chemotaxis, a directional migration of cells towards a gradient of the chemokine that binds to its corresponding G-protein-coupled receptor. These chemokine receptors are selectively found in the surface of their target cells. Receptors can form dimers or oligomers, which significantly increases the sensitivity and strength of the chemokine response.

Chemokines are divided into two main subfamilies depending on the arrangement of two N-terminal cysteine residues: CC chemokines with two adjacent cysteines and CXC chemokines with an amino acid between the two cysteines. There are almost 50 chemokines that bind 25 different types of receptors: while some chemokines bind a single receptor, others can interact with more than one, and, likewise, some chemokine receptors can be activated by several chemokines.

The major role of chemokines is to serve as chemoattractant to guide the migration of cells, and functionally, they can be classified as inflammatory or homeostatic chemokines. Inflammatory chemokines are released in response to bacterial or virus infection and actively participate in the inflammatory response by attracting leukocytes, monocytes and neutrophils from the blood to the infection sites. In contrast, homeostatic chemokines, such as CXCL12, are constitutively secreted by stromal cells of the bone marrow to coordinate cell trafficking and homing, essential processes during development and for immune system activation and homeostasis (28). Moreover, chemokines produced in distinct tissue microenvironments promote survival and cancer cell migration.

2.2. The CXCR4 chemokine receptor

Among chemokine receptors, the chemokine (C-X-C motif) receptor 4 (CXCR4) is the most commonly overexpressed in a variety of cancer types. This receptor belongs to the superfamily of seven transmembrane domain heterotrimeric G protein-coupled receptors (GPCRs) and is functionally expressed on the cancer cell surface. CXCR4 has an

extracellular N-terminus (34 aa), seven transmembrane alpha helices connected by three extracellular and three intracellular loops (ICL), and a C-terminus that is located in the cytoplasm **(Figure 6)**. The CXCR4 natural ligand is the stromal cell-derived factor-1 (SDF-1 or CXCL12) which is mainly secreted by bone marrow stromal cells. Stromal cells secreting CXCL12 can be found in various tissues, such as the liver, lungs, lymphatic tissues and the marrow (29). CXCR4 can form homodimers, heterodimers with other GPCRs such as the CXCR7 receptor or high-ordered oligomers. Recent studies support a 1:1 over a 1:2 CXCL12:CXCR4 binding stoichiometry. Upon ligand binding, CXCR4 is internalized by endocytosis and degraded in the lysosomes, through a degradation motif in its C-terminus and ubiquitination of vicinal lysine residues (30). This binding also triggers signalling cascades activating chemotaxis, enhanced intracellular calcium, cell adhesion, survival, proliferation, and gene transcription, through multiple and divergent pathways.

Although CXCL12 is the best known CXCR4 specific ligand, recent findings showed that there are other natural ligands able to bind and activate CXCR4 such as the pro-inflammatory chemokine macrophage migration inhibitory factor (MIF) (31) and Ubiquitin (32).
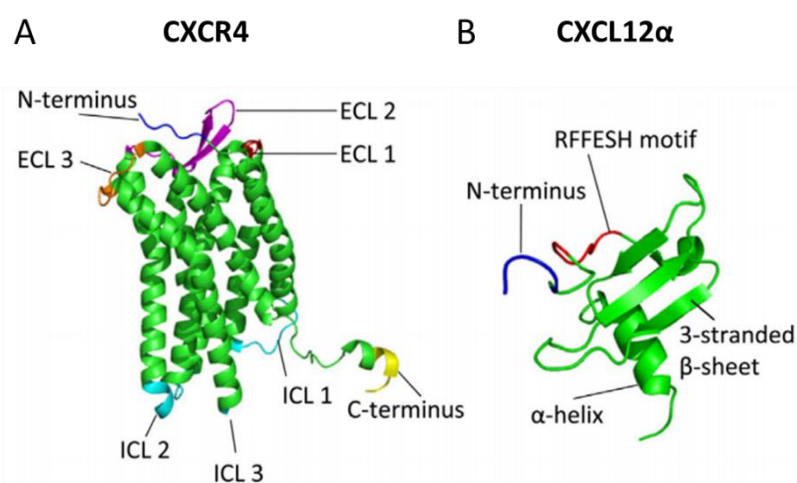
Figure 6. Three-dimensional structure of the CXCR4 receptor and its ligand CXCL12. A) Crystal structure of CXCR4 [Protein data bank identifier 3ODU]. CXCR4 can exist as a homodimer; here, only chain A is depicted. B) Crystal structure of CXCL12 isoform α [Protein data bank identifier 3GV3]. Each monomer includes a three-stranded β-sheet and one α-helix. Adapted from (33).

The CXCL12/CXCR4 signalling pathway plays and important role in many physiological processes. In physiological conditions low numbers of hematopoietic stem and progenitor cells (HSPCs) circulate from the bone marrow to the blood and back. This axis plays a crucial role in the homing and retention of HSPCs on the stem cell niches of the bone marrow and in regulating their mobilization into peripheral tissues upon injury or stress. CXCR4 is commonly expressed on most hematopoietic cell types including macrophages, monocytes, T and B lymphocytes and stem cells in blood or bone marrow. Thus, these CXCR4-expressing cells respond to and migrate along constitutive CXCL12 gradients secreted by endothelial cells in the bone marrow sinusoids as well as by bone marrow stromal cells.

Moreover, the CXCL12/CXCR4 axis has been widely studied in many pathological processes such as HIV infection, cardiovascular disease and cancer. For example, CXCR4 acts as an important coreceptor for human immunodeficiency virus (HIV) facilitating its entry in host CD4-positive T cells. Moreover, different studies have revealed that the CXCL12/CXCR4 axis is also expressed in cardiac myocytes and fibroblasts supporting a protective role after myocardial ischemia through an increase of cardiomyocytes survival and recruitment of protective circulating cells (31). The transcription factor hypoxia-inducible factor-1 (HIF-1), gets upregulated in hypoxic states and induces the local expression of CXCL12, which attracts circulating progenitor cells for tissue repair.

2.3. Role of CXCR4 in cancer

Although the initial studies were focused on the participation of CXCR4 in T-cells HIV infection, both the discovery of its involvement in B-cell trafficking and tissue localization in chronic leukaemia patients (34) and the regulation of organ-specific metastasis in breast cancer models (29) linked CXCR4 to a new research topic in cancer. The expression of CXCR4 is low or absent in many healthy tissues but is overexpressed in different tumor types being the most widely overexpressed chemokine receptor in cancer. Additionally, overexpression of CXCR4 in primary tumors has been associated with metastases in 15 different cancer types and contributes to tumor growth, angiogenesis, metastasis, and therapy resistance. CXCR4 overexpressing tumors, are likely to metastasise in an organ-specific and CXCL12-depedent manner (35), being lung,

liver, brain, kidney, skin and bone marrow the CXCL12 expressing organs. Supporting this fact, inhibition of the CXCL12/CXCR4 axis resulted in a reduced metastatic load in many cancer mouse models (36).

In CRC patients, CXCR4 overexpression in primary tumors correlates with poor survival, metastasis and recurrence (37). In this study, CXCR4 expression of different CRC cell lines, tumors and liver metastases was analysed demonstrating an overexpression of the receptor. Moreover, patients with overexpression of CXCR4 in the primary tumor had increased risk of local recurrence and distant metastases, lymph node involvement, as well as significantly decreased overall survival (9 months vs 23 months; log-rank p=0.03). The comparison of the CXCR4 expression between primary tumor and distant metastases showed a higher expression in metastases, especially in those developed in the liver **(Figure 7)**.
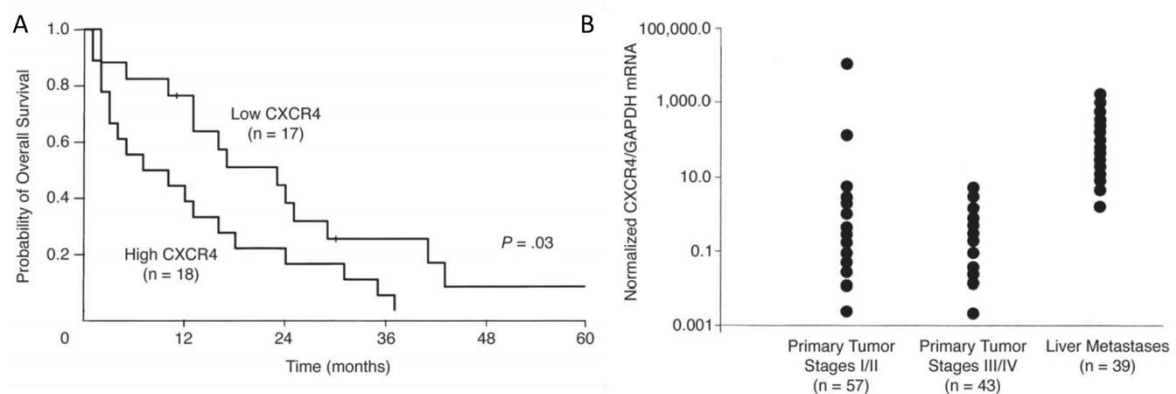
Figure 7. CXCR4 expression as a prognostic factor in metastatic CRC patients. A) Kaplan-Meier survival curves to compare overall survival between stage IV patients with high and low CXCR4 expression (median survival, 9 months v 23 months; log-rank P=0.030). B) Comparison of CXCR4 expression ratios in primary CRC tumors and liver metastases. Liver metastases had significantly elevated CXCR4 expression (P<0.0001). The median CXCR4 expression ratio for primary CRC specimens was used to determine high versus low expression. Adapted from (37).

In other studies, a high percentage of CRC samples stained for CXCR4 by IHC showed an homogenous cytoplasmatic and cell membrane expression pattern and approximately 58% demonstrated a CXCR4 overexpression (37,38). These observations support the role of CXCR4 expression in CRC growth, recurrence, and metastasis.

Surprisingly, *in vitro* CXCR4 surface expression levels were found to be low or absent in CRC cell lines while high expression levels were observed *in vivo* in animal models of liver metastasis (39). These findings suggested that CXCR4 expression by CRC cells is regulated by tumor microenvironment signals and the isolated metastatic cells exploit CXCR4 signalling for proliferation.

2.3. CXCR4 clinical significance

The important roles of the CXCR4 receptor in several diseases, including human immunodeficiency virus (HIV) infection, cancer, hypogammaglobulinemia, myelokathexis (WHIM) syndrome and pulmonary injury, have encouraged the development of viable CXCR4 antagonists for their treatment. Several CXCR4 inhibitors are being developed, especially for targeting CXCR4$^+$ cancer cells. Moreover, intense efforts have also been directed towards the development of suitable CXCR4-targeted molecular imaging agents (40).

Nowadays, the granulocyte colony-stimulating factor (G-CSF) is used in clinical management to stimulate the production of granulocytes, to accelerate patient recovery and reduce neutropenia after chemotherapy. G-CSF is also used in donors for hematopoietic stem cell transplantation to increase the number of hematopoietic stem cells in the blood of donors before collection by leukapheresis. Some studies revealed that G-CSF promotes the degradation of HSC anchorage in bone marrow and the release of these cells into peripheral blood, by down-regulating CXCR4 expression in bone marrow myeloid cells, which attenuate their response to SDF-1.

2.3.1. Anti-cancer drugs targeting CXCR4

Given the clinical relevance of CXCR4 expression concerning tumor growth and spreading in different types of cancer, a multitude of CXCR4-directed antagonists have been developed during the last decade. Among them, the AMD3100 (Plerixafor) is the unique compound approved by the FDA for the mobilization of hematopoietic stem cells and for the treatment of multiple myeloma and non-Hodgkin's lymphoma (41). Plerixafor is commonly used in combination with G-CSF to inhibit hematopoietic stem cell attachment to the bone marrow.

Many other CXCR4 antagonists are being developed and some of them are under clinical trials **(Table 1)**. Four major classes of CXCR4 antagonists can be distinguished: a) small peptide CXCR4 antagonists (T140), b) non-peptide CXCR4 antagonists (AM3100), c) antibodies against CXCR4 and d) modified agonists and antagonists for SDF-1.

Table 1. Synthetic CXCR4 antagonists under clinical investigation.

Drug name	Other names	Mechanism of action	Classification	Indication	Status
Plerixafor	AMD 3100; GZ316455; Mozobil	CXCR4 chemokine antagonist; Neuroplastin inhibitor	Non-peptide	Chronic lymphocytic leukemia; Glioblastoma; Neutropenia; Non-Hodgkin's lymphoma;	Marketed
USL-311	Proximagen	CXCR4 chemokine antagonist	Small molecule	Glioblastoma; Inflammatory disease; Solid tumor	Phase 2 Clinical
LY-2510924	CXCR4 peptide inhibitor	CXCR4 chemokine antagonist; Stromal cell-derived factor 1 ligand inhibitor	Small peptide	Renal cell carcinoma; Small-cell lung cancer	Phase 2 Clinical
PRX17756		CXCR4 chemokine antagonist	Small molecule	Glioblastoma	
BL-8040	TG-0054; bulishafu; burixafor	CXCR4 chemokine antagonist	Small peptide	Acute myelogenous leukemia; Metastatic pancreatic cancer; Multiple myeloma; Thrombocytopenia	Phase 2 Clinical

Ly2510924 is a small cyclic peptide and a potent selective CXCR4 antagonist. In a phase I trial, it showed few adverse effects and the stabilization of the disease in 9 patients (only 20%) (42). Other novel experimental CXCR4 antagonists are PRX17756 and BL-8040. PRX17756 has been shown to actively penetrate the blood-brain barrier and to accelerate GSC differentiation. The combination of PRX177561 with bevacizumab

resulted in a synergistic reduction of tumor growth with an increase of disease-free survival (DSF) and overall survival (OS) in a preclinical model of glioblastoma (43). BL-8040 is a small synthetic peptide with high affinity for CXCR4. When compared to other antagonists such as AMD3100, BL-8040 demonstrates higher affinity and longer receptor occupancy, providing a greater effect on the retention–mobilization balance of bone marrow stem cells in preclinical studies. In a recent clinical trial, safety and efficacy of the treatment with BL-8040 in combination with pembrolizumab and chemotherapy of metastatic pancreatic cancer patients was evaluated. The results suggest that combined CXCR4 and PD-1 blockade may expand the benefit of chemotherapy in pancreatic cancer (44). Therefore, all of these drugs need still to be tested in phase II clinical trials to assess their antitumor efficacy alone or in combination with classic radiotherapy or chemotherapy.

3) MOUSE MODELS IN CANCER RESEARCH

Prior to the development of genetic mouse models, cancer was mainly studied using *in vitro* cell culture systems of cell lines derived from human tumors. Although *in vitro* studies continue to provide valuable information and remain important to cancer research, their main limitations include the inability to examine interactions among tumor cells and their microenvironment, such as the extracellular matrix, and stromal and immune cells. The use of *in vivo* animal models has been crucial to understand the genetic basis of tumor development and cancer progression and continues to be relevant to test the efficacy of novel anti-cancer agents.

The animal model mostly used in cancer research is the mouse (*Mus musculus*). There are some advantages that justify the choice of the mouse as a model, such as its small size, easy handling, short tumor generation and its price, allowing the use of large numbers for statistical assessment. Moreover, it is the best genetically characterized of all mammals used in cancer research.

3.1. CRC mouse models

In the recent decades, despite a growing insight into the biology of CRC and many therapeutic improvements, the development of preclinical *in vivo* models remains

essential. The ideal CRC model must recapitulate the CRC progression from a precancerous adenoma to an invasive carcinoma with metastatic potential and should reflect the molecular heterogeneity of the disease among individuals. Cancer mouse models can be classified into different groups: syngeneic models, carcinogen-induced models, genetically engineered models and xenografts models **(Figure 8)**.

Syngeneic mouse models consist in the implantation of mouse cancer cell lines in an immunocompetent mouse strain. This type of mouse model retains an intact immune system, which is important to study the role of immune cells in the different phases of cancer progression. Moreover, they can provide an effective approach for studying how newly developed cancer therapies respond in the presence of a functional immune system and represents an important tool for efficacy and toxicology preclinical studies. However, the main limitations of these models, are the low number of mouse cancer cell lines available, their usually low metastatic yield and the possible differences between mouse and human tumor development and cancer progression.
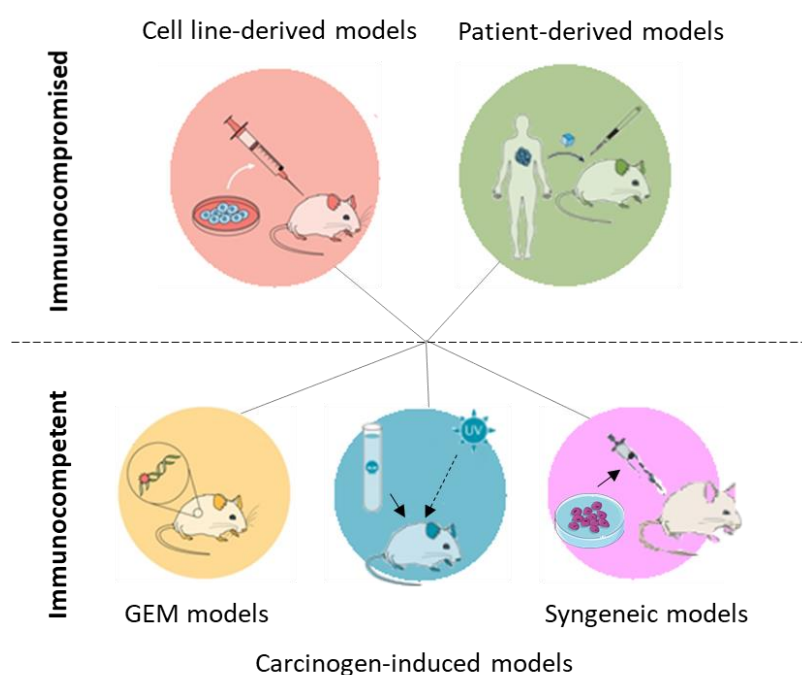
Figure 8. Mouse models for cancer research. Human tumor cell lines or patient-derived tumor samples can be transplanted in immunocompromised mice to develop a xenograft cancer model. In contrast, immunocompetent mouse models are developed by transplanting established mouse cancer cell lines in

recipient mice (syngeneic models) or by generating genetically engineered mouse (GEM) models or carcinogen-induced models. Adapted from (45).

In carcinogen-induced models, mice are exposed to specific carcinogenic compounds, until they develop the cancer of study. In CRC they provide a platform to evaluate the influence of diet, dietary supplements, chemopreventive interventions and the gut microbiome using diverse administration routes such as *ad libitum* feeding, oral, intraperitoneal, subcutaneous or intramuscular injection, or enema. In this model, the immune system remains intact, enabling the study of its contribution in this particular type of carcinogenesis. However, chemical-induced carcinomas are very heterogenous and rarely show invasive properties while distant metastases are usually absent.

Genetically engineered mouse models (GEMM) are obtained by modifying the mouse genome through the use of genetic engineering techniques. Genetic modifications can induce a gain of function of tumorigenic genes (oncogenes) or a loss of function of tumor suppressor genes, and spontaneously originate the cancer of interest. GEMM are the second most used model in cancer research and many CRC GEMM have been developed during the last decades contributing enormously to the understanding of the molecular processes of CRC initiation, progression and crosstalk of common cancer-associated pathways. However, these models have several limitations. First, they are more expensive and time-consuming than the other cancer mouse models because of the difficulty in the breeding to achieve the desired alteration. The breading process also generates many mice which are neither used for further breeding nor for research. Finally, the use of GEMM in preclinical studies is limited due to a lack of genetic heterogeneity and differences with the human tumor development.

3.2. Cell-derived and patient-derived xenografts

The majority of cancer studies use xenograft mouse models (45). Thus, our first objective was improving human CRC mouse models with high metastatic load to evaluate the antineoplastic effect of novel therapeutic nanoparticles. For the development of xenograft mouse models, human tumor grafts are implanted in immunocompromised mice for the successful engraftment and growth of human cells. As human tumor grafts, tumor cells, organoids or tumor tissue pieces can be employed. The original material of

these grafts can be either established human cell lines for the development of cell-derived xenografts or patient tumor samples to generate patient-derived xenografts (PDXs).

Cell-derived xenografts remain the most commonly used mouse models in basic and translational cancer research (82%) (45) because of their low cost, the synchronous tumor growth and their easy manipulation. However, PDXs are able to retain molecular, genetic and histopathological features of their originating tumor, for some limited *in vivo* passages, therefore being the best model to study inter-patient and intra-tumor heterogeneity of human cancer (46).

The use of xenografts models has some advantages compared to other mouse models. The employment of human cell lines or patient samples makes possible the study of specific signalling pathways in tumor progression, which in a syngeneic mouse model could show a different molecular basis. Moreover, the experimental conditions can be more easily controlled by deciding the localization of cell injection or the number of cells injected. However, the use of immunocompromised mice doesn't enable the study of the interactions between immune cells and tumors or the immune response in the development of new therapeutic agents. This limitation can be solved by humanizing the mice by the engraftment of various types of human leukocytes and purified human CD34$^+$ hematopoietic stem cells (HSCs) (47).

In addition, human cancer cells can be implanted in different anatomical locations. Thus, a particularly relevant xenograft mouse model is the orthotopic, which is generated by cell implantation in the organ that coincides with the original location of the primary tumor (e.g. colonic mucosa) while heterotopic xenograft model is considered when cells are implanted in a different location (e.g. subcutis).

3.2.1. Heterotopic mouse models

The subcutaneous models are among the most widely used heterotopic models, in which cells are injected under the skin, normally in the flanks of the mouse. They are frequently used in antitumoral drug development because of their easy establishment, reproducibility and tumor growth monitoring. However, large drug screenings showed

that subcutaneous models are of low value for the prediction of clinical response in humans (48). Moreover, the lack of interactions with the right tumor microenvironment makes that cancer cells rarely metastasise to regional o distant organs which render them unsuitable for the study of mechanisms of metastatic spread or for the development of antimetastatic therapies.

In previous studies, our group has shown that a subcutaneous preconditioning prior to orthotopic microinjection increased the metastatic dissemination of both HCT116 and SW48 orthotopic CRC models by increasing tumor cell survival and invasion at the tumor invasion front (49).

3.2.2. Orthotopic mouse models

The growing need for preclinical models that replicate more accurately human diseases, has led to the development of orthotopic cancer models. In the case of orthotopic CRC mouse models, cancer cells are injected in the serosa layer of the intestine (50) or in the cecal wall (51). These mouse models are more clinically relevant than subcutaneous models, because of their organ-specific tumor microenvironment which differs in each cancer type. The original microenvironment contains the relevant vasculature, a similar hypoxic condition and the stromal cell infiltration of the primary tumor. These adequate conditions can lead to a greater capability of cells to metastasize.

Whereas subcutaneous models are relatively easy to set up, the establishment of orthotopic tumor models requires a surgical procedure, which demands the use of anaesthesia. So, it represents a more invasive procedure that could affect the mouse general condition, being sometimes necessary a recovery time. Moreover, orthotopic tumor models need longer time courses for development and furthermore tumor growth and cancer cells dissemination can compromise animal welfare. Another major challenge is the follow-up of tumor progression in an orthotopic tumor model. Unlike subcutaneous models, primary tumors in orthotopic models are not always visible and bioluminescent or other optical imaging systems may be required (52).

4) NANOPARTICLES FOR CANCER TREATMENT

Currently, nanocarriers are widely studied in cancer diagnosis and therapy, as well as for the treatment of other disorders like cardiovascular and infection diseases. Following, we are describing their properties and their use for targeted drug delivery in oncology.

4.1. Nanoparticles and their key properties

Nanoparticles have unique biological properties given their small size (diameter within 1–100 nm) and high surface-to-volume ratio, which allows them to bind and carry anticancer agents, such as drugs, nucleic acids and proteins, along with imaging agents, with higher efficiency than currently used drugs.

Size is one of the most important features for nanoparticle's proper circulation and biodistribution. Nanoparticles smaller than 7 nm, can be easily cleared by physiological systems (filtration through the kidney), while particles larger than 200 nm may be cleared by phagocytic cells in the reticuloendothelial system (RES). Therefore, therapeutic nanoparticles with a size of <100 nm have longer circulation time in the bloodstream. Consistently, many studies reported that therapeutic nanoparticles in 20–200 nm size showed higher accumulation in tumors because they cannot be recognized by the RES or excreted by the kidney (53).

For different purposes, nanoparticles can be designed and functionalized to increase their efficiency, by controlling their size and surface properties. The surface charge of nanoparticles dictates their interaction with cell surface molecules and hence their cellular uptake (54). In general, nanoparticles functionalized with positively charged ligands exhibit higher internalization into cells compared to the neutral or negatively charged nanoparticles (55). Another issue that can be solved by functionalization is the entrapment of nanoparticles in the endosomes, preventing their access to the cytosol. Thus, the incorporation of signalling peptides in the nanoparticles' surface allows them to escape from endosomes and prevent lysosomal degradation (56). Moreover, in order to use nanoparticles as imaging agents for cancer diagnosis or to study nanoparticles' biodistribution, they can be functionalized by conjugation of fluorescent probes (57) or radioactive isotopes (58).

4.2. Targeted drug delivery for cancer treatment

Conventional therapeutic agents have limitations such as non-selectivity, undesirable side effects, low efficiency, and poor biodistribution. Current cancer research is focused on the use of nanoparticles to deliver drugs to specific cells or tissues. Targeted drug delivery refers to the capacity to direct therapeutic agents, aiming to enhance their accumulation in a desirable site. For efficient targeted delivery, the drug carrier should be retained in the physiological system, evade the immune system, target the specific cell or tissue, and release the payload therapeutic agent in the target site (59).

As a result, delivering drugs only to cancer cells using nanoparticles decreases cytotoxicity in normal cells, increases the antitumor effect and increases its systemic circulation time by avoiding renal and hepatic clearance (which can be retained in the liver sinusoids without being uptaken inside its parenchyma). In addition, highly potent drugs or toxins, or higher doses can be used without affecting normal cells. Tumor-specific targeting can be actively or passively achieved **(Figure 9)**.
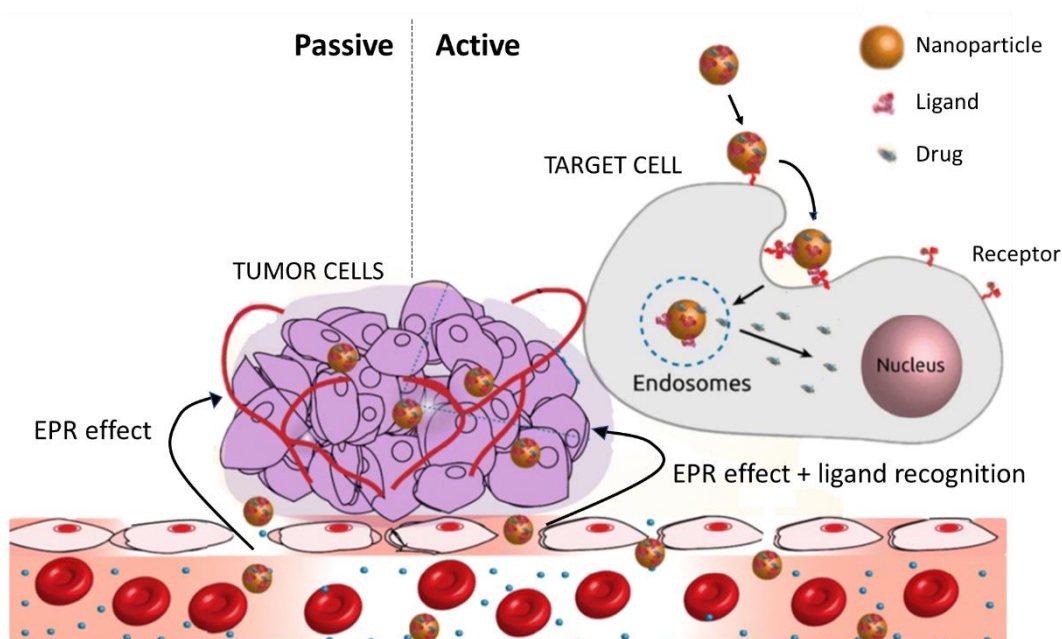
Figure 9. Targeted drug delivery for cancer treatment. Graphical illustration of passive and active drug targeting strategies. In passive targeting, the nanocarriers pass through the fenestrated capillaries irrigating the tumor and accumulate at the tumor tissue by the enhanced permeability and retention (EPR) effect. Active targeting can be achieved using specific ligands that bind to the receptors on the target tumor cell surface to enhance the delivery of the payload drug inside its cytosol. Adapted from (60).

4.2.1. Passive targeting

Passive targeting, in which nanoparticles reach the target tissue through enhanced permeability and retention (EPR) effect resulting from the leaky vasculature of the tumor cells, has been so far the most extensively explored strategy for targeting cancer (61), despite some researchers question their relevance in human tumors. In theory, the EPR effect allows preferential extravasation of the circulating macromolecules and poor lymphatic drainage which can lead to retention and passive accumulation of the nanoparticles in tumor tissues **(Figure 9)**. However, only a small percentage of these nanoparticles accumulate even in high-EPR xenografted tumors (less than 1%) (62). This could be due to multiple physiological barriers (clearance systems, endothelial barrier and plasma membrane) and a high degree of stochasticity involved in nanoparticles extravasation through the tumor vasculature. A major proportion of nanoparticles are also cleared by the mononuclear phagocytic system (MPS), some get trapped in the sinusoids of the liver and others are taken up by hepatocytes and Kupffer cells (63).

4.2.2. Active targeting

To overcome the challenges presented by passive targeting, active cellular targeting strategies have been developed. These approaches involve adding affinity ligands for cell surface markers on the surface of the nanoparticles to trigger specific homing, increased retention at the target site and uptake by target cancer cells **(Figure 9)** (64). The ligands are usually selected to bind to overexpressed receptors on cell membrane (e.g. HER2, CD44, etc).

Active targeting strategies are much more complexes than passive approaches. The major challenge is the complex design and engineering of these systems, which can complicate their pharmaceutical development, the scale-up production and significantly increase the cost of therapy. Despite these difficulties, one major advantage of active targeting nanoparticle-based therapies is their ability to target disseminated locations throughout the body that could potentially improve the treatment of hematological malignancies and metastatic lesions where EPR could not play a role.

4.3. Classification of drug nanocarriers

Generally, the drug nanocarriers used in cancer treatment can be classified into two major types: carriers that use organic molecules as major building blocks and those that use inorganic elements as their main structure. Organic nanocarriers are comprised of polymer-based nanoparticles (nanogels, dendrimers, protein nanoparticles) and lipid-based nanoparticles (liposomes, lipids and micelles). Inorganic nanocarriers as magnetic nanoparticles, quantum dots, gold nanoparticles and carbon nanotubes are commonly used in cancer drug development. Essential properties for nanocarriers success regarding clinical development are biodegradability, low toxicity, high specificity and efficiency and low immunogenicity.

4.3.1. Protein-based nanoparticles

Protein-based nanoparticles have many attributes that make them highly attractive as biological nanomaterials. For example, they are soluble, monodisperse, biodegradable, metabolizable, and easily adaptable by surface modifications to allow attachment of a drug and/or targeting ligands. Moreover, genetic, molecular and crystal structure information of many protein-based nanoparticles are available, facilitating their design and allowing for chemical and genetic modifications (65).

Protein-based nanoparticles can be produced as virus-like particles (VLP), bacterial inclusion bodies, eukaryotic aggresomes or self-assembling proteins, either in their natural hosts, as recombinant proteins in expressions systems (bacteria, yeast, plants and mammalian cells) or by cell-free protein synthesis. Most protein nanoparticles used in cancer therapy have been expressed and produced recombinantly in *Escherichia coli.*

Due to their large macromolecular structures, protein nanoparticle purification protocols tend to involve size exclusion chromatography (SEC) and/or differential centrifugation steps. To achieve higher purity, SEC is generally combined with affinity chromatography, in which the nanoparticle displays a pre-selected purification tag (histidine-tag), or ion-exchange, in which the outer surface charge is exploited.

4.4. FDA approved nanomedicines for cancer therapy

In the last few decades, nanomedicine has contributed significantly to the treatment of cancer and other diseases, however, only a few drugs are available in the market or undergoing clinical trials. Doxil was the first FDA approved (1995) nanodrug for the treatment of metastatic ovarian cancer and AIDS-related Kaposi's sarcoma. It contains doxorubicin, a member of the anthracycline group, encapsulated in an 80-90 nm size unilamellar liposome coated with PEG, that allows a longer recirculation of the drug in the bloodstream increasing the probability to reach cancer cells, while decreasing the cardiotoxicity produced by administration of free doxorubicin (66).

Another FDA approved nanomedicine is the albumin-conjugated nanoparticle (Abraxane®), a version of the anticancer drug paclitaxel. Paclitaxel (Taxol) belongs to an important class of antitumor agents called taxanes. Taxanes are cell cycle-specific agents that bind to microtubules resulting in the inhibition of mitosis and induction of cell death. However, they are highly hydrophobic, showing very low solubility in water. In order to solubilize paclitaxel cremophore and ethanol are used, which cause hypersensitivity reactions. However, Abraxane does not contain cremophore, avoiding the taxane dose-limiting toxicity. Abraxane formulation has increased the bioavailability of paclitaxel and resulted in higher tumor uptake, facilitated by albumin-receptor (gp60) mediated endothelial transcytosis (67). This therapeutic nanoparticle yields lower side effects and improved therapeutic indices than paclitaxel. Abraxane was approved for the treatment of metastatic breast cancer, advanced non-small cell lung cancer and advanced pancreatic cancer (68).

Table 2 summarizes the nanomedicines approved by the FDA for cancer treatment, which include liposomes, metallic and protein-based nanoparticles and the tumor types in which they are currently used.

Table 2. Nanomedicines approved by FDA for cancer therapy.

Nanostructure	Product	Nanoparticle formulation	Drug	Indication
Liposomes	Marqibo®	Sphingomyelin and cholesterol	Vincristine	Acute lymphoid leukaemia
	Mepact®	1-Palmitoyl-2-oleoyl-snglycero-3-phosphocholine and 1,2-Dioleoyl-sn-glycero-3-phospho-l-serine liposomes	Mifamurtide	Non-metastasizing osteosarcoma
	Onivyde®	Nanoliposomes	Irinotecan	Pancreatic cancer, Colorectal cancer
	Vyxeos®	Distearoylphosphatidylcholine, Distearoylphosphatidylglycerol, Cholesterol	Daunorubicin Cytarabine	Acute myeloid leukaemia
Protein-drug conjugates	Kadcyla®	Maytansine derivative, DM1	Trastuzumab	HER2+ breast cancer
	Abraxane®	Albumin	Paclitaxel	Non-small lung cancer, Pancreatic cancer
Metallic nanoparticles	NanoTherm®	Nanoparticles of superparamagnetic iron oxide coated with amino silane	-	Glioblastoma, prostate, pancreatic cancer

4.5. T22-GFP-H6 protein-based nanoparticle targeting CXCR4+ cells

Most FDA-approved nanomedicines for cancer treatment try to exploit passive targeting strategies. In collaboration with the Nanobiotechnology group led by Dr. Villaverde, from the Universitat Autònoma de Barcelona (UAB), our group developed protein-based nanoparticles capable of internalizing in CXCR4+ cancer cells. We exploited the strategy of using the receptor-mediated endocytosis to improve nanocarrier uptake in tumor

cells, that overexpress CXCR4, and consequently enhance its anticancer effect while reducing its systemic toxicity. For that, we initially studied the ability of four different peptide ligands of the CXCR4 receptor with internalization capacity in CXCR4+ cells (69). Only the T22 peptide efficiently penetrated target cells via rapid receptor-specific endosomal route. Thus, we propose T22 as a novel cell-targeting peptide suitable for functionalization of protein nanoparticles and appropriate for intracellular delivery in CXCR4 overexpressing tumors.

4.5.1. Structure of the T22-GFP-H6 nanoparticle

The T22 peptide is an engineered version of the polyphemusin II peptide from the horseshoe crab, in which three substitutions at residues Tyr5, Lys7 and Tyr12 highly increase its natural affinity for CXCR4 (70). This cationic peptide (8 K+R) was fused to the construct formed by the GFP fluorescent protein and a C-terminal polyhistidine tail (His6) and was then produced in recombinant *Escherichia coli*. Ten of these T22-GFP-H6 polypeptides spontaneously self-assemble as 12 nm in diameter nanoparticles with a toroidal architecture which avoid being filtered by the kidneys **(Figure 10)**.
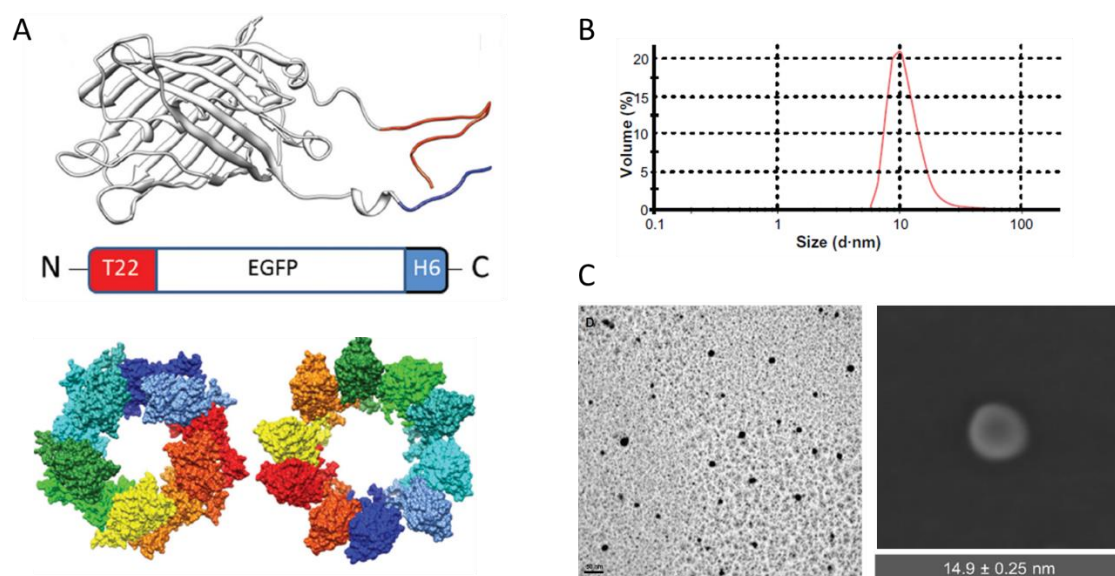
Figure 10. Characterization of the T22-GFP-H6 protein nanoparticles A) Predicted and schematic representation of the CXCR4 targeting nanoparticle formed by the self-assembling of 10 monomers of T22-GFP-H6. The colour code is maintained here for both ligand- (red) and H6- (blue) overhanging ends. B) Dynamic light scattering size analysis of T22-GFP-H6 nanoparticles in NaCO3H buffer. C) Transmission electron microscopy and scanning emission microscopy of T22-GFP-H6 nanoparticles.

The GFP protein allows the localization and quantification of the uptaken nanoparticles through its fluorescence emission, but it also contributes to the stability of the nanoparticles' final structure and to follow-up their *in vivo* biodistribution. The polyhistidine tail is necessary for their purification but it is also a key architectonic player in the supramolecular architecture of the nanoparticles. The presence of both the cationic T22 and the H6-tail is necessary for assembly, as GFP-H6 and T22-GFP solely occur as unassembled proteins. Moreover, divalent cations coming from the Nickel II (Ni^{2+}) cation remaining in the producing bacteria lysates are involved in protein assembly. Thus, the addition of the EDTA chelator promoted efficient disassembling of the nanoparticles. Free Ni^{2+} as well as Cu^{2+}, Ca^{2+} and Zn^{2+}, but not Cs^+ and K^+ cations, recovered the original nanoparticle size when added to the solution of disassembled polypeptides (71). In other studies, we found that changes in the number of histidines forming the tail, also affected the stability of the nanoparticles and their capacity of accumulating in tumor tissue (72).

4.5.2. T22-GFP-H6 functionalization with the endosomal escape peptide HA2

By incorporating the T22 ligand to our protein-based nanoparticles, our group has achieved an active CXCR4$^+$ cancer cell targeting, which directs specific binding and further endosomal-mediated cell uptake. Unfortunately, endosomal uptake drives the internalized material to a lysosomal pathway, resulting in acidification and proteolysis. A fraction of the nanoparticles reaches the cytoplasm due to background endosomal leakage and endosomolytic activities naturally present in the recombinant protein.

In order to increase the fraction of internalized material that escapes from endosomes, we searched for natural or modified peptides identified as endosomolytic. The N-terminal peptide HA2 from the influenza virus hemagglutinin has been widely explored in protein constructs designed for drug delivery (73). In acidic environments, such as the endosome, the anionic amino acids of HA2 get protonated, an alpha helix is formed and the peptide acts as an amphiphilic anionic stretch that destabilizes the cell membrane, promoting endosomal release of fusion proteins (74). Thus, we incorporated the HA2 peptide into the T22-GFP-H6 nanoparticle in two alternative inner positions (in the amino terminus of the core GFP, or its carboxy terminus) **(Figure 11)**. So, by efficiently

combining the selectivity of the T22 peptide with the HA2 endosomal escape domain we have achieved the expected functional improvement, therefore, designing powerful vehicles for targeted drug delivery (75).

	T22-GFP-H6	T22-HA2-GFP-H6	T22-GFP-HA2-H6
MW (kDa)	30.691	33.264	33.264
Size (nm)	14 ± 0	30 ± 1	46 ± 7
Specific fluorescence (unit/mg)	490 ± 6	188 ± 6	66 ± 0
CXCR4	68.7%	ND	31.5%
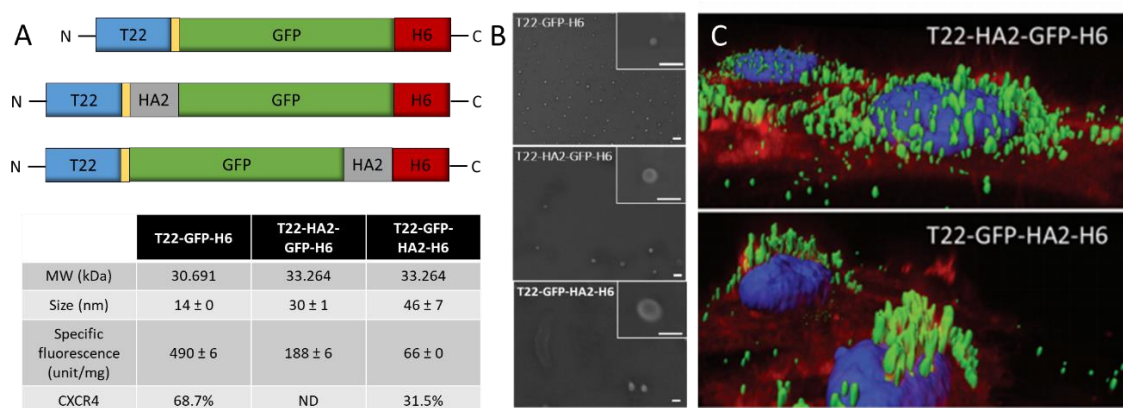
Figure 11. Incorporation of the fusogenic peptide HA2 into the T22-GFP-H6 nanoparticle A) Schematic representation of the polypeptidic building blocks forming the nanoparticles. Box sizes are only indicative. HA2 is the fusogenic HA2 peptide from the influenza virus hemagglutinin. A summary of relevant properties of the nanoparticles is found in the table at the bottom. B) Representative FESEM images of the assembled nanoparticles. Bars represent 40 nm. C) Isosurface representation of cultured HeLa cells within a 3D volumetric z axes stack upon incubation with 0.5 mM protein nanoparticles for 24 h. The cell membrane was labelled with CellMask (rendering a red signal), the nuclear DNA was labelled with Hoechst 33342 (rendering a blue signal) and protein nanoparticles are seen in green because of their intrinsic fluorescence. Bars indicate 5 μm.

4.6. Therapeutic derivatives of the T22-GFP-H6 nanoparticle

Once we developed the T22-GFP-H6 nanocarrier, we demonstrated its capacity to internalize efficiently in CXCR4+ cells of the primary tumor and distant metastasis of an orthotopic CRC mouse model (69) without signs of toxicity. We then proceeded to use it as a promising drug delivery system for cancer treatment, using different strategies to develop novel therapeutic nanoparticles. Firstly, the T22-GFP-H6 nanoparticle was conjugated to different therapeutic drugs, that are chemotherapeutics commonly used in the clinics or to very potent agents, not used in patients because of their toxicity. Secondly, toxins of bacteria (76), animals (77) and plants (78) or human pro-apoptotic factors were incorporated to the T22 polypeptides, to test the selectivity in delivering these agents to CXCR4+ cancer cells and their antitumor activity.

4.6.1. Nanoconjugates

On the basis of these previous results, we generated T22-GFP-H6-based nanoconjugates, using a variety of therapeutic agents covalently bound to the T22-GFP-H6 nanocarrier **(Figure 12A)**. In the first place, a cytotoxic drug commonly used to treat CRC liver metastases, Floxuridine (FdU), was covalently bound to the T22-GFP-H6 nanoparticle. T22-GFP-H6-FdU was synthesized by functionalizing the pentameric nucleotide oligo-FdU with thiol, which was subsequently conjugated to the T22-GFP-H6 nanoparticle previously bound to a chemical linker **(Figure 12B)**. Floxuridine is an antineoplastic pyrimidine analogue produced from a rapid intracellular metabolism of 5-fluorouracil when administered by intravenous injection. FdU is the main active metabolite of 5-fluorouracil and works by interfering with the DNA synthesis, preventing the incorporation of thymidine nucleotides into the DNA strand. We have already demonstrated an antimetastatic activity of T22-GFP-H6-FdU nanoconjugate as well as the absence of toxicity have already been demonstrated in metastatic CRC mouse models (79). In contrast to free oligo-FdU, intravenous repeated administration of T22-GFP-H6-FdU selectively accumulates and internalizes in CXCR4$^+$ cancer cells, triggering DNA damage and apoptosis, which leads to their selective elimination and to reduced tumor re-initiation capacity.

Since, the selective delivery of drugs to cancer cells using nanoparticles allows to increase the administered dose or even the use of highly cytotoxic drugs, we generated an additional nanoconjugate tested for anticancer effect in this thesis work. This novel nanoconjugate was produced by binding the T22-GFP-H6 nanoparticle to the toxin Auristatin E (Aur). Monomethyl Auristatin E (MMAE) is a potent tubulin polymerization inhibitor that was recently introduced in clinical oncohematology using antibody-drug conjugates (ADCs) (80). The T22-GFP-H6-Aur nanoconjugate was synthesized by covalent binding of a maleimide functionalized MMAE (MC-MMAE) to the amine groups of the external lysins of the T22-GFP-H6 nanocarrier **(Figure 12C)**. This reaction yielded an average of 18.5 MMAE molecules per protein monomer, that represents 204.5 MMAE molecules per nanoparticle.
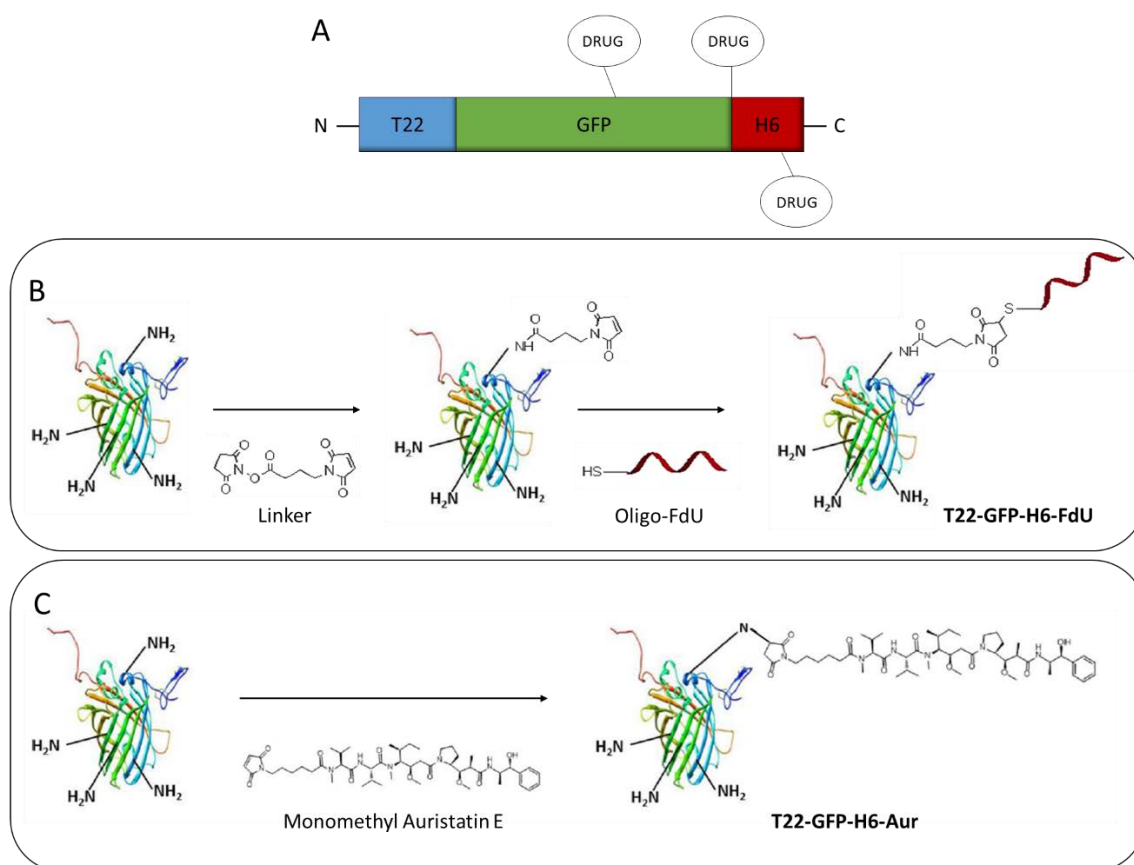
Figure 12. T22-GFP-H6-based nanoconjugates and their synthesis A) Schematic representation of a nanoconjugate, containing the fusion protein composed of the peptide T22 as a CXCR4 ligand, the GFP fluorescent protein and a histidine tail, bound to a generic payload drug. B) T22-GFP-H6-FdU chemical synthesis. C) T22-GFP-H6-Aur chemical synthesis using a maleimide functionalized Monomethyl Auristatin E (MMAE).

4.6.2. Toxin-based nanoparticles

The high potency exhibited by some toxins for toxin-mediated cell killing is an attractive approach to be explored in monotherapy or in combination with conventional chemotherapies. Over the last years, some promising treatments using immunotoxins that incorporated highly cytotoxic bacterial proteins have been tested in clinical trials (81). Only three of them, denileukin diftitox, tagraxofusp, and moxetumomab pasudotox have been FDA-approved for treating hematological cancers (82,83). No immunotoxins against solid tumors have been approved so far for clinical use.
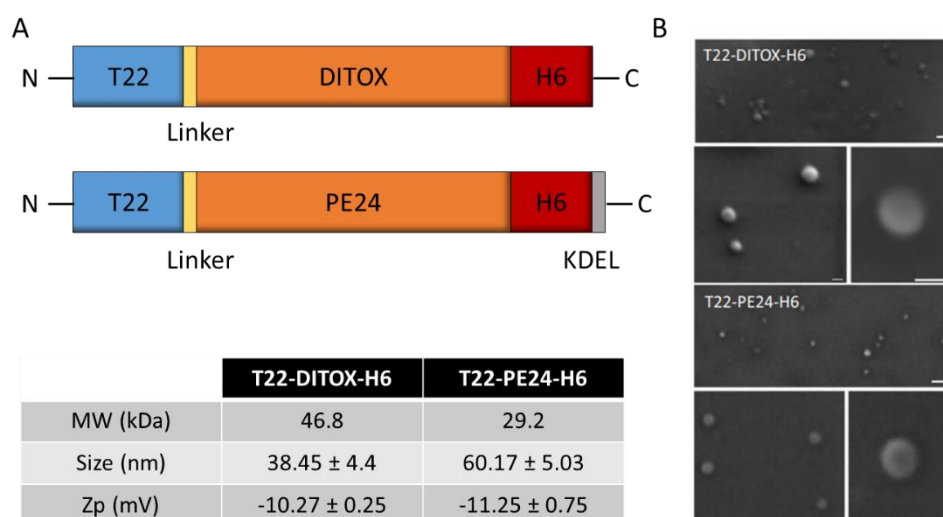
Figure 13. Characterization of toxin-based nanoparticles. A) Schematic representation of the polypeptidic building blocks of toxin nanoparticles. Box sizes are only indicative. Relevant properties of the nanoparticles are shown in the table at the bottom. B) Representative FESEM images of the T22-DITOX-H6 and T22-PE24-H6 nanoparticles. Bars represent 50 nm.

In this context, we produced novel nanotoxins to also test their anticancer activity in CRC models, during the development of this thesis. To that purpose, we engineered self-assembling nanoparticles containing the catalytic domain of the diphtheria toxin from *Corynebacterium diphtheriae* (DITOX) and the *Pseudomonas aeruginosa* exotoxin (PE24), targeting CXCR4, for the treatment of CXCR4$^+$ CRC tumors **(Figure 13)**. Both microbial toxins are ribosome inactivating proteins (RIPs) that inhibit the eukaryotic elongation factor 2 (eEF-2), preventing protein synthesis and consequently leading to irreversible cell death. When DITOX and PE24 toxins are fused to the CXCR4 ligand T22, they self-assemble as nanoparticles of a size between 30 and 60 nm. Moreover, a KDEL sequence was added in the C-terminus of T22-PE24-H6, which allows the efficiently binding to KDEL receptors at the Golgi apparatus during intracellular trafficking (84). Furin-cleavage sites were also inserted between the T22 ligand and each of the toxins to release the amino terminal peptide once internalized into target cells.

II. AIMS AND OBJECTIVES

II. AIMS AND OBJECTIVES

Although the survival for CRC patients has improved because of advancements in diagnosis and treatment, the invasion and metastasis of CRC cells to proximal and distant organs, associated with chemotherapy resistance and relapse, remain the major challenge for its treatment. Therefore, the general aim of this Ph.D. project was to develop highly metastatic CRC models with CXCR4 overexpression (CXCR4^{+}) to study the antineoplastic effect of therapeutic nanoparticles targeting CXCR4^{+} cancer stem cells using different strategies.

The objectives to achieve were:

1) Developing subcutaneous tumor models displaying CXCR4-dependent growth and highly metastatic CRC mouse models with CXCR4-dependent dissemination.

2) Studying *in vitro* the selective internalization and antitumor activity of T22-GFP-H6 and its therapeutic derivatives in CXCR4^{+} CRC cell lines.

3) Studying *in vivo* the biodistribution and toxicity of T22-GFP-H6 and its therapeutic derivatives in CXCR4^{+} subcutaneous tumors and non-tumor organs.

4) Evaluating the antineoplastic activity of the T22-GFP-H6 therapeutic derivatives in the developed CXCR4^{+} CRC mouse models with high metastatic rate.

III. MATERIALS AND METHODS

III. MATERIALS AND METHODS

1. *IN VITRO* EXPERIMENTS

1.1. Cell culture

1.1.2. CRC cell lines

SW1417, SW48 and HT29 CRC cell lines were purchased from the American Type Culture Collection (ATCC) and were cultured at 37 ºC and 5% CO_2 in DMEM (Gibco) supplemented with 10% fetal bovine serum (FBS, Sigma-Aldrich), 50 units/ml penicillin and 50 mg/ml streptomycin (Life Technologies). The SW1417 cell line is a human cell line stablished from a Dukes' type C, grade III, colorectal adenocarcinoma. We have found differences in CXCR4 expression between two vials obtained from different sources of this cell line. We named them as CXCR4$^+$ SW1417 the one with 70% of the cultured cells showing CXCR4 expression and CXCR4$^-$ SW1417 the one with no CXCR4 expression in any of the cultured cells.

1.1.2. Cell transfection with Luciferase reporter vector

The SW1417 CXCR4 expressing cell line was engineered to express firefly luciferase through a plasmid (pPK-CMV-F3, Promokine) transfection process using lipofectamine 2000 protocol (ThermoFisher) followed by an antibiotic selection **(Figure 14)**. For that, SW1417 cells ($2.5×10^5$ cells/well) were seeded in six-well plates overnight. Next day, we incubated the cells for 2 hours with Opti-MEM medium (Gibco) and transfected them with the luciferase plasmid (4 µg and 5 µg) according to the manufacturer's instructions. We tested two different ratios of DNA:lipofectamine (1:2 and 1:3) to find the more efficient condition. The control group was treated under the same condition but without DNA. After 24 hours, the medium was changed for DMEM medium containing 0.8 mg/ml of geneticin (G418, Life Technologies) and after 3 days we isolated the clone expressing higher levels of luciferase using the IVIS Spectrum Imaging System (PerkinElmer). This stable luciferase expressing clone was always maintained with DMEM medium containing 0.4 mg/ml of geneticin.
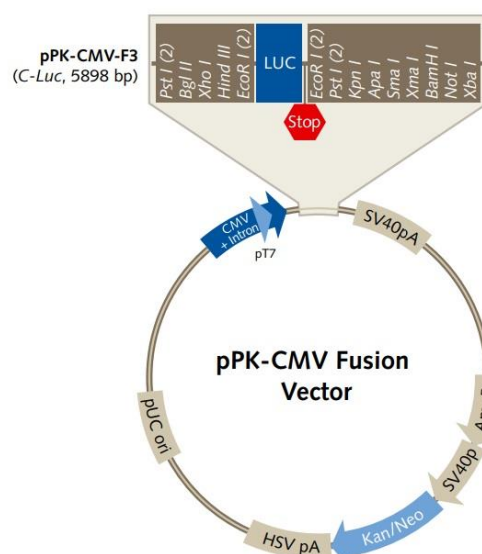
Figure 14. pPK-CMV-F3 plasmid map. Diagram of the plasmid used to transfect SW1417 cells to express luciferase. It shows the position of the luciferase sequence and the location of the plasmid functional elements. Restriction enzyme sites, promoters (CMV and SV40p) and terminators (SV40pA and HSVpA), resistance genes (Kan/Neo) and origin of replication (pUC ori).

1.1.3. Flow cytometry for CXCR4 levels determination

Before conducting all *in vitro* experiments and *in vivo* cell injections to generate CRC models, the levels of CXCR4 expression in the cell membrane were assessed by flow cytometry. For that purpose, we labelled 1 million cells in 100 µl of PBS with 5 µl of the PE-Cy5 Mouse Anti-Human CD184 monoclonal antibody (BD Bioscience) and 1 million cells in 100 µl of PBS with 5 µl of the PE-Cy5 Mouse IdG2a isotype (BD Bioscience) as a negative control. Cells were incubated in the dark for 20 minutes at 4ºC with gentle agitation, washed and analysed in the FACSCalibur cytometer (BD Bioscience). We measured both the percentage of the population expressing CXCR4 and the intensity of the expression expressed as mean fluorescence intensity (MFI).

1.1.4. ELISA for supernatant SDF-1 alpha determination

The enzyme-linked immunosorbent assay (ELISA) is a commonly used analytical biochemistry assay which uses a solid-phase immunoassay to detect the presence of a ligand, normally a protein, using antibodies directed against the protein of interest. In order to analyse and quantify the amount of stromal cell derived factor 1 (SDF-1 alpha)

secreted by different cell lines, we used the commercially available Human SDF-1 alpha ELISA kit (RayBiotech). For that purpose, $5x10^4$ SW1417 cells and 1BR3.G control fibroblasts were cultured in DMEM with 10% FBS, on 24 well plates for 48 and 72 hours. Then, supernatants were collected and analysed. In this case, the kit is designed as a colorimetric sandwich-based ELISA, in which the 96 well plate is coated with a capture antibody. Supernatants were added to the wells so that the SDF-1 alpha present in the samples was captured by the specific antibody. With a washing step, any unbound protein was removed from the wells. Then, an enzyme-linked antibody was added which also bound to the antigen. Finally, the enzyme's substrate was added and converted by the enzyme to a detectable colour. The absorbance of each well was measured using a spectrophotometer (FLUOstar OPTIMA, BMG Labtech) and the values were correlated to those from the standard curve to quantify the amount (pg/ml) of SDF-1 alpha per sample.

1.2. Fluorescent nanoparticles internalization assays

1.2.1. Flow cytometry

To evaluate the capacity of the GFP fluorescent nanoparticles to internalize in the $CXCR4^+$ SW1417 cells, we used flow cytometry after 24 hours of cell exposure to 400 nM nanoparticles concentration. Then, cells were washed with PBS and treated with trypsin 1 mg/ml (Life Technologies) in order to remove non-specific binding of the nanoparticles to the cell membrane. Cells were analysed in the FACSCalibur cytometer (BD Bioscience). The internalization competition assays were done by preincubating the cells with AMD3100 (ratio 1-T22-GFP-H6:10-AMD3100). Results of fluorescence emission were analysed with the Cell Quest Pro software and expressed as mean fluorescence intensity (MFI).

1.2.2. Confocal microscopy

We also evaluated the capacity of the GFP fluorescent nanoparticles to internalize in the $CXCR4^+$ SW1417 cells using confocal microscopy. For that, we seeded $2x10^4$ cells in each well of Lab Tek II Chamber Slides (Thermo Fisher) and incubated with 1 μM of T22-GFP-H6 and GFP-H6 as a negative control for 1, 5 and 24 hours. Then, cell membranes were

labelled with 2.5 µg/mL CellMaskTM Deep Red (Molecular Probes) for 10 minutes in the dark. Cells were washed in PBS and fixed with 3,75% formaldehyde for 10 minutes and mounted with ProLong Gold Antifade DAPI (Life technologies) labelling also the cell nucleus. Cells were imaged with the TSC SP5 II confocal laser microscope (Leica Microsystems) using a HC PL APO 63 × /1.4 oil objective.

1.3. Cell death determination assays

1.3.1. Cell proliferation assays

Cell viability was evaluated measuring the cell metabolic capacity using the XTT colorimetric cell proliferation kit II (Roche Diagnostics). The assay is based on the cleavage of the tetrazolium salt XTT in the presence of an electron-coupling reagent, to produce a soluble formazan salt. This conversion only occurs in viable cells. SW1417 cells were seeded in 96 well plates and incubated O/N at 37ºC. After 24 hours, the T22-GFP-H6 nanoparticle, or its therapeutic derivatives were added at different concentration range [0-2 µM] for 48 hours. Then, they were incubated with the XTT labelling mixture for 4 hours and quantitated the formazan dye formed using a scanning multi-well spectrophotometer at 490 nm (FLUOstar OPTIMA, BMG Labtech). The measured absorbance directly correlates with the number of viable cells. Data were reported as percentage of cell viability of nanoparticle-treated cells in relation to buffer-treated cell viability.

1.3.2. DAPI staining assays to detect DNA condensation

To quantify and determine the mechanism of cell death mediated by T22-GFP-H6-Auristatin in CRC cells, we detected DNA condensation by enhanced nuclear staining with DAPI dye in CXCR4^{+} SW1417 cells exposed to 1 µM T22-GFP-H6-Aur or buffer for 48 hours, in Lab Tek II Chamber Slides (Thermo Fisher). After incubation, cells were rinsed once with PBS and fixed (3.7% p-formaldehyde in PBS, pH= 7.4) for 10 minutes. Finally, cells were mounted with ProLong Gold Antifade DAPI (Life technologies). Under a fluorescence microscope (Olympus BX53, Olympus) the appearance of dead cells bodies (apoptosis) and mitotic figures (mitotic catastrophe) were observed and quantified in 10 high-power fields (200x) of each condition. The total number of cells

adhered to the slide was also quantified in the same fields and results presented as mean ± s.e.m..

1.3.3. Immunocytochemistry analysis of cell blocks

The study of cell death pathways induced by the different therapeutic nanoparticles was performed by aggregating treated cells in cell blocks and analysing them by immunocytochemistry (ICC). CXCR4$^+$ SW1417 cells were treated with 6 nM of T22-PE24-H6 for 2, 5, 24 and 48 hours and then trypsinized and centrifuged. The obtained pellet was mixed with plasma and thrombin (Sigma Aldrich) and quickly agitated to form a clot. The clot was placed in a tissue cassette, fixed with formaldehyde and then paraffin-embedded for further immunocytochemistry analysis (see **2.5.3.** section)**.** Percentage of stained surface and its intensity were calculated using the ImageJ software and the Colour Deconvolution Plugin with the H DAB vector to split the brown staining adjusting the threshold to 100 for NLRP3 images or 120 for caspase-1 images. Then, the Analyse particles plugin was used to detect all stained areas and the mean grey value was obtained combining all selected black areas. The intensity value was calculated by subtracting to 255 the mean grey value obtained in the analysis. Up to 5 high-power fields (400x) of each sample were analysed and the results were expressed as mean ± s.e.m..

1.4. Statistical analysis

All *in vitro* experiments, both internalization and XTT cell viability assays were performed in biological triplicates and the data were expressed as mean ± standard error of mean (s.e.m.). Normal distribution of the values was tested using the Shapiro–Wilk test. Results with normal distribution were analysed using the Student *t*-test whereas Mann-Whitney *U* test was used for the non-normal distribution data. All statistical tests were performed using GraphPad Prism 8 (GraphPad Software, Inc). Differences among groups were considered significant at a $p < 0.05$. IC$_{50}$ were calculated with SigmaPlot (Systat Software, Inc) using non-linear regression test with Hill-3 parameter adjustment

2. *IN VIVO* EXPERIMENTS

2.1. Mouse strains

To generate the CRC models to be used in the evaluation of the biodistribution and antimetastatic effect of the T22-GFP-H6 nanocarrier and its therapeutic derivatives we used different strains of immunodeficient mice. All animals were obtained from *Charles Rivers Laboratories*.

We used four-week-old female **Swiss Nude** (Crl:NU(Ico)-Foxn1^{nu}) mice to generate CRC subcutaneous models for conducting biodistribution and antitumoral assays. They carry a genetic mutation that causes an absent thymus, resulting in an inhibited immune system without mature T cells. The phenotype of the mouse is a lack of body hair.

We used four-week-old female **NOD SCID** (NOS.CB17-Prkdc^{scid}/NcrCrl) mice to generate CRC metastatic models by orthotopic cell implantation, to assess the antimetastatic effect of our tested nanoconjugates and nanotoxins. They are immunodeficient mice due to a mutation in the SCID gene impairing normal T and B lymphocyte development.

We used four-week-old female **NSG or NOD *scid* gamma** (NOD.Cg-Prkdc^{scid} Il2rg^{tm1Wjl}/SzJ) mice to also generate CRC metastatic models by orthotopic cell injection. These mice lack mature T cells, B cells, functional NK cells, and are also deficient in cytokine signalling.

Mice were housed in controlled ventilation racks, under specific-pathogen-free (SPF) conditions and fed with sterile food and water *ad libitum*. All animal experiments were approved by the institutional animal Ethics Committee of Hospital de Sant Pau i la Santa Creu and they were part of *an Animal Experimentation Procedure Protocol* approved by the Generalitat de Catalunya. The experimental conditions, including the mouse strain used for all the *in vivo* experiments are summarized in **Table 3**.

2.2. Cell implantation techniques

2.2.1. Subcutaneous injection of CRC cells

Mice were intraperitoneal (i.p.) anesthetized with a mix of 100 mg/kg of ketamine (Ketolar, Pfizer) and 10 mg/kg of xylazine (Rompun, Bayer). Once asleep, a cellular

suspension mixed with matrigel (1:1, Corning) was injected in one or two subcutaneous flanks using a 21G needle syringe (BD Bioscience). All the material and reagents (matrigel, media, syringes and needles) were previously cooled to avoid matrigel solidification. For all the conditions, we used harvested cell culture, washed with the corresponding media, counted and re-suspended to inject 150-100 µl per flank. The volume of the generated tumor was measured twice per week with a digital caliper.

We also generated a subcutaneous CRC patient derived xenograft (PDX) from the patient sample SP5. For that purpose, mice were anesthetized as explained above, and 10 mg of SP5 tumor tissue were implanted in the subcutis using a trocar. Several mice were used as donor animals to maintain *in vivo* the line. The tumor volume was measured twice per week with a digital caliper.

2.2.2. Tumor disaggregation

We have previously described that the subcutaneous preconditioning increased the invasion and metastatic capacity of CRC cell lines (49). To generate these SC+ORT models we used SP5 subcutaneous derived tumors from donor animals of the same strain. When these subcutaneous tumors reached a volume of 600 mm3, mice were sacrificed by cervical dislocation and tumors were excised, discarding the necrotic areas, and 300 mg of viable tissue was then cut into pieces and disaggregated in 0.05% trypsin (Invitrogen) and 100 mg/ml DNase (Sigma-Aldrich). The mix was pipetted 30 times, using a 10-ml pipette, and incubated for 10 min at 37°C with shaking. It was then re-pipetted 30 times, using 10-, 3-, and 1- pipettes, and re-incubated for 5 min at 37°C with shaking. The obtained cell suspension was filtered through a 0,45 µm cell filter (Millipore) and centrifuged at 1000 g for 10 min before cell counting.

2.2.3. Orthotopic injection of CRC cells to generate metastatic models

Mice were intraperitoneally (i.p) anesthetized with 100 mg/kg of ketamine and 10 mg/kg of xylazine. Once the paw withdrawal reflex disappeared, the cecum was exteriorized by a laparotomy. A total of 2 million cells re-suspended in 50 µl of culture media were then inoculated directly into the mouse cecum wall. A micropipette obtained as described (51) was used for the cell injection **(Figure 15)**. Afterwards, we pulled the pipette out

and cleaned the area around the injection with 3% iodine to avoid seeding of unlikely refluxed tumor cells into the abdominal cavity. The small diameter and flexible tip of the pipette and the angular and slow rate of administration diminished resistance to the injection, limiting tissue damage and bleeding, ensuring the absence of cell reflux. After injection, the gut was returned to the abdominal cavity and closed with surgical staples. Mice were followed once a week and euthanized when they had lost 10% of their body weight or showed signs of pain or illness.
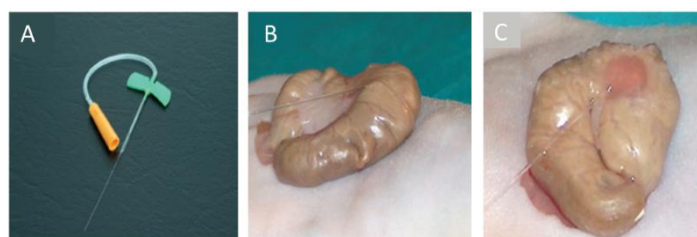
Figure 15. OCMI procedure into the cecum of immunosuppressed mice A) Micropipette made from Vitrex capillaries with a 250 μm-diameter tip B) Injection of two million human CRC cells per animal C) Reddish area depicts the tissue where tumor cell suspension has been injected.

Table 3. Experimental conditions for the *in vivo* CRC mouse models.

Location	Mouse strain	Cell line	Cell number	CXCR4 expression
SC	Swiss Nude	CXCR4 $^+$ SW1417	5×10^6	+
SC	Swiss Nude	CXCR4 $^-$ SW1417	5×10^6	-
SC	Swiss Nude	SP5	10 mg	+++
ORT	NOD/SCID	SW1417	2×10^6	+
ORT	NSG	SW1417	2×10^6	+
SC+ORT	NSG	SP5	2×10^6	+++

2.3. *In vivo* monitoring of tumor growth by bioluminescence

The successful transfection of the luciferase reporter vector in SW1417 CRC cells allowed us to monitor tumor development along time in *in vivo* experiments. Tumor growth in

mice was measured every 2-3 days by injecting intraperitoneally 2.25 mg of D-Luciferin (150 μl of the prepared 15 mg/mL stock, diluted in sterile physiological solution; PerkinElmer). After 5 minutes and under isoflurane anaesthesia (XGI-8 system, Xenogen), bioluminescent signals emitted by tumor cells, were detected and measured using the IVIS Spectrum Imaging System (PerkinElmer). Registration of bioluminescence emission was performed in the mouse ventral or dorsal position depending on the cell injection site. Exposure time was adjusted automatically according to the bioluminescence intensity of each mouse and cell line. Then, the obtained images were analysed with the Living Image Software (PerkinElmer) and the photons/sec emitted by cells were quantified for each mouse.

2.4. Nanoparticle biodistribution and antineoplastic effect

2.4.1. Biodistribution assays in subcutaneous CRC models

To study the biodistribution of different fluorescent nanoparticles such as the T22-GFP-H6 nanocarrier, the modified nanocarrier T22-HA2-GFP-H6 and the nanoconjugate T22-GFP-H6-Aur in tumor tissues and normal organs in mice, we used the subcutaneous CRC model established from the SP5 patient sample. Nanoparticles were administered. when tumors reached a volume of approximately 500 mm^3. Each experimental group of mice (N=2-3) received 200 μg or 326 μg single i.v. bolus of nanoparticle. Control animals (N=2-3) were i.v. administered with 150 μl of the correspondent buffer.

At 2, 5 and 24 hours after the i.v. injection, mice were euthanized and subcutaneous tumors and normal organs, including brain, lung, heart, kidney, liver, and bone marrow were collected. Biodistribution of the containing GFP nanoparticles was determined measuring *ex vivo* the fluorescence emitted by tumors and normal organs using the IVIS Spectrum equipment (PerkinElmer). The fluorescent signal (FLI) was first digitalized, displayed as a pseudocolor overlay, and expressed as radiant efficiency. FLI values were calculated subtracting the FLI signal from the protein-treated mice by the FLI auto-fluorescent signal of control mice.

2.4.2. Biodistribution in CXCR4 competition assays

To study whether the tumor uptake and biodistribution of the tested T22-GFP-H6 and T22-GFP-HA2-H6 nanoparticles was selective and dependent on CXCR4 expression in tumors we used the SP5 subcutaneous model. For these competition studies, we used the CXCR4 antagonist AMD3100 (Sigma-Aldrich), which is able to downregulate CXCR4 in cancer cells. Mice were randomized in 5 groups (N=2). The T22-GFP-H6 and T22-GFP-HA2-H6 groups received a 200 μg i.v. bolus of the corresponding nanoparticle. The AMD3100 competition groups were subcutaneously administered with three doses of 10 mg/kg of AMD3100 (1 hour before, and 1 and 2 hours after the nanoparticle injections). The control group received an i.v. bolus of buffer. Mice were euthanized 5 hours after nanoparticle administration and the GFP fluorescent signals emitted by tumors and non-target organs was recorded **(Figure 16)**.
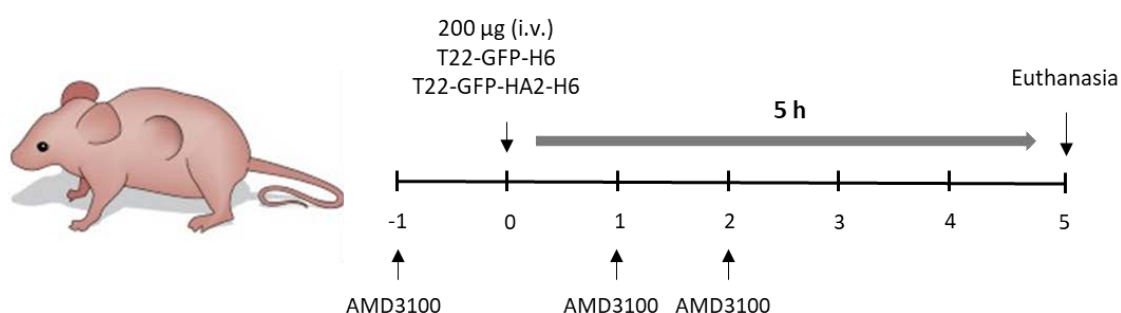
Figure 16. Administration regime for the CXCR4 blocking nanoparticle biodistribution assays. Mice bearing SP5 subcutaneous tumors were injected with three subcutaneous doses of AMD3100 at 10 mg/kg. The time point of mice euthanasia was 5 hours after the i.v nanoparticle. administration, corresponding to the fluorescence intensity (FLI) peak.

2.4.3. Antitumor activity assessment in subcutaneous CRC models

To assess the antitumor activity of the T22-GFP-H6-Aur nanoconjugate and the T22-PE24-H6 nanotoxin we used the SW1417 subcutaneous model in Swiss Nude mice. Once tumors reached approximately 120 mm^3 size, mice were randomized in control or treated group and received intravenous doses of the therapeutic nanoparticles at a repeated dose regime of 100 μg of T22-GFP-H6-Aur (N=10 mice) or 10 μg of T22-PE24-

H6 (N=6 mice), 3 times a week, per 8 doses. The control group received buffer using the same administration schedule. Overall the experimental period, mouse body weight and tumor volume were registered 3 times a week. Tumor bioluminescence was also measured once a week using the IVIS Spectrum equipment. When tumors reached a volume of 600 mm^3, mice were euthanized and mitotic, apoptotic, necrotic rates and CXCR4 expression were assessed in tumor tissue samples **(Figure 18)**.

2.4.4. Antimetastatic activity assessment in orthotopic CRC models

To assess the antimetastatic activity of the nanoconjugate T22-GFP-H6-Aur and the nanotoxin T22-PE24-H6 we used the SW1417 orthotopic model in NSG mice. SW1417 cells were injected in the cecum of NSG mice and 3 days after, primary tumor bioluminescence was measured using the IVIS Spectrum equipment. Mice were then randomized into the control (N=9-10) and the nanoparticle-treated (N=9-10) group. Treated mice received intravenous doses of T22-GFP-H6-Aur or T22-PE24-H6 at repeated dose regime of 100 µg or 5 µg respectively, 3 times a week, for a total of 12 or 18 doses, respectively **(Table 4)**. The control group received buffer using the same administration schedule. Overall the experimental period, mouse body weight and health status were controlled 3 times per week. Primary tumor bioluminescence was registered once per week using the IVIS Spectrum equipment and the experiment was finished when the first mouse of the buffer-treated group needed to be euthanized. Necropsy and *ex vivo* imaging of the organs of interest were performed 24 hours after the last dose **(Figure 18)**.

Table 4. Doses and dose regime details of T22-GFP-H6-Aur nanoconjugate and the T22-PE24-H6 nanotoxin used in the antimetastatic effect experiments with the CXCR4$^+$ SW1417 cells growing orthotopically in NSG mice.

Nanoparticle	Mice number	Dose	Dose regime	Number of bolus	Cumulative dose
NaCOH3 NaCl buffer pH 8	N=10	150 µl	3 times per week	12	-----

T22-GFP-H6-Aur	N=10	100 µg	3 times per week	12	1200 µg
NaCOH3 buffer pH 8	N=9	150 µl	3 times per week	18	-----
T22-PE24-H6	N=9	5 µg	3 times per week	18	90 µg

2.5. Necropsy and tissue processing

2.5.1. Necropsy and bioluminescence *ex vivo* imaging

In all experiments, mice were euthanized by cervical dislocation. Endpoint criteria was different in each experiment according to the objective. In experiments with mice carrying subcutaneous tumors, they were euthanized when the tumor reached a maximum size of 800 mm^3. Tumor final volume was calculated using the formula: V = (Dxd^2)/2 where D is the longer diameter and d the shorter diameter. To assess mouse survival time after orthotopic cell injection, mice were euthanized when the health status of the mouse was poor (mucous secretions, lack of mobility, dishevelled hair), there was loss of body weight (more than 20% of the initial weight) or due to behavioural changes (self-mutilations, hunched posture, passiveness). In antimetastatic effect experiments, all mice were euthanized when the first control mouse met the endpoint criteria explained above.

Animal models derived from bioluminescent cells (SW1417 cell line) were imaged using the IVIS Spectrum Imaging System as explained in **2.3.** section (*in vivo* imaging) before the euthanasia. Then, a complete necropsy procedure was performed and all relevant organs (liver, kidneys, lungs, diaphragm, spleen, pancreas, colon, intestinal tract and mesenteric lymph nodes) were collected and covered in a 0.75 mg/kg D-Luciferin solution in 12 or 6 wells plates and imaged (*ex vivo* imaging). For non-bioluminescent mouse models (SP5 patient-derived samples), a complete necropsy procedure was performed, organs were collected in cassettes (Thermo Fisher), fixed and cut for histopathology and immunohistochemistry analyses.

2.5.2. Sample processing and histopathological analysis

After necropsy, the collected organs were fixed in 4% formaldehyde in phosphate-buffer solution (PBS), dehydrated, paraffin embedded, cut and stained with hematoxylin-eosin or used for immunohistochemistry or immunofluorescence assays.

1. Sample dehydration: after tissue fixation for 24 hours, samples were dehydrated. Dehydration is the removal of water from aqueous-fixed tissue. Since most fixing solutions are aqueous, this step is necessary to prepare the tissue for embedding in non-aqueous media like paraffin. First, organs were washed 3 times with distilled water to remove all the fixing solution. Then, samples were immersed 3 times for 10 minutes each in solutions with increasing concentrations of ethanol (70, 80, 96 and 100%). During this procedure the water in tissues is replaced by alcohol. Last, samples were incubated for 10 minutes in 3 solutions of xylene 100% to dissolve the alcohol in the samples.

2. Paraffin embedding: the dehydrated tissue is ready for infiltration with a suitable histological wax. The most popular is the wax-based paraffin. Paraffin is liquid at 60°C and can be infiltrated into tissue at this temperature. At 20°C it solidifies to a consistency that allows sections to be easily cut. Thus, samples were 3 times immersed for 1 hour in a paraffin solution at 60ºC. After 3 hours, each sample was located in a mould over a cassette, filled with molten paraffin and placed in a cold plate to solidify.

3. Sectioning: once paraffin was solidified, samples were cut in 3-5 µm sections with a microtome and mounted in glass microscope slides.

4. Rehydration: to remove the paraffin from tissues, slides were incubated for 1 hour at 60ºC and then immersed twice in 100% xylene. To hydrate the tissues, slides were immersed twice in 100% ethanol, once in 96% ethanol, 80% ethanol and 50% ethanol.

5. Hematoxylin-eosin staining: slides were incubated for 5 minutes with distilled water, following 5-10 minutes with the Mayer hematoxylin solution and washed with distilled water for 15 minutes. Once some of the tissue structures were distinguished, 2 more washing steps were done, and then slides were incubated

for 0.5-2 minutes with 0.2% eosin. Samples were again dehydrated and covered with mounting media (Toluene-Free Mounting Medium, Dako) and a coverslip.

2.5.3. Immunohistochemistry analysis

Immunohistochemistry (IHC) is the most common application of immunostaining and involves the process of selectively identifying antigens (proteins) in cells of a tissue section. IHC staining is widely used in the diagnosis of abnormal cells such as those found in tumors or detection of specific molecular markers which are characteristic of particular cellular events such as proliferation or cell death.

We have used IHC in the tissue samples obtained from *in vivo* experiments to assess the expression of CXCR4 in subcutaneous tumors, CRC primary tumors and metastases located in distal organs. Markers of apoptosis such as active caspase-3 protein (early apoptosis) or proteolyzed PARP (late apoptosis) or pyroptosis such as NLRP3, cleaved caspase-1 and cleaved GSDMD, were also assessed in tumors to evaluate mechanistically the antitumor effect of the administered nanoconjugate or nanotoxin **(Table 5)**.

Table 5. Primary antibodies used in the IHC studies.

Primary antibody	Dilution	Secondary antibody	Suppliers
CXCR4	1/200	Rabbit	Abcam
Active Caspase-3	1/300	Rabbit	BD Pharmigen
Proteolyzed PARP	1/300	Rabbit	Promega
NLRP3	1/300	Mouse	Adipogen
Cleaved Caspase-1	1/400	Rabbit	Life Technologies
Cleaved GSDMD	1/200	Rabbit	Cell Signaling

All IHC studied samples were fixed, dehydrated, paraffin embedded and sectioned as explained in **2.5.2**. section. Tissue sections were mounted in coated microscope slides

with positive charges (*FLEX IHC* Microscope Slides, Dako) to assure sample adhesion. Then, samples were incubated for 1 hour at 60ºC and rehydrated as explained in **2.5.2**. section. Masked epitopes were recovered by heat-induced antigen retrieval using the *PT Link* system (Dako) at 95ºC for 10 minutes and at 65ºC for 45ºC in a Tris/EDTA buffer solution with pH 9 (high pH, Dako) or a citrate buffer solution with pH 6 (low pH, Dako). The automatized *Autostainer Link* 48 (Dako) was used for the sample staining following the next incubation procedure: 1 minute with *rinse buffer*, 5 minutes with *Peroxidase-Blocking Reagent*, 1 minute washing with *rinse buffer*, 30 minutes with the primary antibody diluted in *rinse buffer* (Table), 1 minute washing with *rinse buffer*, 20 minutes with *EnVision/HRP*, 1 minute washing *with rinse buffer*, minutes with the chromogenic solution (*DAB+ Chromogen and Substrate Buffer*), 1 minute washing with *rinse buffer*, 5 minutes with hematoxylin and 1 minute final washing with *rinse buffer* **(Figure 17)**.
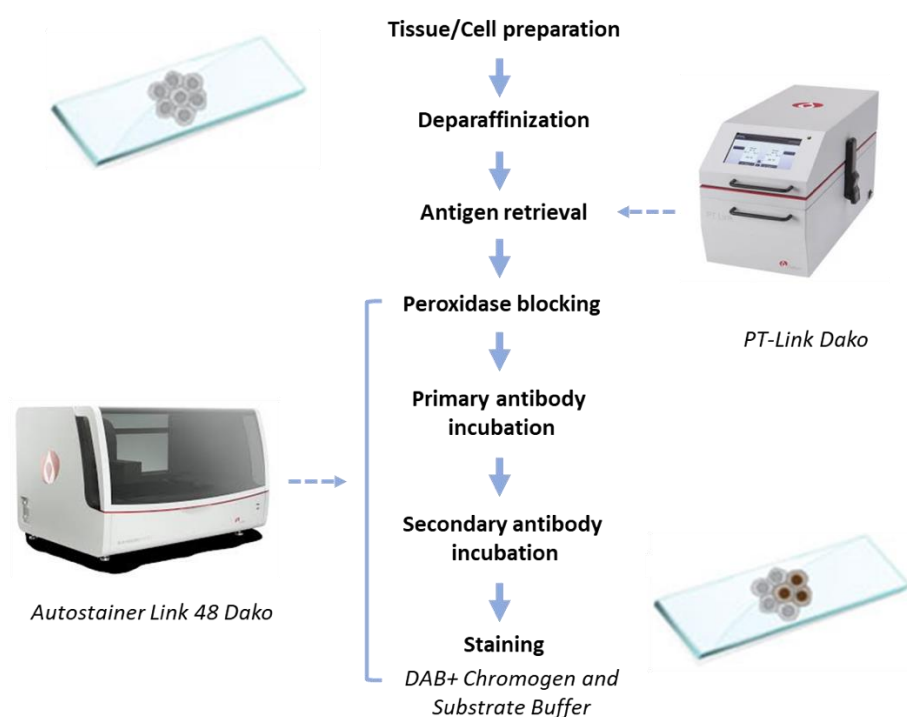
Figure 17. **Overview of the main steps of IHC using Dako systems on paraffin-embedded tissue slides.**

Results were presented as number of stained cells or as percentage of stained surface. The percentage of brown area was calculated using the ImageJ software and the Colour Deconvolution Plugin with the H DAB vector to split the brown staining. Up to 5 high-power fields (400x) per sample were analysed and results were expressed as mean ± s.e.m..

2.5.4. Immunofluorescence analysis

Immunofluorescence assays were used to detect nanoparticles, containing the GFP domain, in mouse tissues and to study their co-localization with the CXCR4 membrane receptor in cancer cells. Paraffin-embedded SP5 tumors treated for 5 hours with T22-GFP-H6 or T22-GFP-H6-Aur were sectioned and then stained with the primary antibodies anti-CXCR4, and anti-GFP together with the DAPI fluorescent stain.

Sample fixation, rehydration and antigen retrieval were completed as explained in the immunohistochemistry analyses section. Subsequently, we performed 3 washing steps with TBS 1x (132 mM NaCl, 10 mM Tris pH 7.5, 0.1% Tween 20) and blocked the unspecific binding of the secondary antibody by incubating the samples 1 hour with a TBS + 0.5% triton + 3% donkey serum solution (Millipore). Primary antibodies were also diluted **(Table 6)** in this solution and samples incubated overnight at 4ºC. They were washed again 3 times with TBS 1x and then incubated with the secondary antibodies **(Table 6)** diluted in TBS 1x for 2 hours at 37ºC. Tissue auto-fluorescence was reduced by incubating the samples with sudan black 1% (Panreac) in 70% OH for 4 minutes. Samples were washed again 3 times with TBS 1x, stained for 10 minutes with a 1/10000 DAPI staining solution (ThermoFisher), covered with a special mounting medium and a coverslip and sealed with nail polish.

Table 6. Antibodies used in the IF studies.

Antibody	Type of antibody	Host species	Dilution	Fluorescent dye	Suppliers
Anti-CXCR4	Primary	Rabbit	1/300	-	Abcam
Anti-GFP	Primary	Chicken	1/250	-	AVES
Anti-Rabbit	Secondary	Donkey	1/200	Alexa Fluor 647	Jackson
Anti-Chicken	Secondary	Donkey	1/50	Alexa Fluor 488	Jackson

Representative pictures were taken using Confocal TCS SPE (Leica) at 200× or 600× magnifications. Immunofluorescence measurements were performed using the ImageJ software.

2.5.5. Assessment of mitotic, apoptotic and necrotic rates

Tumor sections stained with DAPI were also used to evaluate the cancer cell proliferation capacity and tumor growth rate by counting the number of mitotic figures per 10 high-power fields (magnification 400x). To assess the apoptotic effect of the administered nanoparticles in tumors we counted the number of apoptotic bodies in H&E and DAPI stained tissues in 10 high-power fields (magnification 400x). DAPI staining was performed in Triton X-100 (0.5%) permeabilized sections mounted with DAPI mounting media (ProLong Gold antifade reagent, Thermo Fisher). Samples were evaluated under a fluorescence microscope at a wavelength of $\lambda ex = 334$ nm/$\lambda em = 465$ nm. We also analysed the percentage of necrotic areas in H&E stained tumors by using Cell^D Olympus software at 15x magnification.

2.6. Metastatic foci quantitation

In the orthotopic *in vivo* experiments, the spreading of cells from the primary tumor (colon) to other distant organs was analysed in H&E-stained samples. We studied those organs were metastatic dissemination is expected in CRC: liver, lung, mesenteric lymph nodes and peritoneum. These organs were collected at necropsy, imaged *ex vivo* using the IVIS Spectrum and processed for histological analysis. Depending of the experiment and the bioluminescence signal, only one or several slices were analysed. When the signal was high, only one slice of each organ was quantified. If the signal was low because of the low number of metastatic foci, 3 slices of each organ were quantified. An Olympus microscope with the Cell^D Olympus software was used to count the number and measure the size (expressed as μm^2) of all observed metastatic foci. Representative images of them were also taken.
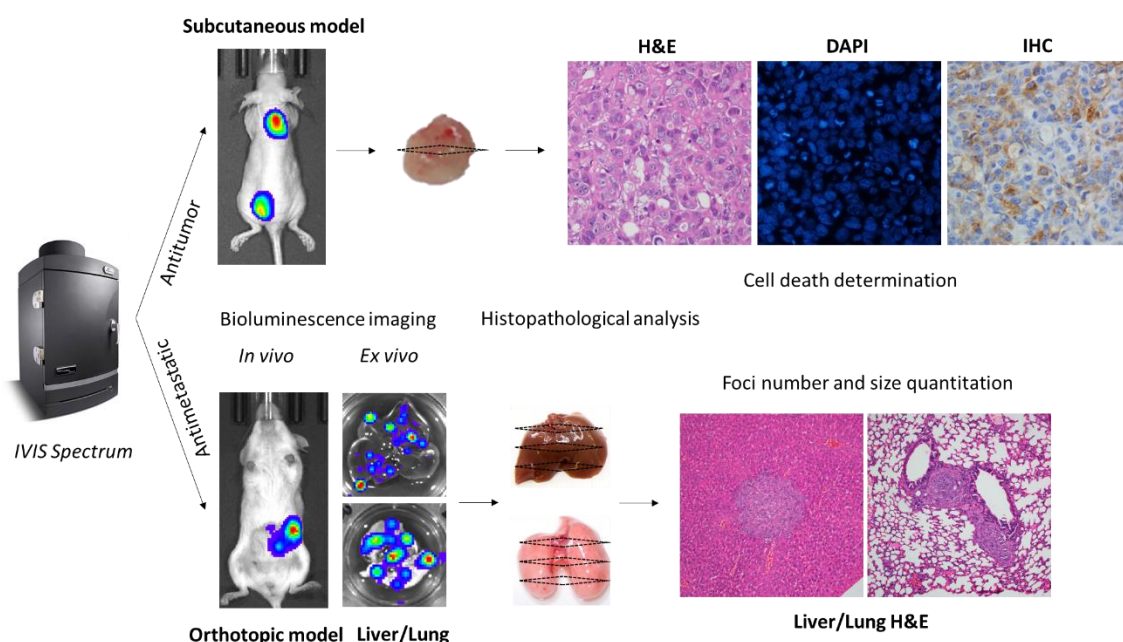
Figure 18. Schematic representation of the antineoplastic effect assessment. Bioluminescent subcutaneous and orthotopic CRC models were used to study the antitumoral and antimetastatic effect, respectively, of therapeutic nanoparticles. Cell death mechanisms were determined in treated subcutaneous tumors in H&E, DAPI and IHC sections. The antimetastatic effect was evaluated counting and measuring metastatic foci in 3 different sections of organs such as lymph nodes, liver, lung and peritoneum.

2.7. Statistical analysis

In all *in vivo* experiments, we analysed whether differences between control and experimental groups are significant, using the Mann-Whitney *U* test, since data obtained for all measured variables did not follow a normal distribution. We analysed differences in the number of metastatic foci and foci size between NOD/SCID vs NSG mice and buffer-treated vs nanoparticle-treated mice. Results on the number of mitotic figures, number of apoptotic bodies, and active-caspase 3, proteolyzed PARP, cleaved caspase-1 and cleaved GSDMD stained cells between groups were analysed using both the Student's t-test and the Mann-Whitney *U* test. Data were reported as mean ± s.e.m. and differences between groups were considered significant at $p < 0.05$. The differences between relevant data were indicated as * for statistically significance among the designated groups. Statistical calculations were performed using GraphPad Prism 8 software.

IV.RESULTS

IV. RESULTS

1) DEVELOPING CXCR4-DEPENDENT SUBCUTANEOUS AND HIGHLY METASTATIC CRC MOUSE MODELS.

In order to generate animal models to test the biodistribution and antineoplastic effect of the T22-GFP-H6 nanoparticle and its therapeutic derivatives, new CRC mouse models were developed. For that purpose, we first studied the CXCR4 cell surface expression in different CRC cell lines and their tumorigenic capacity. Following, we developed non-metastatic subcutaneous CRC models and highly metastatic orthotopic CRC models that replicate the pathogenesis, progression and clinical evolution observed in CRC patients.

As PDX models have become very important in translational cancer research, because they retain tumor heterogeneity and better predict the sensitivity to treatment than cell-line derived models, an orthotopic CRC mouse model derived from a patient sample was also developed. CXCR4 receptor over-expression was observed in cancer cells in all models, both in primary tumors and in distant metastases.

1.1. Cell surface expression of CXCR4 in CRC cell lines

The expression of the CXCR4 chemokine receptor in the cell surface of different CRC cell lines (SW1417, SW48 and HT29) was determined by staining with a specific antibody and subsequent analysis by flow cytometry. Contrary to previous reports, and as shown in **Figure 19**, SW48 and HT29 cell lines were negative for CXCR4 expression (85,86). In the SW1417 cell line analyses, we have noticed differences in CXCR4 expression between this cell line purchased from the ATCC and the same cell line used in different laboratories. These cell lines were maintained separately and named CXCR4$^+$ SW1417 or CXCR4$^-$ SW1417, depending on their presence or absence of CXCR4 receptor expression. We have also noticed that the percentage of cells expressing CXCR4 in their membrane can decrease with consecutive passages or treatments (87) because this receptor tends to internalize into the cytoplasm while being cultured *in vitro*. We determined that the percentage of CXCR4$^+$ cells used for all the *in vitro* testing of our nanoparticles and

therapeutic nanoconjugates, or to generate relevant and consistent CXCR4+ CRC models, had to be around 70-80% to ensure reproducibility and comparability among studies.
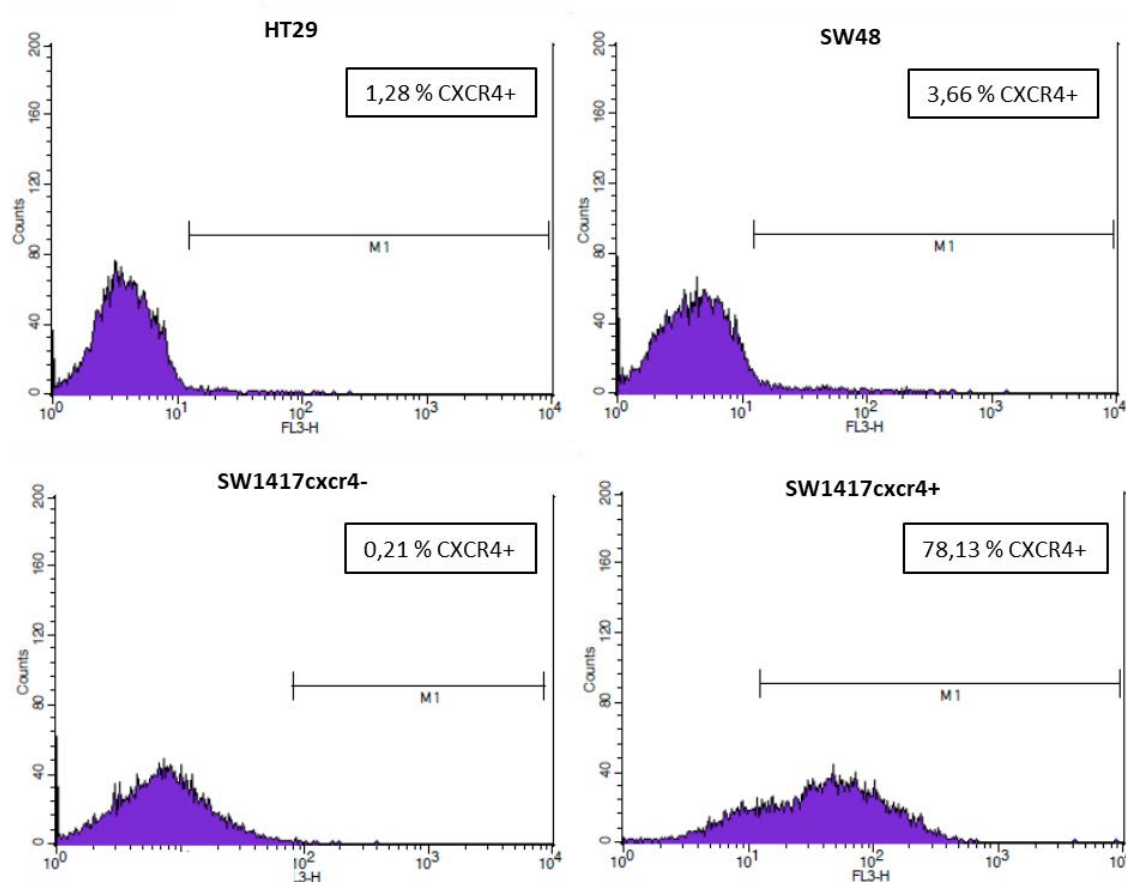
Figure 19. Flow cytometry histograms of the CXCR4 cell surface expression of different CRC cell lines. The CXCR4 cell surface expression was analysed in the HT29, SW48 and SW1417 CRC cell lines. The M1 interval represents the CXCR4 positive cells from the whole population.

1.2. Effect of CXCR4 expression in the tumorigenic capacity of the SW1417 cell line

The differential capacity to develop subcutaneous tumors derived from the CXCR4+ SW1417 and CXCR4- SW1417 cell lines was assessed by injecting them in the subcutis of Swiss nude mice. **Figure 20A** shows tumor growth curves and the differential CXCR4 expression in tumor tissue developed in the subcutis at the end of the experiment. All injected mice formed tumors within 1 week after implantation. However, in CXCR4- SW1417 cells injected mice (N=5) tumor volume decreased at 14 days post-

transplantation, being total tumor growth negligible at the end of the experiment. In contrast, all mice injected with CXCR4+ SW1417 cells (N=5) developed subcutaneous tumors that displayed a constant growth **(Figure 20A)**. Moreover, a significant percentage of cancer cells in the model derived from CXCR4+ cells overexpressed the receptor in their cell membrane **(Figure 20B)**. Thus, we have developed SC CRC models that maintain CXCR4 expression in tumor tissue and could be useful to test CXCR4 targeted therapeutic nanoparticles.
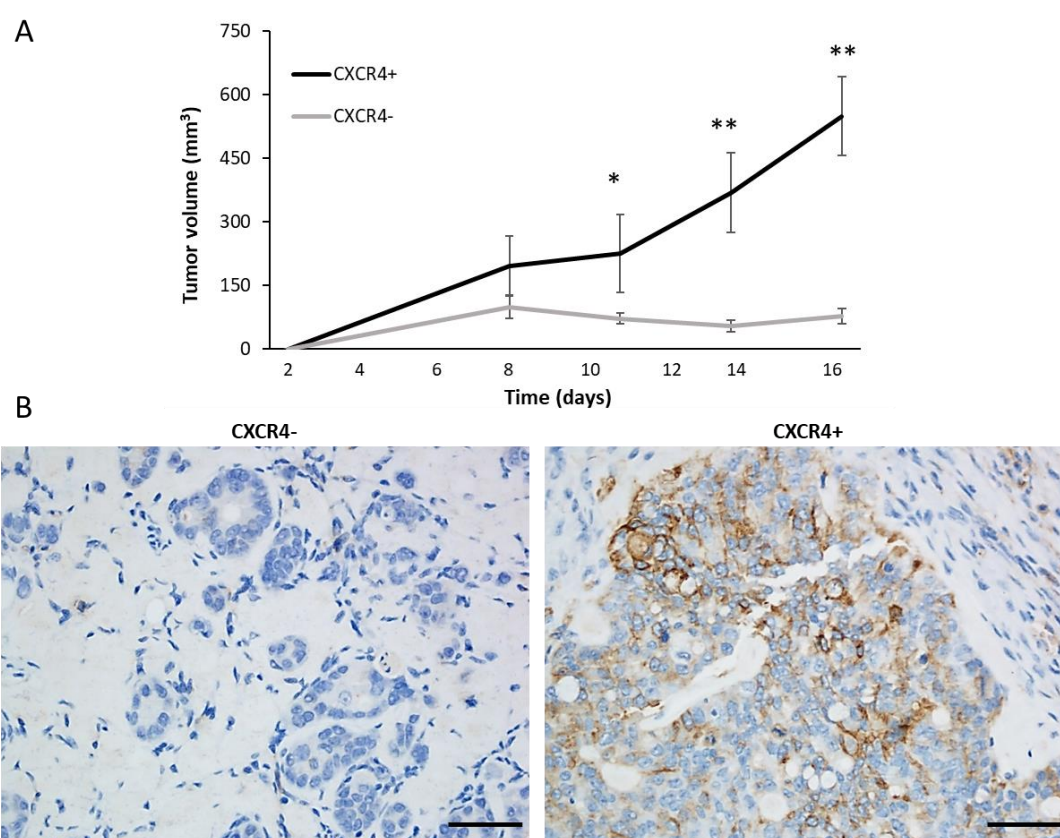
Figure 20. Tumorigenic capacity of the SW1417 cell line A) Tumor growth of subcutaneous tumors derived from CXCR4+ SW1417 or CXCR4- SW1417 cells implanted in Swiss nude mice B) Representative images of CXCR4 immunohistochemistry staining of the developed subcutaneous tumors. * $p<0.05$; ** $p<0.01$. Scale bars: 50 µm.

1.3. Generation of a cell-derived CXCR4+ bioluminescent metastatic CRC mouse model

The microinjection of CXCR4+ SW1417 cells in the cecal wall of NOD/SCID and NSG mice generated new metastatic CRC models. NOD/SCID mice (deficient in T and B cells) died from intestinal obstruction, which caused abdominal distension, as a consequence of high primary tumor growth 71 days after intracecum implantation. In contrast, cell microinjection in NSG mice (deficient in T, B and NK cells) replicated the dissemination pattern observed in patients and caused mice death in only 48 days **(Figure 21A)**. These mice were not sacrificed because of abdominal distension, but because of loss of body weight, indicating that the distant target organs could be affected by metastasis. Moreover, expression of luciferase by the SW1417 injected cells allowed us to follow primary tumor growth **(Figure 21B)**. In NOD/SCID mice primary tumor growth was progressive, causing intestinal obstruction and mouse death. In contrast, in NSG mice, the primary tumor size increased until week 6 after cell injection and remained growing at a constant rate. Representative *in vivo* bioluminescent images of SW1417 tumor growth in NSG mice and macroscopic hepatic metastases, responsible for mice death, are displayed in **(Figure 21C)**. When tissues were microscopically analysed, multiple mesenteric lymph nodes, hepatic, pulmonary and peritoneal metastases were observed in both, the NOD/SCID and the NSG model **(Figure 21D)**. NOD/SCID mice developed very large primary tumors but few metastatic foci in the target sites such as mesenteric lymph nodes, liver, lung and diaphragm. In contrast, NSG mice developed smaller primary tumors but many more metastatic foci in the same distant locations.
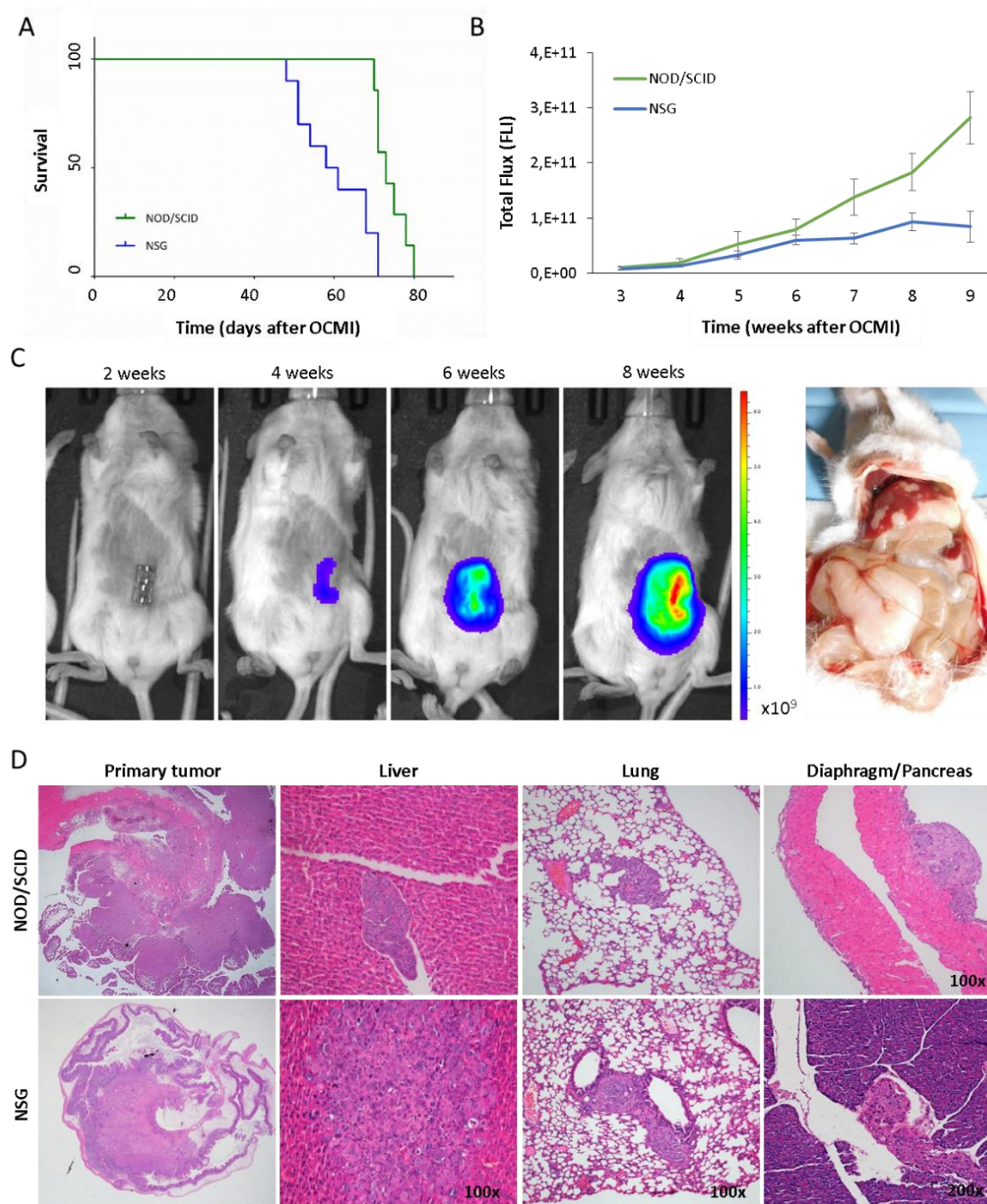
Figure 21. Primary tumor growth and metastatic dissemination of CXCR4+ SW1417 CRC cell-derived orthotopic models A) Kaplan-Meier survival curves of NOD/SCID (N=9) and NSG (N=10) mice injected orthotopically with SW1417 cells (p=0.016, Log-Rank test) B) NOD/SCID and NSG primary tumor growth analysed by measuring the bioluminiscence emitted by SW1417 cells C) Representative *in vivo* bioluminescent images of tumor growth over time in NSG mice, and macroscopic primary tumor and hepatic metastases D) H&E staining of representatives CRC primary tumor and hepatic, pulmonar and other metastases observed in both NOD/SCID and NSG models.

1.3.1. The metastatic capacity of the CXCR4⁺ SW1417 cell line increases in severely immunosuppressed mice

NOD/SCID and NSG mice orthotopically injected with CXCR4$^+$ SW1417 cells showed both 100 % of engraftment. However, the metastatic capacity of the tumors derived from this cell line increased in NSG mice, a more immunosuppressed mouse strain. As compared to the SW1417 NOD/SCID model, the metastatic rate in SW1417 NSG mice resulted in a 5-fold increase in the number of hepatic (p<0.01) and pulmonary (p<0.01) metastases **(Table 7)**. Moreover, the absence of a specific immune cell type in NSG as compared to NOD/SCID mouse strain, that is the lack of NK cells, allowed for a greater growth of metastatic foci, especially in the liver where some of them reached a visible size (p<0.01) **(Figure 22)**. These results are consistent with the fact that NK cells are involved in tumor surveillance by a NKG2D-mediated recognition of cancer cells (88), nevertheless, this hypothesis remains to be proven.
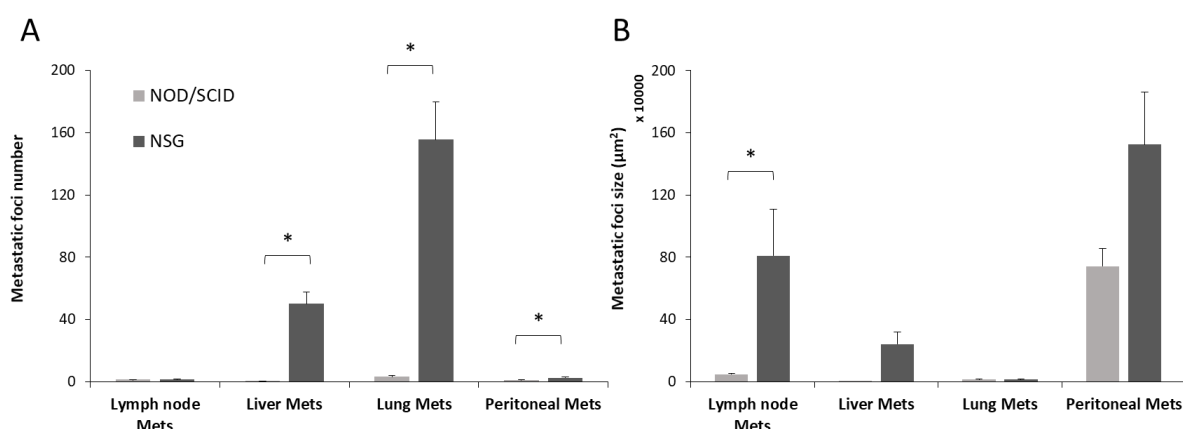
Figure 22. Metastatic colonization of SW1417 CRC cells in NOD/SCID and NSG mice. Total foci number (panel A) and mean foci area (panel B) in organs affected by metastases in NOD/SCID and NSG immunosuppressed mice orthotopically injected with CXCR4$^+$ SW1417 CRC cells. * p<0.01.

Table 7. Dissemination pattern of NOD/SCID and NSG mice orthotopically injected with CXCR4⁺ SW1417 CRC cells.

SW1417 cell-derived ortothopic model					
	Primary tumor	**Lymph node Mets**	**Liver Mets**	**Lung Mets**	**Peritoneal Mets**
Group	mice %	mice % # foci	mice % # foci	mice % # foci	mice % # foci
NOD/SCID	9/9 100%	88% 1.2 ± 0.15	11% **0.11 ± 0.11ᵃ**	89% **3.2 ± 0.66ᵃ**	100% **1.1 ± 0.11ᵇ**
NSG	10/10 100%	60% 1.3 ± 0.52	100% **50.1 ± 7.5ᵃ**	100% **155.5 ± 24.2ᵃ**	90% **2.4 ± 0.45ᵇ**
Metastatic foci size (µm² x 10³)					
Group	**Primary tumor**	**Lymph nods Mets**	**Liver Mets**	**Lung Mets**	**Peritoneal Mets**
NOD/SCID		**48.9 ± 6.9ᶜ**	6.9	14.7 ± 1.9	742.6 ± 115.5
NSG		**809.1 ± 298ᶜ**	241.6 ± 76.4	15.2 ± 4	1523.9 ± 337.5

Mean + s.e.m. metastatic foci number or area (µm²) per mouse, counted in one entire histology section.

ᵃ p<0.0001; ᵇ p=0.02; ᶜ p=0.02

1.4. Generation of a patient-derived metastatic CRC mouse model

To develop a patient-derived orthotopic CRC mouse model, we first established the SP5 subcutaneous tumor line, derived from a CRC patient of our hospital. We used a fragment of this tumor line to generate subcutaneous (SC) tumors in donor animals. When these subcutaneous tumors reached 600 mm³, were disaggregated to obtain a cell suspension that was inocluated directly in the cecum of NSG mice. A short time after cell injection (31 days) mice started showing signs of abdominal distension and developed a large abdominal carcinomatosis tumor mass. At necropsies, visible hepatic, lymph node and ovarian carcinomatosis were observed. When tissues were microscopically analysed, multiple mesenteric lymph nodes, hepatic, pulmonary and peritoneal metastases were observed and quantified **(Table 8)**. As compared to the 100% take rate observed in the cell-derived orthotopic model, the primary tumor take rate of the SP5 model was 85%, since at the end of the experiment there were 2 mice free of both primary tumor and metastases. However, the metastatic rate in the SP5 orthotopic model resulted in a 3.6-fold increase in the number of lymph node metastases as compared to the cell-line derived model in NSG mice **(Table 7)**. Regarding the size of the generated metastatic foci, in the patient-derived model we observed a greater growth of lymph node, pulmonary and peritoneal metastases. In accordance with the fact that mice died because of the rapid growth of the primary tumor, the size

of the peritoneal metastases was 28 times bigger than in the NSG cell-derived model, in which mice died because of the distant metastases **(Table 7)**.

Table 8. Metastatic dissemination in NSG mice orthotopically injected with a patient-derived cell suspension of SP5 disaggregated from subcutaneous tumors in donor mice.

SP5 patient-derived orthotopic model					
	Primary tumor	**Lymph node Mets**	**Liver Mets**	**Lung Mets**	**Peritoneal Mets**
Group	mice %	mice % # foci	mice % # foci	mice % # foci	mice % # foci
NSG	11/13 85%	85% 4.7±0.7	85% 18.2±2.5	85% 191.4±27.2	85% 3.2±1
Metastatic foci size (μm² x 10³)					
Group	**Primary tumor**	**Lymph node Mets**	**Liver Mets**	**Lung Mets**	**Peritoneal Mets**
NSG		7288.8±1506.7	172.7±67.7	48.4±9	43903.9±9616.4

Mean +s.e.m. metastatic foci number or area (μm²) per mouse, counted in one entire histology section.

1.5. CXCR4 expression in primary tumor and distant metastases

Since one of the objectives of this thesis project is to study the T22-GFP-H6 nanoparticle capacity of targeting CXCR4+ cancer cells, the expression of this receptor was studied in the subcutaneous and orthotopic models derived from the CXCR4+ SW1417 cell line or from the CXCR4+ SP5 patient-derived CRC tumor line. Immunohistochemistry was used to analyse the intensity of the membrane expression of CXCR4 and its subcellular localization pattern in subcutaneous tumors, primary tumors and metastases. **Figure 23** depicts representative images of anti-CXCR4 immunohistochemistry in the cell-derived and patient-derived subcutaneous tumors and orthotopic models. The SP5 patient-derived model showed CXCR4 expression in a larger percentage of tumor cells, with a higher intensity than the reached in SW1417 tumors and with a clear membrane localization in both models. Moreover, in both models, the CXCR4 expression was maintained in distant metastases, especially in metastatic foci affecting lymph nodes and liver.
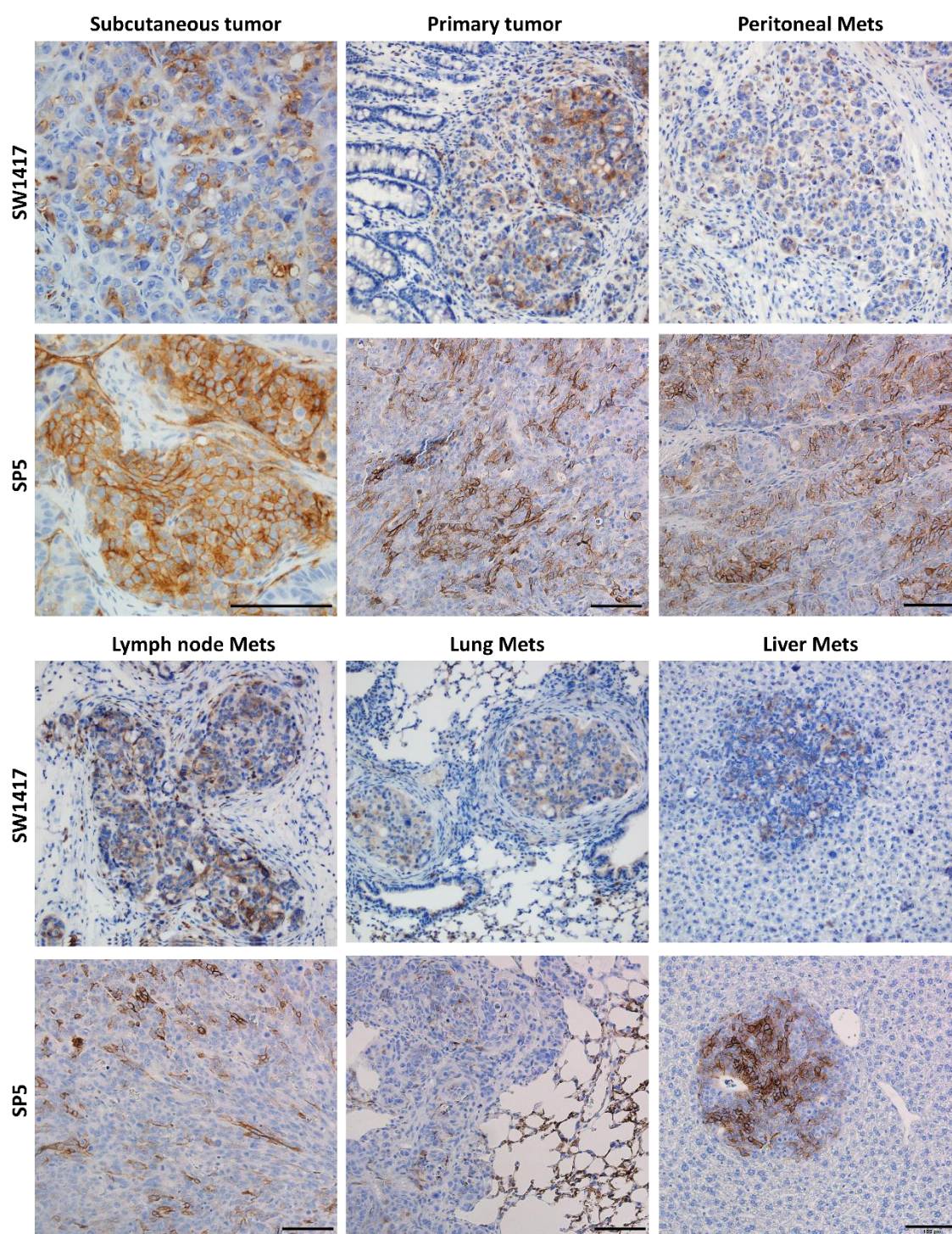
Figure 23. CXCR4 receptor expression in cancer tissues determined by immunohistochemistry analysis. Images of a subcutaneous tumor, CRC primary tumor, peritoneal, lymph node, lung and liver metastases of the cell-derived (SW1417) and the patient-derived (SP5) orthotopic models in NSG mice. Scale bars: 100 µm.

2) *IN VITRO* SELECTIVE INTERNALIZATION AND ANTITUMOR ACTIVITY OF T22-GFP-H6 AND ITS THERAPEUTIC DERIVATIVES IN CXCR4+ CRC CELL LINES.

In collaboration with the Nanobiotechnology group from the Universitat Autònoma de Barcelona (UAB), led by Dr. Villaverde, we developed protein-based nanoparticles capable of internalizing in CXCR4+ cells. All these nanoparticles are built around the T22-GFP-H6 nanocarrier basic structure. On the one hand, we developed nanoconjugates by conjugating therapeutic agents to the nanocarrier. Floxuridine (FdU), the cytotoxic drug currently used to treat liver metastases (89) was covalently bound to the T22-GFP-H6 nanocarrier, and assayed for selective internalization and FdU delivery in CXCR4+ cancer cells, that demonstrated to induce their specific depletion in a CRC model (79). In an attempt to further increase the antineoplastic effect of these nanoconjugates we chose as a first option to bind a therapeutic agent with higher potency, the Auristatin E toxin (Aur), to develop the new T22-GFP-H6-Aur nanoconjugate. So, we tested the *in vitro* capacity of the T22-GFP-H6 nanocarrier and the T22-GFP-H6-Aur nanoconjugate for selectively internalizing into CXCR4+ CRC cells, expecting to deliver the Auristatin payload in their cytosol, and to kill them.

On the other hand, we developed derivatives of the T22-GFP-H6 nanoparticle with intrinsic therapeutic activities by incorporating proapoptotic peptides (BAK, PUMA or BAXPORO) or bacterial toxin domains (PE24 or DITOX) to their chimeric sequences. Thus, we studied the sensitivity of the CXCR4+ CRC cells to these therapeutic nanoparticles and selected those with CXCR4-dependent cytotoxic activity *in vitro* for *in vivo* testing. In all the *in vitro* studies, we used the SW1417 CRC cell line due to its success in generating a mouse model of metastatic CRC by orthotopic implantation.

2.1. CXCR4-dependent internalization of T22-GFP-H6 in a human CXCR4+ CRC cell line

To understand the kinetics of the T22-GFP-H6 nanoparticle's internalization in the SW1417 CXCR4+ CRC cell line, confocal microscopy imaging was performed exposing the

cells to 1 µM of T22-GFP-H6 for different time periods (1, 5 and 24 hours). To prove CXCR4-dependent internalization of the nanoparticles we used the unliganded GFP-H6 protein version (lacking the T22 peptide) as a control. Moreover, we stained the cell membrane with a red dye (CellMask) and the cell nucleus with a blue dye (DAPI) to localize the green fluorescent signal emitted by the nanoparticles inside the cell. According to previous data obtained with HeLa (69) no cell penetration of GFP-H6 (negative control) was observed. In contrast, 1 hour after T22-GFP-H6 exposure, nanoparticles were already bound in low abundance to the plasma membrane and progressively increased their cell uptake until 24 hours, displaying a perinuclear pattern **(Figure 24)**. The cytosolic location of T22-GFP-H6 near the nuclear region indicates that T22-GFP-H6 nanoparticles were able to escape from degradation in the endosomes because of the accompanying hexahistidine tag, that has powerful endosomolytic properties.
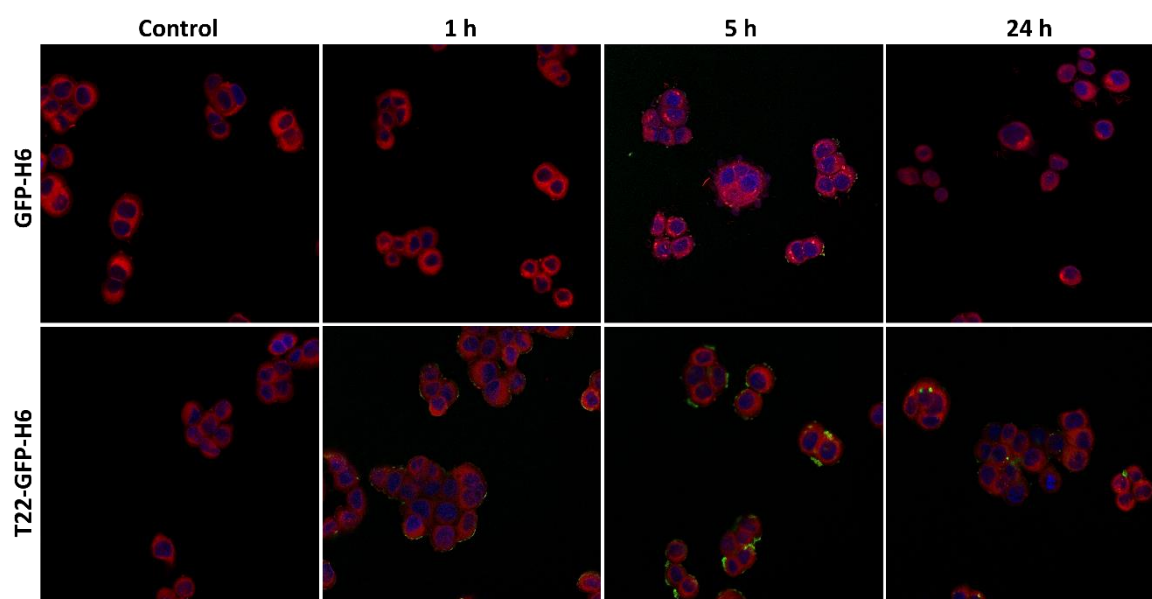
Figure 24. T22-GFP-H6 selective internalization in CXCR4^{+} SW1417 cells determined by confocal microscopy. SW1417 cells were exposed to 1 µM of T22-GFP-H6 or GFP-H6 (as a negative control) for internalization selectivity, during 1, 5, and 24 h. Plasma cell membranes were stained with a red dye (CellMask) whereas cell nucleus in blue (DAPI) and imaged with confocal microscopy. Green signal corresponds to the GFP contained in the nanoparticles. Magnification: 200x.

2.2. The T22-GFP-H6-Aur nanoconjugate maintains CXCR4-dependent internalization in CXCR4⁺ CRC cells

Following, we evaluated whether the conjugation of the Auristatin toxin to the T22-GFP-H6 nanoparticle could alter the protein conformation or function by measuring its CXCR4 targeting capacity. To that aim, we first tested the levels of CXCR4 in the cell membrane of SW1417 cells by immunohistochemistry. This CRC cell line shows high expression of the CXCR4 receptor, having a very clear membrane staining, but not in all the cell population **(Figure 25A)**. Afterwards, we measured and confirmed the absence of endogenous production of the natural CXCR4 ligand SDF-1α, by the SW1417 cells to discard a possible competition of this ligand with the nanoparticles for cell internalization **(Figure 25B)**. The human 1BR3.G fibroblasts were used as a positive control of SDF-1α production and release. Then, we evaluated by flow cytometry the internalization capacity of the T22-GFP-H6 nanocarrier and the T22-GFP-H6-Aur nanoconjugate in the SW1417 cell line. The T22-GFP-H6 nanocarrier internalized in SW1417 cells after 24 hours exposure at a 1000 nM concentration. In contrast, the GFP-H6 protein, used as negative control for CXCR4-dependent internalization, did not internalize in these cells as expected **(Figure 25C)**. The exposure of the SW1417 cells to a lower concentration of the T22-GFP-H6-Aur (400nM) showed similar capacity to internalize in this cell line but less efficiently. The nanoconjugate also maintained the dependence on CXCR4 for internalization, since a 30 minutes pre-treatment with the CXCR4 antagonist AMD3100 was able to decrease its internalization **(Figure 25D).**

A

B

C

D
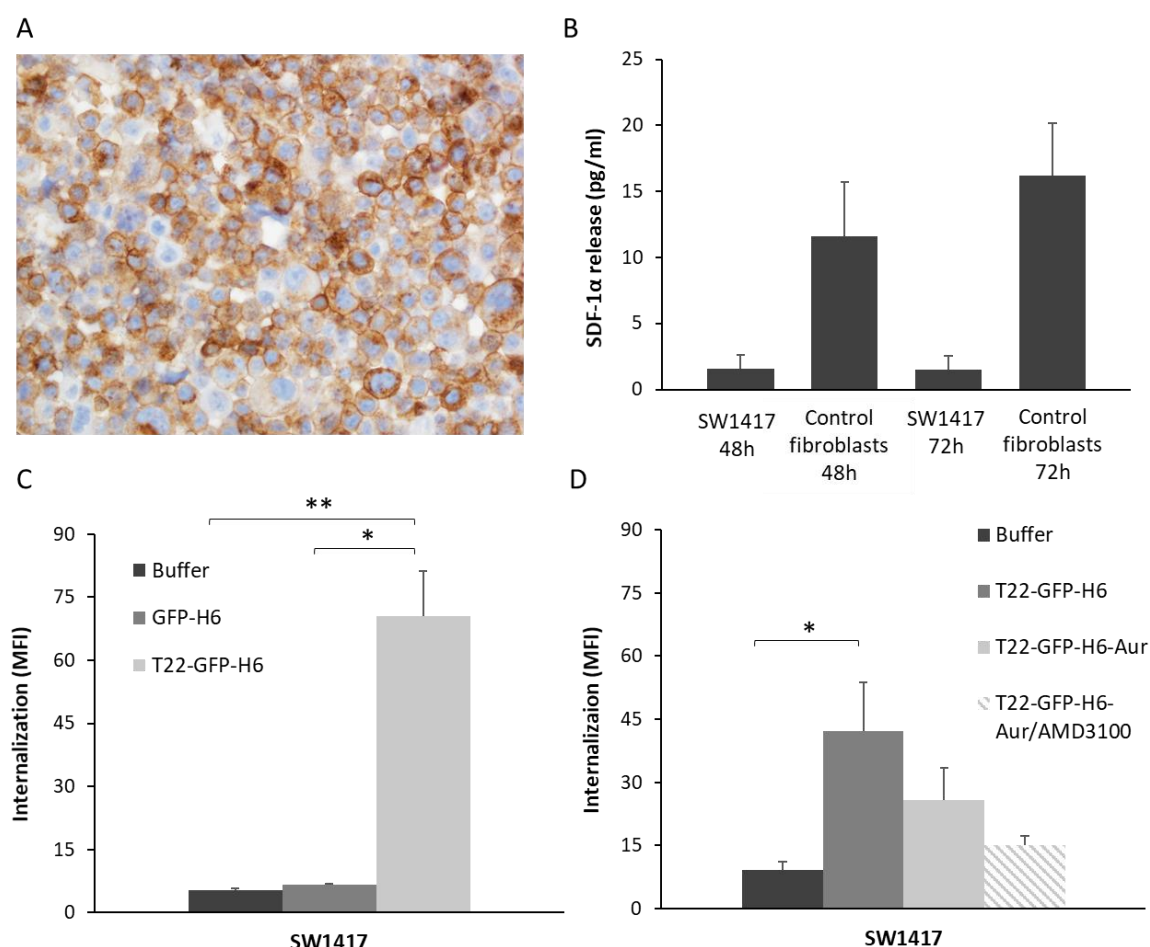
Figure 25. *In vitro* **T22-GFP-H6 and T22-GFP-H6-Aur selective internalization in the CXCR4^{+} SW1417 CRC cell line** A) Assessment of CXCR4 membrane expression by anti-CXCR4 immunocytochemistry in SW1417 cells in culture. Magnification: 400x B) Lack of human SDF-1α release from cultured SW1417 cells, as measured by ELISA, whereas human control 1BR3.G fibroblasts express high SDF-1α levels, after 48 or 72 h of growth in culture C) T22-GFP-H6 selective internalization in SW1417 cells measured as intracellular fluorescence by flow cytometry, after 24 h exposure to 1000 nM of T22-GFP-H6 or GFP-H6 D) T22-GFP-H6-Aur internalization in SW1417 cells after 24 h exposure to 400 nM of the nanoconjugate or after a 30 min pre-treatment with the antagonist AMD3100 (4 µM). Data presented as mean ± s.e.m., N=3, * p<0.05; ** p<0.01.

2.3. Cytotoxic effect of T22-GFP-H6-Aur and induction of cell death in CRC cells by mitotic catastrophe

Once we demonstrated the selective T22-GFP-H6-Aur nanoconjugate internalization in CXCR4^{+} cells, its cytotoxic activity was also evaluated *in vitro* in the SW1417 cell line, using XTT cell viability assays (which measures the metabolic activity of the cells) or DAPI nuclear staining assays. We used the T22-GFP-H6 nanocarrier and the T22-GFP-H6-FdU

nanoconjugate, as negative or positive controls respectively, because of their known cytotoxic effects. Surprisingly, we observed no effect of the T22-GFP-H6-Aur nanoconjugate on the viability of the SW1417 cells upon 48 hours exposure to a range of low (0, 10, 25 and 50 nM), intermediate (200 and 500 nM) and high (1 µM) concentrations **(Figure 26A)**.

Since we expected a high cytotoxic effect because Auristatin is usually a more potent drug than Floxuridine in different cell types, cell death was analysed using a different method, that is the nuclear staining with DAPI (to measure cell detachment, induction of DNA condensation and blockade in mitosis) of cells exposed to 1 µM of T22-GFP-H6-Aur for 48 hours. In these assays, we observed that the number of cells adhered to the slide surface was significantly lower than cells treated with buffer, T22-GFP-H6 nanocarrier or T22-GFP-H6-FdU **(Figure 26B)**. Moreover, the evaluation of the obtained images allowed us to study if the mechanism of cell death induced by the T22-GFP-H6-Aur nanoconjugate was the one described for the microtubule inhibitor Auristatin (90). As expected, the nuclear morphology of dead cells indicated that cells treated with the nanoconjugate died because of mitotic catastrophe in contrast with the apoptosis caused by the T22-GFP-H6-FdU nanoconjugate **(Figure 26D)**.

Additionally, the CXCR4 dependence of the T22-GFP-H6-Aur cytotoxic effect was also evaluated with a competition assay using the CXCR4 antagonist AMD3100. The pre-treatment of cultures with AMD3100 showed a significant decrease in the number of cells affected by mitotic catastrophe, but cell death was not completely reverted maybe due to drug leakage, and therefore, having free Auristatin in the nanoconjugate solution **(Figure 26C)**. In summary, the T22-GFP-H6-Aur nanoconjugate is active against SW1417 CRC cells at 1 µM concentration, an effect that is, at least, partially dependent on CXCR4. In contrast, cell viability measured by the metabolic XTT assay could not be adequate to study the induction of cell death by Auristatin or our conjugates that include a microtubule inhibitor as a payload. Further studies will be necessary to explain the differences observed between the results that determine cell death by XTT with those measuring mitotic catastrophe induction.
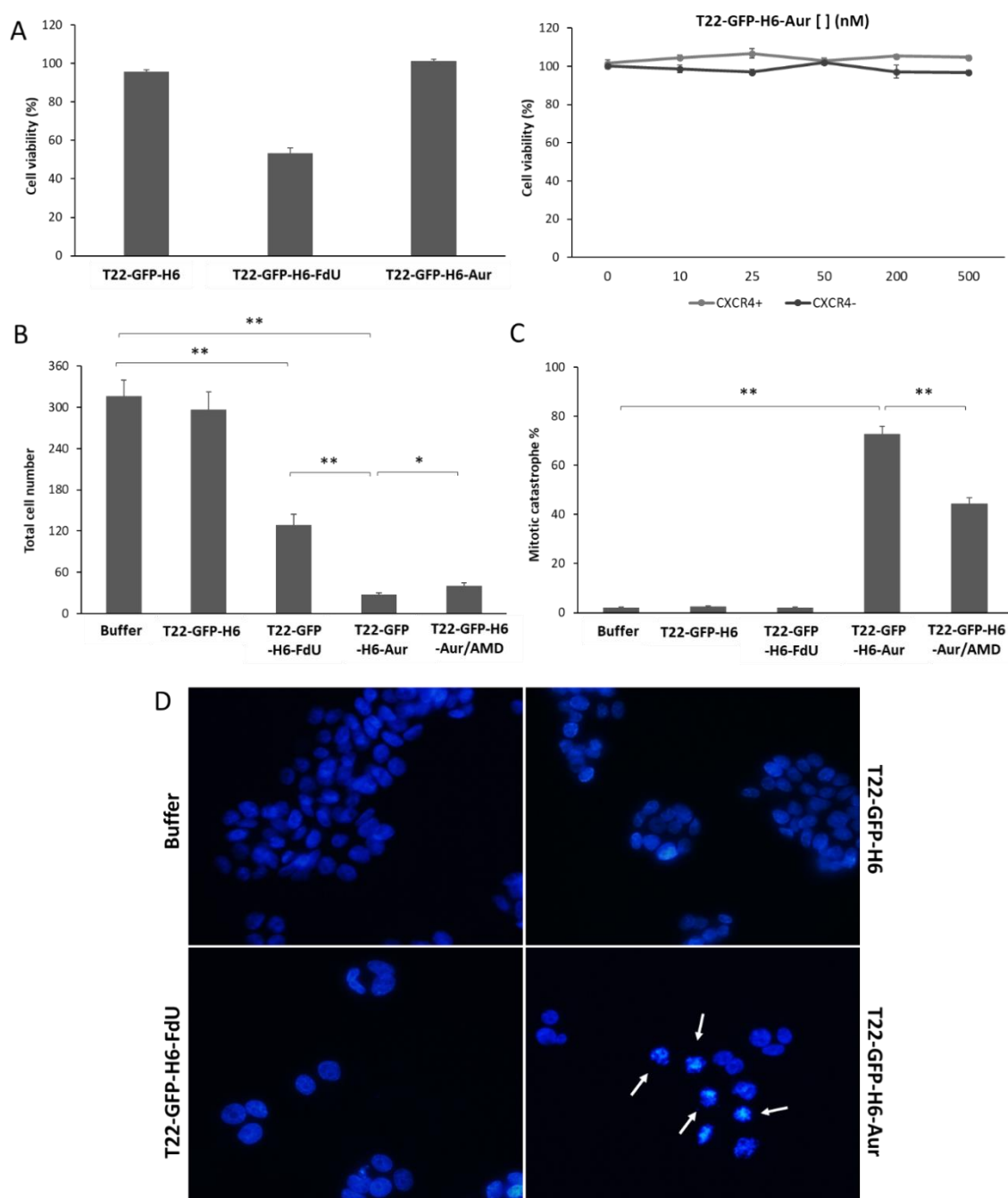
Figure 26. Cytotoxic activity of the T22-GFP-H6-Aur nanoconjugate in CXCR4+ SW1417 cells, measured with two different methods A) Lack of cytotoxicity after 48 h exposure to high concentrations of T22-GFP-H6-Aur (1 μM) or to a range of concentration (0, 10 25, 50, 200 and 500 nM) measured as percentage of cell viability (XTT assay) in CXCR4+ SW1417 cells (N=2 in triplicate experiments) B) Detection of cytotoxic effect as measured by total cell number remaining attached to the culture plate, quantified in DAPI staining assays after 48 h exposure to 1 μM of T22-GFP-H6-Aur C) Percentage of cells in mitotic catastrophe (DAPI staining assay) after 48 h exposure to 1 μM of T22-GFP-H6-Aur D) Representative images of the DAPI staining of SW1417 cells treated with different nanoparticles. White arrows show cells in mitotic catastrophe. Magnification: 400x. In DAPI staining assays 10 high-power fields (200x) were

counted and data expressed as mean ± s.e.m. T22-GFP-H6 was used as a negative control and T22-GFP-H6-FdU as a positive control.

2.4. Highly potent and CXCR4-dependent cytotoxic effect of the T22-PE24-H6 nanotoxin in CXCR4⁺ CRC cells

Given the unexpected low potency of the tested T22-GFP-H6-Aur nanoconjugate in CRC cells *in vitro*, we decided to perform an *in vitro* antitumor activity screening of alternative agents for the treatment of this tumor type, consisting in fully polypeptidic proapoptotic and bacterial toxin-based nanoparticles in SW1417 cells using XTT cell viability assays. Similarly to the T22-GFP-Aur nanoconjugate, T22-PUMA-GFP-H6, T22-BAXPORO-GFP-H6 and T22-BAK-GFP-H6 proapoptotic nanoparticles, which production has been described by our group in (91), also showed lack of effect on SW1417 cells after 48 hours exposure to 1 µM or 2 µM of each nanoparticle **(Figure 27A)**.

Again, when testing toxin-based nanoparticles, we found that SW1417 cells were neither sensitive to T22-DITOX-GFP-H6 nanoparticle, which contains a cytotoxic domain of *Corynebacterium diphtheriae*.

In contrast, SW1417 cell exposure to 1 µM or 2 µM of T22-PE24-H6 nanotoxin, containing a cytotoxic domain of *Pseudomonas aeruginosa*, showed a dramatic reduction in their viability **(Figure 27A)**. Then, the cytotoxic effect of the T22-PE24-H6 nanotoxin was evaluated in both CXCR4⁺ and CXCR4⁻ SW1417 cell lines. XTT assays in which cells were exposed for 48 hours to a concentration range of 0-20 nM showed that, as expected, T22-PE24-H6, had no cytotoxic effect in CXCR4⁻ SW1417 cells. In contrast, the nanotoxin displayed a dose-dependent antineoplastic effect in CXCR4⁺ SW1417 cells with an IC_{50} of 6.56 nM **(Figure 27B)**. Finally, the competition assays showed that pre-treating the CXCR4⁺ SW1417 cells with AMD3100 significantly decreased T22-PE24-H6 anticancer activity, preventing the nanotoxin-induced cell death and maintaining the cell viability close to 100% **(Figure 27B)**. So, the T22-PE24-H6 nanotoxin displays a completely CXCR4-dependent cytotoxic effect in CXCR4⁺ SW1417 cells.
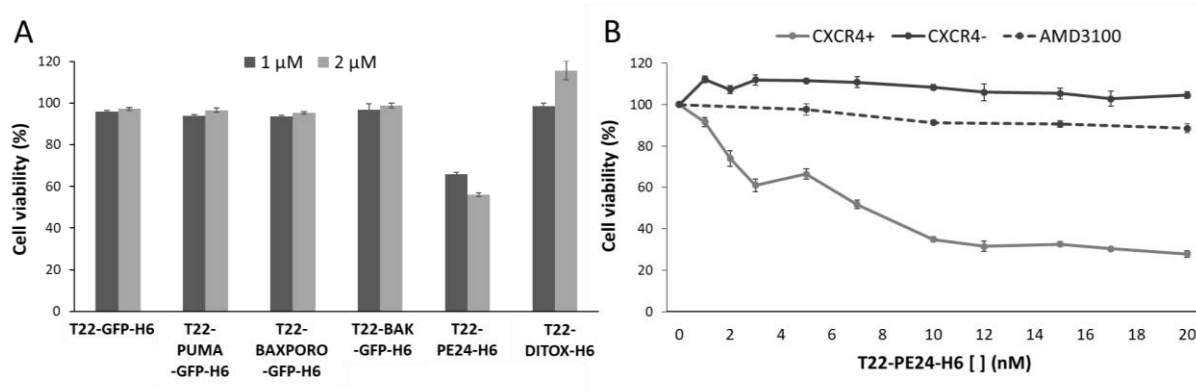
Figure 27. Antitumor activity of the proapoptotic nanoparticles and nanotoxins in CXCR4+ SW1417 cells
A) Cell viability of the CXCR4+ SW1417 cells upon exposure to 1 μM or 2 μM of the proapoptotic nanoparticles (T22-PUMA-GFP-H6, T22-BAXPORO-GFP-H6 and T22-BAK-GFP-H6) and the toxin-based nanoparticles (T22-PE24-H6 and T22-DITOX-H6) for 48 h B) Dose-response curve of CXCR4+ and CXCR4- SW1417 cells upon 48 h exposure to the T22-PE24-H6 nanotoxin. The selectivity of the cytotoxic effect was also studied by performing a 30 minutes pre-treatment with the antagonist AMD3100 previous to nanotoxin exposure in CXCR4+ SW1417 cells. Data presented as mean ± s.e.m. (N=2 in triplicate experiments).

2.4.1. *In vitro* activation of the pyroptotic cell death pathway induced by the T22-PE24-H6 nanotoxin

We wanted to molecularly characterize the different cell death pathways activated by the T22-PE24-H6 nanotoxin. We know that diverse therapeutic nanoparticles developed so far using different cytotoxic agents kill cells through different cell death mechanisms, mainly by apoptosis or mitotic catastrophe. In previous cell proliferation assays we determined that this toxin-based nanoparticle has a CXCR4-dependent highly potent cytotoxic effect in SW1417 CRC cells. Moreover, it has recently been described a new mechanisms of programmed cell death occurring upon infection with intracellular bacterial pathogens, known as pyroptosis (92). Therefore, to analyse if the PE24 exotoxin induces pyroptosis in our CRC models, different molecular components of the pyroptotic pathway were analysed in T22-PE24-H6 treated SW1417 cells by immunohistochemistry **(Figure 28A)**.
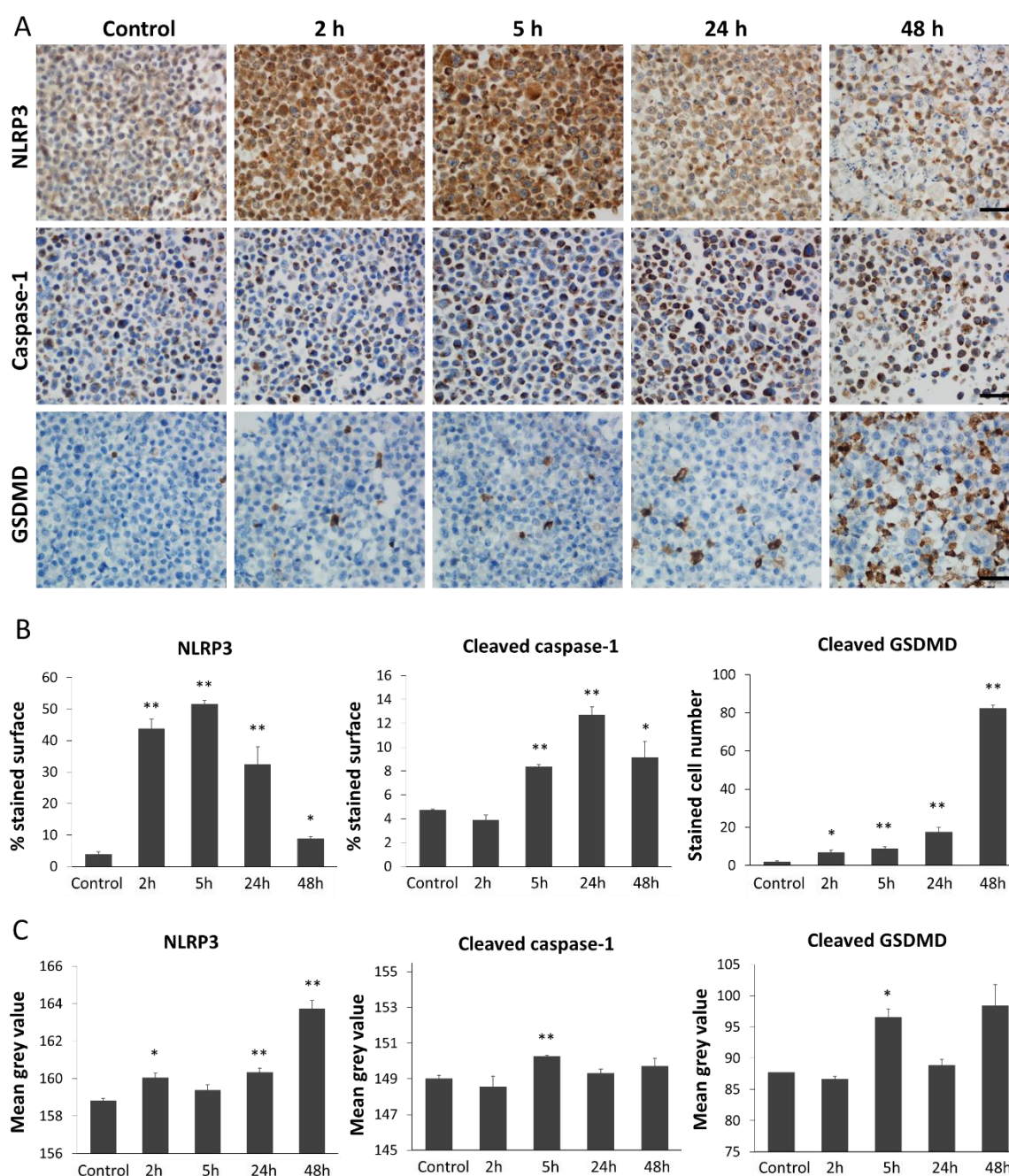
Figure 28. Activation of the pyroptotic pathway in CXCR4⁺ SW1417 cells after treatment with T22-PE24-H6 A) Detection of pyroptosis markers such as NLRP3, cleaved caspase-1 and cleaved GSDMD by ICC in cell blocks of CXCR4⁺ SW1417 cells treated during 2, 5, 24 or 48 h with 6 nM of T22-PE24-H6. Stained sections were compared to untreated control CXCR4⁺ SW1417 cells. Scale bars: 50 µm B) Quantitation values of each marker staining in SW1417 control cells or in cells treated with T22-PE24-H6. In ICC of NLRP3 and caspase-1 up to 5 high-power fields (400x) were imaged and the percentage of stained surface measured with ImageJ. In GSDMD staining, up to 5 high-power fields (400x) were analysed by counting the number of GSDMD positive cells C) Quantitation of NLRP3, cleaved caspase-1 and cleaved GSDMD staining intensity in the ICC sections presented as mean grey value obtained using the ImageJ Software (see Methods **1.3.3.** section). All the results are presented as the mean ± s.e.m. * $p < 0.05$; ** $p < 0.001$.

For that purpose, CXCR4^{+} SW1417 cells were cultured and treated with the calculated IC$_{50}$ of T22-PE24-H6 (6 nM) at different exposure times: 2, 5, 24 and 48 hours. Control SW1417 cells were also cultured without being exposed to the nanotoxin. After treatment, cells were collected, fixed as cell blocks and stained using immunocytochemistry. At short times, such as 2 and 5 hours, we found an overexpression of the NLRP3 marker, which participate at the beginning of the signalling cascade of pyroptosis. This overexpression is maintained from 24 to 48 hours showing a few stained cancer cells that expressed NLRP3 with high intensity **(Figure 28C).** The activation of the NLRP3 inflammasome increases the production of active caspase-1 at longer exposure times (5, 24 and 48 hours) which, in turn, cleaves pro-Gasdermin D (pro-GSDMD) in an active fragment which translocates to the plasma membrane, where it oligomerizes and forms pores **(Figure 28B)**. This translocation is clearly and highly observed at 48 hours exposure to T22-PE24-H6.

3) *IN VIVO* BIODISTRIBUTION OF T22-GFP-H6 AND ITS THERAPEUTIC DERIVATIVES TO CXCR4^{+} TUMORS AND NON-TUMOR ORGANS.

Once we proved that the T22-GFP-H6 nanoparticle and its therapeutic derivatives internalized selectively in CXCR4^{+} CRC cell lines, we assessed their *in vivo* biodistribution in tumor and non-tumor tissues. In all biodistribution assays, we used the patient-derived SP5 subcutaneous CRC mouse model because of its high expression of CXCR4 in the cancer cell membranes. All assessed nanoparticles were injected as a single i.v. bolus dose and 2, 5 and 24 hours after we measured the *ex vivo* fluorescence emission in the different organs.

On one hand, as we have previously described that changes in the structure of the nanoparticles could change their tissue biodistribution (72), consequently decreasing their accumulation in tumors, while increasing their liver uptake, we first studied the effect on T22-GFP-H6 *in vivo* biodistribution caused by the conjugation of the

therapeutic agent Auristatin. Moreover, the possible antitumor effect after the internalization of the nanoconjugate T22-GFP-H6-Aur in CXCR4^{+} cells was also assessed.

On the other hand, in an attempt to improve the payload delivery capacity of the T22-GFP-H6 nanocarrier, we engineered an enhanced endosomal escape capacity by the incorporation of the fusogenic HA2 peptide from the influenza virus hemagglutinin (73,93) into the T22-GFP-H6 building blocks of the self-assembled nanoparticle.

Considering the proteolytic degradation of protein-based materials, this new peptide could induce an early escape of endosomes, thus avoiding the lysosomal route and their proteolytic processing. This approach could represent an important step ahead in their engineering and adaptation to intracellular delivery. Therefore, we assessed the *in vivo* biodistribution of the T22-GFP-H6 nanoparticles containing the HA2 peptide, as well as their selectivity for CXCR4^{+} cancer cells.

3.1. Maintenance of a highly selective tumor uptake for the T22-GFP-H6-Aur in mice bearing subcutaneous CXCR4^{+} CRC tumors

As we previously described for the cell-derived SW1417 SC CRC model (94), the T22-GFP-H6 nanocarrier increased progressively its tumor uptake from the 2 to 24 hours period. In this study, we used the patient-derived SC SP5 CRC model that shows higher levels of CXCR4 overexpression than the SW1417 model. After administering 326 µg of T22-GFP-H6, T22-GFP-H6-Aur or buffer, the GFP-emitted fluorescence of both, the nanocarrier and the nanoconjugate was measured. The T22-GFP-H6 nanocarrier accumulated in tumor at short times, increasing its uptake from 2 to 5 hours period, followed by a slow decrease at 24 hours **(Figure 29)**. Interestingly, the T22-GFP-H6-Aur nanoconjugate showed similar kinetics at 2 and 5 hours but continued increasing its tumor accumulation at 24 hours. The fluorescent intensity of both, the nanocarrier and the nanoconjugate, was similar but the peak intensity for the tumor uptake of the nanocarrier was registered at 5 hours, whereas the peak for the nanoconjugate occurred at 24 hours. Therefore, the T22-GFP-H6-Aur nanoconjugate maintained the highly selective tumor uptake observed for the T22-GFP-H6 nanocarrier, even improving tumor accumulation for a longer time.
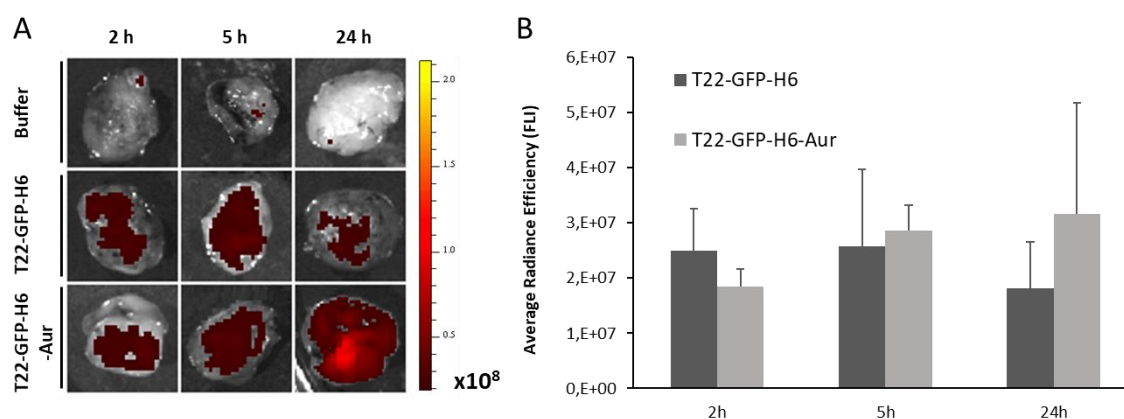
Figure 29. Tumor accumulation of the T22-GFP-H6-Auristatin nanoconjugate and the T22-GFP-H6 nanocarrier. The nanoparticle T22-GFP-H6 conjugated to Auristatin and the unconjugated nanocarrier had a similar tumor uptake, but the nanoconjugate showed a higher tumor uptake at 24 h, after the administration of 326 µg i.v. dose each, in the SP5 CXCR4$^+$ subcutaneous CRC model. No fluorescence was detected in buffer-treated controls (panel A).

3.1.1. T22-GFP-H6 and CXCR4 receptor co-localization in the cell membrane

To confirm the T22-GFP-H6 uptake by tumor tissues and its selective internalization in CXCR4$^+$ cancer cells, a dual anti-GFP and anti-CXCR4 immunofluorescence study was performed. Immunofluorescences were run in tumors from mice administered with a 326 µg T22-GFP-H6 single i.v. dose and euthanized 5 hours after injection, at the peak of tumor fluorescence emission. Using confocal microscopy imaging, we observed in buffer-treated tumors, a high expression of CXCR4 localized in the cell membrane (red staining with anti-CXCR4 antibody) and a dot-like staining pattern representing the internalization of the receptor within endocytic vesicles. In contrast, in nanoparticle-treated tumors we observed a lower CXCR4 cell membrane staining that co-localized with T22-GFP-H6 nanoparticles (green staining with anti-GFP). Merged images showed co-localization of the CXCR4 receptor and nanoparticles (yellow) mainly in the cell membrane but also in the cytosolic endosomal vesicles that are being dissociated afterwards **(Figure 30)**. These results suggest that T22-GFP-H6 binds the CXCR4 receptor located in the cell membrane and after internalizing together via endosomal vesicles, they release the nanoparticle into de CXCR4$^+$ cell cytosol.
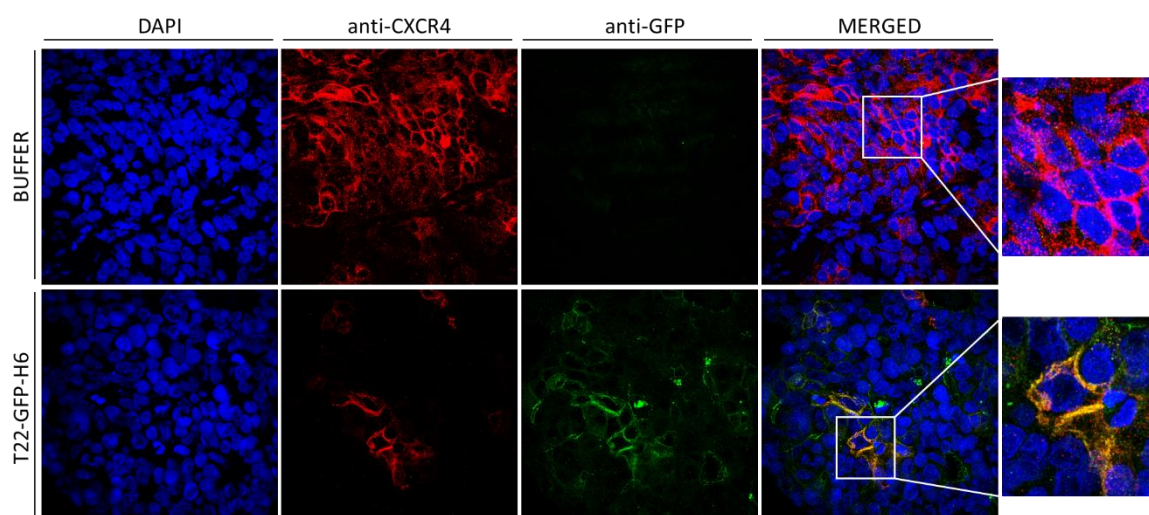
Figure 30. Co-localization of T22-GFP-H6 and the CXCR4 receptor in the cell membrane. Representative immunofluorescence images from SP5 SC tumors of mice 5 h after treatment with 326 μg of T22-GFP-H6 or buffer. T22-GFP-H6 and CXCR4 co-localization was seen in the cell membrane (yellow) followed by T22-GFP-H6 internalization in endosomal vesicles towards the cytosol. DAPI staining for nuclei (blue), anti-GFP protein (green), anti-CXCR4 receptor (red) and merged images from the three stains. Magnification: 630x.

3.1.2. Biodistribution of the T22-GFP-H6-Aur nanoconjugate in non-tumor organs and absence of toxicity

We also assessed whether the T22-GFP-H6 nanocarrier and the T22-GFP-H6-Aur nanoconjugate accumulated in non-tumor tissues, and their toxicity on normal cells. Biodistribution in non-tumor tissues such as liver, kidney, lung and heart and brain was studied 2, 5 and 24 hours after the i.v. injection of 326 μg of the nanoparticles. At 2, 5 and 24 hours we did not detect *ex vivo* fluorescence emission in brain, lung or heart, since the fluorescence emission (FLI) signal was undistinguishable from background auto-fluorescence measured in buffer-treated mice **(Figure 31)**.

In contrast, a differential biodistribution of the nanocarrier and the nanoconjugate in non-tumor drug clearance organs (liver and kidney) was observed. The T22-GFP-H6 nanocarrier was detected in low amounts in liver at 24 hours and at constant levels along the studied period in kidneys. However, the fluorescence emission signal in these organs was very low compared to the signal detected in tumors where it was 4 times higher. Differently, the T22-GFP-H6-Aur nanoconjugate accumulated more rapidly in non-tumor tissues, reaching a peak of accumulation in liver and kidneys at 2 hours post-injection,

that decreased progressively to become undetectable at 24 hours **(Figure 31)**. The signal of fluorescence emission measured at the 2-hour peak in the kidneys (2.5×10^7 p/s/cm²/sr) was higher than the emission coming from the tumor (1.8×10^7 p/s/cm²/sr, **Figure 29**) and in the liver was moderately lower (1.5×10^7 p/s/cm²/sr).

We also assessed in haematoxylin and eosin (H&E) stained samples of normal tissues, if the accumulation of these nanoparticles, specially the conjugate carrying a potent antimitotic drug, caused any toxic effect. No histological alterations were found in non-tumor organs (liver, kidney, lung and brain) 24 hours after nanoparticle's administration, since treated tissues had similar histology, and lack of apoptotic bodies, to the buffer-treated mice **(Figure 31)**.

Accordingly, the conjugation of the drug Auristatin to the T22-GFP-H6 nanocarrier changed its biodistribution, probably by changing the structure of the nanoconjugate, showing similar tumor accumulation, but accelerating and increasing its uptake in liver and kidneys, without causing any toxicity.
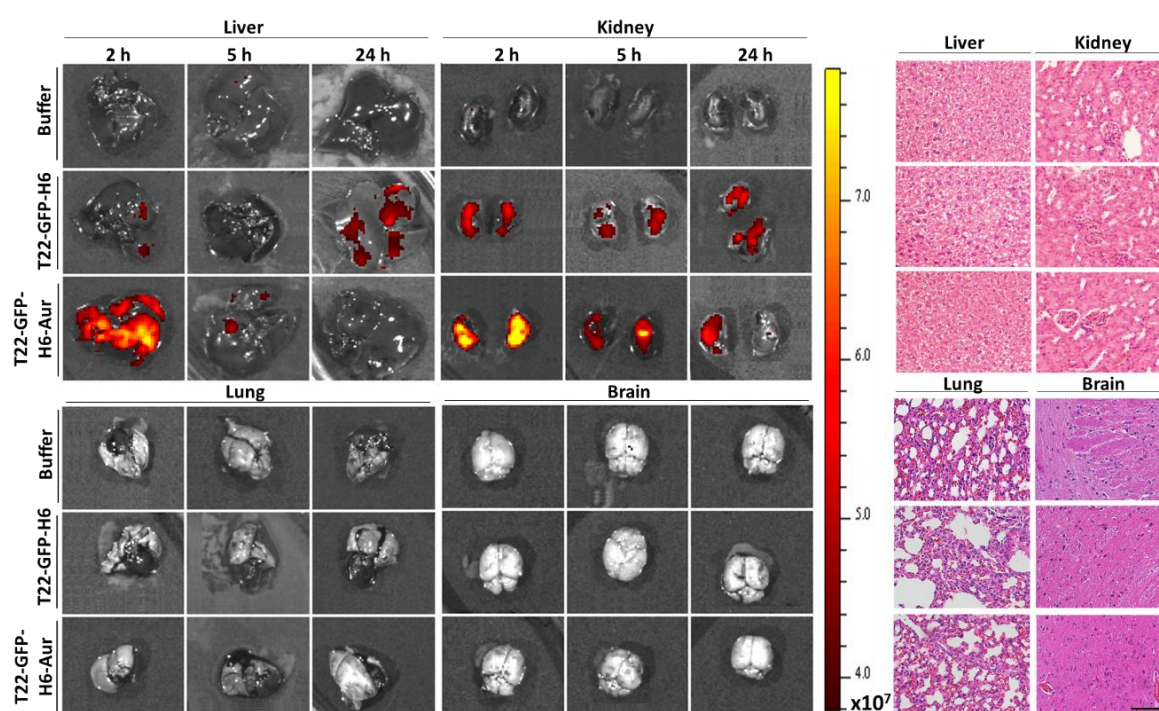
Figure 31. Organ biodistribution of T22-GFP-H6 and T22-GFP-H6-Aur. Representative *ex vivo* fluorescence images (FLI) of normal organs (liver, kidney, lung and brain tissues) after i.v. administration of 326 µg dose of each nanoparticle at 2, 5 and 24 h. Lack of histological alterations are observed after 24 h of the administration by H&E staining of paraffin-embedded tissues. Scale bars: 100 µm.

3.1.3. T22-GFP-H6-Aur achieves targeted drug delivery leading to selective depletion of CXCR4+ cells

Once confirmed the receptor-dependent tumor uptake of the T22-GFP-H6-Aur nanoconjugate in CXCR4 highly expressing subcutaneous tumors, we assessed whether the selective internalization and the Auristatin delivery into the cytosol of target CXCR4+ cells was followed by target cancer cell depletion. For this purpose, we analysed cell death in the SP5 subcutaneous tumors of mice 2, 5 and 24 hours after treatment with buffer, T22-GFP-H6 or T22-GFP-H6-Aur each at a single 326 µg i.v. dose. Since Auristatin is a potent antimitotic agent which inhibits cell division by blocking the polymerization of tubulin, cells in mitotic catastrophe were quantified in H&E and DAPI stained sections of treated or control tumors. Cells in mitotic catastrophe are characterized by the formation of giant, multinucleated cells carrying uncondensed chromosomes, as shown in **Figure 32A** in H&E and DAPI stained sections. Two hours after T22-GFP-H6-Aur treatment the number of cells in mitotic catastrophe in treated tumors (17,4 ± 1,1) was significantly higher than in buffer-treated tumors (11,6 ± 1,8) but not in T22-GFP-H6 treated tumors (15,4 ± 1,6). At 5 hours, higher tumor uptake led to higher cell death, finding a 1.6-fold increase in the number of cells in mitotic catastrophe in T22-GFP-H6-Aur treated tumors than in buffer or T22-GFP-H6 treated tumors **(Figure 32)**. Consequently, at 24 hours cell death induction is maintained due to the increased tumor uptake of the nanoconjugate. T22-GFP-H6-Aur induction of cell death by mitotic catastrophe proved the capacity of the nanoconjugate to release Auristatin in the cytosol of target CXCR4+ cells and block cell division.
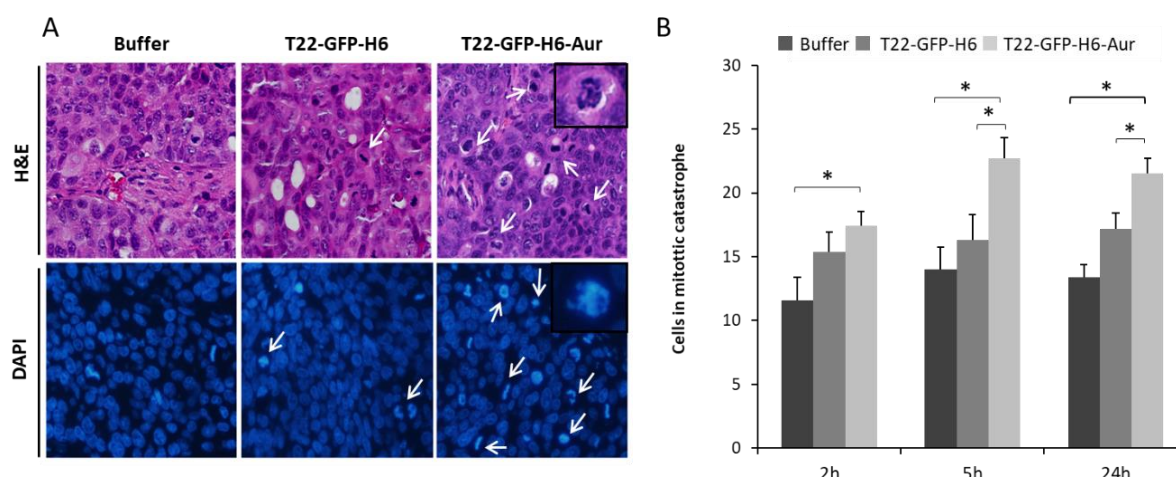
Figure 32. Tumor cell death at 2, 5 and 24 h after T22-GFP-H6-Aur administration A) Representative H&E and DAPI staining of tumor sections 24 h after buffer, T22-GFP-H6 and T22-GFP-H6-Aur administration. Cells in mitotic catastrophe (white arrows) were counted in 5 high-power fields (x400) per sample B) Quantitation of tumor cells in mitotic catastrophe at 2, 5 and 24 h after administration of 326 µg i.v. dose in H&E staining sections. *p < 0.05 bars indicate a statistically significant between the designated groups.

3.2. HA2 endosomal escape peptide site-dependent accommodation in the T22-GFP-H6 construct enhances tumor uptake

In an attempt to improve the T22-GFP-H6 nanocarrier regarding its tumor uptake, we incorporated a known endosomal escape domain with cell penetration capacity to avoid lysosomal degradation. Thus, to discriminate between exclusive or cooperative effects of membrane activity and receptor-mediated cell penetrability, we studied the biodistribution of T22-HA2-GFP-H6 and T22-GFP-HA2-H6 modular proteins, in which the fusogenic peptide HA2 had been placed in alternative accommodation sites, using mice bearing SP5 subcutaneous tumors with high expression of CXCR4. For that purpose, 200 µg of T22-HA2-GFP-H6 or T22-GFP-HA2-H6 were administered intravenously, as well as the parental T22-GFP-H6 protein acting as control.

At different time points upon single dose injections, T22-GFP-H6 accumulated in subcutaneous tumors at levels comparable to those previously described in similar animal models (95), and a similar result was observed for T22-HA2-GFP-H6 nanoparticle **(Figure 33)**. However, a fast and efficient tumor retention of T22-GFP-HA2-H6 was unexpectedly observed, peaking at 2 hours, a fact that was necessarily linked to the incorporation of the viral HA2 peptide at the particular site between GFP and H6 modules.
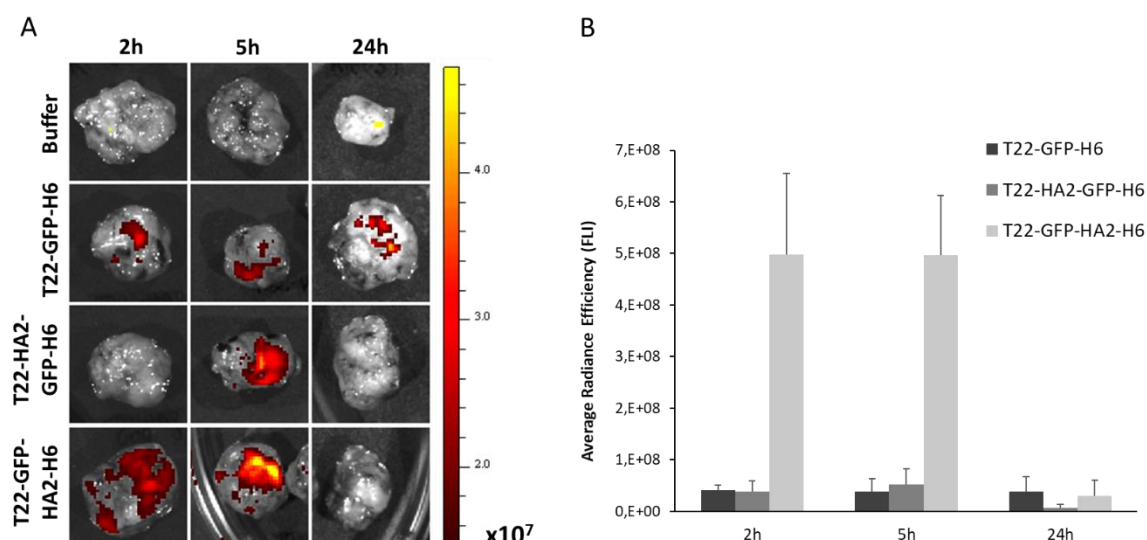
Figure 33. Tumor biodistribution of nanoparticles in the highly CXCR4^{+} expressing SP5 patient-derived CRC model A) Representative *ex vivo* images of GFP-emitted fluorescence by the tumor at 2, 5 and 24 h after the i.v. administration of 200 µg dose of each protein nanoparticle in the patient-derived SP5 subcutaneous CRC model B) Quantitative analysis of tumor emitted fluorescence by each nanoparticle at the studied time points. Data were corrected by specific fluorescence of each protein, so they are indicative of protein amounts.

None of these proteins were observed at significant levels in non-target organs, at exception of some background of T22-GFP-HA2-H6 in the liver **(Figure 34A)**. However, the histopathology of liver and kidney in T22-GFP-HA2-H6-treated animals revealed a complete absence of lesions indicative of side toxicity **(Figure 34C)**, supporting the biological safety of the protein.
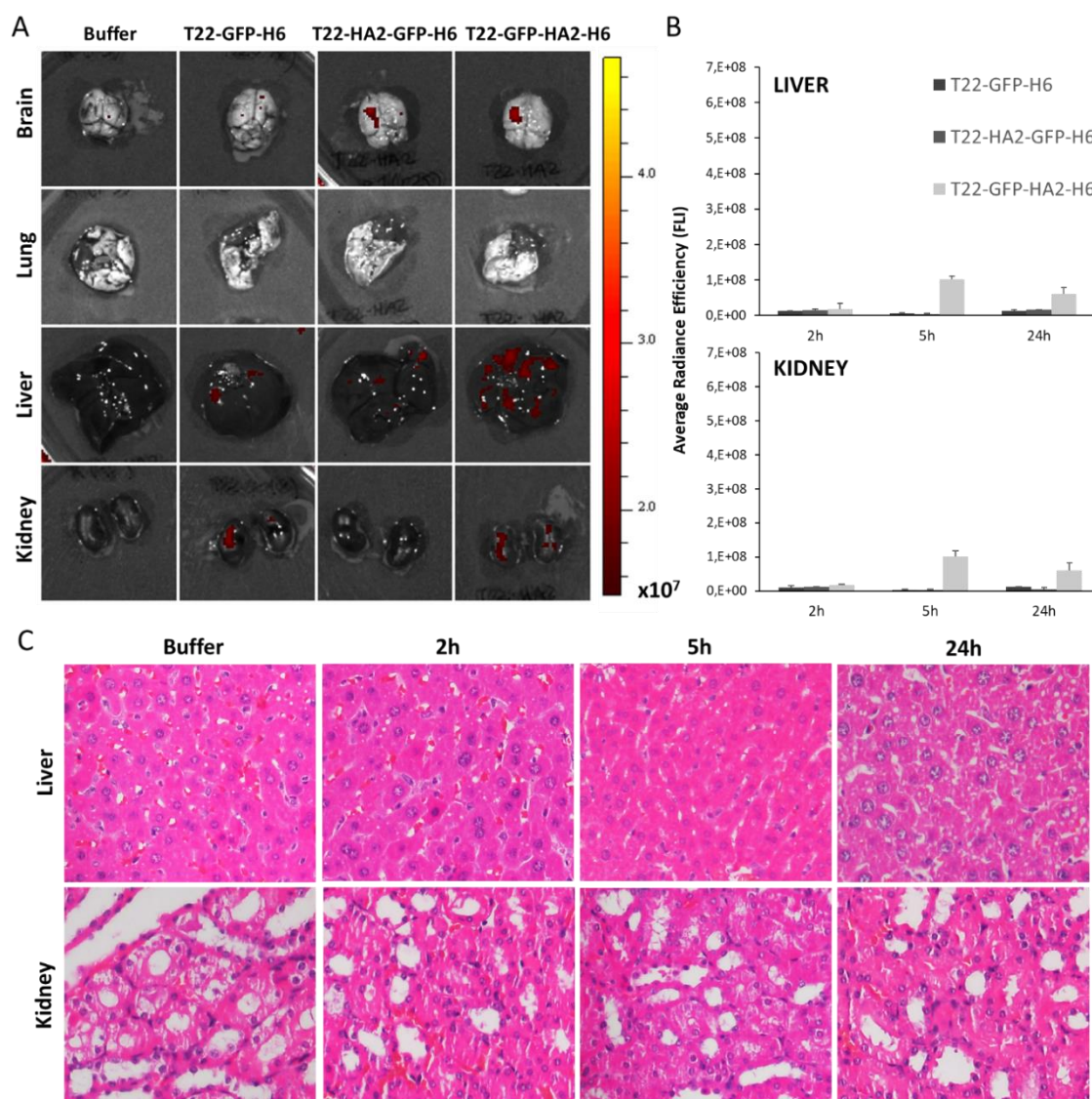
Figure 34. Biodistribution and lack of toxicity of the nanoparticles in non-target organs A) Representative *ex vivo* images of GFP-emitted fluorescence in the main non-tumor organs at 5 h in the SC SP5 colorectal cancer model B) Quantitative analysis of liver and kidney emitted fluorescence by each nanoparticle at 2, 5 and 24 h of emitted fluorescence C) Absence of histopathological alterations in liver or kidney in H&E stained tissue sections, at the studied time points after the administration of the T22-GFP-HA2-H6 nanoparticle. Magnification: 200x.

The numerical analyses of the accumulated materials (AUC, area below the curve, was fully convincing regarding the superiority of T22-GFP-HA2-H6 as a CXCR4-targeted material, that combined the cell specificity of T22 and the cell-penetrating abilities empowered by HA2 **(Figure 35).**
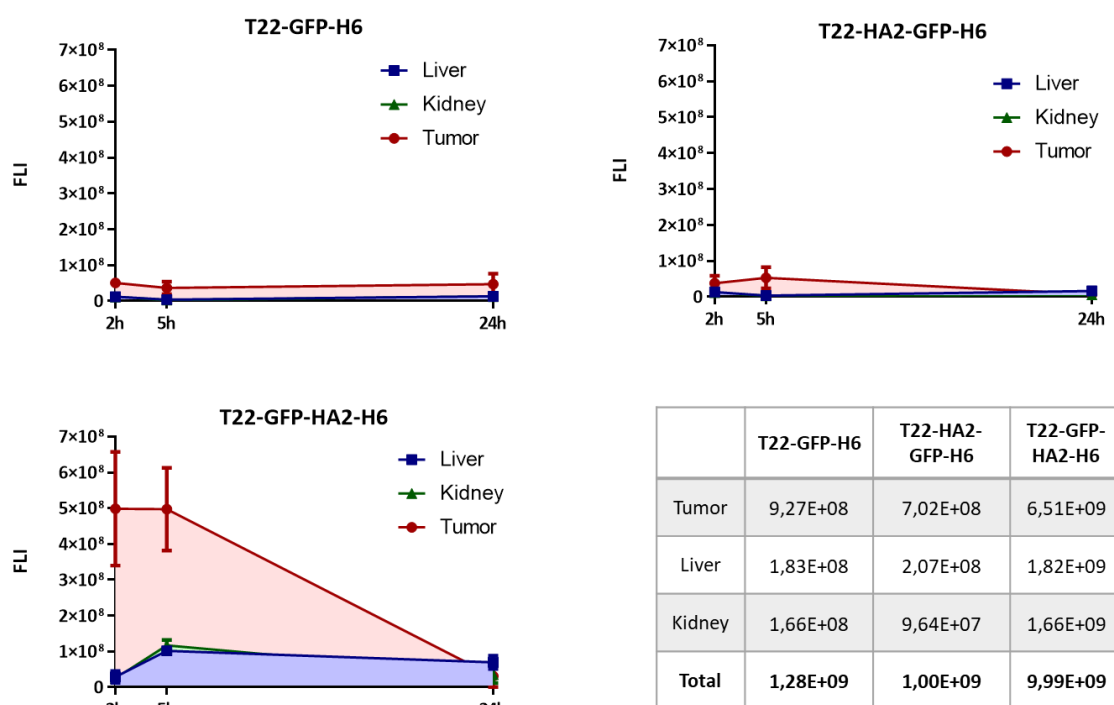
Figure 35. Graphic representation of total nanoparticle exposure. Area under the curve: (AUC = FLI emission x time (h)) registered in tumor and non-tumor organs along the studied period (2-24 h) for all three tested nanoparticles (200 µg dose) using the SC SP5 colorectal cancer model, and its quantitation. Fluorescence emission intensity (FLI) signal from experimental mice was calculated subtracting the FLI auto-fluorescence of control buffer-treated mice. FLI, fluorescent intensity (expressed as average radiance efficiency).

3.3. Selective CXCR4-dependent T22-GFP-H6 and T22-GFP-HA2-H6 tumor uptake in subcutaneous CRC tumors

An obvious concern was whether the extraordinary tumor targeting manifested by T22-GFP-HA2-H6 was the result of the expected CXCR4 selectivity or it was rather mediated by a combination of the cell-penetrating properties of HA2 and of an enhanced permeability and retention (EPR) effect (96), or alternative ways to enter tumor tissues, such as endothelial transcytosis (97). To discriminate between these two possibilities, an *in vivo* competition experiment was designed in which the CXCR4 antagonist, AMD3100 (98), was used to block tumor accumulation of the administered protein materials. As observed **(Figure 36)**, the antagonist dramatically minimized the presence of T22-GFP-H6 nanoparticles in tumoral tissues, supporting again the role of T22 in active targeting for CXCR4+ cancers. Interestingly, AMD3100 equally reduced the tumor

accumulation of T22-GFP-HA2-H6 nanoparticles, at levels comparable to those determined for T22-GFP-H6 **(Figure 36)**. This result confirmed that T22 was fully active in T22-GFP-HA2-H6 as a targeting agent, and even a certain reduction of specificity could not be completely discarded, the tumor deposition of this construct was the result of an active targeting process. In summary, we have improved the T22-GFP-H6 nanocarrier regarding its uptake in tumor tissues by incorporating the fusogenic peptide H2A, while maintaining the CXCR4-dependence of its biodistribution.
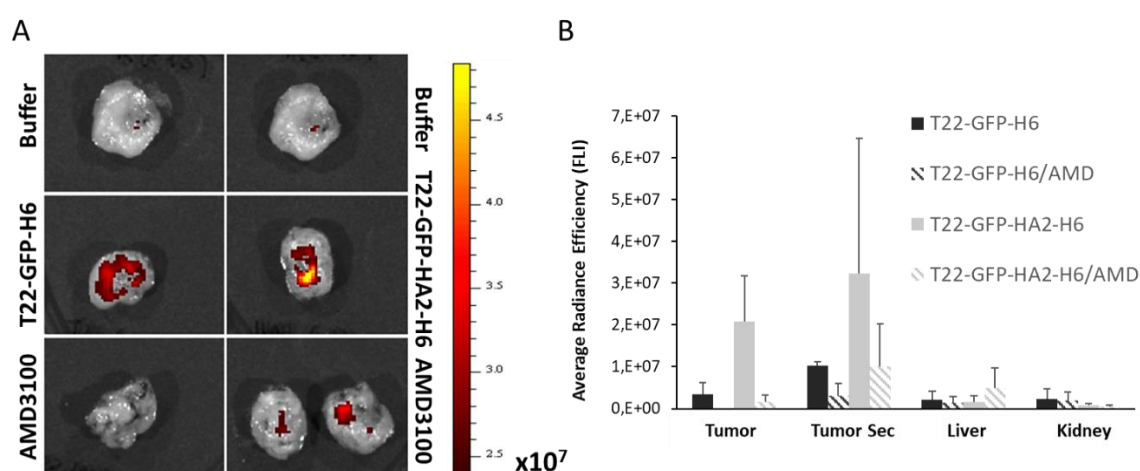
Figure 36. CXCR4-dependent biodistribution of T22-GFP-H6 and T22-GFP-HA2-H6 nanoparticles A) Inhibition of T22-GFP-H6 or T22-GFP-HA2-H6 nanoparticle accumulation in tumor tissue 5 h after their i.v. injection (200 µg dose) by the administration of the CXCR4 antagonist AMD3100 (10 mg/kg dose, 1 h before, 1 h after and 2 h after nanoparticle injection) B) Quantitation of the fluorescence-emitted in tumor (images in panel A), liver and kidney. Notice CXCR4-dependence for tumor accumulation for both nanoparticles and their lack of receptor-dependence and low level of accumulation in liver and kidney.

4) *IN VIVO* EVALUATION OF THE ANTINEOPLASTIC ACTIVITY OF T22-GFP-H6 THERAPEUTIC DERIVATIVES IN THE DEVELOPED HIGHLY METASTATIC CXCR4^{+} CRC MOUSE MODEL.

Once demonstrated that T22-GFP-H6 and its therapeutic derivatives selectively internalized *in vitro* in CXCR4^{+} CRC cells and accumulated *in vivo* in subcutaneous CXCR4^{+}

tumors without causing any systemic toxicity, we next evaluated the therapeutic potential of the engineered T22-GFP-H6 therapeutic derivatives.

First, we assessed the antitumor activity of the T22-GFP-H6-Aur nanoconjugate and the T22-PE24-H6 nanotoxin. For that purpose, we studied the capacity of each therapeutic nanoparticle to block tumor growth in the SW1417 cell-derived subcutaneous model, by administering them on a repeated dose regime. Next, we evaluated the antimetastatic activity of the same nanoparticles. In this case, the previously developed highly metastatic CRC model derived from the SW1417 cell line was used to study whether these therapeutic nanoparticles were able to prevent cancer cell dissemination from the primary tumors to other organs and inhibit metastases formation.

4.1. T22-GFP-H6-Aur repeated dose administration activates a lethal immunogenic response in Swiss nude mice

To study the possible antitumor effect of the T22-GFP-H6-Aur nanoconjugate, we used the SW1417 cell-derived subcutaneous model. When subcutaneous tumors reached an approximate volume, around 120 mm^3, mice were randomized in two groups; the buffer-treated group (N=10), i.v. administered with 150 µl of buffer, and the experimental group i.v. administered with 100 µg of T22-GFP-H6-Aur three times per week (N=10). Surprisingly, 8 out of 10 mice administered with T22-GFP-H6-Aur died minutes after the fourth dose. At that time, the tumor volume of the T22-GFP-H6-Aur treated group was smaller than the buffer-treated group, but without being significant **(Figure 37A)**.

Subcutaneous tumors and other normal organs were collected to evaluate the mouse cause of death. Surprisingly, none of the studied organs (liver, kidneys, brain, lungs and heart) showed any histological alteration in H&E stained sections **(Figure 37B)**; thus, the cause of death remains unknown. The fact that all mice died after the fourth nanoconjugate bolus and the certitude that Swiss nude mice maintain active B cell and robust NK cell responses, made us think that the activation of an immunogenic response by T22-GFP-H6-Aur could be the cause of the 80% death in the treated mice; however, this remains to be proven in future studies. Taking into account the high lethality

observed in nanoconjugate-treated mice, the preclinical development of this nanoconjugate is uncertain.
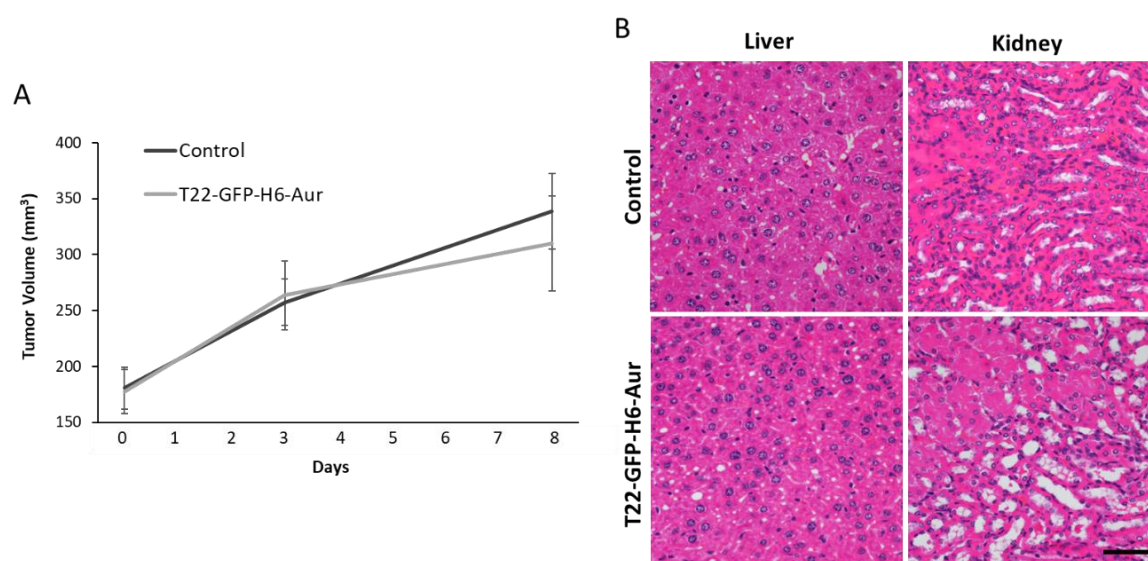
Figure 37. Antitumor effect of T22-GFP-H6-Aur and absence of toxicity in normal organs of dead mice A) SW1417 subcutaneous tumor growth of mice treated with buffer or the T22-GFP-H6-Aur nanoconjugate. Mice died after the fourth dose B) Representative H&E images of liver and kidneys from both, buffer and T22-GFP-H6-Aur treated mice, showing normal histological features. Scale bars: 50 μm.

4.2. T22-GFP-H6-Aur prevents only transcelomic metastases in the SW1417 cell-derived CRC model

We then evaluated the capacity of T22-GFP-H6-Aur to prevent metastasis using a more immunosuppressed mouse strain than Swiss nude to avoid the immunogenic reaction described above. Thus, we used the previously developed NSG mouse model to be treated with this nanoconjugate at a repeated dose schedule and to analyse at the end of the treatment period the percentage of mice free of metastasis and the reduction in foci number and foci size in mice with detectable metastases. For this purpose, we used the bioluminescent SW1417 cell-derived orthotopic model, which is highly metastatic, developing cancer foci in lymph nodes, liver, lung and peritoneum, and expresses moderate levels of CXCR4. We started the treatment with the T22-GFP-H6-Aur nanoconjugate three days after cecum cell injection, following a schedule of 100 μg, three times per week and a total of 12 doses.

At the end of the experiment, all target metastatic organs were collected and quantified in three H&E stained sections the number and size of the developed metastatic foci, in each affected organ **(Table 9)**. In contrast with the buffer-treated group, T22-GFP-H6-Aur treatment did not have the expected prevention capacity since only transcelomic metastases development were reduced. The percentage of mice affected by transcelomic metastases was slightly lower than in the buffer-treated group, but the number of peritoneal metastasis was significantly lower (3.2-fold reduction). Lymphatic (lymph node) and hematogenous (liver and lung) metastases development were not inhibited by the T22-GFP-H6-Aur treatment, since we did not find significant differences either in the percentage of mice affected by lymph node, hepatic or pulmonary metastasis, nor in the number of metastatic foci in these organs. Moreover, the growth of metastatic foci in lymph node, liver, lung and peritoneum was not either inhibited by the T22-GFP-H6-Aur nanoconjugate, since we did not find differences between the size of foci found in nanoconjugate-treated versus buffer-treated mice **(Table 9)**. Thus, based on the *in vitro* results and the lack of antimetastatic activity in lymph node, liver and lung, the T22-GFP-H6-Aur nanoconjugate, which carries a potent inhibitor of tubulin polymerization, is not a good candidate to treat CRC metastases, consequently excluding its further development as treatment for this indication.

Table 9. Evaluation of T22-GFP-H6-Aur antimetastatic effect by preventing the development of metastases in the SW1417 cell-derived CRC metastatic model.

T22-GFP-H6-Aur prevention of metastasis					
SW1417 cell-derived ortothopic model					
	Primary tumor	**Lymph node Mets**	**Liver Mets**	**Lung Mets**	**Peritoneal Mets**
Group	mice %	mice % # foci	mice % # foci	mice % # foci	mice % # foci
Buffer	10/10 100%	90%	100%	90%	100%
		3.2 ± 0.7	3.5 ± 0.4	17.6 ± 5.4	**5.5 ± 1.6[a]**
T22-GFP-H6-Aur	10/10 100%	80%	80%	90%	90%
		2.9 ± 0.7	3.6 ± 1.6	9.2 ± 4.1	**1.7 ± 0.4[a]**
Metastatic foci size (μm^2 x 10^3)					
Group	**Primary tumor**	**Lymph nods Mets**	**Liver Mets**	**Lung Mets**	**Peritoneal Mets**
Buffer	9990.5 ± 5137.9	449.7 ± 127.2	13.79 ± 3.1	4.4 ± 0.9	4702.2 ± 2353
T22-GFP-H6-Aur	7390.7 ± 3168.8	719.6 ± 125.1	45.3 ± 25.9	8.9 ± 3.4	8781.3 ± 3633

Mean + s.e.m. metastatic foci number or area (μm^2) per mouse, counted in three entire histology sections.

[a] **p=0.03**

4.3. T22-PE24-H6 repeated dose administration reduces tumor volume without toxicity in non-target organs

We next evaluated the antitumor effect of CXCR4-targeted nanoparticles carrying cytotoxic payloads capable of activating cell death mechanisms alternative to the apoptosis induced by chemotherapy genotoxic drugs or to the antimitotic microtubule inhibitors. Thus, active fragments of *Pseudomonas aeruginosa* exotoxin (PE24) were produced in *Escherichia coli* as self-assembled nanoparticles composed by modular fusion protein T22-PE24-H6 monomers, with the aim to induce targeted CXCR4^{+} cancer cell death through the activity of the catalytic fragments of this protein nanodrug. As explained in **2.4.** section, purified T22-PE24-H6 nanoparticles were first tested *in vitro* in SW1417 CXCR4^{+} cells, showing a specific reduction of cell viability in a dose-dependent manner and with a low IC_{50} (6.56 nM) compared to other therapeutic nanoparticles. To perform the T22-PE24-H6 nanotoxin *in vivo* evaluation we started by studying its antitumor effect in the subcutaneous cell-derived SW1417 model. SW1417 CXCR4^{+} cells were injected in Swiss nude mice, in which we have previously observed that a high dose of 10 μg of T22-PE24-H6 did not produce any toxic effect in non-target organs. Thus, when subcutaneous tumors reached a volume of approximately 120 mm^3, mice were randomized in two groups (N=7) and buffer or the nanotoxin were administered in a dose regime of 10 μg, three times per week, per 8 doses.

After only four doses of T22-PE24-H6, significant differences (p=0.02) in tumor volume were already detected between control mice treated with buffer and mice treated with T22-PE24-H6 **(Figure 38B)**. Moreover, at the end of the experiment after the eighth dose, we observed a 1.6-fold reduction in tumor volume, as compared to buffer-treated mice (p=0.005), associated with a reduction in tumor final weight (p=0.04) **(Figure 38C)**. This antitumor effect was most likely a consequence of the 3.0-fold increase in cell death bodies in tumor tissue (p<0.05) **(Figure 38D)**, with no significant differences in body weight between nanotoxin-treated and control groups **(Figure 38A)**. The lack of toxicity in non-target organs, such as liver and kidneys, was assessed by H&E stained sections and no histological alteration were found.
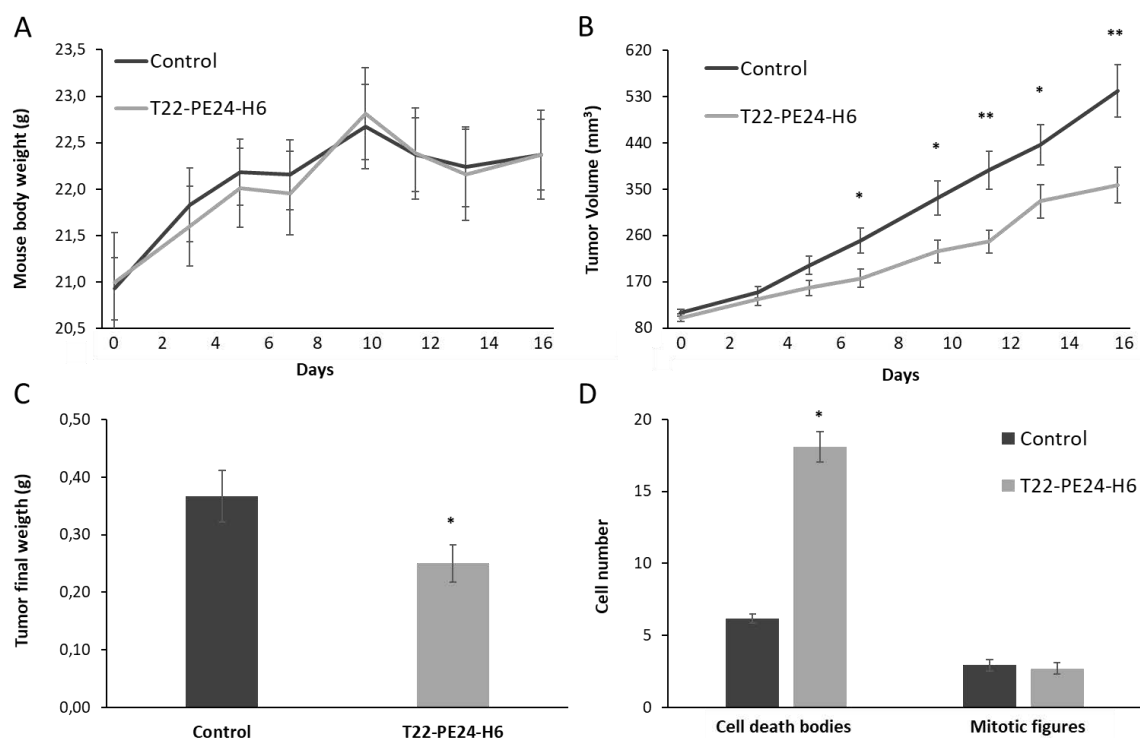
Figure 38. T22-PE24-H6 antitumoral effect in the cell-derived subcutaneous SW1417 CRC model A) Follow-up of mouse body weight (g) during the repeated dose administration of 10 µg of T22-PE24-H6 (three times a week, 8 total doses) B) Antitumor effect of T22-PE24-H6 measured by the analysis of tumor volume (mm^3) C) Antitumor effect of T22-PE24-H6 measured by the tumor weight (g) at the end of the experiment D) Increase in the number of cell death bodies in the SC SW1417 tumors collected at the end of the experiment. All data are presented as mean ± s.e.m., N=7. * $p<0.05$; ** $p<0.01$.

4.3.1. T22-PE24-H6 triggers pyroptotic cell death in SW1417 tumors

$CXCR4^+$ SW1417 subcutaneous tumors treated with repeated doses of 10 µg of T22-PE24-H6 allowed us to study the cell death mechanism induced by T22-PE24-H6 *in vivo*. Since we have found an *in vitro* activation of pyroptosis in SW1417 cells and an *in vivo* 3-fold increase in the number cell death bodies in nanotoxin-treated tumors, we evaluated whether the observed cell death bodies were a result of apoptosis or, as expected from the *in vitro* results, of the induction of pyroptosis. By performing immunohistochemistry assays against apoptotic markers in tumor tissue sections, we found no detectable or very low signal in active caspase-3 and proteolyzed-PARP staining of nanotoxin-treated tumors **(Figure 39A)**, suggesting that the mechanism of cell death was not mediated by apoptosis induction.
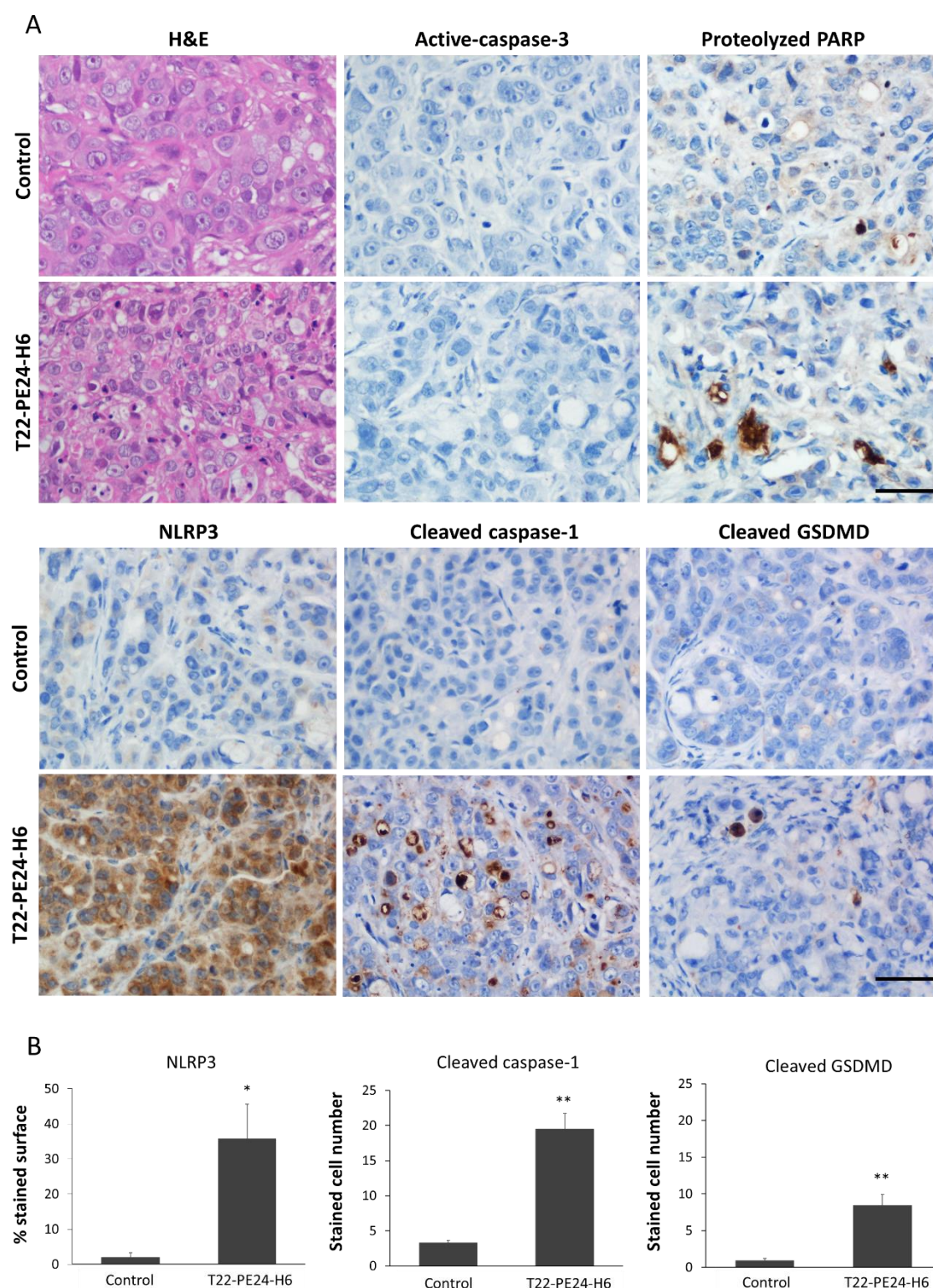
Figure 39. *In vivo* assessment of T22-PE24-H6-induced activation of the apoptotic or the pyroptotic cell death pathways A) Representative images of H&E and IHC staining of apoptotic (active-caspase-3 and proteolyzed PARP) and pyroptotic markers (NLRP3, cleaved caspase-1 and cleaved GSDMD) of SW1417 subcutaneous tumors from Swiss nude mice treated with 10 µg of T22-PE24-H6, three times a week and 8 total doses. Scale bars: 50 µm B) Quantification of each marker staining in buffer-treated mice and T22-

PE24-H6 treated mice. In NLRP3 stained sections, 5 high-power fields (400x) were analysed with ImageJ and quantification expressed as percentage of stained surface. In caspase-1 and GSDMD stained sections, 5 high-power fields (400x) were analysed by counting positive cells. Measurements in tissue sections were performed 24 h after the last administered dose and were compared to buffer-treated control mice. All the data are expressed as mean ± s.e.m.. * p<0.05; ** p<0.001.

As we have described before, besides apoptosis, there are other cell death mechanisms playing general physiopathological roles that may also have therapeutic implications. Pyroptosis, is an inflammatory caspase-dependent form of programmed cell death that occurs usually in response to microbial infection and similarly to apoptosis promotes nuclear condensation and chromatin DNA fragmentation. Expectedly, pyroptosis markers activated at different points of the pyroptotic pathway, display a high expression in tumors treated with T22-PE24-H6 compared to their expression in buffer-treated tumors. Thus, NLRP3, cleaved caspase-1 and cleaved Gasdermin D (GSDMD) showed a higher expression 24 hours after the last dose in the repeated T22-PE24-H6 nanotoxin administration **(Figure 39B)**. As observed in the *in vitro* experiments, the first marker to be activated is NLRP3 with a cytoplasmatic expression that represents a 35% of the stained surface tissue. After that, caspase-1 is activated showing a very specific staining of already pyroptotic bodies which increased 6 times compared to buffer-treated tumors. Finally, GSDMD is also activated in those pyroptotic bodies causing pore formation and cell death because of its pyroptotic cell effector role. These *in vivo* results, which are in full agreement with our *in vitro* observations, indicate that the T22-PE24-H6 nanotoxin induces pyroptosis in SW1417 subcutaneous tumors.

4.4. Definition of a dose regime for repeated T22-PE24-H6 administration in NSG mice

Since the different immunosuppressed mouse strains have a different tolerance to the diverse developed therapeutic nanoparticles, particularly regarding its toxicity on normal tissues, a preliminary experiment was performed to find the necessary T22-PE24-H6 repeated dose schedule that would achieve antimetastatic effect while showing lack of toxicity on non-tumor organs of NSG mice. For that purpose, we used the cell-derived CXCR4+ SW1417 bioluminescent orthotopic model in NSG mice and

assessed two different dosages. Thus, mice were randomized in three different groups; the buffer, 5 µg T22-PE24-H6 and 10 µg T22-PE24-H6 treated groups (N=3). The nanotoxin was administered three times per week for a total of 11 doses, starting the third day after CRC cell injection in the cecum. During treatment, body weight and cancer cells bioluminescence emission were registered twice per week. Mice were sacrificed after the eleventh dose due to a decrease in body weight of mice treated with the highest dose schedule of 10 µg **(Figure 40A)**. In contrast, we did not find differences in body weight between control buffer-treated mice and those treated with 5 µg T22-PE24-H6 dosage. The reduction in body weight observed in the 10 µg T22-PE24-H6 schedule was associated with renal amyloidosis, seen as protein deposits in renal tubules **(Figure 40C)**, provoking disabled renal filtering and kidney failure. Histological alterations were not found in other tested organs such as liver, lung, heart and brain at the 10 µg dosage. In mice treated with the 5 µg T22-PE24-H6 repeated dose schedule, no histological alterations were found in the kidney or any other normal organ.
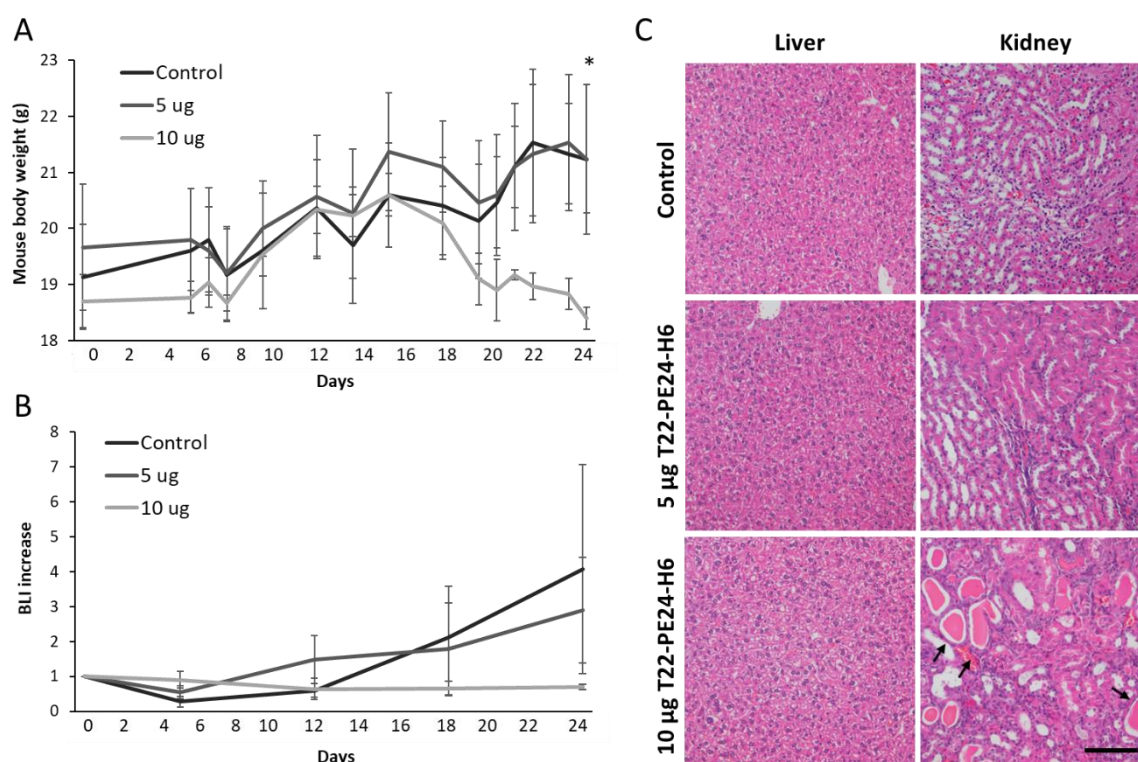
Figure 40. Definition of an effective and safe T22-PE24-H6 dosage to be administered in NSG mice A) Evolution of mouse body weight (g) during the repeated dose administration of 5 µg or 10 µg of T22-PE24-H6 (three times a week, 11 total doses) * p<0.05 B) Analysis of total bioluminescence showing an increase in NSG mice treated with T22-PE24-H6 compared to buffer-treated mice C) Representative H&E staining

images showing normal liver and kidney histology in control and 5 µg T22-PE24-H6 mice and protein deposits (arrows) in the renal tubules of 10 µg T22-PE24-H6 treated mice. Scale bars: 100 µm.

When analysing the progression of bioluminescence emission by SW1417-luciferase expressing cancer cells *in vivo*, we observed a 4.0-fold increase in control mice, while this increase was less pronounced (2.9-fold) in mice treated with the 5 µg repeated dose schedule than in those treated with 10 µg of T22-PE24-H6. Here, it is relevant to state that this small decrease in full body bioluminescence in nanotoxin-treated mice included the signal emitted by the primary tumor as well as that coming from the metastatic foci. Importantly, the *ex vivo* analysis of the different organs affected by metastasis, showed differences in bioluminescence emission in mice treated with both dose schedules of the nanotoxin, that were due to the growth inhibition of metastases rather than to their effect on the primary tumor **(Figure 41)**. The bioluminescence emitted by the tested organs of the nanotoxin-treated mice, which included metastatic foci disseminated to peritoneum, liver and lung, was lower than that emitted by the same organs of control mice, showing a dose-dependent effect, which correlates with a reduced metastatic load. Therefore, the 5 µg T22-PE24-H6 repeated dose was selected as the schedule to be administered in a new experiment with higher number of NSG mice bearing orthotopic tumors, to test whether the T22-PE24-H6 achieves an antimetastatic effect that significantly reduces the mouse metastatic load in the absence of associated systemic toxicity.
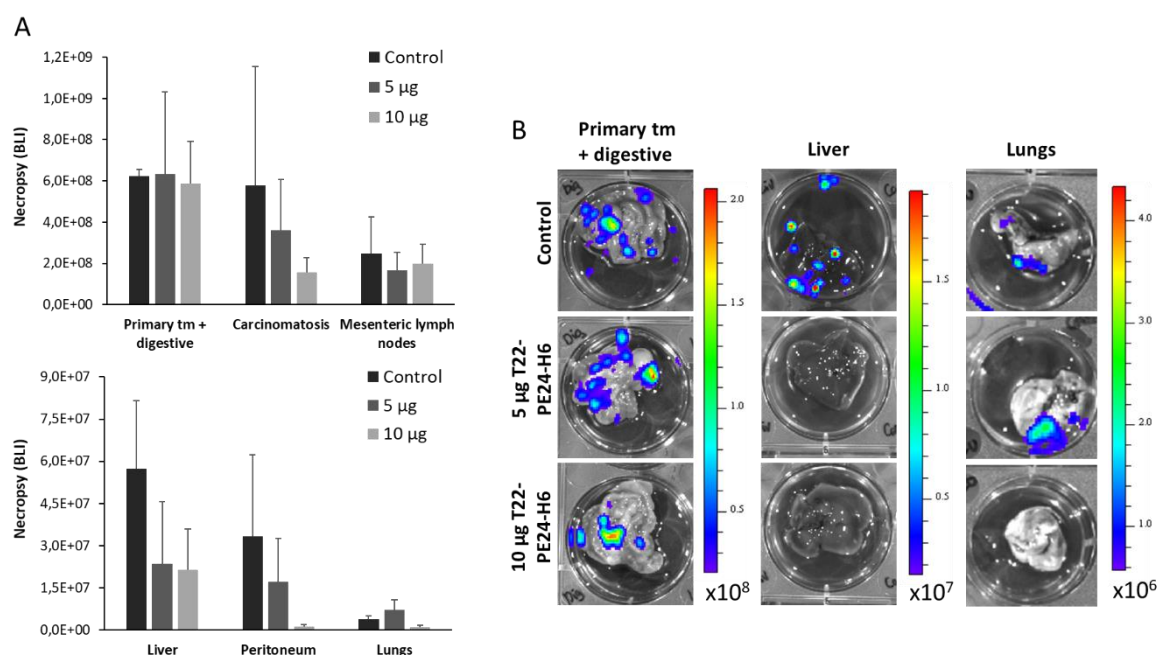
Figure 41. Antimetastatic activity induced by T22-PE24-H6 in regional and distant sites, measured *ex vivo* A) Comparison of bioluminescence emission between the buffer-treated, 5 µg T22-PE24-H6 and 10 µg T22-PE24-H6 repeated dose schedule groups in primary tumor, mesenteric lymph nodes, liver, lung and peritoneum. Results are presented as mean ± s.e.m. bioluminescence values in photons per second (total flux [p/s]) B) Representative bioluminescence images comparing primary tumor and metastatic dissemination in liver and lungs of mice treated with the nanotoxin (5 µg or 10 µg T22-PE24-H6) or buffer (control).

4.5. T22-PE24-H6 prevents the development of lymphatic and hematogenous metastasis in the SW1417 cell-derived CRC model

Once we selected the 5 µg T22-PE24-H6 repeated dose schedule as the non-toxic dose that achieves antimetastatic effect in NSG mice, we performed an assay to determine the capacity of this nanotoxin to prevent cancer cell dissemination and metastatic foci growth at the different target organs in the cell-derived orthotopic CXCR4^{+} SW1417 CRC model. This model metastasizes to lymph nodes, liver, lung and peritoneum, expecting that the treatment with T22-PE24-H6 could reduce the number and size of metastatic foci at the end of the experiment. So, a total of 18 NSG mice were implanted in the cecum with 2 million CXCR4^{+} SW1417 CRC cells. Three days after cell implantation, mice were randomized into two groups and we started administering the nanotoxin to the mice in the experimental group (N=9) following a dose schedule of 5 µg, three days per week for a total of 18 doses, or buffer following the same schedule (N=9). The treatment

continued until the first mouse belonging, either to the control or treated group, achieved the euthanasia criteria.

After 18 doses, control mice started to lose weight due to metastatic dissemination, a time point at which all mice were euthanised **(Figure 42A)**. At this point, we could find differences close to significance in total body bioluminescence between mice treated with T22-PE24-H6 and buffer-treated mice **(Figure 42B)**. The *ex vivo* bioluminescence analysis of each cancer-affected organ was performed, showing differences between both groups, as we previously found in the preliminary assay of dose definition.
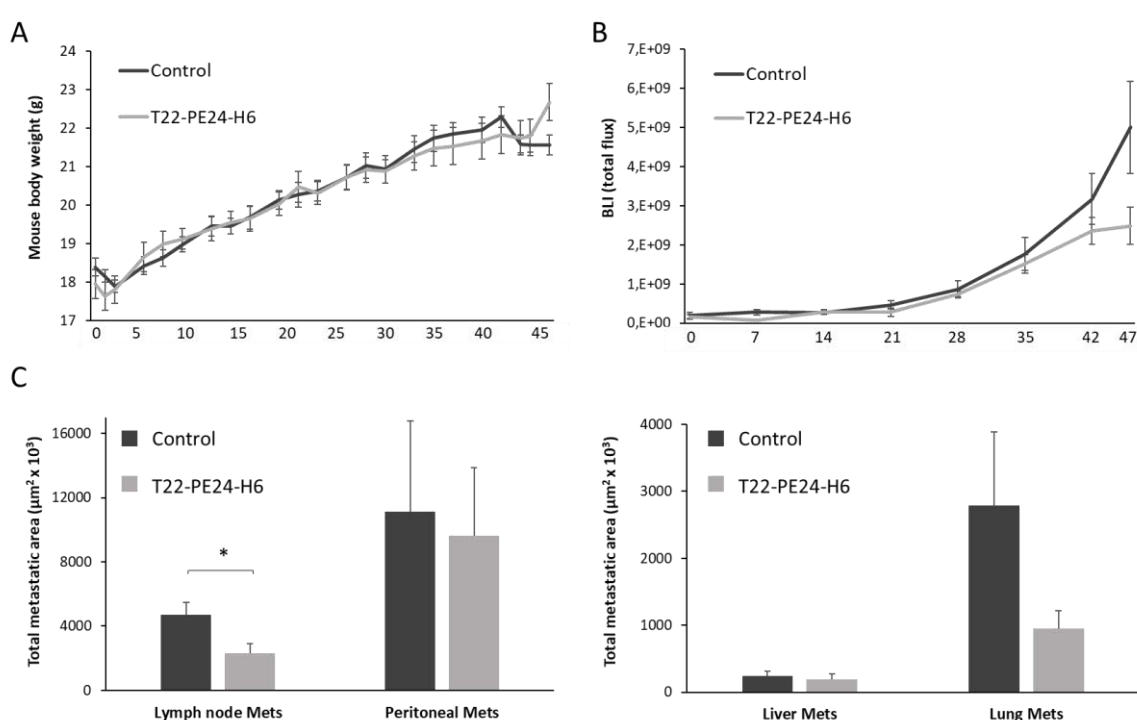
Figure 42. T22-PE24-H6 antimetastatic effect in the cell-derived orthotopic SW1417 CRC model A) Evolution of mouse body weight (g) the repeated dose administration of 5 µg of T22-PE24-H6 (three times a week, 18 total doses) B) Total body bioluminescence (BLI; Total Flux [p/s]) of buffer- and T22-PE24-H6 treated mice, measured once per week along all the experiment C) All data are expressed as mean ± s.e.m., N=9. * p<0.05.

Next, a histological evaluation of metastatic foci number and size was performed for each metastatic localization. Mice treated with T22-PE24-H6 presented a reduction in metastatic load (total metastatic area) in all affected organs, especially evident in lymph nodes (p<0.05) **(Figure 42C)**. In contrast to the findings in buffer-treated group, T22-

PE24-H6 treatment potently prevented lymphatic (Lymph node Mets) and hematogenous (Liver Mets and Lung Mets) metastasis development, whereas its capacity to prevent transcelomic metastases (Peritoneal Mets) was low. Consistent with the *ex vivo* bioluminescence results, mice treated with T22-PE24-H6 showed a 2-fold reduction in mean metastatic foci number in lymph node (p=0.008), a 2.1-fold reduction in liver (p=0.007) and a 2.5-fold reduction in lung (p=0.01), as compared to metastatic foci number of the corresponding sites in buffer-treated mice **(Table 10)**. However, we did not find a significant reduction in the number of peritoneal metastatic foci neither in their size. Moreover, primary tumors, lymph node metastases and lung metastases in T22-PE24-H6 treated mice tended to have a smaller mean size but they did not achieve statistically significant differences.

Table 10. T22-PE24-H6 antimetastatic effect measured by prevention of metastases development in the SW1417 cell-derived CRC metastatic model.

T22-PE24-H6 prevention of metastasis					
SW1417 cell-derived ortothopic model					
	Primary tumor	**Lymph node Mets**	**Liver Mets**	**Lung Mets**	**Peritoneal Mets**
Group	mice %	mice % # foci	mice % # foci	mice % # foci	mice % # foci
Buffer	9/9 100%	100% **7.1 ± 1.1**[a]	100% **15 ± 1.9**[b]	100% **49.2 ± 9.6**[c]	89% 4.4 ± 0.7
T22-PE24-H6	9/9 100%	100% **3.4 ± 0.5**[a]	100% **7.1 ± 1.6**[b]	89% **19.7 ± 4.1**[c]	89% 3.2 ± 0.9
Metastatic foci size (μm² x 10³)					
Group	**Primary tumor**	**Lymph nods Mets**	**Liver Mets**	**Lung Mets**	**Peritoneal Mets**
Buffer	9428.8 ± 1081.1	739.8 ± 94.6	15.7 ± 3.5	44.1 ± 9.1	2423.4 ± 1141.2
T22-PE24-H6	7331.5 ± 978.8	513.8 ± 99.3	16.5 ± 4.2	36.1 ± 8.9	2579.2 ± 1345.9

Mean + s.e.m. metastatic foci number or area (μm²) per mouse, counted in three entire histology sections.

[a] **p=0.008;** [b] **p=0.007;** [c] **p=0.01**

V. DISCUSSION

V. DISCUSSION

Colorectal cancer (CRC) is one of the most common neoplasias in developed countries, accounting for almost 900,000 deaths per year. Its incidence is progressively rising worldwide due to the adoption of sedentary and unhealthy lifestyles such as red meat, alcohol and tobacco consumption. However, the promotion of early detection tests and new treatment options have reduced its mortality. Despite this advance, nearly a quarter of CRC patients are diagnosed at an advanced stage carrying already metastases, which hinders their surgical removal and subsequent tumor-related deaths. For these patients, treatment consists in shrinking the tumor and supressing cancer spread and growth, using radiotherapy and chemotherapy or combination with targeted therapies.

Current chemotherapy for CRC is mainly based in fluoropyrimidine (5-FU), which results in the improvement in survival of approximately 30%, with an addition of 20% improvement when used in a combined regime with oxaliplatin in stage III CRC (99). Some targeted therapies that inhibit VEGF and EGFR pathways have also demonstrated to improve the outcome in metastatic CRC patients when combined with chemotherapy. However, both chemotherapy and molecularly targeted agents, especially that have a low molecular weight, display a passive diffusion affecting non-tumor and tumor tissues, without any selectivity for cancer cells; thus, damaging normal cells and inducing systemic toxicity. Chemotherapy interferes with cell division targeting all rapidly dividing cells in the body, harming also healthy tissues, especially those tissues that have a high replacement rate (intestinal lining and immune cells). Moreover, chemotherapy has other limitations apart from systemic toxicity, such as low response rate, development of resistance and absence of tumor selectivity. Molecularly targeted therapies, mainly based in monoclonal antibody development, also present limitations like toxicities due to the fact of targeting a general biological process in the human body such as angiogenesis or a lack of response in the case of *KRAS* mutated tumors when treated with anti-EGFR therapies. For all these observations, the tolerated doses of these agents are low, which is translated in insufficient antitumor effect.

Due to the limitations of current therapies, further investigations are still required to develop new strategies to improve current metastatic CRC treatments. One main goal

of these new approaches pursues the complete elimination of cancer cells without damaging non-tumor cells or organs of the rest of the body. For this purpose, nanoparticles are being exploited as nanocarriers attempting to deliver cytotoxic drugs only to cancer cells. The acquired knowledge about the mechanisms leading to cancer progression and metastasis is a valuable tool for the selection of specific cancer cell antigens, which can be actively targeted by these nanocarriers.

In this thesis, we aimed at taregting cancer stem cells (CSCs) which current therapies are failing to eliminate (100). Within the tumor, CSCs are a subset of cells that possess the ability to self-renew and to differentiate into all cell populations. Moreover, recent findings demonstrate that a subpopulation of CSCs with epithelial-mesenchymal transition (EMT) properties or partial EMT, can initiate tumor growth in secondary sites (metastatic CSCs) (101,102). Thus, we chose the CXCR4 receptor as a specific target present in metastatic CSCs, whose overexpression has been associated with chemotherapy resistance, relapse, metastasis (103) and poor clinical outcome (37) in CRC and other cancer types (29). According to the homing theory, target organs produce and release specific chemokines such as CXCL12 and attract distant CXCR4$^+$ cancer cells. Moreover, it is known that CRC cells with metastatic initiation capacity possess both stemness/EMT (CD133$^+$) and metastatic (CXCR4$^+$) properties. It has also been shown that CD133$^+$CXCR4$^+$ CRC cells have enhanced migratory capacity *in vitro* and higher metastatic potential *in vivo* than CD133$^+$CXCR4$^-$ cells (104). CXCR4 is also expressed on circulating tumor cells (CTCs) and the number of CD133$^+$CXCR4$^+$ cells in the bloodstream correlates with poor prognosis (104). Taken together, these findings indicate that metastatic CSCs expressing CXCR4 are clinically relevant targets; thus, their selective elimination could represent an advance in metastases control.

As described in the introduction, in collaboration with the Nanobiotechnology group of the UAB, we developed self-assembled protein-only nanoparticles for actively targeting CXCR4$^+$ cells which present high biocompatibility, biodegradability and functional versatility. The narrow therapeutic window of classic cytotoxic drugs can be solved by loading them in these nanoparticles, enhancing their pharmacokinetic characteristics, enabling passive targeting in tumors via the EPR effect described in mouse tumors (105), or alternatively increasing tumor uptake by endothelial

transcytosis. Since the existence of EPR effect is being questioned in human tumors (106), nanoparticles allow as well functionalization with specific peptides for active targeting of tumor cells, thus reducing systemic toxicity.

Therefore, the main objective of this work has been the preclinical validation of the different T22-GFP-H6 therapeutic derivatives as potential treatments for metastatic CRC. The selective biodistribution of the nanoparticles and the antitumor effect of their therapeutic derivatives had to be studied *in vitro* and in newly developed CXCR4+ CRC mouse models. Using both established CRC cell lines and patient samples, we developed highly metastatic CRC models, which were then used to assess the antimetastatic effect of T22-GFP-H6-derived nanoconjugates or of newly synthesized protein-only nanoparticles with intrinsic cytotoxic activity.

1) DEVELOPMENT OF CXCR4+ SUBCUTANEOUS AND HIGHLY METASTATIC CRC MOUSE MODELS FOR THEIR USE IN PRECLINICAL STUDIES

The discovery and preclinical testing of novel therapeutic strategies in CRC, as in other cancers, requires the use of *in vitro* and *in vivo* models of each cancer type. *In vitro* cancer models, using cell culture, are important tools for cancer research and have been widely used as low-cost screening platforms for anticancer agents. Nowadays, three dimensional (3-D) organoid tissue cultures derived from self-renewing stem cells, are able to recapitulate the *in vivo* architecture, functions and genetic and molecular imprints of their original tissues, representing an advanced *in vitro* tool for anticancer drug discovery (107,108). However, they present some limitations since they are not able to replicate important processes or mechanisms activated during tumor progression that occur only *in vivo*, such as their interactions with the tumor microenvironment, invasion and metastatic dissemination, which is the cause of the majority of cancer-related deaths. On this basis, *in vivo* CRC models that recapitulate the pathogenesis observed in patients (angiogenesis, metastasis and response to therapy) are essential for the development of effective therapies. Currently, the most used *in vivo* models for therapeutic studies are murine xenografts, where CRC cells are injected

subcutaneously in immunosuppressed mice, but they still have limitations that could be overcome by the development of patient-derived xenografts (PDXs) and orthotopic models.

1.1. Cell and patient-derived subcutaneous xenografts for nanoparticle preclinical evaluation

In this thesis, we developed CXCR4$^+$ subcutaneous CRC models for their use in the assessment of nanoparticle biodistribution and antitumor effect, in which we could also study their selective internalization in cancer cells and the induction of specific mechanisms of cell death. All these models were generated in Swiss nude mice, which is the cheapest and the less immunosuppressed mouse strain. We used xenograft models for these assays because of their low cost, which allows the use of a bigger experimental number to reach sufficient statistical power, the short time needed to develop it and their ease of use, especially for measuring tumor growth.

On the one hand, cell-derived xenograft models were developed by injecting the CXCR4-overexpressing (CXCR4$^+$) SW1417 cell line in the subcutis of Swiss nude mice. The tumors derived from these cells maintained a constant growth rate that was dependent on CXCR4 expression, since CXCR4$^-$ SW1417 cells were unable to generate subcutaneous tumors at all. These results correlate with those reported for prostate cancer *in vivo* experiments, in which NOD/SCID mice injected with cells that expressed higher levels of CXCR4 (PC3LG-CXCR4 and 22Rv1G-CXCR4) developed larger tumors than mice injected with the parental cells (109). Moreover, exposure to specific antibodies against CXCR4 inhibited the CXCR4-dependent growth in the PC3LG-CXCR4 cell line. Other results suggested that the activation of the CXCL12/CXCR4 axis which promotes tumor growth in prostate cancer, is driven by the loss of PTEN, frequently observed in cancer, and subsequent activation of Akt (110). In CRC, approximately 40% of tumors show decreased expression of PTEN, often in association with its mutation or deletion (111). Moreover, *in vitro* studies demonstrated a correlation between PTEN loss and CXCL12/CXCR4/Akt activation, promoting an increase in cell proliferation and invasion (112). So, the CXCR4 overexpression might exert favourable conditions not only for

invasion and migration, but also in enhancing tumor growth, which cloud lead to a more efficient seeding of CTCs to distant metastatic sites.

On the other hand, we also developed patient-derived xenografts (PDXs) by engrafting portions of tumor patient tissue into immunosuppressed mice. CRC tumor samples were collected in collaboration with the Department of General and Digestive Surgery of the Hospital de la Santa Creu i Sant Pau after obtaining the informed and signed patient consent, and they were implanted in the subcutis of Swiss nude mice. A total of 30% of the collected and implanted tumor samples, developed viable subcutaneous tumors. One of them, the SP5 sample was maintained *in vivo* as a tumor line through successive passes in Swiss nude mice. Moreover, the SP5 subcutaneous tumor line maintained *in vivo* showed a significantly higher membrane expression of the CXCR4 receptor than that observed in SW1417 cell-derived subcutaneous tumors. In contrast to cell-derived xenografts, in PDXs tumors, both stromal and cancer cells grow, allowing for tumor-stroma crosstalk and conserving cellular and molecular heterogeneity. Furthermore, PDXs tumors maintain important characteristics of tumor histology, vascularity and architecture of primary CRCs; therefore, their use could be more appropriate for the development of novel therapeutic approaches than cell-derived tumor models.

1.2. Severe immunosuppression increases the metastatic capacity of CRC cells, disseminating to clinically relevant sites in orthotopic mouse models

Despite metastasis is the main cause of death in CRC patients, GEM and subcutaneous xenografts mouse models fail in reproducing the pathogenesis observed in patients, since they are barely metastatic. In contrast, the orthotopic implantation of cancer cells into the mouse cecum is a promising approach for the development of metastatic CRC models. However, it is scarcely used because of the technical challenges and difficulty in tumor monitoring. In this thesis, we also developed highly metastatic CRC mouse models in a short time (1-2 months to develop distant metastases) using the orthotopic microinjection of CRC cell lines or disaggregated patient tumor samples in immunosuppressed mice, which displayed overexpression of the CXCR4 receptor in

epithelial cancer cells. These models were used for the evaluation of the antimetastatic effect of the newly developed therapeutic nanoparticles targeting the CXCR4 receptor.

The OCMI procedure which consists on the microinjection of CRC cells between the mucosa and the muscularis externa layers of the cecal wall, was used for this purpose. In previous studies where CRC cells lines (HCT116, SW620 and DLD1) were microinjected in Swiss nude mice, we found that the dissemination pattern closely replicated all relevant metastatic sites observed in humans and enhanced the metastatic rate compared to previous methods (51). Despite this advance, when metastases developed, mostly microfoci having an area lower than 750,000 μm^2 were observed, limiting their use for the preclinical evaluation of antimetastatic compounds.

Previous reports have described the role of the immune system in the control of cancer progression and immune surveillance. Thus, considering the limitations of our previous models, our next aim was to increase the metastatic rate of the newly developed orthotopic model by depleting tumor surveillance, therefore using alternative mouse strains with an increased immunosuppression condition. We chose to orthotopically inject CXCR4$^+$ SW1417 CRC cells, which are also bioluminescent allowing to monitor tumor and metastases growth. These cells were implanted orthotopically in two immunosuppressed mouse strains; NOD/SCID and NSG mice. Both mouse strains have a total lack of adaptive immune cells such as B and T lymphocytes and impairment in the innate immunity including loss of complement and impaired NK, macrophage, and dendritic cell functions (113). Neutrophils and defective dendritic cells and macrophages constitute most of the remaining mouse immune cells detectable in peripheral blood in both mouse strains. However, NOD/SCID mice contain residual NK activities, which are totally absent in NSG mice (114). Therefore, we observed that the lack of NK cells reduced the survival of NSG mice carrying CRC tumors in comparison to NOD/SCID mice. Our results showing a high increase in metastatic rate when using NSG mice, are consistent with several studies in different types of human cancers, including CRC, where an improved overall survival was observed in patients with higher levels of tumor-infiltrating lymphocytes (TILs) and NK cells, that mediate cytotoxic functions independent of MHC-mediated antigen presentation (115,116). Other studies using models of spontaneous leukemia and prostate cancer, showed an accelerated

development of cancer in animals with a depletion of NK cells compared to animals with a normal NK cells activity (117).

In our hand, both NOD/SCID and NSG mouse models displayed a high dissemination pattern. We observed that SW1417 cells were able to infiltrate the lymph nodes of the intestinal wall draining the tumor, developing first mesenteric lymph node metastases, then migrating through the hematogenous route into the liver and lung, and through the transcelomic cavity to generate metastases in the peritoneum, as observed in CRC patients. The orthotopic placement of cancer cells into the submucosal compartment improves the dissemination of the cells compared to other methods such as GEM or tail vein injection by replicating the interactions with tumor microenvironment, extracellular matrix (ECM) of the lymphatic system and vasculature, both, playing significant roles in migration, intravasation and colonization at distant sites (118).

Moreover, in NSG mice the hematogenous dissemination rate of SW1417 cells was higher compared to NOD/SCID mice, presenting a 5-fold increase in metastatic foci in lung and liver. In contrast, we did not find differences in the number of metastatic foci in lymph node; however, the developed metastases presented a larger area in NSG mice. So, the immunosuppressed background of NSG, totally deficient in NK cells, allowed the SW1417 cells to colonize distant organs through the hematogenous route with a higher efficiency and also to enhance the growth of liver and lymph node metastases to reach a macrofoci size or even visible metastases. Massagué et al. described that in early stages of cancer progression, the primary tumor cells capable to enter the circulation (CTCs) and infiltrate the distant organs, are particularly vulnerable to immune surveillance; however, some of them can remain as latent disseminated tumor cells (DTCs), single cells or micrometastases (119). The process by which latent DTCs are able to proliferate and develop macrometastases is not completely understood. It is known that the DTCs have an attenuation of Wnt signalling and that a depletion of NK cells by different means can lead to an aggressive metastatic outgrowth of latent cancer cells (120). Thus, consistent with our findings, when the immune surveillance is suppressed, latent cancer cells can enter the cell cycle, and generate proliferative clusters that will progress to macrometastases. Moreover, the specific presence of immune cells in an organ can also influence its susceptibility to be colonized by cancer cells. For example,

the liver, in which we found greater differences in SW1417 cells colonization between NOD/SCID and NSG mice, is particularly rich in NK cells. Consistently, in some studies the neutralization of the pro-apoptotic NK-derived factor TRAIL or genetic depletion of NK cells in mice, increased hepatic metastasis (121).

Since CRC cell lines commonly show low or moderate levels of CXCR4 and its expression is not always maintained *in vivo*, we also developed a patient-derived CRC orthotopic model (SP5) using NSG mice, which was generated in a time as short as 1 month. The severe mouse immunosuppression allowed the dissemination of cancer cells derived from a SP5 disaggregated subcutaneous tumor to relevant sites (lymph nodes, liver, lung and peritoneum), while showing in parallel an accelerated primary tumor growth, which caused mouse death. In this model, both primary tumor cells and metastatic foci maintained the high levels of membrane CXCR4 expression observed in the resected patient tumor sample. This might be explained because PDXs do not lose tumor-microenvironment interactions which make them preserve intratumor heterogeneity that has been demonstrated to be stable along the time in neuroblastoma orthotopic PDXs (122,123).

2) T22-GFP-H6 ACHIEVES HIGHLY SELECTIVE INTERNALIZATION AND TUMOR UPTAKE IN CXCR4$^+$ CRC MODELS

Once, we had developed highly metastatic CRC mouse models that overexpress the CXCR4 receptor, we studied the T22-GFP-H6 nanocarrier biodistribution, using these models, to evaluate whether they are sufficiently selective in reaching cancer tissues before testing their antimetastatic effect. Regarding this issue, recent studies report that nanomedicines present a huge limitation in delivering drugs to cancer cells due to the fact that only the 0.07-7% of the injected dose reaches the tumor (62,124). The combination of nanoparticle size and its functionalization by PEGylation, the incorporation of endosomal escape peptides or peptide-mediated active targeting might solve this problem by improving tumor uptake. In this thesis we demonstrated that active targeting of CXCR4$^+$ cancer cells achieves a selective internalization and a high

tumor tissue uptake for the T22-GFP-H6 nanocarrier in the newly developed CXCR4+ CRC models.

In cell culture, the CXCR4 peptide ligand T22 confers the T22-GFP-H6 nanocarrier the capacity to selectively bind to the CXCR4 receptor and internalize in CXCR4+ SW1417 cells *in vitro*, reaching within 24 hours a perinuclear location as demonstrated before in HeLa cells (69). This perinuclear location shows that the T22-GFP-H6 nanocarrier is able to efficiently escape from endosomes due to proton-sponge activity of the accompanying polyhistidines tail, which also has important structural and stability roles (72), and to escape degradation in the lysosome, efficiently delivering the cargo into the cytoplasm.

Furthermore, when the T22-GFP-H6 was tested in the patient-derived SP5 subcutaneous CRC mouse model, we observed that tumor uptake achieved 72% of the total emitted fluorescence (tumor + non-tumor organs fluorescence) and the rest was mainly found in normal organs, especially in liver and kidney. Fluorescence emission from other CXCR4- organs such as brain, lung or heart and from CXCR4+ non-tumor organs (bone marrow and spleen) was undetectable or very low. Our approach achieves the goal of targeting cancer cells by exploiting their CXCR4 membrane overexpression as compared to cells of non-tumor tissues **(Figure 43)**. We have recently reported other studies in diffuse large B-cell lymphoma (DLBCL) models, where we also found a very high tumor uptake of approximately 86% of the total emitted fluorescence (125). The higher accumulation of the T22-GFP-H6 nanocarrier in the DLBCL models might be explained by the high membrane levels of CXCR4 expressed by the DLBCL Toledo cell line and the capacity of the T22-GFP-H6 to highly internalize in target cells after interacting with CXCR4 because of the T22 ligand multivalency displayed by its nanostructure. Thus, our results showed that most of the proteolytic metabolism of T22-GFP-H6 occurs in the tumor, whereas clearance in liver or kidney is not significant. The T22-GFP-H6 nanocarrier has been detected in these two normal organs, probably by transiently accessing the fenestrated vessels during a short time period to finally return to bloodstream circulation, but without reaching their parenchyma or causing toxicity.

Virus have been evolving during millions of years to overcome degradation once they have internalized in the host cell to increase their survival (126). Interestingly, when combining active targeting and the accommodation of the fusogenic HA2 peptide from the influenza virus, in a particular site between the GFP and H6 modules within the designed fusion protein, dramatically enhanced the accumulation of nanoparticles in target tumor tissues. A fast and efficient tumor retention of T22-GFP-HA2-H6 was unexpectedly observed, peaking between 2 and 5 hours, and proving cooperativity between endosomal escape and receptor-based tumor cell targeting, leading to an extremely high accumulation of this nanoparticle in the target cell cytosol, a finding that could be exploited in future therapeutic nanoparticle development.
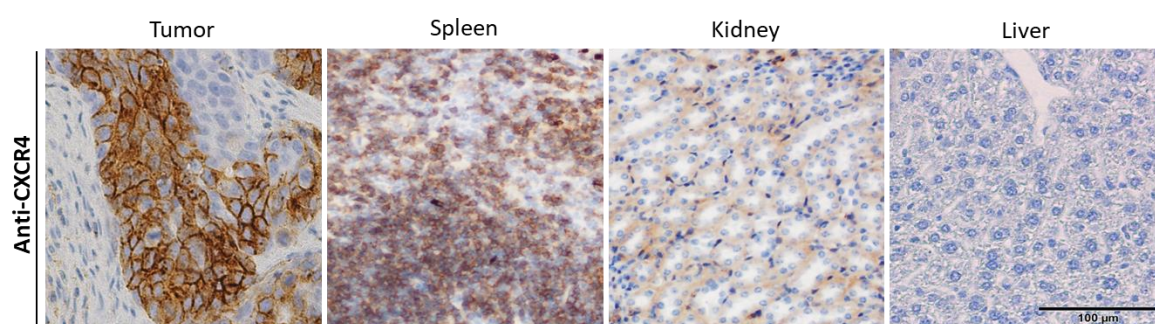
Figure 43. Differential expression of CXCR4 in tumor and non-tumor organs. High overexpression of the CXCR4 receptor in the membrane of cancer cells in SP5 subcutaneous tumors. In contrast, non-tumor organs showed moderate and mostly cytosolic CXCR4 expression (spleen) or negligible CXCR4 expression (kidney and liver). Scale bars: 100 µm.

The results on the T22-GFP-H6 biodistribution in the subcutaneous PDX model confirmed the selective internalization of the nanocarrier in CXCR4 expressing cells. On the one hand, we observed a specific co-localization of the nanocarrier and the CXCR4 receptor in the cell membrane. Moreover, the presence of the nanocarrier also in endosomal vesicles confirmed their internalization via endocytosis, the capacity to escape from endosomes and the delivery of the material into the cytoplasm, before its final intracellular proteolysis (69). On the other hand, competition assays with the CXCR4 antagonist AMD3100 showed a reduced tumor uptake of both T22-GFP-H6 and T22-GFP-HA2-H6 nanoparticles in the subcutaneous PDX model, demonstrating their selectivity in targeting CXCR4$^+$ cancer cells.

The enhancement of T22-GFP-H6 tumor uptake that reached 70% of the total emitted fluorescence in CRC models may represent an advance for its use as a drug carrier in cancer treatment compared to the uptake reached by passively targeted nanomedicines. This success may be explained not only by the incorporation of a targeting peptide but also by the nature of the nanocarrier material. Several studies have demonstrated that active targeting enhances selective intracellular uptake at the same time that plays a role in enhancing tumor accumulation (127). Mesoporus silica nanoparticles (MSN) binding to CD105 on tumor neovasculature through the TRC105 antibody achieved a 10 % ID/g (Injected Dose/g) tumor uptake in murine breast cancer models, that was 3 times higher than the achieved by the non-targeted nanoparticle, as measured by positron emission tomography (PET) imaging (128). Nevertheless, despite this progress, TRC105-MSN were mostly accumulated in the liver, an issue pervasively observed in both inorganic (gold, silica, iron) and organic (dendrimers, liposomes polymers, hydrogels) nanoparticles, but not found in protein-based nanoparticles (129). When the non-protein-based nanoparticles reach the systemic circulation, proteins circulating in blood bind to the nanoparticle surface creating a protein corona, which changes nanoparticles surface properties, blocking their capacity to reach target cells in cancer mouse models (despite having demonstrated targeting capacity in cell culture) and making them easily recognized by the innate immune system. Consequently, they undergo a quick clearance by phagocytic cells located in organs such as lungs, liver and spleen (130,131). Therefore, the use of proteins as drug carriers has had a great impact in the development of nanomedicines for cancer therapies because of their high biodegradability, low toxicity and their non-immunogenic character, especially when using protein sequences of the same species as the one being treated.

In conclusion, our results validate T22-GFP-H6 as a highly efficient nanocarrier for selective drug delivery to CXCR4^{+} cancer cells, showing a high specific tumor uptake and absence of toxicity in non-tumor organs. This novel approach could significantly improve current cancer treatment increasing the antitumor effect by delivering higher concentrations of anticancer agents to CXCR4^{+} cells responsible for cancer growth and dissemination.

3) CXCR4⁺ TARGETED NANOPARTICLES CONJUGATED TO THE AURISTATIN TOXIN ACHIEVE POOR ANTIMETASTATIC EFFECT IN CRC MODELS

We conjugated different therapeutic agents to the T22-GFP-H6 nanocarrier to be evaluated as anticancer agents. Our first targeted drug delivery strategy, aiming at selectively eliminating CXCR4⁺ cancer cells, was tested in metastatic CRC models. Specifically, we evaluated T22-GFP-H6-Aur obtained by the conjugation of the nanocarrier to the potent antimitotic agent Auristatin E, which is a microtubule destabilizing toxin recently introduced in haematological cancer treatment (132). We demonstrated that the T22-GFP-H6-Aur nanoconjugate replicated the capacity for self-assembling and selective internalization in CXCR4⁺ CRC cells previously observed for the T22-GFP-H6 nanocarrier *in vitro,* as well as maintained its *in vivo* biodistribution by showing a high tumor uptake and poor accumulation in non-tumor organs. Moreover, this nanoconjugate was able to transport and release the Auristatin into the cytosol of CXCR4⁺ cancers cells, leading to cell death through induction of mitotic catastrophe. Surprisingly, repeated administration of the T22-GFP-H6-Aur nanoconjugate activated a lethal immunogenic response and only inhibited the development of transcelomic metastases, having no impact on lymphatic or hematogenous metastases, in the highly metastatic cell-derived CRC model in NSG mice, which questions its further preclinical development.

Biocompatibility and low immunogenicity are key properties for biomaterials to be used in targeted drug delivery. We found that our highly biocompatible protein-based nanoconjugates T22-GFP-H6-Aur and T22-GFP-H6-FdU (results not shown) administered at repeated doses, activated a lethal immunogenic response only in Swiss nude mice, the less immunosuppressed mouse strain. Swiss nude mice present a deletion in the FOXN1 gene causing a deteriorated or absent thymus, which results in deficient adaptive immunity due to a reduction of mature T lymphocytes. In contrast, they have intact B cells and innate immunity with functional macrophages, granulocytes and NK cells, therefore being able to induce immunogenicity as it would happen in immunocompetent mice (e.g. syngeneic or humanized mouse models). When protein

therapeutics are administered, antigen presenting cells (APCs), such as B or dendritic cells, present them as peptides to T cells being recognized as foreign (133). This immune cell cascade can result in unwanted immunogenicity, by the generation of anti-drug antibodies (ADAs) which might neutralize or compromise their clinical effect, being sometimes associated with serious adverse effects related to cross-reactivity with autologous proteins (134). Interestingly and in accordance with our results, a T-cell-independent immune response has been demonstrated for polyvalent antigens of bacterial and viral origin. This T-independent stimulation of B cells may occur when the protein forms a multimeric structure that can effectively cross-link the B-cell receptor to a point where co-stimulation from T cells is not required (135,136).

Contrarily, the repeated administration of low doses of similar nanoparticles with intrinsic cytotoxic activities such as the T22-PE24-H6 nanotoxin, where the GFP protein had been replaced by the deimmunized PE24 toxin, did not show any immunogenic response in Swiss nude mice. Thus, the GFP protein might be the responsible for the activation of the lethal immune response, due to its non-human nature. So, our lab is working on decreasing this effect by replacing the GFP protein of the nanocarrier by a human protein (e.g. albumin or entactin), which could also maintain the structure and the self-assembling capacity of the nanoparticles.

The obtained results did not show the expected increase in antimetastatic effect of the nanoconjugate that covalently binds the T22-GFP-H6 nanocarrier to the Auristatin E toxin, which a priori had a higher therapeutic potency as compared to current chemotherapeutics such as Floxuridine (FdU). In previous studies, shown in Annex 1, we demonstrated that the repeated administration of the nanocarrier conjugated to FdU achieved a potent and site-dependent metastasis prevention, observing a reduction of metastatic foci number and size in lymph nodes, liver, lung and peritoneum compared to buffer and free-oligo-FdU treated mice. Furthermore, our group also demonstrated that the T22-GFP-H6-Aur nanoconjugate achieved anticancer activity in a CXCR4^{+} acute myeloid leukemia (AML) model, by significantly reducing the leukemic cell burden in the bone marrow and circulating blood, and by inducing a potent blockade of leukemic cell spread to extramedullar organs (137). T22-GFP-H6-Aur had a potent cytotoxic effect in AML cell lines *in vitro*, showing an IC50 of 100-150 nM, which we did not observed in

CRC cells by XTT assays, finding a complete lack of antitumor effect with a 1 µM cell exposure. Thus, the poor antimetastatic effect displayed by the T22-GFP-H6-Aur in CRC models, could be due to a lower sensitivity of CRC cells to the Auristatin toxin compared to AML cells, but not due to the anticancer conjugation protocol, which showed effectiveness when conjugated, using the same procedure, to FdU.

Current therapeutic agents using Auristatin E for cancer treatment, are mainly developed as antibody-drug conjugates (ADC). Brentuximab vedotin was the first FDA approved ADC based on Auristatin E, made by conjugation of the monomethyl auristatin E (MMAE), to an anti-CD30 antibody, which is a marker of activated lymphocytes and it is highly expressed in Hodgkin lymphoma and anaplastic large-cell lymphoma malignant cells (138). Recently, another MMAE-derived ADC, polatuzumab vedotin-piiq, was approved to treat relapsed or refractory diffuse large B-cell lymphoma (139). Thus, all FDA approved Auristatin therapies have proved efficacy in haematological cancer and few of them are under clinical trials for the treatment of solid tumors (140–142). This fact shows that Auristatin ADCs or nanoconjugates could be less efficient in eliminating solid cancers cells due to their reduced sensitivity to Auristatin compared to haematological malignant cells. Moreover, in hematological neoplasias, targeted antigens are generally well-characterized, uniformly expressed and thought to be more accessible to molecules circulating in plasma, as compared to those present on solid tumors (143).

Multiple drug resistance is a major limiting factor of chemotherapeutic drug treatment. Observations in different cancer types models, including CRC, suggest that some tumors may be refractory to MMAE conjugated ADCs, despite the maintenance of the target antigen overexpression (144,145). The major mechanisms of drug resistance involve the interaction of the anticancer agents with efflux transporters located in the lysosomal membrane, which pump the cytotoxic drugs out of tumors cells to minimize intracellular exposure (146). It has been demonstrated that Auristatin E and maytasine are substrates for efflux transporters such as p-glycoprotein (147) and specifically P-gp-MDR1, that can sequester its substrates in the lysosomes and prevents the cytotoxic payloads from reaching their intracellular targets such as the nucleus or microtubules

(148). Furthermore, tumor cells that highly express P-gp-MDR1 on the plasma or lysosomal membranes show resistance to the MMAE payload of brentuximab vedotin.

Other *in vitro* studies, indicated that dysregulation of spindle checkpoint regulators compromise the sensitivity of cancer cells to microtubule inhibitors such as paclitaxel and docetaxel (149,150). This can explain why these agents and MMAE conjugated ADCs have failed to demonstrate significant clinical benefit in CRC. Approximately 80-85% of CRC tumors display chromosomal instability that can lead to abnormalities or mutations in spindle checkpoint regulators.

In conclusion, in spite of its selective tumor accumulation and lack of toxicity in normal organs, the T22-GFP-H6-Aur nanoconjugate showed low antitumor and antimetastatic effect in CRC models due to their intrinsic resistance or low sensitivity to Auristatin E. Moreover, our results show the importance of using a metastatic CRC model for preclinical evaluation of the antineoplastic effect, since the PDX subcutaneous model could not predict the low therapeutic index of the T22-GFP-H6-Aur.

4) CXCR4$^+$ TARGETED NANOPARTICLES WITH INTRINSIC CYTOTOXIC ACTIVITIES INDUCE PYROPTOSIS AND DISPLAY HIGH THERAPEUTIC INDEX IN CRC MODELS

The development of self-assembling protein-based nanoparticles with intrinsic cytotoxic activity could be a promising approach to overcome the previous described limitations of using nanoconjugates for the treatment of metastatic CRC. The previously designed nanoconjugates presented difficulties in their chemical synthesis, especially in the conjugation reactions, intrinsic resistance to the payloads and immunogenicity. Moreover, the efficacy of the drug-conjugated nanocarriers could be inadequate due to the possibility of drug leakage during circulation leading to side effects (151).

Therefore, in this thesis we selected different cytotoxic agents to replace the GFP, and therefore to be accommodated in the same position as the GFP protein in the T22-GFP-H6 nanoparticle. Among all cytotoxic domains found in organisms, bacterial toxins are already being used in new strategies for cancer therapy (152) and exhibit highly potent

anticancer effects. In this thesis work, the de-immunized version of the catalytic domain of the exotoxin A from *Pseudomonas aeruginosa* was incorporated to the T22 peptide and His-tag, generating the self-assembling T22-PE24-H6 nanotoxin. This new approach allowed us to avoid the conjugation steps which hindered the synthesis and production of the therapeutic nanoparticles and intrinsic resistance to microtubule inhibitors by incorporating mechanistically different cytotoxic agents.

Resistance to the classical chemotherapy regimens is an important problem in different types of cancer treatment, including CRC. Previous reports demonstrated that continuous exposure to 5-fluorouracil can cause tumor relapse by the emergence of a population of cancer cells with stem-like properties, resistant to this drug. Cancer cells acquire resistance to chemotherapy through the emergence of genetic mutations or epigenetic changes, favouring the activation of signalling pathways related to chemotaxis, cell survival or proliferation, including the CXCL12/CXCR4 axis (153). In human cancers, the anti-apoptotic proteins (e.g. Bcl-2, Bcl-XL and Mcl1) are often upregulated in cancer cells, enabling them to evade apoptotic cell death and losing the capacity to undergo apoptosis in response to chemotherapeutic drugs (154,155). The Bcl-2 gene has been shown to be overexpressed in many solid tumor cell lines (156–158) and clinically, a high Bcl-2 expression in patient samples correlates with a poor response to therapy (159). Furthermore, it has been demonstrated that the downregulation of Bcl-2 and Bcl-XL using antisense techniques was able to sensitise cells to chemotherapy (160), whereas a loss of Bax (pro-apoptotic protein) expression resulted in increased resistance (161). Thus, treatment with the T22-PE24-H6 nanotoxin could represent a promising tool for targeting CXCR4^{+} cancer stem cells and rendering sensitive the CRC tumors with acquired resistance to chemotherapy-induced apoptosis after their treatment, by inducing alternative cell death mechanisms.

The GFP protein is extensively used as a tracking agent, allowing us to follow our nanocarrier within the mouse whole-body but playing also an important role as a scaffold protein. In the context of nanotoxin development, GFP becomes a dispensable and exchangeable part in the whole multifunctional domain. Moreover, as observed after the repeated administration of T22-GFP-H6-derived nanoconjugates, the GFP protein could be responsible for causing a lethal immunogenic response in Swiss nude

mice that have low level of immunosuppression, since they have functional all immune cells except for the T cells. Furthermore, the presence of the GFP in the nanodrug could be a concerning aspect regarding immunogenicity and cytotoxicity for the approval of a drug-delivery system by the regulatory agencies (162). Thus, by replacing the GFP protein by the deimmunized PE24 toxin we conferred cytotoxic activity to the construct, maintaining the structure and the self-assembling capacity, and reducing the possible immunogenicity.

Our results demonstrated that the T22-PE24-H6 nanotoxin displays a potent CXCR4$^+$ dependent cytotoxic effect in CRC cells and also that its use at low doses in a repeated treatment regimen is capable of inhibiting tumor growth and metastasis development without associated toxicity. Thus, exposure of the CXCR4$^+$ SW1417 cell line to the toxin showed a reduction in cell viability, and a lack of antitumor activity in the CXCR4$^-$ cell line or after competition with the AMD3100 antagonist. Furthermore, T22-PE24-H6-treated mice bearing subcutaneous tumors underwent a 1.6-fold reduction in tumor volume and a 3-fold increase in tumor cell death body induction at the end of the experiment, compared to buffer-treated mice. Moreover, when repeatedly administering low doses of T22-PE24-H6 in the highly metastatic cell-derived orthotopic model, we observed a significant 2-fold reduction in the number of lymphatic and hematogenous metastatic foci and a decreasing trend in the primary tumor and metastatic foci size. Consistently with these results, our group also proved the T22-PE24-H6 capacity to block dissemination in a diffuse large B-cell lymphoma (DLBCL) model without associated toxicity, by the elimination of CXCR4$^+$ cancer cells (163).

The success of this new approach relies again in achieving highly selective targeted drug delivery by exploiting the CXCR4 membrane overexpression of CRC cells as compared to normal tissues but also, and importantly, because of the capacity of the PE24 toxin to trigger a mechanism of cell death alternative to apoptosis. Thus, we found that target cell death induction by the T22-PE24-H6 nanotoxin in *in vitro* and *in vivo* CRC models follows the following steps: the nanotoxin binds to CXCR4 receptors exposed in the membrane of target cells through its T22 ligands, internalizes by endocytosis, releasing afterwards the toxin active fragment into the cytosol. Furin-cleavage sites inserted between the T22 peptide and the cytotoxic PE24 domain allow this cleavage and its

intracellular release. Finally, this protein domain will block protein synthesis by inhibition of the elongation factor 2 (EF2) to induce the activation of pyroptosis, a scarcely explored non-apoptotic cell death mechanism in cancer therapy (164,165). Thus, in this thesis, we described the activation of the main mediators of pyroptosis, namely, NLRP3, active caspase-1 and active Gasdermin-D (GSDMD), in CXCR4$^+$ tumors treated with repeated doses of T22-PE24-H6, after 24 hours of the last injection. Furthermore, we found absence or low activation of apoptotic markers such as active caspase-3 and proteolyzed PARP, in the same tumor samples. A sequential timing on the signalling cascade for pyroptotic activation was clearly observed in CXCR4$^+$ SW1417 cells exposed to the T22-PE24-H6 nanotoxin. At short times, we found an overexpression of the NLRP3 protein, which in turn, promoted the activation of caspase-1 and then, GSDMD increased expression at 48 hours. We also observed the translocation of the activate GSDMD to the cell membrane where it undergoes oligomerization, leading to pore formation and the induction of pyroptotic cell death (166).

The use of immunotoxins for cancer therapy gained importance during recent years. Many toxin-based therapies are under clinical trials, but Moxetumomab pasudotox is one of the few approved by the FDA for the treatment of hairy-cell leukemia. This immunotoxin is composed of an anti-CD22 antibody fused to a 38 kDa portion of the Pseudomonas exotoxin A (167). However, immunotoxin therapy has been successfully achieved against hematological malignancies and several issues still represent significant barriers for their effective use for solid cancers treatment (168). These hurdles include dose-limiting toxicities, immunogenicity and cytosolic delivery efficacy (169). Most of the developed immunotoxins fused to the Exotoxin A use the PE38 fragment. Recent studies, demonstrated that de-immunization of recombinant toxins by identifying and removing B-cell epitopes, decreased the immune response when administered in mice. Investigations have focused, for instance, in the elimination of the B-cell epitopes of the 25 kDa portion (HA22-LR-8M) of the PE toxin to produce a fully cytotoxic protein effective against leukemia cell lines (170). Therefore, in this thesis we incorporated the PE24 toxin to our T22-based nanoparticles which has been demonstrated to be less immunogenic and better tolerated than previous versions of this toxin.

In conclusion, our novel therapeutic approach has developed intrinsically cytotoxic nanoparticles with reduced immunogenicity and a wider therapeutic index than the previously developed nanoconjugates used to treat metastasis in CRC models. Moreover, the T22-PE24-H6 nanotoxin could be a promising tool for effectively overcome the apoptosis blockade associated with chemotherapeutic-resistant tumors, by triggering the induction of pyroptosis, an alternative cell death pathway, mechanistically different to apoptosis.
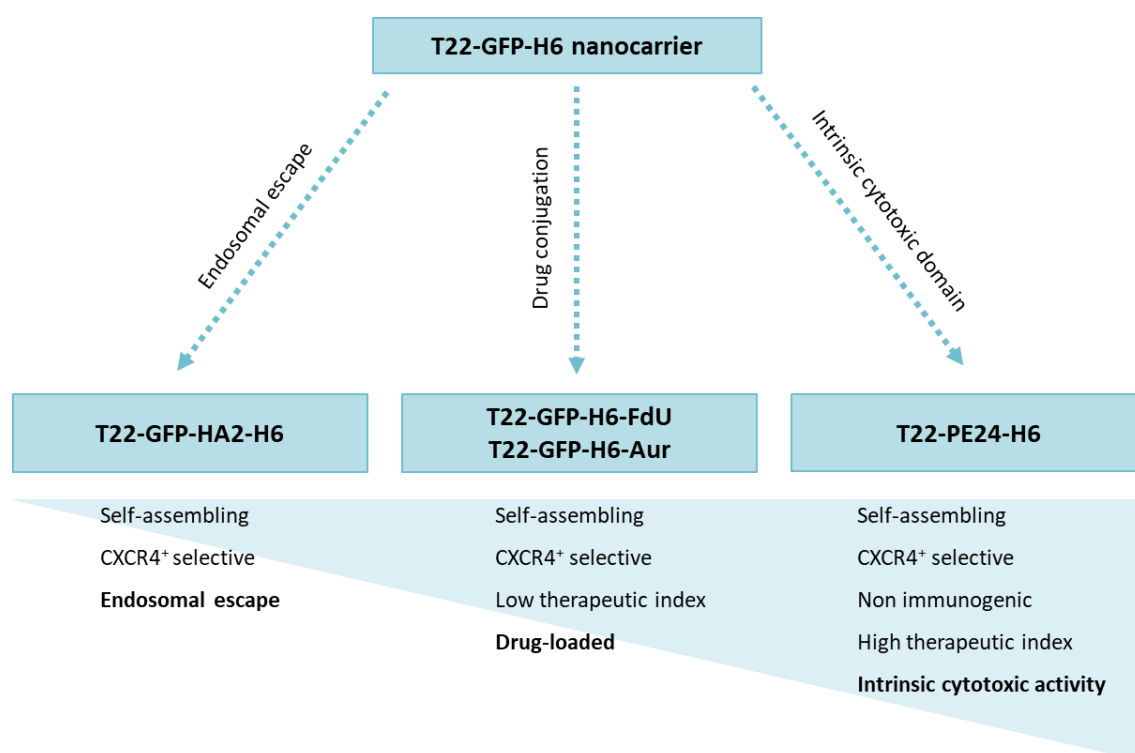
Figure 44. Schematic representation of the different strategies used for nanoparticle functionalization. The novel properties achieved by each approach are explained for each nanoparticle; from endosomal escape to drug conjugation and finally, incorporation of intrinsic cytotoxic domains.

VI. CONCLUSIONS

VI. CONCLUSIONS

1) Subcutaneous CRC mouse models are useful to evaluate tumor and normal tissue biodistribution of nanoparticles targeting CXCR4^{+} CRC cells (e.g. T22-GFP-H6) and reveal the mechanistic pathways leading to cancer cell death. However, they are limited for the evaluation of the antimetastatic effect of newly developed therapeutic nanoparticles.

2) Severe immunosuppression, and particularly the lack of NK cells, highly increases the metastatic capacity of CRC models derived from cell lines (i.e. SW1417) or patient samples (i.e. SP5) after their orthotopic implantation.

3) We successfully developed CXCR4-overexpressing SW1417 and SP5 CRC models in NSG mice displaying increased metastatic colonization by large tumor foci in all clinically relevant sites.

4) Patient-derived xenografts, such as the SP5 model, maintain tumor heterogeneity, representing a more clinically relevant platform than cell line-derived models, for preclinical drug evaluation.

5) T22-GFP-H6, a protein-only nanoparticle targeting CXCR4, achieves *in vivo* active targeting in CXCR4^{+} CRC models. This is a highly selective and effective nanocarrier that reaches a 70% tumor uptake of the total emitted fluorescence after nanoparticle injection, with low or negligible accumulation in non-tumor organs.

6) The accommodation of the HA2 fusogenic peptide in a specific localization within the T22-GFP-H6 nanocarrier sequence, highly increases tumor uptake by boosting endosomal escape and avoiding lysosomal degradation, without losing CXCR4 selectivity in CXCR4^{+} CRC models.

7) The green fluorescent protein present in the T22-empowered nanoconjugates could be responsible for the activation of a lethal immunogenic response when administered at repeated doses in Swiss nude mice. They display a lack of T cells but still maintain the innate and a partial adaptive immune response, suggesting the need to substitute the GFP by a human scaffold protein that reduces its immunogenicity, allowing clinical translation.

8) The T22-GFP-H6-Aur nanoconjugate achieves poor antimetastatic effect, since it only prevents the development of transcelomic metastasis in a CXCR4+ highly metastatic CRC model. CRC cells are clearly much less sensitive to microtubules destabilizing agents than hematological malignant cells.

9) The replacement of the GFP within the T22-GFP-H6 nanoparticle, for the de-immunized PE24 *Pseudomonas aeruginosa* toxin, improves its therapeutic efficacy by reducing immunogenicity and achieving high antimetastatic effect due to its intrinsically potent cytotoxic activity. Thus, the T22-PE24-H6 nanotoxin prevents the development of lymphatic and hematogenous metastasis in the SW1417 CXCR4+ highly metastatic CRC model.

10) The T22-PE24-H6 nanotoxin displays a wide therapeutic index that relies on its capacity to induce cell death to CXCR4+ cancer cells through pyroptosis, a non-apoptotic cell death mechanism. Thus, this nanotoxin could represent a promising tool for the treatment of CXCR4+ chemotherapy-resistant CRC tumors, which have developed a blockade of the apoptotic mechanisms.

VII. REFERENCES

VII. REFERENCES

1. Kosinski C, Li VSW, Chan ASY, Zhang J, Ho C, Tsui WY, et al. Gene expression patterns of human colon tops and basal crypts and BMP antagonists as intestinal stem cell niche factors. Proc Natl Acad Sci U S A. 2007 Sep 25;104(39):15418–23.

2. Frank SA. Dynamics of Cancer: Incidence, Inheritance, and Evolution [Internet]. Princeton (NJ): Princeton University Press; 2007 [cited 2020 Oct 16]. Available from: http://www.ncbi.nlm.nih.gov/books/NBK1568/

3. Stryker SJ, Wolff BG, Culp CE, Libbe SD, Ilstrup DM, MacCarty RL. Natural history of untreated colonic polyps. Gastroenterology. 1987 Nov;93(5):1009–13.

4. Bray F, Ferlay J, Soerjomataram I, Siegel RL, Torre LA, Jemal A. Global cancer statistics 2018: GLOBOCAN estimates of incidence and mortality worldwide for 36 cancers in 185 countries. CA Cancer J Clin. 2018;68(6):394–424.

5. Keum N, Giovannucci E. Global burden of colorectal cancer: emerging trends, risk factors and prevention strategies. Nat Rev Gastroenterol Hepatol. 2019 Dec;16(12):713–32.

6. Riihimäki M, Hemminki A, Sundquist J, Hemminki K. Patterns of metastasis in colon and rectal cancer. Sci Rep [Internet]. 2016 Jul 15 [cited 2020 Jul 16];6. Available from: https://www.ncbi.nlm.nih.gov/pmc/articles/PMC4945942/

7. Knijn N, van Erning FN, Overbeek LIH, Punt CJA, Lemmens VEPP, Hugen N, et al. Limited effect of lymph node status on the metastatic pattern in colorectal cancer. Oncotarget. 2016 Apr 27;7(22):31699–707.

8. Lynch HT, de la Chapelle A. Hereditary Colorectal Cancer. N Engl J Med. 2003 Mar 6;348(10):919–32.

9. Fedirko V, Tramacere I, Bagnardi V, Rota M, Scotti L, Islami F, et al. Alcohol drinking and colorectal cancer risk: an overall and dose-response meta-analysis of published studies. Ann Oncol Off J Eur Soc Med Oncol. 2011 Sep;22(9):1958–72.

10. Liang PS, Chen T-Y, Giovannucci E. Cigarette smoking and colorectal cancer incidence and mortality: systematic review and meta-analysis. Int J Cancer. 2009 May 15;124(10):2406–15.

11. Martinez-Useros J, Garcia-Foncillas J. Obesity and colorectal cancer: molecular features of adipose tissue. J Transl Med. 2016 Jan 22;14:21.

12. Song M, Garrett WS, Chan AT. Nutrients, foods, and colorectal cancer prevention. Gastroenterology. 2015 May;148(6):1244-1260.e16.

13. GRADY WM, CARETHERS JM. Genomic and Epigenetic Instability in Colorectal Cancer Pathogenesis. Gastroenterology. 2008 Oct;135(4):1079–99.

14. Walther A, Johnstone E, Swanton C, Midgley R, Tomlinson I, Kerr D. Genetic prognostic and predictive markers in colorectal cancer. Nat Rev Cancer. 2009 Jul;9(7):489–99.

15. Hurwitz H, Fehrenbacher L, Novotny W, Cartwright T, Hainsworth J, Heim W, et al. Bevacizumab plus Irinotecan, Fluorouracil, and Leucovorin for Metastatic Colorectal Cancer. N Engl J Med. 2004 Jun 3;350(23):2335–42.

16. Willett CG, Boucher Y, di Tomaso E, Duda DG, Munn LL, Tong RT, et al. Direct evidence that the VEGF-specific antibody bevacizumab has antivascular effects in human rectal cancer. Nat Med. 2004 Feb;10(2):145–7.

17. Jonker DJ, O'Callaghan CJ, Karapetis CS, Zalcberg JR, Tu D, Au H-J, et al. Cetuximab for the Treatment of Colorectal Cancer. N Engl J Med. 2007 Nov 15;357(20):2040–8.

18. Misale S, Yaeger R, Hobor S, Scala E, Janakiraman M, Liska D, et al. Emergence of KRAS mutations and acquired resistance to anti EGFR therapy in colorectal cancer. Nature. 2012 Jun 28;486(7404):532–6.

19. Ma B, Bt C. Salmonella induces macrophage death by caspase-1-dependent necrosis. Mol Microbiol. 2000 Oct 1;38(1):31–40.

20. Yu J, Li S, Qi J, Chen Z, Wu Y, Guo J, et al. Cleavage of GSDME by caspase-3 determines lobaplatin-induced pyroptosis in colon cancer cells. Cell Death Dis. 2019 25;10(3):193.

21. Weaver BAA, Cleveland DW. Decoding the links between mitosis, cancer, and chemotherapy: The mitotic checkpoint, adaptation, and cell death. Cancer Cell. 2005 Jul;8(1):7–12.

22. Castedo M, Perfettini J-L, Roumier T, Valent A, Raslova H, Yakushijin K, et al. Mitotic catastrophe constitutes a special case of apoptosis whose suppression entails aneuploidy. Oncogene. 2004 May 27;23(25):4362–70.

23. Tounekti O, Pron G, Belehradek J, Mir LM. Bleomycin, an apoptosis-mimetic drug that induces two types of cell death depending on the number of molecules internalized. Cancer Res. 1993 Nov 15;53(22):5462–9.

24. Torres K, Horwitz SB. Mechanisms of Taxol-induced Cell Death Are Concentration Dependent. :8.

25. Pantel K, Speicher MR. The biology of circulating tumor cells. Oncogene. 2016 Mar;35(10):1216–24.

26. Chitty JL, Filipe EC, Lucas MC, Herrmann D, Cox TR, Timpson P. Recent advances in understanding the complexities of metastasis. F1000Research [Internet]. 2018 Sep 10 [cited 2020 Jul 17];7. Available from: https://www.ncbi.nlm.nih.gov/pmc/articles/PMC6073095/

27. Fidler IJ. The pathogenesis of cancer metastasis: the 'seed and soil' hypothesis revisited. Nat Rev Cancer. 2003 Jun;3(6):453–8.

28. Moser B, Loetscher P. Lymphocyte traffic control by chemokines. Nat Immunol. 2001 Feb;2(2):123–8.

29. Müller A, Homey B, Soto H, Ge N, Catron D, Buchanan ME, et al. Involvement of chemokine receptors in breast cancer metastasis. Nature. 2001 Mar;410(6824):50–6.

30. Kufareva I, Stephens BS, Holden LG, Qin L, Zhao C, Kawamura T, et al. Stoichiometry and geometry of the CXC chemokine receptor 4 complex with CXC ligand 12: molecular modeling and experimental validation. Proc Natl Acad Sci U S A. 2014 Dec 16;111(50):E5363-5372.

31. Döring Y, Pawig L, Weber C, Noels H. The CXCL12/CXCR4 chemokine ligand/receptor axis in cardiovascular disease. Front Physiol [Internet]. 2014 [cited 2020 Jul 8];5. Available from: https://www.frontiersin.org/articles/10.3389/fphys.2014.00212/full

32. Saini V, Marchese A, Majetschak M. CXC Chemokine Receptor 4 Is a Cell Surface Receptor for Extracellular Ubiquitin. J Biol Chem. 2010 May 14;285(20):15566–76.

33. Pawig L, Klasen C, Weber C, Bernhagen J, Noels H. Diversity and Inter-Connections in the CXCR4 Chemokine Receptor/Ligand Family: Molecular Perspectives. Front Immunol [Internet]. 2015 Aug 21 [cited 2020 Jul 7];6. Available from: https://www.ncbi.nlm.nih.gov/pmc/articles/PMC4543903/

34. Burger JA, Burger M, Kipps TJ. Chronic lymphocytic leukemia B cells express functional CXCR4 chemokine receptors that mediate spontaneous migration beneath bone marrow stromal cells. Blood. 1999 Dec 1;94(11):3658–67.

35. Ben-Baruch A. Organ selectivity in metastasis: regulation by chemokines and their receptors. Clin Exp Metastasis. 2008 Jun 1;25(4):345–56.

36. Kim SY, Lee CH, Midura BV, Yeung C, Mendoza A, Hong SH, et al. Inhibition of the CXCR4/CXCL12 chemokine pathway reduces the development of murine pulmonary metastases. Clin Exp Metastasis. 2008;25(3):201–11.

37. Kim J, Takeuchi H, Lam ST, Turner RR, Wang H-J, Kuo C, et al. Chemokine receptor CXCR4 expression in colorectal cancer patients increases the risk for recurrence and for poor survival. J Clin Oncol Off J Am Soc Clin Oncol. 2005 Apr 20;23(12):2744–53.

38. Schimanski CC, Schwald S, Simiantonaki N, Jayasinghe C, Gönner U, Wilsberg V, et al. Effect of Chemokine Receptors CXCR4 and CCR7 on the Metastatic Behavior of Human Colorectal Cancer. Clin Cancer Res. 2005 Mar 1;11(5):1743–50.

39. Zeelenberg IS, Stalle LR-V, Roos E. The Chemokine Receptor CXCR4 Is Required for Outgrowth of Colon Carcinoma Micrometastases. Cancer Res. 2003 Jul 1;63(13):3833–9.

40. Weiss ID, Jacobson O. Molecular imaging of chemokine receptor CXCR4. Theranostics. 2013;3(1):76–84.

41. Rapid Mobilization of CD34+ Cells Following Administration of the CXCR4 Antagonist AMD3100 to Patients With Multiple Myeloma and Non-Hodgkin's Lymphoma | Journal of Clinical Oncology [Internet]. [cited 2020 Jul 10]. Available from: https://ascopubs.org/doi/full/10.1200/JCO.2004.07.131?url_ver=Z39.88-2003&rfr_id=ori:rid:crossref.org&rfr_dat=cr_pub%20%200pubmed

42. Galsky MD, Vogelzang NJ, Conkling P, Raddad E, Polzer J, Roberson S, et al. A phase I trial of LY2510924, a CXCR4 peptide antagonist, in patients with advanced cancer. Clin Cancer Res Off J Am Assoc Cancer Res. 2014 Jul 1;20(13):3581–8.

43. Gravina GL, Mancini A, Marampon F, Colapietro A, Delle Monache S, Sferra R, et al. The brain-penetrating CXCR4 antagonist, PRX177561, increases the antitumor effects of bevacizumab and sunitinib in preclinical models of human glioblastoma. J Hematol OncolJ Hematol Oncol [Internet]. 2017 Jan 5 [cited 2020 Jul 10];10. Available from: https://www.ncbi.nlm.nih.gov/pmc/articles/PMC5217647/

44. Bockorny B, Semenisty V, Macarulla T, Borazanci E, Wolpin BM, Stemmer SM, et al. BL-8040, a CXCR4 antagonist, in combination with pembrolizumab and chemotherapy for pancreatic cancer: the COMBAT trial. Nat Med. 2020 Jun;26(6):878–85.

45. Gengenbacher N, Singhal M, Augustin HG. Preclinical mouse solid tumour models: status quo, challenges and perspectives. Nat Rev Cancer. 2017 Dec;17(12):751–65.

46. Hidalgo M, Amant F, Biankin AV, Budinská E, Byrne AT, Caldas C, et al. Patient-derived xenograft models: an emerging platform for translational cancer research. Cancer Discov. 2014 Sep;4(9):998–1013.

47. Morton JJ, Bird G, Refaeli Y, Jimeno A. Humanized Mouse Xenograft Models: Narrowing the Tumor-Microenvironment Gap. Cancer Res. 2016 01;76(21):6153–8.

48. Voskoglou-Nomikos T, Pater JL, Seymour L. Clinical predictive value of the in vitro cell line, human xenograft, and mouse allograft preclinical cancer models. Clin Cancer Res Off J Am Assoc Cancer Res. 2003 Sep 15;9(11):4227–39.

49. Alamo P, Gallardo A, Pavón MA, Casanova I, Trias M, Mangues MA, et al. Subcutaneous preconditioning increases invasion and metastatic dissemination in mouse colorectal cancer models. Dis Model Mech. 2014 Mar;7(3):387–96.

50. Rajput A, Agarwal E, Leiphrakpam P, Brattain MG, Chowdhury S. Establishment and Validation of an Orthotopic Metastatic Mouse Model of Colorectal Cancer. ISRN Hepatol [Internet]. 2013 Apr 21 [cited 2020 Jun 15];2013. Available from: https://www.ncbi.nlm.nih.gov/pmc/articles/PMC4907346/

51. Céspedes MV, Espina C, García-Cabezas MA, Trias M, Boluda A, Gómez del Pulgar MT, et al. Orthotopic Microinjection of Human Colon Cancer Cells in Nude Mice Induces Tumor Foci in All Clinically Relevant Metastatic Sites. Am J Pathol. 2007 Mar;170(3):1077–85.

52. Jenkins DE, Oei Y, Hornig YS, Yu S-F, Dusich J, Purchio T, et al. Bioluminescent imaging (BLI) to improve and refine traditional murine models of tumor growth and metastasis. Clin Exp Metastasis. 2003;20(8):733–44.

53. Ernsting MJ, Murakami M, Roy A, Li S-D. Factors controlling the pharmacokinetics, biodistribution and intratumoral penetration of nanoparticles. J Control Release Off J Control Release Soc. 2013 Dec 28;172(3):782–94.

54. Nel AE, Mädler L, Velegol D, Xia T, Hoek EMV, Somasundaran P, et al. Understanding biophysicochemical interactions at the nano-bio interface. Nat Mater. 2009 Jul;8(7):543–57.

55. Cho EC, Xie J, Wurm PA, Xia Y. Understanding the role of surface charges in cellular adsorption versus internalization by selectively removing gold nanoparticles on the cell surface with a I2/KI etchant. Nano Lett. 2009 Mar;9(3):1080–4.

56. Varkouhi AK, Scholte M, Storm G, Haisma HJ. Endosomal escape pathways for delivery of biologicals. J Control Release Off J Control Release Soc. 2011 May 10;151(3):220–8.

57. Caponetti V, Trzcinski JW, Cantelli A, Tavano R, Papini E, Mancin F, et al. Self-Assembled Biocompatible Fluorescent Nanoparticles for Bioimaging. Front Chem [Internet]. 2019 [cited 2020 Jun 1];7. Available from: https://www.frontiersin.org/articles/10.3389/fchem.2019.00168/full

58. CHAKRAVARTY R, GOEL S, DASH A, CAI W. Radiolabeled inorganic nanoparticles for positron emission tomography imaging of cancer: an overview. Q J Nucl Med Mol Imaging Off Publ Ital Assoc Nucl Med AIMN Int Assoc Radiopharmacol IAR Sect Soc Of. 2017 Jun;61(2):181–204.

59. Davis ME, Shin DM. Nanoparticle therapeutics: an emerging treatment modality for cancer. Drug Discov. :12.

60. Navya PN, Kaphle A, Srinivas SP, Bhargava SK, Rotello VM, Daima HK. Current trends and challenges in cancer management and therapy using designer nanomaterials. Nano Converg. 2019 Jul 15;6(1):23.

61. Peer D, Karp JM, Hong S, Farokhzad OC, Margalit R, Langer R. Nanocarriers as an emerging platform for cancer therapy. Nat Nanotechnol. 2007 Dec;2(12):751–60.

62. Wilhelm S, Tavares AJ, Dai Q, Ohta S, Audet J, Dvorak HF, et al. Analysis of nanoparticle delivery to tumours. Nat Rev Mater. 2016 Apr 26;1(5):1–12.

63. Sadauskas E, Wallin H, Stoltenberg M, Vogel U, Doering P, Larsen A, et al. Kupffer cells are central in the removal of nanoparticles from the organism. Part Fibre Toxicol. 2007 Oct 19;4:10.

64. Byrne JD, Betancourt T, Brannon-Peppas L. Active targeting schemes for nanoparticle systems in cancer therapeutics. Adv Drug Deliv Rev. 2008 Dec 14;60(15):1615–26.

65. Moon H, Lee J, Min J, Kang S. Developing genetically engineered encapsulin protein cage nanoparticles as a targeted delivery nanoplatform. Biomacromolecules. 2014 Oct 13;15(10):3794–801.

66. Park JW. Liposome-based drug delivery in breast cancer treatment. Breast Cancer Res. 2002 Jun 1;4(3):95.

67. Desai N, Trieu V, Yao Z, Louie L, Ci S, Yang A, et al. Increased antitumor activity, intratumor paclitaxel concentrations, and endothelial cell transport of cremophor-free, albumin-bound paclitaxel, ABI-007, compared with cremophor-based paclitaxel. Clin Cancer Res Off J Am Assoc Cancer Res. 2006 Feb 15;12(4):1317–24.

68. Von Hoff DD, Ramanathan RK, Borad MJ, Laheru DA, Smith LS, Wood TE, et al. Gemcitabine plus nab-paclitaxel is an active regimen in patients with advanced pancreatic cancer: a phase I/II trial. J Clin Oncol Off J Am Soc Clin Oncol. 2011 Dec 1;29(34):4548–54.

69. Unzueta U, Céspedes MV, Ferrer-Miralles N, Casanova I, Cedano J, Corchero JL, et al. Intracellular CXCR4+ cell targeting with T22-empowered protein-only nanoparticles. Int J Nanomedicine. 2012;7:4533–44.

70. Murakami T, Zhang TY, Koyanagi Y, Tanaka Y, Kim J, Suzuki Y, et al. Inhibitory mechanism of the CXCR4 antagonist T22 against human immunodeficiency virus type 1 infection. J Virol. 1999 Sep;73(9):7489–96.

71. López-Laguna H, Unzueta U, Conchillo-Solé O, Sánchez-Chardi A, Pesarrodona M, Cano-Garrido O, et al. Assembly of histidine-rich protein materials controlled through divalent cations. Acta Biomater. 2019 Jan 1;83:257–64.

72. López-Laguna H, Sala R, Sánchez JM, Álamo P, Unzueta U, Sánchez-Chardi A, et al. Nanostructure Empowers Active Tumor Targeting in Ligand-Based Molecular Delivery. Part Part Syst Charact. 2019;36(11):1900304.

73. Wagner E, Plank C, Zatloukal K, Cotten M, Birnstiel ML. Influenza virus hemagglutinin HA-2 N-terminal fusogenic peptides augment gene transfer by transferrin-polylysine-DNA complexes: toward a synthetic virus-like gene-transfer vehicle. Proc Natl Acad Sci U S A. 1992 Sep 1;89(17):7934–8.

74. Ye S, Tian M, Wang T, Ren L, Wang D, Shen L, et al. Synergistic effects of cell-penetrating peptide Tat and fusogenic peptide HA2-enhanced cellular internalization and gene transduction of organosilica nanoparticles. Nanomedicine Nanotechnol Biol Med. 2012 Aug;8(6):833–41.

75. Sánchez-García L, Serna N, Mattanovich M, Cazzanelli P, Sánchez-Chardi A, Conchillo-Solé O, et al. The fusogenic peptide HA2 impairs selectivity of CXCR4-targeted protein nanoparticles. Chem Commun. 2017;53(33):4565–8.

76. Sánchez-García L, Serna N, Álamo P, Sala R, Céspedes MV, Roldan M, et al. Self-assembling toxin-based nanoparticles as self-delivered antitumoral drugs. J Control Release Off J Control Release Soc. 2018 28;274:81–92.

77. Díaz R, Sánchez-García L, Serna N, Sánchez-Chardi A, Cano-Garrido O, Sánchez JM, et al. Engineering a recombinant chlorotoxin as cell-targeted cytotoxic nanoparticles. Sci China Mater. 2019 Jun 1;62(6):892–8.

78. Díaz R, Pallarès V, Cano-Garrido O, Serna N, Sánchez-García L, Falgàs A, et al. Selective CXCR4+ Cancer Cell Targeting and Potent Antineoplastic Effect by a Nanostructured Version of Recombinant Ricin. Small Weinh Bergstr Ger. 2018;14(26):e1800665.

79. Céspedes MV, Unzueta U, Aviñó A, Gallardo A, Álamo P, Sala R, et al. Selective depletion of metastatic stem cells as therapy for human colorectal cancer. EMBO Mol Med [Internet]. 2018 Oct [cited 2020 Apr 21];10(10). Available from: https://www.ncbi.nlm.nih.gov/pmc/articles/PMC6180303/

80. Bates D, Eastman A. Microtubule destabilising agents: far more than just antimitotic anticancer drugs. Br J Clin Pharmacol. 2017;83(2):255–68.

81. Alewine C, Hassan R, Pastan I. Advances in anticancer immunotoxin therapy. The Oncologist. 2015 Feb;20(2):176–85.

82. Nobre CF, Newman MJ, DeLisa A, Newman P. Moxetumomab pasudotox-tdfk for relapsed/refractory hairy cell leukemia: a review of clinical considerations. Cancer Chemother Pharmacol. 2019;84(2):255–63.

83. Jen EY, Gao X, Li L, Zhuang L, Simpson NE, Aryal B, et al. FDA Approval Summary: Tagraxofusp-erzs For Treatment of Blastic Plasmacytoid Dendritic Cell Neoplasm. Clin Cancer Res [Internet]. 2019 Sep 23 [cited 2020 Jun 11]; Available from: https://clincancerres.aacrjournals.org/content/early/2019/11/19/1078-0432.CCR-19-2329

84. Seetharam S, Chaudhary VK, FitzGerald D, Pastan I. Increased cytotoxic activity of Pseudomonas exotoxin and two chimeric toxins ending in KDEL. J Biol Chem. 1991 Sep 15;266(26):17376–81.

85. Dwinell MB, Eckmann L, Leopard JD, Varki NM, Kagnoff MF. Chemokine receptor expression by human intestinal epithelial cells. Gastroenterology. 1999 Aug 1;117(2):359–67.

86. Jordan NJ, Kolios G, Abbot SE, Sinai MA, Thompson DA, Petraki K, et al. Expression of functional CXCR4 chemokine receptors on human colonic epithelial cells. J Clin Invest. 1999 Oct 15;104(8):1061–9.

87. Nieto JC, Cantó E, Zamora C, Ortiz MA, Juárez C, Vidal S. Selective loss of chemokine receptor expression on leukocytes after cell isolation. PloS One. 2012;7(3):e31297.

88. Waldhauer I, Steinle A. NK cells and cancer immunosurveillance. Oncogene. 2008 Oct;27(45):5932–43.

89. Shi L, Zhao J, Lu Q, Chen X, Wang H, Jiang Y, et al. Initial hepatic artery infusion and systemic chemotherapy for asymptomatic colorectal cancer with un-resectable liver metastasis. Int J Clin Exp Med. 2015 Jan 15;8(1):1000–8.

90. Buckel L, Savariar EN, Crisp JL, Jones KA, Hicks AM, Scanderbeg DJ, et al. Tumor radiosensitization by monomethyl auristatin E: mechanism of action and targeted delivery. Cancer Res. 2015 Apr 1;75(7):1376–87.

91. Sánchez-García L, Sala R, Serna N, Álamo P, Parladé E, Alba-Castellón L, et al. A refined cocktailing of pro-apoptotic nanoparticles boosts anti-tumor activity. Acta Biomater. 2020 Jun 27;

92. Jorgensen I, Miao EA. Pyroptotic cell death defends against intracellular pathogens. Immunol Rev. 2015 May;265(1):130–42.

93. Neundorf I, Rennert R, Hoyer J, Schramm F, Löbner K, Kitanovic I, et al. Fusion of a Short HA2-Derived Peptide Sequence to Cell-Penetrating Peptides Improves Cytosolic Uptake, but Enhances Cytotoxic Activity. Pharmaceuticals. 2009 Sep;2(2):49.

94. Céspedes MV, Unzueta U, Álamo P, Gallardo A, Sala R, Casanova I, et al. Cancer-specific uptake of a liganded protein nanocarrier targeting aggressive CXCR4+ colorectal cancer models. Nanomedicine Nanotechnol Biol Med. 2016;12(7):1987–96.

95. Rueda F, Céspedes MV, Conchillo-Solé O, Sánchez-Chardi A, Seras-Franzoso J, Cubarsi R, et al. Bottom-Up Instructive Quality Control in the Biofabrication of Smart Protein Materials. Adv Mater. 2015;27(47):7816–22.

96.   Nel A, Ruoslahti E, Meng H. New Insights into "Permeability" as in the Enhanced Permeability and Retention Effect of Cancer Nanotherapeutics. ACS Nano. 2017 Oct 24;11(10):9567–9.

97.   Pandit S, Dutta D, Nie S. Active transcytosis and new opportunities for cancer nanomedicine. Nat Mater. 2020 May;19(5):478–80.

98.   Song JS, Kang CM, Kang HH, Yoon HK, Kim YK, Kim KH, et al. Inhibitory effect of CXC chemokine receptor 4 antagonist AMD3100 on bleomycin induced murine pulmonary fibrosis. Exp Mol Med. 2010 Jun 30;42(6):465–72.

99.   de Gramont A, Boni C, Navarro M, Tabernero J, Hickish T, Topham C, et al. Oxaliplatin/5FU/LV in adjuvant colon cancer: Updated efficacy results of the MOSAIC trial, including survival, with a median follow-up of six years. J Clin Oncol. 2007 Jun 20;25(18_suppl):4007–4007.

100.   Sleeman J, Steeg PS. Cancer metastasis as a therapeutic target. Eur J Cancer Oxf Engl 1990. 2010 May;46(7):1177–80.

101.   Brabletz T, Jung A, Spaderna S, Hlubek F, Kirchner T. Migrating cancer stem cells — an integrated concept of malignant tumour progression. Nat Rev Cancer. 2005 Sep;5(9):744–9.

102.   Oskarsson T, Batlle E, Massagué J. Metastatic stem cells: sources, niches, and vital pathways. Cell Stem Cell. 2014 Mar 6;14(3):306–21.

103.   Schimanski CC, Bahre R, Gockel I, Müller A, Frerichs K, Hörner V, et al. Dissemination of hepatocellular carcinoma is mediated via chemokine receptor CXCR4. Br J Cancer. 2006 Jul;95(2):210–7.

104.   Zhang S, Han Z, Jing Y, Tao S, Li T, Wang H, et al. CD133+CXCR4+ colon cancer cells exhibit metastatic potential and predict poor prognosis of patients. BMC Med. 2012 Aug 7;10(1):85.

105.   Fang J, Nakamura H, Maeda H. The EPR effect: Unique features of tumor blood vessels for drug delivery, factors involved, and limitations and augmentation of the effect. Adv Drug Deliv Rev. 2011 Mar 18;63(3):136–51.

106.   Danhier F. To exploit the tumor microenvironment: Since the EPR effect fails in the clinic, what is the future of nanomedicine? J Control Release Off J Control Release Soc. 2016 28;244(Pt A):108–21.

107.   Bartfeld S, Clevers H. Stem cell-derived organoids and their application for medical research and patient treatment. J Mol Med. 2017 Jul 1;95(7):729–38.

108.   Takahashi T. Organoids for Drug Discovery and Personalized Medicine. Annu Rev Pharmacol Toxicol. 2019 Jan 6;59(1):447–62.

109.   Darash-Yahana M, Pikarsky E, Abramovitch R, Zeira E, Pal B, Karplus R, et al. Role of high expression levels of CXCR4 in tumor growth, vascularization, and metastasis. FASEB J. 2004;18(11):1240–2.

110. Conley-LaComb MK, Saliganan A, Kandagatla P, Chen YQ, Cher ML, Chinni SR. PTEN loss mediated Akt activation promotes prostate tumor growth and metastasis via CXCL12/CXCR4 signaling. Mol Cancer. 2013 Jul 31;12(1):85.

111. Goel A, Arnold CN, Niedzwiecki D, Carethers JM, Dowell JM, Wasserman L, et al. Frequent inactivation of PTEN by promoter hypermethylation in microsatellite instability-high sporadic colorectal cancers. Cancer Res. 2004 May 1;64(9):3014–21.

112. Ma J, Sun X, Wang Y, Chen B, Qian L, Wang Y. Fibroblast-derived CXCL12 regulates PTEN expression and is associated with the proliferation and invasion of colon cancer cells via PI3k/Akt signaling. Cell Commun Signal CCS [Internet]. 2019 Sep 10 [cited 2020 Sep 18];17. Available from: https://www.ncbi.nlm.nih.gov/pmc/articles/PMC6734448/

113. Kikutani H, Makino S. The murine autoimmune diabetes model: NOD and related strains. Adv Immunol. 1992;51:285–322.

114. Okada S, Vaeteewoottacharn K, Kariya R. Application of Highly Immunocompromised Mice for the Establishment of Patient-Derived Xenograft (PDX) Models. Cells [Internet]. 2019 Aug 13 [cited 2020 Oct 6];8(8). Available from: https://www.ncbi.nlm.nih.gov/pmc/articles/PMC6721637/

115. Idos GE, Kwok J, Bonthala N, Kysh L, Gruber SB, Qu C. The Prognostic Implications of Tumor Infiltrating Lymphocytes in Colorectal Cancer: A Systematic Review and Meta-Analysis. Sci Rep. 2020 Feb 25;10(1):3360.

116. Coca S, Perez-Piqueras J, Martinez D, Colmenarejo A, Saez MA, Vallejo C, et al. The prognostic significance of intratumoral natural killer cells in patients with colorectal carcinoma. Cancer. 1997 Jun 15;79(12):2320–8.

117. Guerra N, Tan YX, Joncker NT, Choy A, Gallardo F, Xiong N, et al. NKG2D-deficient mice are defective in tumor surveillance in models of spontaneous malignancy. Immunity. 2008 Apr;28(4):571–80.

118. Liotta LA, Kohn EC. The microenvironment of the tumour-host interface. Nature. 2001 May 17;411(6835):375–9.

119. Massagué J, Obenauf AC. Metastatic Colonization. Nature. 2016 Jan 21;529(7586):298–306.

120. Malladi S, Macalinao DG, Jin X, He L, Basnet H, Zou Y, et al. Metastatic Latency and Immune Evasion Through Autocrine Inhibition of WNT. Cell. 2016 Mar 24;165(1):45–60.

121. Milsom CC, Lee CR, Hackl C, Man S, Kerbel RS. Differential Post-Surgical Metastasis and Survival in SCID, NOD-SCID and NOD-SCID-IL-2Rγnull Mice with Parental and Subline Variants of Human Breast Cancer: Implications for Host Defense Mechanisms Regulating Metastasis. PLoS ONE [Internet]. 2013 Aug 14 [cited 2020 Sep 22];8(8). Available from: https://www.ncbi.nlm.nih.gov/pmc/articles/PMC3743873/

122. Braekeveldt N, Stedingk K von, Fransson S, Martinez-Monleon A, Lindgren D, Axelson H, et al. Patient-Derived Xenograft Models Reveal Intratumor Heterogeneity and Temporal Stability in Neuroblastoma. Cancer Res. 2018 Oct 15;78(20):5958–69.

123. Sprouffske K, Kerr G, Li C, Prahallad A, Rebmann R, Waehle V, et al. Genetic heterogeneity and clonal evolution during metastasis in breast cancer patient-derived tumor xenograft models. Comput Struct Biotechnol J. 2020 Jan 1;18:323–31.

124. Lammers T, Kiessling F, Ashford M, Hennink W, Crommelin D, Storm G. Cancer nanomedicine: is targeting our target? Nat Rev Mater. 2016 Sep 7;1(9):1–2.

125. Falgàs A, Pallarès V, Unzueta U, Céspedes MV, Arroyo-Solera I, Moreno MJ, et al. A CXCR4-targeted nanocarrier achieves highly selective tumor uptake in diffuse large B-cell lymphoma mouse models. Haematologica. 2020 Mar;105(3):741–53.

126. Skehel JJ, Cross K, Steinhauer D, Wiley DC. Influenza fusion peptides. Biochem Soc Trans. 2001 Aug 1;29(4):623–6.

127. Pirollo KF, Chang EH. Does a targeting ligand influence nanoparticle tumor localization or uptake? Trends Biotechnol. 2008 Oct 1;26(10):552–8.

128. Chen F, Hong H, Shi S, Goel S, Valdovinos HF, Hernandez R, et al. Engineering of Hollow Mesoporous Silica Nanoparticles for Remarkably Enhanced Tumor Active Targeting Efficacy. Sci Rep. 2014 May 30;4(1):5080.

129. Morales-Cruz M, Delgado Y, Castillo B, Figueroa CM, Molina AM, Torres A, et al. Smart Targeting To Improve Cancer Therapeutics. Drug Des Devel Ther. 2019;13:3753.

130. Cai H, Ma Y, Wu Z, Ding Y, Zhang P, He X, et al. Protein corona influences liver accumulation and hepatotoxicity of gold nanorods. NanoImpact. 2016 Jul 1;3–4:40–6.

131. Rampado R, Crotti S, Caliceti P, Pucciarelli S, Agostini M. Recent Advances in Understanding the Protein Corona of Nanoparticles and in the Formulation of "Stealthy" Nanomaterials. Front Bioeng Biotechnol [Internet]. 2020 [cited 2020 Sep 24];8. Available from: http://www.ncbi.nlm.nih.gov/pmc/articles/PMC7145938/

132. Field JJ, Kanakkanthara A, Miller JH. Microtubule-targeting agents are clinically successful due to both mitotic and interphase impairment of microtubule function. Bioorg Med Chem. 2014 Sep 15;22(18):5050–9.

133. Chirino AJ, Ary ML, Marshall SA. Minimizing the immunogenicity of protein therapeutics. Drug Discov Today. 2004 Jan 15;9(2):82–90.

134. De Groot AS, Scott DW. Immunogenicity of protein therapeutics. Trends Immunol. 2007 Nov;28(11):482–90.

135. Martin F, Oliver AM, Kearney JF. Marginal zone and B1 B cells unite in the early response against T-independent blood-borne particulate antigens. Immunity. 2001 May;14(5):617–29.

136. Vos Q, Lees A, Wu ZQ, Snapper CM, Mond JJ. B-cell activation by T-cell-independent type 2 antigens as an integral part of the humoral immune response to pathogenic microorganisms. Immunol Rev. 2000 Aug;176:154–70.

137. Pallarès V, Unzueta U, Falgàs A, Sánchez-García L, Serna N, Gallardo A, et al. An Auristatin nanoconjugate targeting CXCR4+ leukemic cells blocks acute myeloid leukemia

dissemination. J Hematol OncolJ Hematol Oncol [Internet]. 2020 Apr 15 [cited 2020 Sep 28];13. Available from: https://www.ncbi.nlm.nih.gov/pmc/articles/PMC7160905/

138. Garnock-Jones KP. Brentuximab vedotin: a review of its use in patients with hodgkin lymphoma and systemic anaplastic large cell lymphoma following previous treatment failure. Drugs. 2013 Mar;73(4):371–81.

139. Sehn LH, Flowers C, McMillan A, Morschhauser F, Salles G, Felizzi F, et al. Estimation of Long-Term Survival with Polatuzumab Vedotin Plus Bendamustine and Rituximab for Patients with Relapsed/Refractory Diffuse Large B-Cell Lymphoma (r/R Dlbcl). Hematol Oncol. 2019;37(S2):257–8.

140. Newman DJ. The "Utility" of Highly Toxic Marine-Sourced Compounds. Mar Drugs [Internet]. 2019 May 31 [cited 2020 Oct 16];17(6). Available from: https://www.ncbi.nlm.nih.gov/pmc/articles/PMC6627392/

141. Cleary JM, Calvo E, Moreno V, Juric D, Shapiro GI, Vanderwal CA, et al. A phase 1 study evaluating safety and pharmacokinetics of losatuxizumab vedotin (ABBV-221), an anti-EGFR antibody-drug conjugate carrying monomethyl auristatin E, in patients with solid tumors likely to overexpress EGFR. Invest New Drugs. 2020 Oct 1;38(5):1483–94.

142. Tolaney SM, Do KT, Eder JP, LoRusso PM, Weekes CD, Chandarlapaty S, et al. A Phase I Study of DLYE5953A, an Anti-LY6E Antibody Covalently Linked to Monomethyl Auristatin E, in Patients with Refractory Solid Tumors. Clin Cancer Res [Internet]. 2020 Jul 21 [cited 2020 Oct 16]; Available from: http://clincancerres.aacrjournals.org/content/early/2020/09/19/1078-0432.CCR-20-1067

143. Sharkey RM, Goldenberg DM. Use of antibodies and immunoconjugates for the therapy of more accessible cancers. Adv Drug Deliv Rev. 2008 Sep;60(12):1407–20.

144. Yu S-F, Zheng B, Go M, Lau J, Spencer S, Raab H, et al. A Novel Anti-CD22 Anthracycline-Based Antibody–Drug Conjugate (ADC) That Overcomes Resistance to Auristatin-Based ADCs. Clin Cancer Res. 2015 Jul 15;21(14):3298–306.

145. Gallery M, Zhang J, Bradley DP, Brauer P, Cvet D, Estevam J, et al. A monomethyl auristatin E-conjugated antibody to guanylyl cyclase C is cytotoxic to target-expressing cells in vitro and in vivo. PLOS ONE. 2018 Jan 25;13(1):e0191046.

146. Conseil G, Deeley RG, Cole SPC. Polymorphisms of MRP1 (ABCC1) and related ATP-dependent drug transporters. Pharmacogenet Genomics. 2005 Aug;15(8):523–33.

147. Kovtun YV, Audette CA, Mayo MF, Jones GE, Doherty H, Maloney EK, et al. Antibody-maytansinoid conjugates designed to bypass multidrug resistance. Cancer Res. 2010 Mar 15;70(6):2528–37.

148. Liu-Kreyche P, Shen H, Marino AM, Iyer RA, Humphreys WG, Lai Y. Lysosomal P-gp-MDR1 Confers Drug Resistance of Brentuximab Vedotin and Its Cytotoxic Payload Monomethyl Auristatin E in Tumor Cells. Front Pharmacol [Internet]. 2019 Jul 17 [cited 2020 Sep 29];10. Available from: https://www.ncbi.nlm.nih.gov/pmc/articles/PMC6650582/

149. Masuda A, Maeno K, Nakagawa T, Saito H, Takahashi T. Association between Mitotic Spindle Checkpoint Impairment and Susceptibility to the Induction of Apoptosis by Anti-Microtubule Agents in Human Lung Cancers. Am J Pathol. 2003 Sep 1;163(3):1109–16.

150. Ganguly A, Yang H, Pedroza M, Bhattacharya R, Cabral F. Mitotic Centromere-associated Kinesin (MCAK) Mediates Paclitaxel Resistance. J Biol Chem. 2011 Oct 21;286(42):36378–84.

151. Sharma A, Madhunapantula SV, Robertson GP. Toxicological considerations when creating nanoparticle based drugs and drug delivery systems? Expert Opin Drug Metab Toxicol. 2012 Jan;8(1):47–69.

152. Weldon JE, Pastan I. A guide to taming a toxin: recombinant immunotoxins constructed from Pseudomonas exotoxin A for the treatment of cancer. FEBS J. 2011 Dec;278(23):4683–700.

153. Touil Y, Igoudjil W, Corvaisier M, Dessein A-F, Vandomme J, Monté D, et al. Colon Cancer Cells Escape 5FU Chemotherapy-Induced Cell Death by Entering Stemness and Quiescence Associated with the c-Yes/YAP Axis. Clin Cancer Res. 2014 Feb 15;20(4):837–46.

154. Wilson TR, Longley DB, Johnston PG. Chemoresistance in solid tumours. Ann Oncol Off J Eur Soc Med Oncol. 2006 Sep;17 Suppl 10:x315-324.

155. Pan S-T, Li Z-L, He Z-X, Qiu J-X, Zhou S-F. Molecular mechanisms for tumour resistance to chemotherapy. Clin Exp Pharmacol Physiol. 2016;43(8):723–37.

156. Yang X, Zheng F, Xing H, Gao Q, Wei W, Lu Y, et al. Resistance to chemotherapy-induced apoptosis via decreased caspase-3 activity and overexpression of antiapoptotic proteins in ovarian cancer. J Cancer Res Clin Oncol. 2004 Jul 1;130(7):423–8.

157. Goldsmith KC, Gross M, Peirce S, Luyindula D, Liu X, Vu A, et al. Mitochondrial Bcl-2 Family Dynamics Define Therapy Response and Resistance in Neuroblastoma. Cancer Res. 2012 May 15;72(10):2565–77.

158. Yip KW, Reed JC. Bcl-2 family proteins and cancer. Oncogene. 2008 Oct 27;27(50):6398–406.

159. Geng M, Wang L, Li P. Correlation between chemosensitivity to anticancer drugs and Bcl-2 expression in gastric cancer. Int J Clin Exp Pathol. 2013 Oct 15;6(11):2554–9.

160. Hayward RL, Macpherson JS, Cummings J, Monia BP, Smyth JF, Jodrell DI. Enhanced oxaliplatin-induced apoptosis following antisense Bcl-xl down-regulation is p53 and Bax dependent: Genetic evidence for specificity of the antisense effect. :10.

161. Zhang L, Yu J, Park BH, Kinzler KW, Vogelstein B. Role of BAX in the apoptotic response to anticancer agents. Science. 2000 Nov 3;290(5493):989–92.

162. Ansari AM, Ahmed AK, Matsangos AE, Lay F, Born LJ, Marti G, et al. Cellular GFP Toxicity and Immunogenicity: Potential Confounders in in Vivo Cell Tracking Experiments. Stem Cell Rev Rep. 2016 Oct 1;12(5):553–9.

163. Falgàs A, Pallarès V, Serna N, Sánchez-García L, Sierra J, Gallardo A, et al. Selective delivery of T22-PE24-H6 to CXCR4+ diffuse large B-cell lymphoma cells leads to wide therapeutic index in a disseminated mouse model. Theranostics. 2020 Apr 6;10(12):5169–80.

164. Tait SWG, Ichim G, Green DR. Die another way – non-apoptotic mechanisms of cell death. J Cell Sci. 2014 May 15;127(10):2135–44.

165. Nagarajan K, Soundarapandian K, Thorne RF, Li D, Li D. Activation of Pyroptotic Cell Death Pathways in Cancer: An Alternative Therapeutic Approach. Transl Oncol. 2019 Jul 1;12(7):925–31.

166. Mulvihill E, Sborgi L, Mari SA, Pfreundschuh M, Hiller S, Müller DJ. Mechanism of membrane pore formation by human gasdermin-D. EMBO J [Internet]. 2018 Jul 13 [cited 2020 Oct 6];37(14). Available from: https://www.ncbi.nlm.nih.gov/pmc/articles/PMC6043855/

167. Kreitman RJ, Tallman MS, Robak T, Coutre S, Wilson WH, Stetler-Stevenson M, et al. Phase I trial of anti-CD22 recombinant immunotoxin moxetumomab pasudotox (CAT-8015 or HA22) in patients with hairy cell leukemia. J Clin Oncol Off J Am Soc Clin Oncol. 2012 May 20;30(15):1822–8.

168. Shan L, Liu Y, Wang P. Recombinant Immunotoxin Therapy of Solid Tumors: Challenges and Strategies. J Basic Clin Med. 2013;2(2):1–6.

169. Kim J-S, Jun S-Y, Kim Y-S. Critical Issues in the Development of Immunotoxins for Anticancer Therapy. J Pharm Sci. 2020 Jan 1;109(1):104–15.

170. Onda M, Beers R, Xiang L, Lee B, Weldon JE, Kreitman RJ, et al. Recombinant immunotoxin against B-cell malignancies with no immunogenicity in mice by removal of B-cell epitopes. Proc Natl Acad Sci U S A. 2011 Apr 5;108(14):5742–7.

VIII. ANNEXES

VIII. ANNEXES

1) ANNEX 1: ARTICLE 1

Research Article

TRANSPARENT PROCESS   OPEN ACCESS

EMBO
Molecular Medicine

Selective depletion of metastatic stem cells as therapy for human colorectal cancer

María Virtudes Céspedes[1,2,†], Ugutz Unzueta[1,2,†], Anna Aviñó[2,3], Alberto Gallardo[2,4], Patricia Álamo[1,2], Rita Sala[1,2], Alejandro Sánchez-Chardi[5], Isolda Casanova[1,2], María Antònia Mangues[1,2,6], Antonio Lopez-Pousa[2,7], Ramón Eritja[2,3] (iD), Antonio Villaverde[2,8,9,*] (iD), Esther Vázquez[2,8,9,‡] & Ramón Mangues[1,2,‡,**] (iD)

Abstract

Selective elimination of metastatic stem cells (MetSCs) promises to block metastatic dissemination. Colorectal cancer (CRC) cells over-expressing CXCR4 display trafficking functions and metastasis-initiating capacity. We assessed the antimetastatic activity of a nanoconjugate (T22-GFP-H6-FdU) that selectively delivers Flox-uridine to CXCR4^{+} cells. In contrast to free oligo-FdU, intravenous T22-GFP-H6-FdU selectively accumulates and internalizes in CXCR4^{+} cancer cells, triggering DNA damage and apoptosis, which leads to their selective elimination and to reduced tumor re-initiation capacity. Repeated T22-GFP-H6-FdU administration in cell line and patient-derived CRC models blocks intravasation and completely prevents metastases development in 38–83% of mice, while showing CXCR4 expression-dependent and site-dependent reduction in foci number and size in liver, peritoneal, or lung metastases in the rest of mice, compared to free oligo-FdU. T22-GFP-H6-FdU induces also higher regression of established metastases than free oligo-FdU, with negligible distribution or toxicity in normal tissues. This targeted drug delivery approach yields potent antimetastatic effect, through selective depletion of metastatic CXCR4^{+} cancer cells, and validates metastatic stem cells (MetSCs) as targets for clinical therapy.

Introduction

Control of metastatic spread remains an unmet medical need. In colorectal cancer (CRC), as in other tumor types, adjuvant therapy controls metastases and prolongs survival at the expense of high toxicity; however, metastases remain the primary cause of death (Schrag, 2004; Mehlen & Puisieux, 2006; Spano *et al*, 2012; Riihimäki *et al*, 2016). There is an urgent need to develop less toxic and more effective antimetastatic agents. To achieve this goal, preclinical and clinical drug development should shift its focus from primary tumor to metastasis control, using metastatic cancer models and evaluating promising drugs in patients with limited or non-metastatic disease (Steeg & Theodorescu, 2008; Steeg, 2016). This is relevant because metastases differ from primary tumors in their mutational or gene expression profiles (Rhodes & Chinnaiyan, 2005; Vignot *et al*, 2015) and response to drugs (Takebayashi *et al*, 2013; Chen *et al*, 2015).

Metastatic stem cells (MetSCs) are a subset of cancer stem cells (CSCs) that, in addition to self-renewal and differentiation capacities, have trafficking functions (Steeg, 2016; Brabletz *et al*, 2005; Sleeman & Steeg, 2010; Oskarsson *et al*, 2014). In CRC, CXCR4 receptor enhances metastatic dissemination and confers poor patient prognosis (Kim *et al*, 2005, 2006; Schimanski *et al*, 2005), a finding similar to other cancers (Müller *et al*, 2001; Balkwill, 2004; Kucia *et al*, 2005; Schimanski *et al*, 2006; Hermann *et al*, 2007; Sun *et al*, 2010). Moreover, CXCR4-overexpressing (CXCR4^{+}) cells have metastasis-initiating capacity (MICs) in CRC (Croker & Allan, 2008; Zhang *et al*, 2012), whereas CXCR4 RNAi-mediated downregulation or blockade of membrane localization inhibits hepatic and lung metastases (Murakami *et al*, 2013; Wang *et al*, 2014). These

1 Institut d'Investigacions Biomèdiques Sant Pau, Hospital de Santa Creu i Sant Pau, Barcelona, Spain
2 CIBER de Bioingeniería, Biomateriales y Nanomedicina (CIBER-BBN), Barcelona, Spain
3 Institute for Advanced Chemistry of Catalonia (IQAC), CSIC, Barcelona, Spain
4 Department of Pathology, Hospital de la Santa Creu i Sant Pau, Barcelona, Spain
5 Servei de Microscòpia, Universitat Autònoma de Barcelona, Barcelona, Spain
6 Department of Pharmacy, Hospital de la Santa Creu i Sant Pau, Barcelona, Spain
7 Department of Medical Oncology, Hospital de la Santa Creu i Sant Pau, Barcelona, Spain
8 Institut de Biotecnologia i de Biomedicina, Universitat Autònoma de Barcelona, Barcelona, Spain
9 Departament de Genètica i de Microbiologia, Universitat Autònoma de Barcelona, Barcelona, Spain
   *Corresponding author. Tel: +34 935813086; E-mail: antoni.villaverde@uab.cat
   **Corresponding author. Tel: +34 935537918; E-mail: rmangues@santpau.cat
   †These authors contributed equally to this work
   ‡These authors contributed equally to this work as senior authors

findings support a MetSC function for CXCR4$^+$ CRC cells. Nevertheless, the formal proof for MetSCs clinical relevance will only come by demonstrating that their selective targeting and elimination leads to antimetastatic effect.

Nanomedicine pursues targeted drug delivery, which aims at increasing anticancer effect while reducing toxicity (Das *et al*, 2009). We here use targeted drug delivery to CXCR4$^+$ MetSCs in an attempt to achieve their selective elimination. We produced the drug nanoconjugate T22-GFP-H6-FdU by covalently binding a protein nanoparticle, which selectively targets CXCR4$^+$ cancer cells (Unzueta *et al*, 2012a; Céspedes *et al*, 2016) to Floxuridine (FdU), a cytotoxic drug used to treat CRC liver metastases (Shi *et al*, 2015). We here demonstrate selective T22-GFP-H6-FdU biodistribution to tumor and metastatic foci in cell line- and patient-derived CRC models. We also observed its internalization and selective FdU delivery in CXCR4$^+$ MetSCs, leading to their depletion. After repeated T22-GFP-H6-FdU administration, and in contrast to free oligo-FdU, we achieved highly significant activity in the prevention and regression of metastases in the absence of toxicity, supporting the clinical relevance of developing drugs that selectively target MetSCs to achieve metastasis control.

Results

Development of T22-GFP-H6-FdU, a nanoconjugate that targets CXCR4$^+$ CRC cells

The previous demonstration of MIC capacity for CXCR4-overexpressing (CXCR4$^+$) CRC cells (Croker & Allan, 2008; Zhang *et al*, 2012), and its inhibition by CXCR4 downregulation (Murakami *et al*, 2013; Wang *et al*, 2014), identifies these cells as MetSCs (Oskarsson *et al*, 2014). On this basis, we generated a CXCR4-targeted nanoconjugate to evaluate its capacity to achieve antimetastatic effect by selectively eliminating CXCR4$^+$ CRC cells. The structure and physico-chemical characterization of this new T22-GFP-H6-FdU nanoconjugate are described in Fig 1A–C, and Appendix Figs S1 and S2, which contains T22 (a ligand that targets the CXCR4 receptor), a green fluorescent

protein (allowing its *in vivo* monitoring) and oligo-FdU, an oligonucleotide of a drug active against CRC (Shi *et al*, 2015), which allows to load a high number of drug molecules into the nanoconjugate.

T22-GFP-H6-FdU was synthesized by functionalizing oligo-FdU with thiol (Fig 1C and Appendix Fig S1A), which was subsequently conjugated to the previously described T22-GFP-H6 protein nanoparticle (Unzueta *et al*, 2012a) once bound to a chemical linker (Fig 1C).

We physico-chemically characterized the HS-oligo-FdU. The functionalized pentamer FdU-HEG-SH was quantified by absorption at 260 nm and confirmed by MALDI mass spectrometry (MALDI-TOF), yielding a MW of 1,976.2, being the expected MW 1,974.0. The control pentanucleotide (free oligo-FdU) characterized by mass spectrometry (MALDI-TOF) yield a MW of 1,476.5, being the expected MW: 1,478.1. The analysis of the conjugation products was performed by MALDI-TOF spectra identifying the peaks corresponding to one or two molecules of pentaoligonucleotides of FdU bound to the nanoparticle with the MW indicated in Appendix Figs S1 and S2. The T22-GFP-H6-FdU size was determined by dynamic light scattering, being 14.6 + 0.14, as compared to 13.4 + 0.11 for the control T22-GFP-H6 nanoparticle, a size consistent with that determined by transmission electron microscopy.

This product had an approximate FdU/nanoparticle (DNR) ratio of 20 (Appendix Fig S2), and maintained its capacity for self-assembling (Unzueta *et al*, 2012a; Rueda *et al*, 2015; Appendix Fig S2D). The determined size was higher than the renal filtration cutoff (6–7 nm) ensuring a high re-circulation time in blood, a requirement for effective targeted drug delivery (Unzueta *et al*, 2012b, 2015).

T22-GFP-H6-FdU selectively internalizes and kills CXCR4$^+$ CRC cells *in vitro*

Following, we used the human SW1417 CRC cell line to assess if the loaded oligo-FdU conferred cytotoxic activity to the nanoparticle while maintaining its CXCR4 targeting capacity, provided that drug conjugation can alter protein conformation and function (Goswami *et al*, 2013). We first determined that this cell line constitutively

Figure 1. T22-GFP-H6-FdU nanoconjugate synthesis and selective internalization and killing of CXCR4$^+$ CRC cells *in vitro*.

A   The nanoconjugate contains a fusion protein [T22-GFP-H6—composed of the peptide T22 as a CXCR4 ligand, a green fluorescent protein and a histidine tail—bound to the payload drug (Unzueta *et al*, 2012a)].

B   Three to four pentameric oligonucleotides (approximately 20 molecules) of the antitumor drug 5-Fluoro-2′-deoxyuridine (FdU), named oligo-FdU, are conjugated to the T22-GFP-H6 targeting vector using a linker.

C   T22-GFP-H6-FdU chemical synthesis: T22-GFP-H6 is first covalently bound to the 6-Maleimidohexanoic acid N-hydroxysuccinimide ester linker through its amino groups in the external lysines (Hermanson, 2013). The thiol-functionalized oligo-FdU (oligo-(FdU)5-SH; see Appendix Fig S1) is then reacted with T22-GFP-H6 functionalized with maleimide (Michael reaction).

D   High and constitutive expression of CXCR4 in the membrane of SW1417 CRC cells as measured by flow cytometry.

E   Lack of human SDF-1α release from cultured SW1417 CRC cells, as measured by ELISA, whereas human control 1BR3.G fibroblasts express high SDF-1α levels, after 48 or 72 h of growth in culture (mean ± s.e.m., *N* = 2 experiment in duplicate).

F   Nanoconjugate internalization in CXCR4-overexpressing (CXCR4$^+$) SW1417 CRC cells after 1-h exposure at 1 μM, as measured by fluorescence emission using flow cytometry (mean ± s.e.m., *N* = 3 experiments in duplicate). Significant difference at **P = 0.002 between the T22-GFP-H6-FdU and the T22-GFP-H6-FdU + AMD3100 groups, Mann–Whitney *U*-test.

G   Intracellular trafficking of T22-GFP-H6-FdU in CXCR4$^+$ SW1417 cells by confocal microscopy after exposure at 1 μM for 24 h. The green staining corresponds to GFP-containing nanoconjugates, and the red staining corresponds to plasma cell membranes stained with a red dye (CellMask™), whereas cell nucleus was stained in blue with Hoechst. The insets show detail of the intracellular localization of nanostructured, fluorescent entities, in an isosurface representation within a three-dimensional volumetric x-y-z data field.

H   Linearized T22-GFP-H6-FdU dose–response trend line representation compared with unconjugated free oligo-FdU exposure. Antitumor effect was measured as CXCR4$^+$ SW1417 cell viability by MTT after 72-h exposure as the described concentrations (mean ± s.e.m., *N* = 3 experiments in duplicate).

I   Reduction in cell viability determined by optical microscope images of SW1417 cells exposed to 1 μM T22-GFP-H6-FdU for 72 h, as compared to T22-GFP-H6 or free oligo-FdU (*N* = 3 experiments in duplicate; Scale bar, 100 μm).
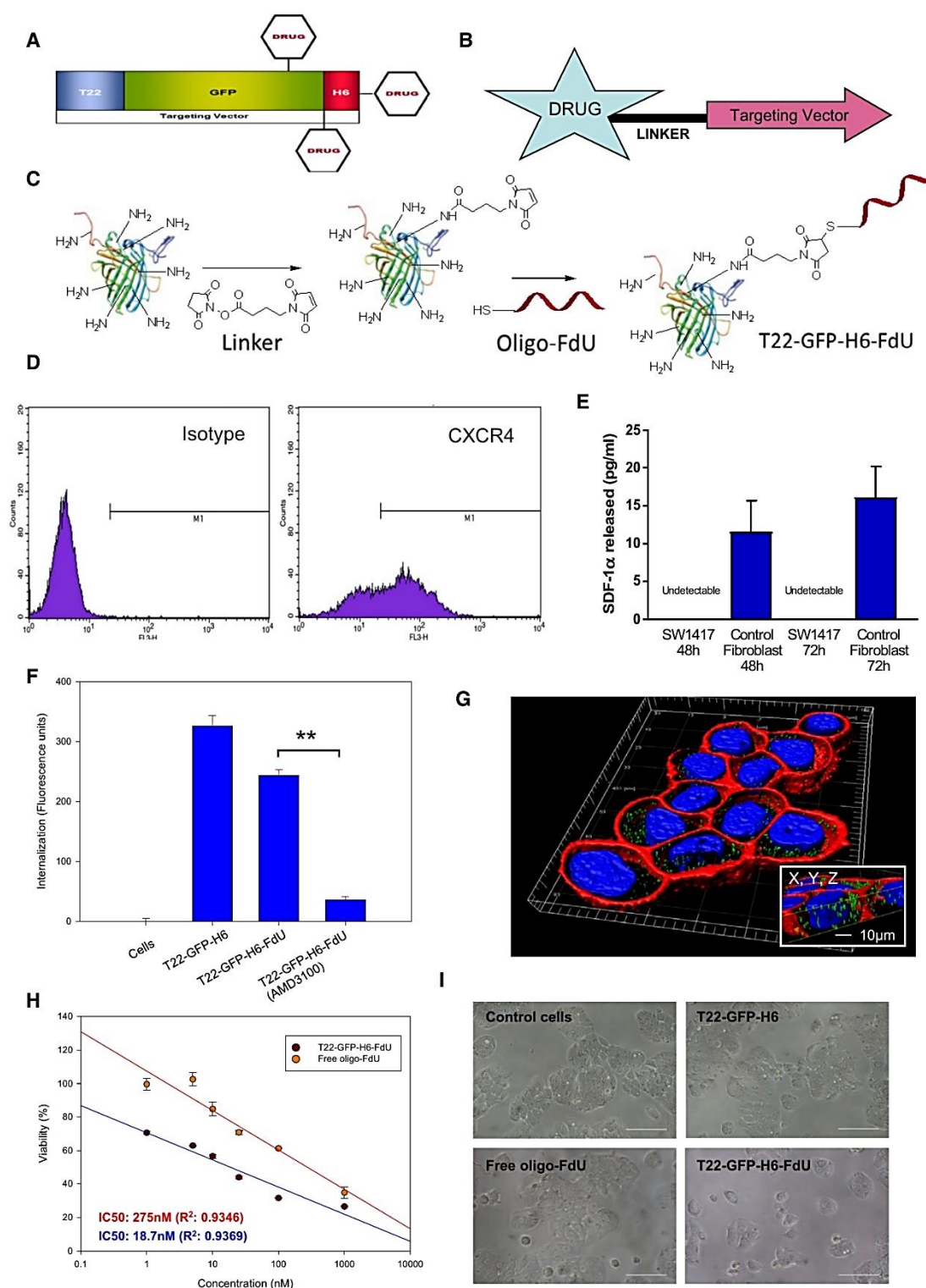
Figure 1.

expresses membrane CXCR4 (Fig 1D) while lacking SDF-1α expression (Fig 1E). Then, we demonstrated T22-GFP-H6-FdU capacity to internalize in CXCR4$^+$ SW1417, as measured by fluorescence emission using flow cytometry (Fig 1F), and to accumulate and traffic into its cytosol as observed by confocal microscopy (Fig 1G). The nanoconjugate maintains also its dependence on CXCR4 for internalization, since AMD3100, a CXCR4 antagonist, was able to downregulate CXCR4 receptor in the membrane and completely blocked nanoconjugate internalization (Fig 1F). In addition, T22-GFP-H6-FdU induced significantly higher cytotoxicity than free oligo-FdU in the same cells, as measured by cell viability (Fig 1H) or phase-contrast microscopy (Fig 1I). We confirmed CXCR4-dependent nanoconjugate internalization and higher cytotoxicity than free oligo-FdU in human CXCR4$^+$ HeLa cells (Appendix Fig S3A–D).

T22-GFP-H6-FdU selectively targets CXCR4$^+$ CRC cells *in vivo*

Once CXCR4-dependence for T22-GFP-H6-FdU *in vitro* activity was established, we investigated whether the nanoconjugate could achieve targeted drug delivery after its intravenous administration in the subcutaneous (SC) CXCR4$^+$ SW1417 CRC model. We assayed its selectivity and CXCR4 dependence regarding tumor tissue uptake, internalization in CXCR4-overexpressing MetSCs (target cells), intracellular release of the cytotoxic drug FdU, and selective CXCR4$^+$ MetSC killing (Fig 2A).

T22-GFP-H6-FdU showed selective tumor uptake, as measured by fluorescence emission, 5 h after the injection of a 100 μg dose in mice (Fig 2B) as previously demonstrated for T22-GFP-H6 (Céspedes *et al*, 2016). Moreover, T22-GFP-H6-FdU selectively internalized into CXCR4$^+$ tumor cells as determined by their co-localization (merged yellow color) in the cell membrane, using dual anti-GFP and anti-CXCR4 immunofluorescence, as well as the detection of released nanoconjugate into the CXCR4$^+$ cell cytosol (green dots; Fig 2C). In addition, administering the CXCR4 antagonist AMD3100 to mice prior to the nanoconjugate completely blocked its tumor uptake (Fig 2D) as well as its internalization in CXCR4$^+$ cancer cells (Fig 2E and F). Therefore, the nanoconjugate achieves not only selective tumor biodistribution, but also its specific internalization into target CXCR4$^+$ cancer cells, in a CXCR4-dependent manner.

T22-GFP-H6-FdU achieves targeted drug delivery leading to selective depletion of CXCR4$^+$ cancer cells in CRC tumors

We next used the same SC SW1417 CRC model to assess if the selective internalization into the cytosol of CXCR4$^+$ target cancer cells achieved by the nanoconjugate led to selective FdU delivery. We also evaluated whether the delivered FdU could induce DNA damage and caspase-3-dependent cell death, triggering the specific elimination of CXCR4$^+$ tumor cells. To that aim, we used γ-H2AX IHC to measure the generation of DNA double-strand breaks (DSBs), since they mediate FdU antitumor activity (Longley *et al*, 2003). Five hours after T22-GFP-H6-FdU treatment, the number of cells containing DSBs foci in tumors (22.8 ± 1.4) was significantly higher ($P = 0.02$) than after free oligo-FdU treatment (13.4 ± 0.7), whereas cells containing DSBs in control T22-GFP-H6 or Buffer-treated tumors were barely detectable (Fig 3A and B).

T22-GFP-H6-FdU induction of DSBs indicated its capacity to release FdU in target cells to reach the nucleus and incorporate into DNA to induce DNA damage. In addition, the number of cleaved caspase-3-positive cells signaling for apoptosis (IHC measured using anticleaved caspase-3 antibody) 5 h after T22-GFP-H6-FdU treatment (10.1 ± 1.0) was significantly higher ($P = 0.03$) than after free oligo-FdU (5.2 ± 0.9) treatment (Fig 3A and B). Moreover, increased DSB-positive cells led to higher antitumor activity, since the number of cell dead bodies, measured by Hoechst staining, which identify nuclear condensation or defragmentation, in tumor tissue 24 h after T22-GFP-H6-FdU injection was significantly ($P = 0.03$) higher (13.9 ± 0.5) than free oligo-FdU (7.1 ± 0.6), T22-GFP-H6 (3.0 ± 0.3), or Buffer (1.9 ± 0.4) treatment (Fig 3A and B).

Following, we analyzed the fraction of CXCR4$^+$ cancer cells (CXCR4$^+$ CCF) remaining in tumor tissue, along time, after a single 100 μg T22-GFP-H6-FdU dose, as compared to free oligo-FdU, using the SC CXCR4$^+$ SW1417 CRC model in NOD/SCID mice. Before treatment, both groups showed a similar CXCR4$^+$ CCF in tumor tissue (Fig 4A and B); however, after T22-GFP-H6-FdU treatment, the CXCR4$^+$ CCF was reduced at 24 h and reached its valley at 48 h

Figure 2. Selective biodistribution and receptor-dependent uptake of T22-GFP-H6-FdU in CXCR4$^+$ cells *in vivo*.

A   Approach to achieve targeted drug delivery and selective killing of metastatic stem cells: CXCR4-nanoconjugate interaction triggers CXCR4-mediated internalization in MetSCs, in primary tumors and metastatic foci, followed by FdU release to the cytosol and diffusion to the nucleus to induce double-strand breaks leading to selective killing of CXCR4$^+$ cells.

B   Selective T22-GFP-H6-FdU nanoconjugate biodistribution in subcutaneous CXCR4$^+$ SW1417 CRC tumor tissue 5 h after a 100 μg single intravenous dose, as measured by fluorescence emission using IVIS Spectrum 200 (*N* = 5/group). Biodistribution is similar to that achieved by the T22-GFP-H6 targeting vector and undetectable after Buffer or free oligo-FdU treatment (*N* = 5 mice/group).

C   Co-localization (yellow merged) of the T22-GFP-H6-FdU (green) and the CXCR4 receptor (red) and release of T22-GFP-H6-FdU into the cytosol in CXCR4$^+$ tumor cells 5 h after a 100 μg dose of nanoconjugate, as measured by dual anti-GFP/anti-CXCR4 immunofluorescence (IF). DAPI (blue nuclear staining). Fluorescence emission was measured in the green and red channels using the ImageJ software and expressed as mean area (A) ± s.e.m (μm^2) (*N* = 10, 2 tumor fields × 5 mice; 200×). Note the significant (*P* = 0.003) increase in the area occupied by the green dots (nanoconjugate released to the cell cytosol) in T22-GFP-H6-FdU-treated tumors, compared to free oligo-FdU-treated control tissues. Scale bar, 50 μm.

D   Administration of the CXCR4 antagonist AMD3100 completely blocks T22-GFP-H6-FdU tumor biodistribution, as measured by fluorescence emission. Fluorescence is not detected in Buffer or free oligo-FdU controls (*N* = 5 tumor fields/group).

E   The uptake of T22-GFP-H6-FdU observed in CXCR4$^+$ SW1417 tumor tissues is almost completely blocked by prior AMD3100 administration, as quantified using the anti-GFP IHC H-score (mean ± s.e.m., *N* = 5 tumor fields/group). Comparison of T22-GFP-H6 uptake between groups: (B: Buffer; F: free oligo-FdU; T-F: T22-GFP-H6-FdU; T-F+A: T22-GFP-H6-FdU+AMD3100). *P*-values for statistical differences B vs. T-F, **P* = 0.000; F vs. T-F, **P* = 0.000; T-F vs. TFA, **P* = 0.004. Mann–Whitney *U*-test.

F   Representative images of T22-GFP-H6-FdU uptake and AMD3100 competition by anti-GFP immunostaining, which quantitation is reported in panel (E). Scale bar, 50 μm.
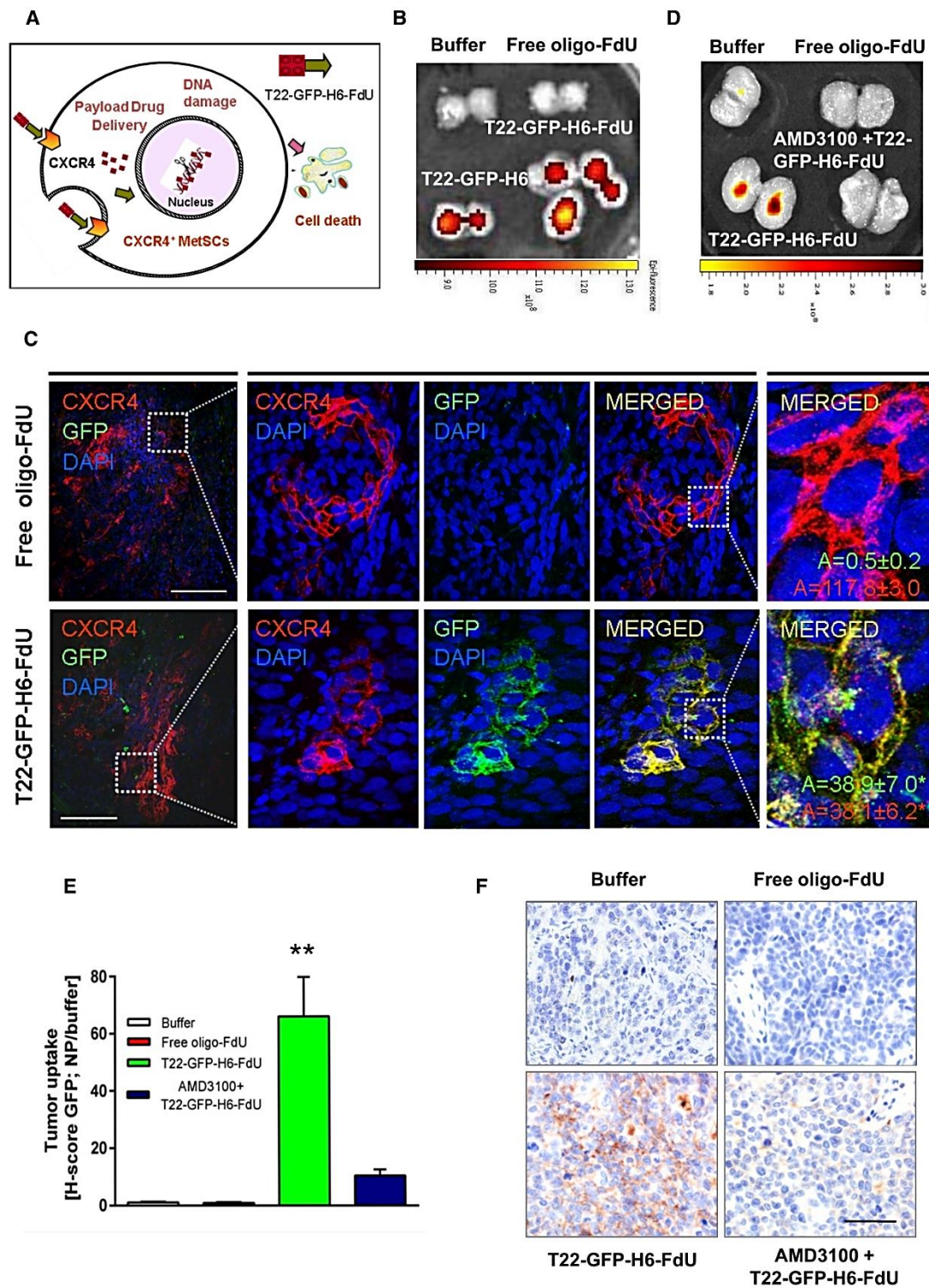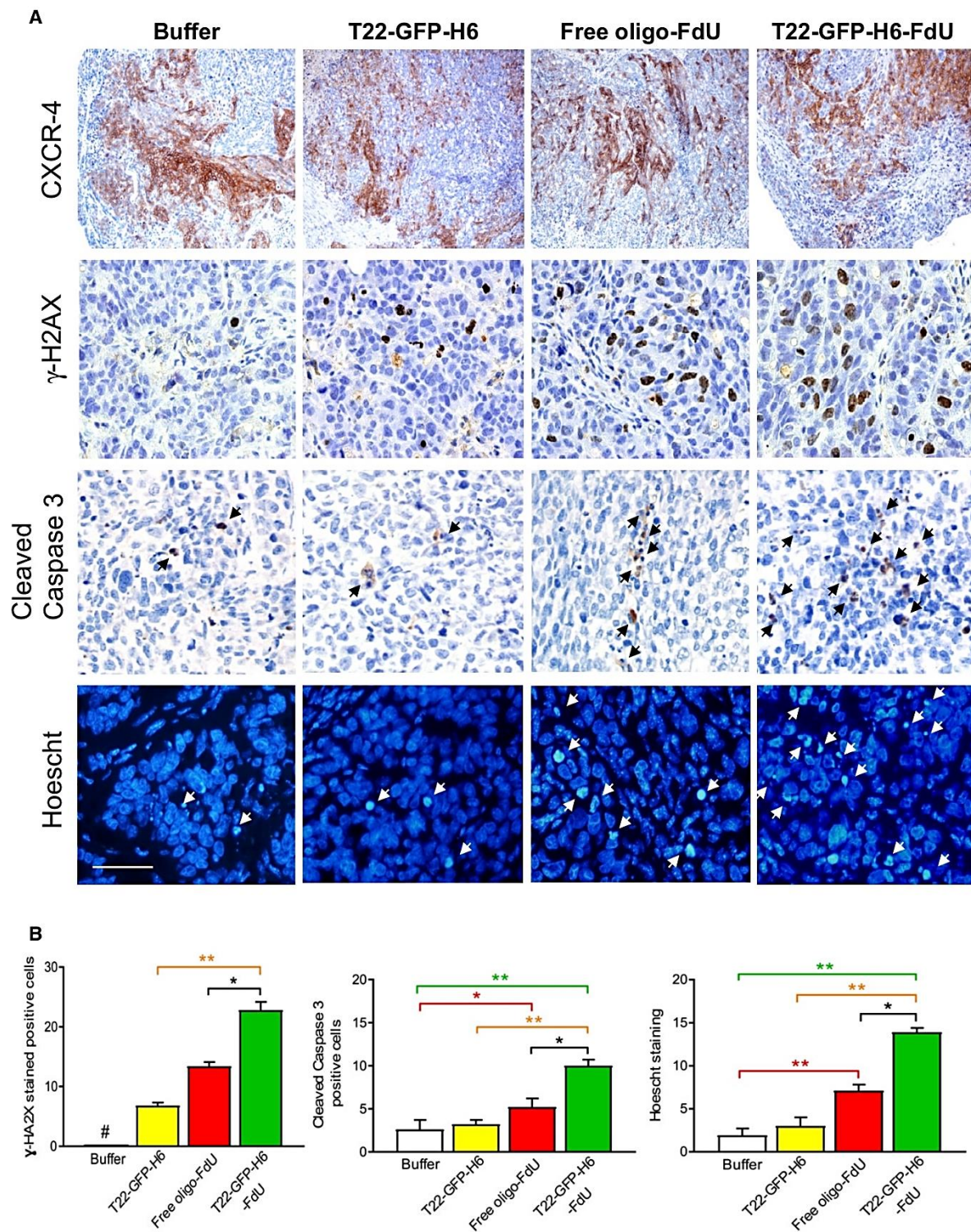
Figure 2.

Figure 3.

EMBO Molecular Medicine

Figure 3. T22-GFP-H6-FdU-induced depletion of CXCR4-overexpressing cancer cells in tumor tissue.

A   Representative images of CXCR4 overexpression in subcutaneous tumor tissue, showing similar CXCR4 levels among compared groups (N = 5/group; Buffer, T22-GFP-H6-FdU, T22-GFP-H6, and free oligo-FdU) before treatment (upper panels). Representative images of DNA double-strand break induction and caspase-3 activation (measured with anti-γ-H2AX or anticleaved caspase-3 by IHC) 5 h post-administration (middle panels). Apoptotic induction (Hoechst staining, 24 h post-administration, lower panels). Note the higher number of cells positive for DSBs, caspase-3 activation, and apoptosis induction in the T22-GFP-H6-FdU as compared to free oligo-FdU. Black or white arrows indicate dead cells. Scale bar, 50 μm.

B   Quantitation of the number of cells containing DSBs or active caspase-3 in IHC-stained tumor sections 5 h post-treatment and the number of condensated or disaggregated nuclei (by Hoechst staining) 24 h post-treatment in tumor sections of 10 high-power fields (400× magnification) using the Cell^D software (N = 50; 10 tumor fields/mice; 5 mice/group). Data expressed as mean ± s.e.m. Parameter comparison between groups: (B: Buffer; T: T22-GFP-H6; F: free oligo-FdU; T-F: T22-GFP-H6-FdU). *P*-values for statistical differences: γ-H2AX staining quantitation: B vs. T, [#]*P* = 0.001; B vs. F, [#]*P* = 0.000; B vs. T-F, [#]*P* = 0.000; T vs. T-F, **P* = 0.001; F vs. T-F, **P* = 0.02. Cleaved caspase-3 quantitation: B vs. F, **P* = 0.034; B vs. T-F, ***P* = 0.009; T vs. T-F, ***P* = 0.003; F vs. T-F, **P* = 0.012. Hoechst staining quantitation: B vs. F, ***P* = 0.01; B vs. T-F, ***P* = 0.001; T vs. T-F, ***P* = 0.000; F vs. T-F, **P* = 0.032. Mann Whitney *U*-test.

(Fig 4A and B). In contrast, the CXCR4$^+$ CCF in tumor tissue after an equimolecular dose of free oligo-FdU remained similar to its basal level along time. Taken together, these results indicate that T22-GFP-H6-FdU achieves selective biodistribution to tumor tissue and FdU delivery to target CXCR4$^+$ cancer cells, as indicated by an enhancement in DNA damage and apoptotic tumor cell death, which triggers selective elimination of CXCR4$^+$ cancer cells *in vivo*, achieving, therefore, targeted FdU delivery to target cancer cells.

Transient target cell elimination and definition of a dose interval for repeated T22-GFP-H6-FdU injection

Despite T22-GFP-H6-FdU achieved selective depletion of CXCR4$^+$ target cells in tumor tissue observed 48 h after its administration, we found this effect to be transient, since 72 h post-injection CXCR4$^+$ cancer cell fraction in tumor tissue grew back, nevertheless, to reach a level lower than that basal before therapy (Fig 4A and B). In contrast, the CXCR4$^+$ CCF in tumor tissue after free oligo-FdU therapy was maintained over time, remaining similar at 24, 48, or 72 h after treatment as before therapy (Fig 4A and B). Therefore, in contrast to T22-GFP-H6-FdU effect, cancer killing by free oligo-FdU did not show selectivity toward CXCR4$^+$ cancer cells. Based on these results, and in order to evaluate T22-GFP-H6-FdU antimetastatic effect, we defined a 72 h (3 days) dose interval as optimal for its administration in a repeated dose schedule. We expected this regime to maintain sufficiently low the fraction of CXCR4$^+$ cancer cells remaining in primary tumors and metastatic foci, along the treatment period, as to efficiently block metastasis and/or foci growth, provided that CXCR4$^+$ cancer cells act as MetSCs.

T22-GFP-H6-FdU-treated tumors reduce their spheroid formation and tumor re-initiation capacities

We next used the CXCR4$^+$ luciferase$^+$ SW1417 SC CRC model to assess if the selective CXCR4$^+$ cancer cell killing induced by T22-GFP-H6-FdU treatment *in vivo* was capable of blocking spheroid formation *in vitro*. Thus, we cultured 1×10^6 disaggregated cells in stem cell-conditioned media and low-adhesion plates that were obtained from CXCR4$^+$ luciferase$^+$ SW1417 subcutaneous tumors, 24 h after 100 μg T22-GFP-H6-FdU i.v. doses, for 2 consecutive days, and observed a reduction in spheroid formation (Fig 4C), as compared to cells obtained after an equimolar free-FdU or Buffer treatment. The bioluminescence intensity emitted by the spheroids generated after T22-GFP-H6-FdU treatment ($9.1 \times 10^7 \pm 3.2 \times 10^7$) was significantly (*P* = 0.02) reduced as compared to free oligo-FdU

($19.0 \times 10^7 \pm 0.38 \times 10^7$) or Buffer ($40.0 \times 10^7 \pm 1.9 \times 10^7$) treatment (Fig 4D). Similarly, culture of 1×10^6 disaggregated cells obtained from patient-derived CXCR4$^+$ M5 subcutaneous tumors, treated with the same T22-GFP-H6-FdU dosage, leads to a significant (*P* = 0.001) reduction in the number of formed spheroids (19.1 ± 1.2), as compared to free oligo-FdU-treated (46.3 ± 3.1) or Buffer-treated (73.1 ± 7.0) mice (Fig 5A and B).

In addition, the inoculation of 5×10^6 cells, subcutaneously in recipient NSG mice, derived from disaggregated tumor cells obtained from CXCR4$^+$ M5 SC tumors after the administration of 100 μg T22-GFP-H6-FdU intravenous doses, for 2 consecutive days, leads to a reduction in tumor re-initiation (as measured as diminished number and size of tumors) 10 days after the end of treatment, as compared to free oligo-FdU-treated or Buffer-treated mice (Fig 5C and D). Thus, in both, the SW1417 and the M5 CRC models CXCR4$^+$ cancer cells behave as cancer stem cells since their selective elimination reduces their tumor re-initiation capacity.

T22-GFP-H6-FdU-induced blockade of tumor emboli intravasation

Following, we assessed if T22-GFP-H6-FdU treatment of patient-derived CXCR4$^+$ M5 orthotopic tumors blocked dissemination from the primary tumors at an early time. To this aim, 7 days after implantation of two million M5 tumor cells in the mouse cecum, we administered 100 μg T22-GFP-H6-FdU intravenous doses, for 2 consecutive days, and 24 h later sacrificed the mice and proceed to H&E staining of samples from tumors and peri-tumoral areas. We observed that T22-GFP-H6-FdU administration induced a significant (*P* = 0.016) reduction in the number of intravasated tumor emboli within the vessels of the peri-tumoral area (1.6 ± 0.4), which were microscopically detected, in comparison with free oligo-FdU-treated (5.4 ± 1.3) or Buffer-treated (5.1 ± 2.0) tumors (Fig 5E and F). Moreover, T22-GFP-H6-FdU treatment reduced also significantly (*P* = 0.027) the H-score (percent and intensity of IHC stained and normalized by foci area) for CXCR4 expression in peri-tumoral intravasated tumor emboli (0.017 ± 0.012), as compared to free oligo-FdU-treated (0.043 ± 0.010) or Buffer-treated (0.038 ± 0.005) tumors (Fig 5E–G). Thus, T22-GFP-H6-FdU blocks tumor emboli intravasation in the primary tumor peri-tumoral vessels.

T22-GFP-H6-FdU induces the regression of established metastases

We assessed T22-GFP-H6-FdU capacity to inhibit growth of established metastases, as compared to equimolecular doses of T22-GFP-
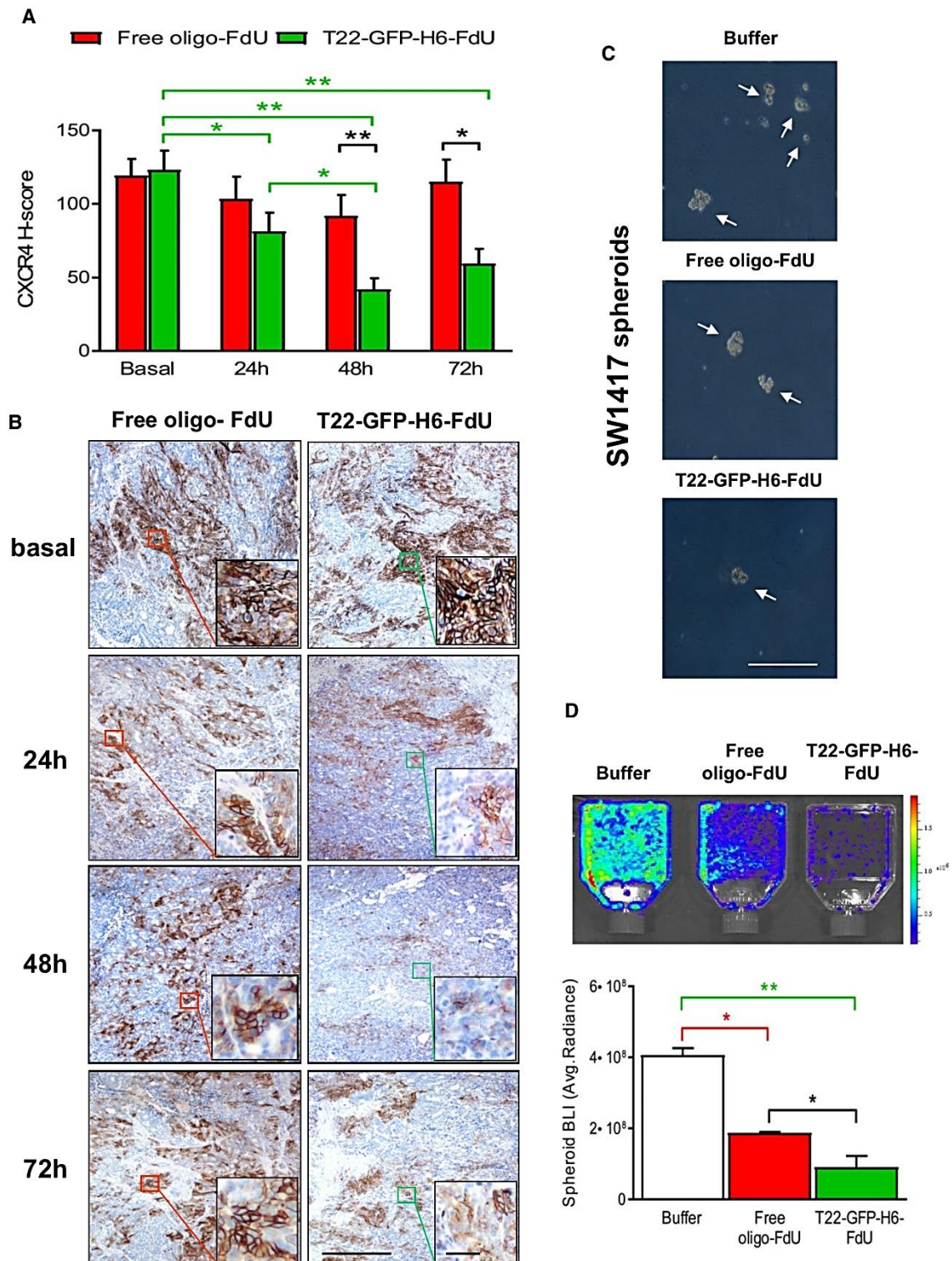

MetSCs killing as antimetastatic therapy   *María Virtudes Céspedes et al*

Figure 4.

166

María Virtudes Céspedes et al   MetSCs killing as antimetastatic therapy   **EMBO Molecular Medicine**

Figure 4. T22-GFP-H6-FdU-induced depletion of CXCR4-overexpressing cancer cells in tumor tissue leading to reduced spheroid formation capacity.

A, B   T22-GFP-H6-FdU depletes CXCR4$^+$ cancer cells from SW1417 CRC tumor tissue after a 100 μg single-dose administration. Note the reduction in CXCR4$^+$ cell fraction in the tumor 24 h after injection, their almost complete elimination at 48 h, and the re-emergence of CXCR4$^+$ cells 72 h post-administration, using anti-CXCR4 IHC. In contrast, the CXCR4$^+$ cancer cell fraction (CXCR4$^+$ CCF) in tumor tissue remains constant along time after free oligo-FdU treatment. The 3-day time-lapse for CXCR4$^+$ tumor cell re-appearance defines the dosage interval used in a repeated dose schedule of nanoconjugate administration in the experiments to evaluate its antimetastatic effect (N = 5: 5 mice/group; 1 samples/mouse). Scale bar, 50 μm. Data expressed as mean ± s.e.m. CXCR4 H-score comparison for T22-GFP-H6-FdU(T-F)-treated tumors among time points (green line, panel A). *P*-values for statistical differences: T-F Basal vs. T-F 24 h, *P = 0.038; T-F Basal vs. T-F 48 h, **P = 0.001; T-F Basal vs. T-F 72 h, **P = 0.003; T-F 24 h vs. T-F 48 h, *P = 0.033. CXCR4 H-score comparison between T22-GFP-H6-FdU (T-F) and free oligo-FdU (F) (black line, panel A). *P*-values for statistical differences: T-F vs. F at 48 h, **P = 0.001; T-F vs. F at 72 h, *P = 0.034. Mann–Whitney *U*-test.

C, D   Significant reduction in the number of spheroid formed (C, optical microscope) and their bioluminescence emission (D, IVIS Spectrum 200), generated by 1 × 10^6 disaggregated cells (cultured in stem cell-conditioned media and low-adhesion plates), obtained from CXCR4$^+$ luciferase$^+$ SW1417 subcutaneous tumors, 24 h after 100 μg T22-GFP-H6-FdU intravenous doses, for 2 consecutive days, as compared to Buffer-treated or free oligo-FdU-treated mice. (D) Quantitation of the bioluminescent signal (BLI) expressed as average radiant intensity, obtained using the IVIS spectrum 200 equipment (N = 2 plates/group). Data expressed as mean ± s.e.m. Comparison of emitted BLI between groups: (B: Buffer; F: free oligo-FdU; T-F: T22-GFP-H6-FdU). *P*-values for statistical differences: T-F vs. B, **P = 0.001 (green line, panel D); F vs. B, *P = 0.011 (red line); T-F vs. F at *P = 0.02 (black line, panel D). Mann–Whitney *U*-test.

H6 or free oligo-FdU, using an orthotopic bioluminescent CXCR4$^+$ CRC model in *Swiss nude* mice, which generates lymph node (LN) and lung (LG) metastases (Mets), starting therapy 2 months after CRC cell implantation, given a 20 μg i.v. q3d dosage (Appendix Fig S5A). At the end of the regression of metastasis experiment, T22-GFP-H6-FdU-treated mice registered a lower number of LG Mets than free oligo-FdU, as measured by *ex vivo* bioluminescence emission (Appendix Fig S6A). This was confirmed by the finding of 3.0- and 2.9-fold reduction in total and mean LG foci number in histology sections of the T22-GFP-H6-FdU group as compared to free oligo-FdU (P = 0.04) mice (Appendix Fig S6B and C). T22-GFP-H6-FdU mice had a significantly lower number of LN Mets than Buffer-treated mice (P = 0.03); however, its effect was similar to that achieved by free oligo-FdU treatment.

T22-GFP-H6-FdU prevents hematogenous and transcelomic metastases in the SW1417 cell line-derived CRC model

We also evaluated T22-GFP-H6-FdU capacity to prevent metastasis as compared to free oligo-FdU, by registering the percent of mice with undetectable metastases at the end of treatment (Mets-free mice) and the reduction in number and size of Mets foci in mice with detectable metastases (Mets$^+$ mice) at the end of the experiment, using the CXCR4$^+$ SW1417 orthotopic bioluminescent CRC model, which metastasizes to lymph nodes (LN), liver (LV), lung (LG), and peritoneum (PTN), starting treatment 1 week after CRC implantation and following a schedule of 20 μg, q3d, 12 doses (Appendix Fig S5B).

At the end of the experiment, and in contrast to findings in Buffer or oligo-FdU groups, T22-GFP-H6-FdU treatment potently prevented hematogenous (LV and LG) and transcelomic (PTN) Mets development, whereas its capacity to prevent LN Mets was low. Thus, the percent of LV, LG, and PTN Mets-free mice after Buffer treatment was 45–55 and 27–64% for oligo-FdU, whereas T22-GFP-H6-FdU treatment increased significantly (P = 0.004) to reach 83% of Mets-free mice at all sites (Table 1 and Appendix Table S1). The differences in Mets-free mice between Buffer and oligo-FdU mice were not significant.

Consistently, in Mets$^+$ mice, T22-GFP-H6-FdU reduced the LV and LG Mets number, as measured by *ex vivo* bioluminescence compared to free oligo-FdU effect (data not shown). Moreover, a histological analysis of the foci number and size in LV, LG, and PTN Mets$^+$ mice at the end of treatment showed that T22-GFP-H6-FdU

mice had a 7.3- and 7.0-fold reduction in the total and mean PTN foci number (P = 0.0001), and a 2.4-fold reduction in PTN foci size (P = 0.01) as compared to free oligo-FdU (Appendix Fig S8A and Table 1). Similarly, T22-GFP-H6-FdU induced a 2.7- and 5.0-fold reduction in total and mean number of LV (P = 0.001) or LG (4.5- and 3.5-fold, P = 0.006) Mets as compared to free oligo-FdU, and only a mild effect on LN Mets. Importantly, free oligo-FdU did not reduce the total or mean Mets foci number at any site (LN, LV, LG, PTN), as compared to Buffer-treated animals (Appendix Fig S8A and Table 1).

T22-GFP-H6-FdU prevents hematogenous and transcelomic metastases in the M5 patient-derived CRC model

We, next assessed T22-GFP-H6-FdU capacity to prevent LN, LV, LG, and PTN Mets development in the CXCR4$^+$ M5 orthotopic CRC model, which shows higher metastatic efficiency at all sites (Table 1). To that aim, we measured all parameters described above in the SW1417 model and applied a schedule of 20 μg, q3d, per seven doses, starting 1 week after tumor cell implantation (Appendix Fig S5C). T22-GFP-H6-FdU treatment potently prevented LV, LG, and PTN Mets development, whereas its capacity to prevent LN Mets was low (Table 1). Thus, the percent of LV, LG, and PTN Mets-free mice was 0% after Buffer treatment and 15–30% after free oligo-FdU treatment, whereas T22-GFP-H6-FdU treatment significantly (P = 0.05) increased this effect to reach 38–63% of LV, LG, and PTN Mets-free mice. The differences between Buffer and oligo-FdU treatment were not significant (Table 1 and Appendix Table S1).

The histological evaluation of LV, LG, and PTN foci in Mets$^+$ mice at the end of treatment showed that T22-GFP-H6-FdU mice registered a 9.0- and 9.4-fold reduction in the total and mean LV foci number (P = 0.001), and 12.1-fold reduction in LV foci size (P = 0.007) as compared to free oligo-FdU (Fig 6A and Table 1). Similarly, T22-GFP-H6-FdU induced a 5.7- and 2.7-fold reduction in total and mean number of PTN (P = 0.022) or LG (2.4- and 2.8-fold, P = 0.003) Mets as compared to free oligo-FdU and having, and only a mild effect on LN Mets (Fig 6A and Table 1). Importantly, in contrast to T22-GFP-H6-FdU, free oligo-FdU did not reduce the total or mean Mets foci number at any site (LN, LV, LG, PTN), as compared to Buffer-treated animals (Fig 6A and Table 1).

In summary, repeated T22-GFP-H6-FdU administration potently prevented the development of hematogenous (LV and LG) and transcelomic (PTN) metastases yielding a 38–83% of Mets-free mice,
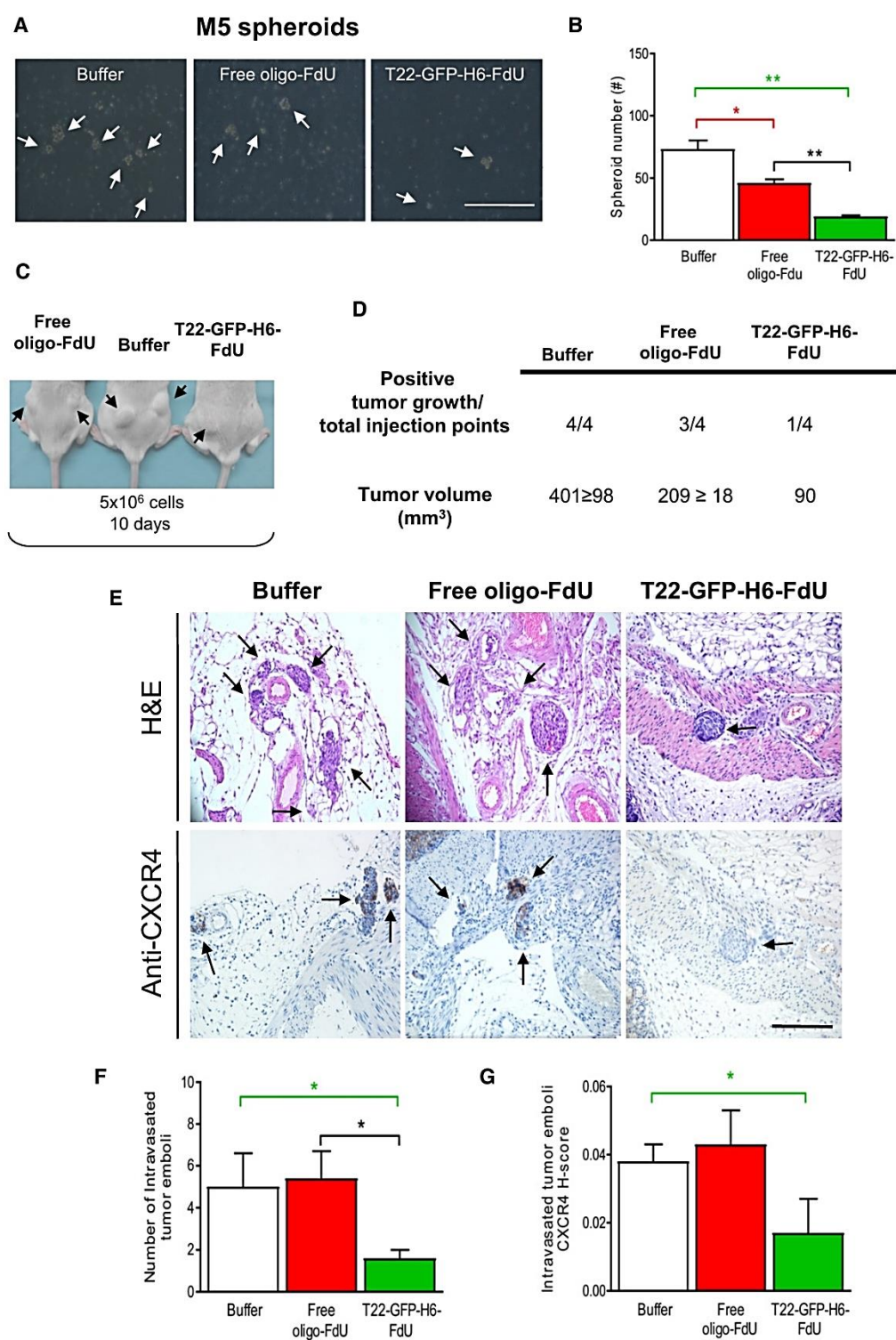

Figure 5.

168

Figure 5. T22-GFP-H6-FdU-induced reduction in tumor re-initiation capacity and blockade of tumor emboli intravasation in the CXCR4$^+$ patient-derived M5 model.

A, B   Reduction in the number of formed spheroids (white arrows, optical microscope) generated by 1×10^6 disaggregated cells (cultured in stem cell-conditioned media and low-adhesion plates) obtained from CXCR4$^+$ M5 subcutaneous tumors, 24 h after 100 μg T22-GFP-H6-FdU intravenous doses, for 2 consecutive days, as compared to Buffer-treated or free oligo-FdU-treated mice (mean ± s.e.m., $N = 8$; 2 mice/group; 4 plates/mouse). Scale bar, 100 μm. Comparison of spheroid formation between groups: (B: Buffer; F: free oligo-FdU; T-F: T22-GFP-H6-FdU). *P*-values for statistical differences: T-F vs. B, **$P = 0.001$ (green line, Panel B); F vs. B, *$P = 0.012$ (red line); T-F vs. F, **$P = 0.001$ (black line). Mann–Whitney *U*-test.

C, D   Reduction in tumor re-initiation capacity after subcutaneous inoculation of 5×10^6 cells in NSG mice ($N = 4$ tumors/group) derived from disaggregated tumor cells obtained from SC tumors 10 days after administration of 100 μg T22-GFP-H6-FdU intravenous doses, for 2 consecutive days, as compared to free oligo-FdU-treated or Buffer-treated mice. Recording of the number and size of positive tumors (black arrows, $N = 4$; 2 mice/group, 2 injection points/mouse).

E–G   (E) Representative images of tumor emboli intravasation determined by microscopic analyses of H&E-stained tumor sections ($N = 5$/group). (F) T22-GFP-H6-FdU-induced reduction in the number of intravasated tumor emboli (black arrows) in peri-tumoral vessels of the M5-orthotopic primary tumor (E: optical images; F: emboli number quantitation) and reduction in CXCR4 expression in these emboli (G), treated 7 days after tumor cell implantation with 100 μg T22-GFP-H6-FdU intravenous doses, for 2 consecutive days, as compared to Buffer-treated or free oligo-FdU-treated mice. Tumor emboli counting in 10 high-power field at 200× magnification in H&E-stained sections from each tumor (mean ± s.e.m., $N = 5$/group). Comparison of tumor emboli number between groups: (B: Buffer; F: free oligo-FdU; T-F: T22-GFP-H6-FdU). *P*-values for statistical differences: T-F vs. B, *$P = 0.038$ (green line), T-F vs. F, *$P = 0.016$ (black line). Scale bar, 100 μm. (G) CXCR4 expression per tumor emboli determined by using anti-CXCR4 IHC and calculating H-score (multiplying percent of CXCR4$^+$ cells out of total cell number in the emboli area by their staining intensity, scoring each from 0 to 3 (where 3 is the maximal intensity) per tumor emboli area (mean ± s.e.m., $N = 5$ mice/group). Comparison of CXCR4 H-score between groups: (B: Buffer; T-F: T22-GFP-H6-FdU). *P*-values for statistical differences: T-F vs. B at *$P = 0.027$ (green line). Mann–Whitney *U*-test.

depending on the site and studied model. It also reduced significantly the number and/or size of LV, LG, and PTN foci in Mets$^+$ mice. Nevertheless, T22-GFP-H6-FdU was unable to block LN Mets development. In contrast, free oligo-FdU did not prevent metastases at any site. In addition, T22-GFP-H6-FdU was more potent than free oligo-FdU in inducing the regression of established LG Mets. Interestingly, both T22-GFP-H6-FdU and free oligo-FdU showed a similar inhibitory effect on primary tumor growth as measured by *in vivo* bioluminescence emission along time or *ex vivo* at the end of treatment, both in the prevention or regression of metastasis experiments (Appendix Figs S6A and B, and S7A–D).

Site-dependent CXCR4 regulation, T22-GFP-H6-FdU CXCR4$^+$ cell targeting, and antimetastatic effect

Based on the clear site-dependent antimetastatic potency achieved by T22-GFP-H6-FdU in the prevention of metastasis experiments (Fig 6A, Appendix Fig S8A, and Table 1), on its dependence on CXCR4 membrane expression for cell internalization (Fig 2E) and capacity to selectively kill CXCR4$^+$ cancer cells (Fig 3A and B), we investigated if CXCR4 expression after therapy correlated with the observed antimetastatic effect at the different sites.

We observed a site-dependent reduction in CXCR4$^+$ target cancer cell fraction (CXCR4$^+$ CCF) in Mets foci at the end of T22-GFP-H6-FdU treatment, as detected by anti-CXCR4 IHC, (and as compared to basal levels) which correlated with the antimetastatic effect at the different sites in both SW1417 and M5 patient-derived CRC models (Fig 6B, Appendix Fig S8B, and Table 1). The LV, LG, and PTN Mets, highly sensitive to T22-GFP-H6-FdU treatment in terms of increased percent of Mets-free mice and reduction in foci number and size in Mets$^+$ mice, reached the lowest level of CXCR4$^+$ CCF at the end of treatment at these sites. In contrast, in both the M5 and SW1417 models we observed only a low and non-significant reduction in CXCR4$^+$ CCF in the organs showing low sensitivity to T22-GFP-H6-FdU, such as the primary tumor or LN Mets (Fig 6B and C, and Appendix Fig S8B and C). Moreover, conversely to findings with to T22-GFP-H6-FdU, free oligo-FdU did not reduce CXCR4$^+$ CCF at any Mets site (Fig 6A and Appendix Fig S8A). Similarly, in the regression of metastasis experiment, we observed a CXCR4$^+$

CCF reduction in LG Mets and higher antimetastatic effect at this site than in LN Mets, which showed no reduction in CXCR4$^+$ CCF and poor response to T22-GFP-H6-FdU therapy (Appendix Fig S6C and D and Table 1).

Lack of T22-GFP-H6-FdU accumulation or toxicity in normal tissues

To estimate the T22-GFP-H6-FdU therapeutic window, we analyzed its biodistribution and induction of DNA damage and apoptosis in non-tumor tissues. T22-GFP-H6-FdU injection led to highly selective tumor tissue accumulation (Fig 2B) as measured by fluorescence emission, whereas uptake in CXCR4-positive (bone marrow or spleen) or CXCR4-negative (kidney, lung, brain, heart or liver) normal tissues was undetectable, except for a transient accumulation in the liver (Fig 7A), in the same experiment. Moreover, the number of cells containing DSBs, detected by anti-γ-H2AX IHC, in normal bone marrow 5 h after T22-GFP-H6-FdU treatment (6.1 ± 1.2) was significantly lower ($P = 0.047$) than in free oligo-FdU-treated mice (11.4 ± 0.9; Fig 7B), whereas DSB-positive cells in normal liver or kidney were similarly low in all compound-treated groups or Buffer-treated animals. Moreover, DSBs induction did not lead to apoptosis or histological alteration in any group, since no histological alterations were detected in bone marrow, liver, or kidney 24 h post-administration (Fig 7C). Therefore, consistently with the negligible nanoconjugate distribution to normal tissues, the lack of detectable apoptosis or histological alterations in all analyzed tissues, including bone marrow or circulating blood monocytes (Appendix Fig S9), the lack of mouse body weight loss in the regression or prevention (Fig 7D–F) of metastases experiments, and the absence of any sign of clinical toxicity indicate a wide therapeutic index for T22-GFP-H6-FdU at a dosage that achieves potent antimetastatic effect.

Discussion

The identification of CXCR4$^+$ tumor cells as metastasis stem cells (MetSCs) (Oskarsson *et al*, 2014) in colorectal cancer (CRC; Croker

Table 1. T22-GFP-H6-FdU antimetastatic effect, observed in the prevention of metastasis experiments in the SW1417 and M5 CRC metastatic models, measured as percent of mice free of metastases at the end of treatment and as reduction in mean foci number and foci size in metastasis-positive mice[†].

Prevention of metastasis protocol

SW1417 cell line-derived orthotopic model

Groups	Lymph node Mets (LNm)		Liver Mets (LVm)		Lung Mets (LGm)		Peritoneal Mets (PTNm)	
	% Mice free of LN Mets	Foci # in Mets[+] mice	% Mice free of LV Mets	Foci # in Mets[+] mice	% Mice free of LG Mets	Foci # in Mets[+] mice	% Mice free of PTN Mets	Foci # in Mets[+] mice
Buffer	0%	3.7 ± 0.3^a	64%	0.7 ± 0.3^b	27%	6.6 ± 1.5^d	36%	2.0 ± 0.6^f
Free oligo-FdU	0%	3.1 ± 0.4	45%	1.0 ± 0.3^c	45%	4.5 ± 1.6^e	55%	2.8 ± 1.0^g
T22-GFP-H6-FdU	25%	2.0 ± 0.4^a	83%	$0.2 \pm 0.1^{b,c}$	83%	$1.3 \pm 0.9^{d,e}$	83%	$0.4 \pm 0.3^{f,g}$

Metastatic Foci size[‡] ($\mu m^2 \times 10^{-3}$)

Groups	Lymph node Mets (LNm)	Liver Mets (LVm)	Lung Mets (LGm)	Peritoneal Mets (PTNm)
Buffer	110.7 ± 15.5^o	11.2 ± 3.4	21.2 ± 1.3^p	435.7 ± 67.2^q
Free oligo-FdU	77.0 ± 14.2^o	9.6 ± 2.3	17.9 ± 1.6	304.8 ± 22.3^r
T22-GFP-H6-FdU	79.3 ± 11.1	8.7 ± 2.6	15.1 ± 2.2^p	$126.6 \pm 18.7^{q,r}$

M5 patient-derived orthotopic model

Groups	Lymph node Mets (LNm)		Liver Mets (LVm)		Lung Mets (LGm)		Peritoneal Mets (PTNm)	
	% Mice free of LN Mets	Foci # in Mets[+] mice	% Mice free of LV Mets	Foci # in Mets[+] mice	% Mice free of LG Mets	Foci # in Mets[+] mice	% Mice free of PTN Mets	Foci # in Mets[+] mice
Buffer	0%	50.0 ± 18.4^h	0%	10.5 ± 2.5^i	0%	19.5 ± 7.1^k	0%	$40.0 \pm 11.4^{l,m}$
Free oligo-FdU	0%	39.6 ± 14.6	15%	7.5 ± 2.7^j	30%	16.2 ± 6.9	15%	$19.7 \pm 8.4^{l,n}$
T22-GFP-H6-FdU	0%	22.7 ± 4.1^h	63%	$0.8 \pm 0.5^{i,j}$	50%	5.8 ± 2.4^k	38%	$7.2 \pm 1.8^{m,n}$

Metastatic Foci size[‡] ($\mu m^2 \times 10^{-3}$)

Groups	Lymph node Mets (LNm)	Liver Mets (LVm)	Lung Mets (LGm)	Peritoneal Mets (PTNm)
Buffer	$1,749.4 \pm 434.7$	20.0 ± 6.1^s	10.8 ± 1.5	$3,603.3 \pm 976.6$
Free oligo-FdU	$1,808.4 \pm 289.2$	38.7 ± 11.7^t	7.7 ± 0.9^u	$3,665.6 \pm 589.2$
T22-GFP-H6-FdU	$1,752.2 \pm 426.3$	$3.2 \pm 0.7^{s,t}$	10.2 ± 1.4^u	$3,057.7 \pm 1,415.4$

Mean + s.e.m. metastatic foci number per mouse counted in three randomly chosen histology sections.
Free oligo-FdU: equimolecular doses of free oligo-FdU.
[†]See Appendix Table S1 for detailed data on metastasis-free mice and statistical analysis.
[‡]Mean + s.e.m. metastatic foci area (μm^2) per mouse counted in three randomly chosen histology sections.
[a]$P = 0.04$; [b]$P = 0.01$; [c]$P = 0.001$; [d]$P = 0.002$; [e]$P = 0.006$; [f]$P = 0.002$; [g]$P = 0.006$; [h]$P = 0.006$; [i]$P = 0.001$; [j]$P = 0.001$; [k]$P = 0.003$; [l]$P = 0.015$; [m]$P = 0.001$;
[n]$P = 0.022$; [o]$P = 0.009$; [p]$P = 0.032$; [q]$P = 0.002$; [r]$P = 0.01$; [s]$P = 0.02$; [t]$P = 0.007$; [u]$P = 0.017$.

& Allan, 2008; Zhang *et al*, 2012; Murakami *et al*, 2013; Wang *et al*, 2014) allowed us to evaluate the clinical relevance of targeting CRC MetSCs by assessing whether their selective elimination induces antimetastatic activity. Our nanotechnology approach achieved the goal of targeted drug delivery (Das *et al*, 2009) to MetSCs by taking advantage of their membrane CXCR4 overexpression, as compared to normal tissues (Kim *et al*, 2005, 2006; Schimanski *et al*, 2005). The T22-GFP-H6-FdU nanoconjugate replicates the nanoparticle capacities for self-assembling, lack of renal filtration, high re-circulation in blood, and selective internalization in target CXCR4$^+$ cells, which we described for T22-GFP-H6 (Unzueta *et al*, 2012a,b, 2015; Rueda *et al*, 2015; Céspedes *et al*, 2016) adding the ability to

transport and intracellularly release FdU, which induces an increase in genotoxic damage and apoptosis, leading to selective CXCR4$^+$ cancer cell elimination as well as to a reduction in tumor re-initiation capacity.

The nanoconjugate achieved potent and site-dependent metastasis prevention, since its administration generated a significantly higher percent of Mets-free mice at the end of treatment, and a significant reduction in metastatic foci number and size. These effects associated with a reduction in CXCR4$^+$ target cancer cell fraction in tumor tissue, being both the antimetastatic effect and the reduction in CXCR4$^+$ CCF highly significant in LV, LG, and PTN Mets, whereas they were non-significant in primary tumor or LN
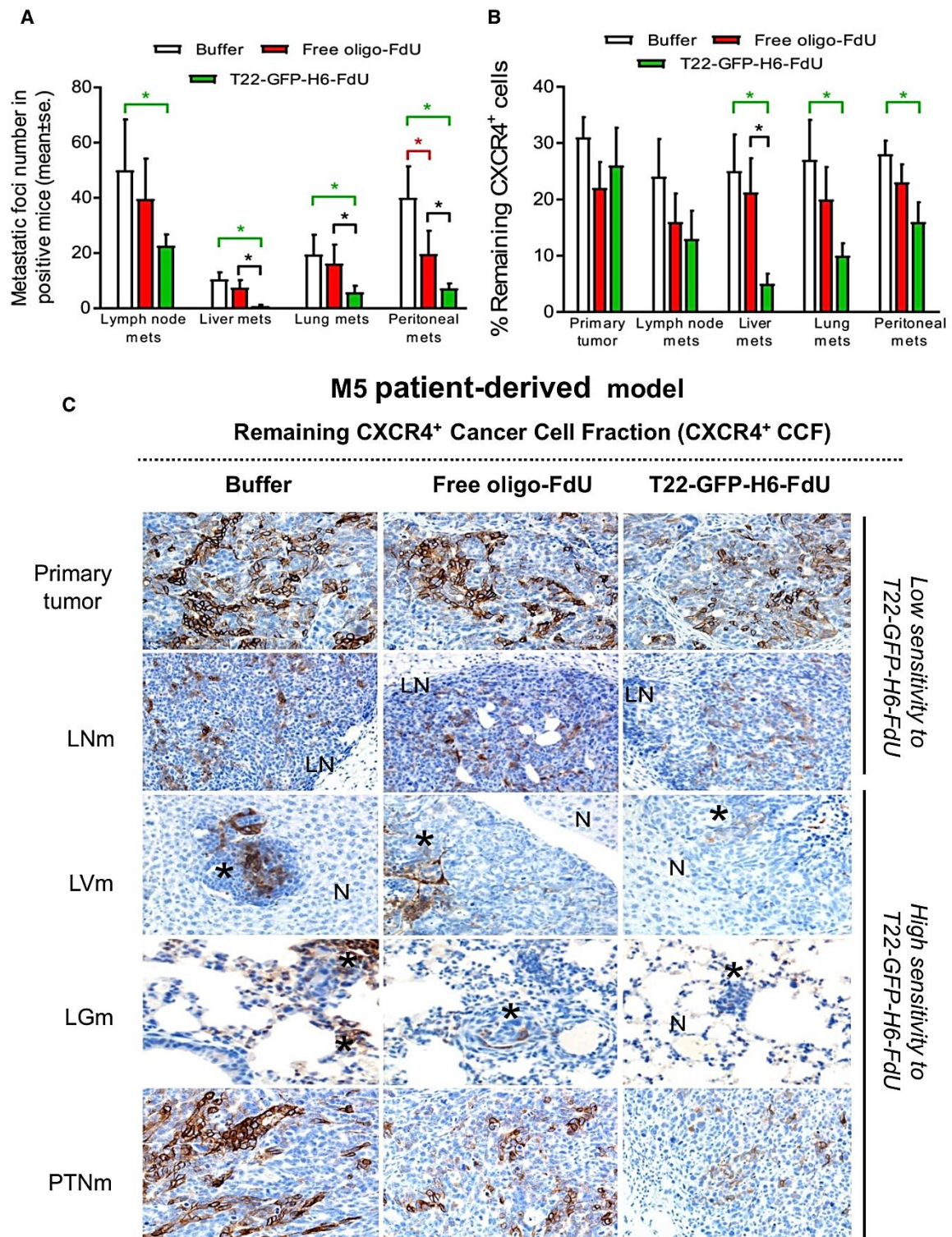
170

M5 patient-derived model

Remaining CXCR4⁺ Cancer Cell Fraction (CXCR4⁺ CCF)

Figure 6.

171

MetSCs killing as antimetastatic therapy   *María Virtudes Céspedes et al*

Figure 6. T22-GFP-H6-FdU prevents metastasis in the M5 patient-derived model in a CXCR4-dependent manner.

A   T22-GFP-H6-FdU prevents metastases in the CXCR4^{+} patient-derived M5 model by potently reducing the total and mean number of liver, lung, and peritoneal Mets, as recorded in H&E-stained histology sections at the end of treatment, in comparison with free oligo-FdU or Buffer treatment. In contrast, the number of LN Mets is not reduced after T22-GFP-H6-FdU or free oligo-FdU administration (N = 6 mice per Buffer group; N = 7 mice per free oligo-FdU group; and N = 8 mice per T22-GFP-H6-FdU group; 3 samples/mouse). Data expressed as mean ± s.e.m. Comparison of metastatic foci number by site between groups: (B: Buffer; F: free oligo-FdU; T-F: T22-GFP-H6-FdU). P-values for statistical differences: T-F vs. B: *P = 0.006 for LN Mets; *P = 0.001 for LV Mets; *P = 0.003 for LG Mets; *P = 0.001 for PTN Mets (green lines), F vs. B: *P = 0.015 for PTN Mets (red line), T-F vs. F: *P = 0.001 for LV Mets, *P = 0.022 for PTN Mets (black line). Mann–Whitney U-test. See Table 1 for the recording of the percent of metastasis-free mice (mice with undetectable metastases at the end of treatment, and therefore with an absence of CXCR4^{+} tumor cells) after T22-GFP-H6-FdU treatment. Also, Table 1 describes the reduction in mean foci number and foci size in metastasis-positive mice after T22-GFP-H6-FdU treatment, as compared to Buffer or free oligo-FdU.

B   T22-GFP-H6-FdU induces a higher reduction in CXCR4^{+} cancer cell fraction (CXCR4^{+} CCF) in liver, lung, and peritoneal metastatic tissue, at the end of treatment, than free oligo-FdU, as measured by anti-CXCR4 IHC. In contrast, T22-GFP-H6-FdU or free oligo-FdU does not reduce the CXCR4^{+} CCF in LN Mets or primary tumor tissue after therapy (N = 6 mice per Buffer group; N = 7 mice per free oligo-FdU group; and N = 8 mice per T22-GFP-H6-FdU group; 3 samples/mouse). Data expressed as mean ± s.e.m. Comparison of remaining CXCR4^{+} CCF by site between groups: (B: Buffer; F: free oligo-FdU; T-F: T22-GFP-H6-FdU). P-values for statistical differences: T-F vs. B: *P = 0.012 for LV Mets, *P = 0.027 for LG Mets; *P = 0.038 for PTN Mets (green lines), T-F vs. F: *P = 0.013 for LV Mets (black line). Mann–Whitney U-test.

C   Representative CXCR4 IHC images of the reduction in CXCR4^{+} CCF induced by T22-GFP-H6-FdU (or its absence in free oligo-FdU mice) at the end of treatment, in the M5 patient-derived CRC model, which quantitation is reported in panel (B). In the M5 model, the highest reduction in foci number and size occurs in liver metastases, which show the highest reduction in CXCR4^{+} CCF. Note the correlation between the reduction in CXCR4^{+} CCF induced by T22-GFP-H6-FdU and its antimetastatic effect at each site, measured as number of liver, lung, or peritoneal Mets (Table 1) in the M5 metastatic CRC models [as it happens in the SW1417 model (Appendix Fig S8)]. Note in both Table 1 and Appendix Table S1 that 83% of mice in the T22-GFP-H6-FdU group remained free of liver, lung, or peritoneal metastases at the end of treatment in the SW1417 CRC model, whereas in the M5 CRC model these parameters were in the 38–63% range. Scale bar, 100 μm. Asterisks, tumor tissue; N, normal tissue; LN, lymphatic metastasis.

Mets. Thus, the repeated dose administration at the CXCR4 expression peak in tumors (q3d) achieved our goal of maintaining the CXCR4^{+} CCF absent, or low, leading to a complete elimination of Mets (achieving, therefore, a complete elimination of CXCR4^{+} cancer cells) in a portion of mice, in both cell line and patient-derived CCR models. Based on our previous findings of high T22-GFP-H6 nanoparticle internalization in high CXCR4-expressing PTN Mets and low internalization in low CXCR4-expressing LN Mets in CRC mouse models (Céspedes *et al*, 2016), our results suggest that the high T22-GFP-H6-FdU antimetastatic effect observed in peritoneal metastases may come from its high internalization in these foci, leading to high intracellular FdU concentration and DNA damage above DNA repair capacity, triggering in turn high cell killing and a reduction in foci number as well as in CXCR4^{+} CCF at the end of treatment. This is opposite to the observation of a low internalization of the nanoconjugate and lack of antimetastatic effect and no reduction in CXCR4^{+} CCF in primary tumor or LN Mets. These findings are reminiscent of the association between antitumor effect by inhibition of Bmi-1 self-renewal protein and reduction in the Bmi1^{+} CSCs fraction (Kreso *et al*, 2014), and identify the

CXCR4[+] CCF in cancer tissue as a possible marker for monitoring metastasis response to T22-GFP-H6-FdU therapy.

In sharp contrast, an equimolecular dosage of unconjugated FdU did not prevent metastases nor reduced the CXCR4^{+} CCF in metastatic tissue, which may relate to its unselective biodistribution, reaching low FdU concentration in MetSCs and triggering an insufficient level of DNA damage or apoptosis. Despite T22-GFP-H6-FdU also induced a higher level of regression of established LG Mets than free oligo-FdU and a similar effect on LN Mets, our results suggest that T22-GFP-H6-FdU may be more effective at blocking metastasis early, while disseminating from the primary tumor or during secondary organ colonization, than at inhibiting metastatic growth. The significant reduction in tumor emboli intravasation in peri-tumoral vessels observed in T22-GFP-H6-FdU-treated tumors supports this argument. This is also consistent with the functions described for CXCR4 during early metastatic dissemination, including tumor cell trafficking at the invasion front, intravasation, extravasation, or organ colonization in CRC, as described in other tumor types (Zeelenberg *et al*, 2003; Gassmann *et al*, 2009; Hernandez *et al*, 2011; Jin *et al*, 2012a,b; Wendel *et al*,

Figure 7. Negligible T22-GFP-H6-FdU biodistribution or toxicity on non-tumor tissues.

A   Undetectable T22-GFP-H6-FdU emitted fluorescence in normal tissues, except for a transient accumulation 5 h after a 100 μg dose in the liver, which disappears at 24 h. Liver emitted fluorescence is transient and significantly lower than the one registered in tumor tissue. Tumor/Liver ratio = 7.5 (see tumor intensity in Fig 2B, which was registered in the same experiment; N = 5 mice/group). Scale bar, 1 cm. Color key, radiant efficiency units.

B   Representative images depicting the level of DNA double-strand break (DSB) induction in histologically normal bone marrow 5 h after treatment, as measured by anti-γ-H2AX, which is higher in free oligo-FdU-treated mice than in T22-GFP-H6-FdU (P = 0.047). Low level of cells containing DSBs in histologically normal kidney after T22-GFP-H6-FdU or free oligo-FdU treatment, a finding occurring in all normal tissues analyzed (N = 50, 5 mice/group; 10 fields/mouse). Scale bar, 100 μm.

C   Representative images showing lack of histopathological alterations in H&E-stained tissue or apoptotic induction in H&E-stained samples of CXCR4^{+} (bone marrow) and CXCR4^{−} (brain, kidney, liver, lung, and heart) normal tissues 24 h after the administration of a 100 μg dose of T22-GFP-H6-FdU or an equimolecular dose of free oligo-FdU (N = 5/group). Note that the transient nanoconjugate distribution to liver or the DNA damage induced in bone marrow does not lead to cytotoxicity on these non-tumor tissues (N = 50, 5 mice/group; 10 fields/mouse). Scale bar, 100 μm.

D   Lack of differences in body weight among groups registered along time in the SW1417-derived CCR model and the regression of metastases protocol (mean ± s.e.m., N = 10 mice/group).

E   Lack of differences in body mouse weight among groups registered along time in the SW1417 cell line-derived model and the prevention of metastasis protocol [mean ± s.e.m., Buffer (N = 11; free oligo-FdU (N = 12), T22-GFP-H6-FdU (N = 12)].

F   Lack of differences in body mouse weight among groups registered along time in the M5 patient-derived model and the prevention of metastasis protocol [mean ± s.e.m., Buffer (N = 6); free oligo-FdU (N = 17); T22-GFP-H6-FdU (N = 8)].
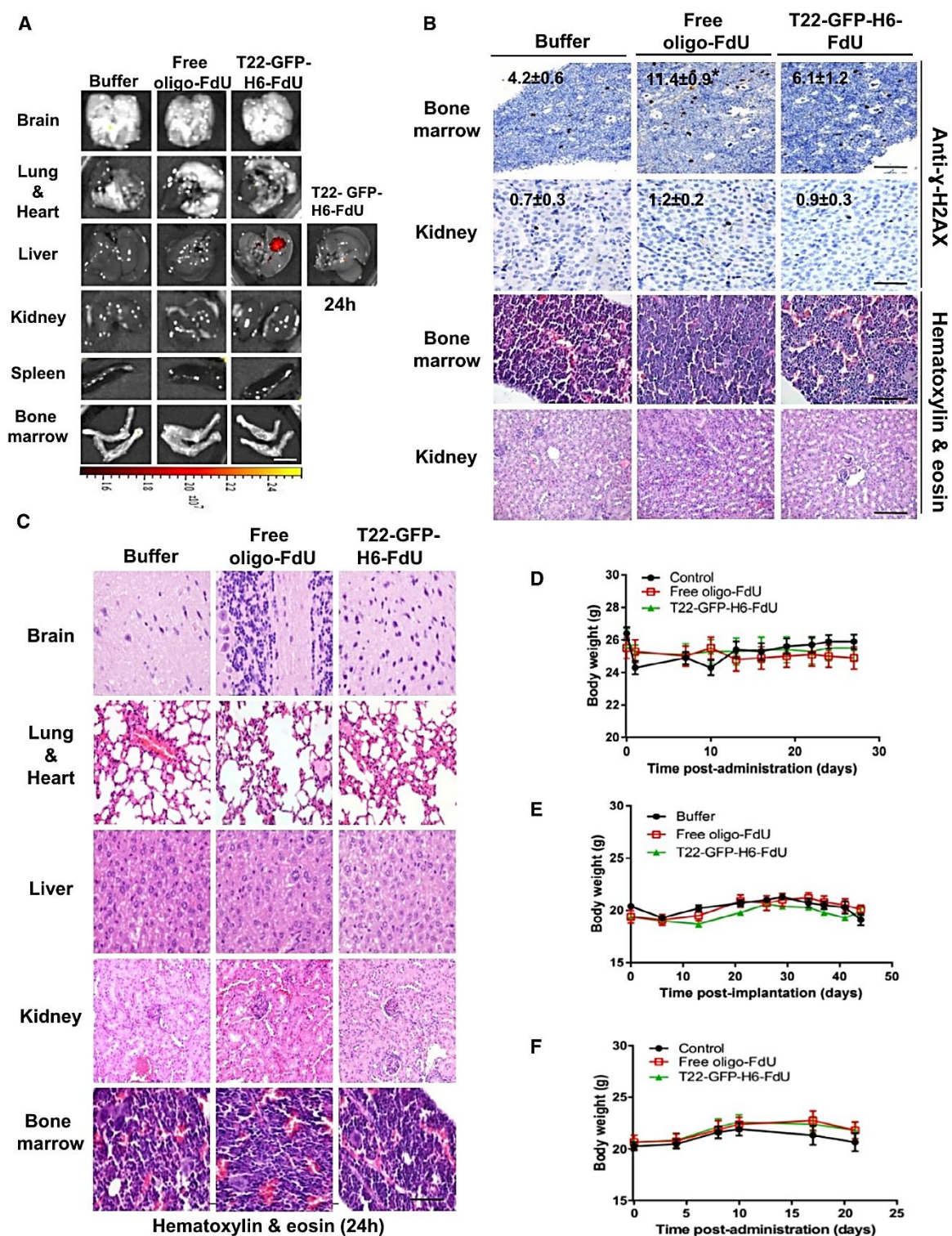
Figure 7.

2012). As expected, this nanoconjugate shows also low potency at controlling primary tumor growth, which relates to self-renewal rather than to cell trafficking (Steeg, 2016; Brabletz *et al*, 2005; Sleeman & Steeg, 2010; Oskarsson *et al*, 2014). This is also in agreement with CRC CD133$^+$CXCR4$^+$ CRC cells displaying CSC and MetSC capacities, whereas CD133$^+$ CXCR4$^-$ cells have only CSC capacity (Zhang *et al*, 2012), which further supports the notion that T22-GFP-H6-FdU selectively targets the subset of CXCR4$^+$ MetSCs rather than CSCs.

Our nanoconjugate displayed also a high therapeutic window, since we achieved selective CXCR4$^+$ tumor cell uptake and high antimetastatic effect while achieving negligible distribution (as reported for T22-GFP-H6; Céspedes *et al*, 2016) or histological alterations in normal tissues (expressing or not CXCR4) with no sign of toxicity or body weight lost. This is consistent with the very high level of CXCR4 expression in poor prognosis CRC (Kim *et al*, 2005, 2006; Schimanski *et al*, 2005) and other neoplasias (Fischer *et al*, 2008; Nimmagadda *et al*, 2009; van den Berg *et al*, 2011) in comparison with non-tumor tissues.

In summary, we demonstrated that targeted drug delivery to metastatic stem cells (MetSCs) aimed at their selective depletion is a clinically relevant and reachable therapeutic goal for metastasis control in CRC, with no associated toxicity, when using protein-based nanoconjugates such as T22-GFP-H6-FdU. To our knowledge, this is the first compound that achieves selective antimetastatic effect, which supports a change in drug development focus from primary tumor to metastasis control (Steeg & Theodorescu, 2008; Weber, 2013; Steeg, 2016) that is expected to highly enhance its clinical impact, considering that metastases continue causing most cancer deaths (Mehlen & Puisieux, 2006; Spano *et al*, 2012; Riihimäki *et al*, 2016). Our results support its use mostly in the neoadjuvant setting to achieve early-stage metastasis control in non-metastatic high-risk patients or in patients with limited disease as proposed (Steeg, 2012, 2016; Weber, 2013). We also expect to increase therapeutic precision in the use of the nanoconjugate by selecting candidate patients with high CXCR4 overexpression, who are likely to respond, and determining CXCR4$^+$ CCF along time to monitor their response to treatment. A similar therapeutic approach could be implemented for metastasis control in a variety of cancer types in which CXCR4$^+$ MetSCs associate with poor prognosis (Balkwill, 2004; Kucia *et al*, 2005; Hermann *et al*, 2007).

Materials and Methods

Synthesis of the T22-GFP-H6-FdU therapeutic nanoconjugate

T22-GFP-H6 is a protein nanoparticle produced in bacteria using a recombinant DNA strategy, as previously described (Unzueta *et al*, 2012a). The nanoconjugate was synthesized by covalent binding of the targeting vector and oligo-FdU, a pentameric oligonucleotide of Floxuridine (5-Fluoro-2′-deoxyuridine; Sigma-Aldrich Chemie GmbH, Steinheim, Germany), both functionalized before their conjugation. The oligo-FdU was functionalized with a thiol group as described in Appendix Fig S1, and T22-GFP-H6 was functionalized by reacting with the linker 4-maleimido hexanoic acid *N*-hydroxysuccinimide ester (Thermo Fisher, Waltham, MA, USA), following

the protocol for biofunctionalization of proteins described by Hermanson (2013). This linker binds the amino groups of the external lysines of the T22-GFP-H6 protein adding maleimido groups. The final T22-GFP-H6-FdU nanoconjugate was obtained reacting T22-GFP-H6 functionalized with maleimide and oligo-FdU-thiol (Michael reaction; Nair *et al*, 2014). The final reaction product was purified by dialysis, as previously described for T22-GFP-H6 (Unzueta *et al*, 2012b). The functionalization and physico-chemical characterization of oligo-FdU with thiol are described in Appendix Fig S1. The physico-chemical and functional characterization of the reaction products for the synthesis of T22-GFP-H6-FdU is described in Appendix Fig S2.

CXCR4 and SDF-1α expression in SW1417 cells

CXCR4$^+$ luciferase$^+$ SW1417 CRC cells expressing the luciferase reporter gene (derived from the parental SW1417 human colorectal cell line, ATCC® CCL238™, Manassas, VA, USA) were cultured in modified Eagle's medium (Gibco, Thermo Fisher, Waltham, MA, USA) supplemented with 10% fetal calf serum (Gibco) and incubated at 37°C and 5% CO$_2$ in a humidified atmosphere.

Fluorescence-activated cell sorting (FACS) analysis was performed in duplicate to verify cell surface expression of CXCR4. Briefly, one million CXCR4$^+$ luciferase$^+$ SW1417 cells were washed in phosphate-buffered saline containing 0.5% bovine serum albumin (PBS–BSA) and incubated for 30 min at 4°C with PE-Cy5 mouse anti-human CXCR4 monoclonal antibody or PE-Cy5 mouse IgG2a as an isotype control (BD Biosciences, Becton Dickinson, Franklin Lakes, NY, USA). Unbound antibody was removed by two washes with PBS–BSA. Data acquisition was performed using flow cytometry (FACSCalibur, Becton Dickinson, Franklin Lakes, NY, USA) and analyzed by Cell Quest Pro software.

To quantify SDF-1α release, 5×10^4 CXCR4$^+$ luciferase$^+$ SW1417 or 1BR3.G fibroblasts (SDF-1α-expressing cells used as control; ECACC, Cat. No. 90020507, Salisbury, UK cells) were cultured in DMEM with 10% FBS on a 24-well plate, for 48 or 72 h. Media was recovered at these times to measure their level of SDF-1α using a commercially SDF-1α ELISA kit (RayBiotech, Norcross, GA, USA). Experiments were performed in duplicate.

T22-GFP-H6-FdU internalization, CXCR4 specificity, and cytotoxicity in CXCR4$^+$ cells *in vitro*

We assessed the internalization capacity of the nanoconjugate by exposing CXCR4$^+$ luciferase$^+$ SW1417 cells for 1 h to 1 μM T22-GFP-H6-FdU concentration, treating them with 1 mg/ml trypsin (Gibco, Waltham, MA, USA) for 15 min, and measuring the green emitted fluorescence of the internalized nanoconjugate particles in the FACSCanto system cytometer (Becton Dickinson, Franklin Lakes, NJ, USA), using a 15 mW air-cooled argon ion laser at 488 nm excitation. Fluorescence emission was measured with a D detector (530/30-nm band-pass filter).

To assess specificity for CXCR4 receptor-mediated internalization, we performed competition studies incubating CRC SW1417 cells with the CXCR4 antagonist AMD3100 (Sigma-Aldrich, Saint Louis, MO, USA) in a 1:10 (protein:antagonist) molar ratio for 1 h before exposure to the nanoconjugate at 1 μM for an additional hour.

T22-GFP-H6-FdU subcellular localization was performed by culturing the cells in MatTek culture dishes (MatTek Co., Ashland, MA, USA); then, T22-GFP-H6-FdU was added in OptiPro medium supplemented with L-glutamine. The nuclei were labeled with 0.2 µg/ml Hoechst 33342 (Molecular Probes, Eugene, OR, USA) and the plasma membranes with 2.5 µg/ml CellMaskTM Deep Red (Molecular Probes, Eugene, OR, USA) for 10 min in the dark and washed in phosphate-buffered saline (Sigma-Aldrich). Live cells were recorded by TCS-SP5 confocal laser scanning microscopy (Leica Microsystems, Wetzlar, Germany) using a Plan Apo 63×/1.4 (oil HC × PL APO lambda blue) objective. To determine particle localization inside the cell, stacks of 10–20 sections for every 0.5 µm of cell thickness were collected and three-dimensional models were generated using Imaris version 7.2.1 software (Bitplane, Zurich, Switzerland).

Next, we studied T22-GFP-H6-FdU cytotoxic activity measuring cell viability and using the MTT metabolic test (Roche, Basel, Switzerland), following manufacturer recommendations. To that purpose, we exposed SW1417 CRC cells to T22-GFP-H6-FdU at 1.0–1,000 nM concentration range and measured their viability at 72 h as compared to equimolecular concentrations of T22-GFP-H6 or free oligo-FdU. We then construct a dose–response curve and determine the linearized T22-GFP-H6-FdU dose–response trend line for each compound.

Generation of CCR mouse models

Experiments were approved by the Mouse Ethics Committee at Hospital de la Santa Creu i Sant Pau.

We used three different CRC mouse models, one generated by subcutaneous CRC cell implantation to study nanoconjugate biodistribution and induction of CRC apoptosis, and two generated by orthotopic cell implantation to study the antimetastatic effect, either for prevention of metastases or regression of established metastases. To generate two of these models, we used 5-week-old *Swiss nude* mice, whereas in one model we used *NOD-SCID* mice. They were all female mice weighing 18–20 g (Charles River, L'Arbresle, France) and were housed in a sterile environment with bedding, water, and γ-ray-sterilized food *ad libitum*.

Subcutaneous (SC) mouse CRC model
We generated a subcutaneous CRC model injecting 1×10^7 CXCR4$^+$ luciferase$^+$ SW1417 human CRC cells (expressing luciferase to allow bioluminescence monitoring of tumor growth) re-suspended in 250 µl of media in the mouse flank. When tumors reached 700 mm^3 were excised and implanted SC tumor aliquots ($3 \times 3 \times 3$ mm) by the trocher system in a cohort of mice. SC model was used to assess tumor uptake, nanoconjugate internalization, and *in vivo* competition studies by co-administration of the CXCR4 antagonist AMD3100. It was also used to determine the induction of DNA double-strand breaks, tumor cell apoptosis, and the fraction of CXCR4$^+$ cancer cells remaining in tumor tissue (CXCR4$^+$ CCF) along time after treatment, as described below. These data were used to design the required dosage interval for the nanoconjugate repeated dose therapy in subsequent experiments aimed to determine its antimetastatic effect.

Orthotopic (ORT) CRC mouse model used to study regression of established metastases
Swiss nude mice were anesthetized with ketamine and xylazine, exteriorizing their cecum by a laparotomy. 2×10^6 CXCR4$^+$ luciferase$^+$ SW1417 CRC cells (expressing luciferase, to allow *ex vivo* bioluminescent identification of metastatic foci in affected organs) were suspended in 50 µl of modified Eagle's medium and loaded into a sterile micropipette. We slowly injected the cell suspension, under a binocular lens, with an approximate 30° angle, and its tip introduced 5 mm into the cecal wall (intracecal microinjection) as described (Céspedes *et al*, 2007). We sealed the entry injection point using BioGlue Surgical Adhesive (CryoLife Inc, Kennesaw, GA, USA) to avoid the reflux of implanted cells and to ensure that no seeding in the peritoneal wall occurred during the procedure. This model was used to evaluate the capacity of the T22-GFP-H6-FdU nanoconjugate to induce the regression of established metastases.

Orthotopic (ORT) CRC mouse model to study prevention of metastases
We generated an efficient metastatic model in *NOD/SCID* mice that received an intracecal microinjection (ORT) of CXCR4$^+$ luciferase$^+$ SW1417 CRC cells disaggregated from SC tumors previously generated in a different cohort of *NOD/SCID* mice. We also generated a highly efficient metastatic model in NSG mice that received an intracecal microinjection of M5 patient-derived CRC tumor cells disaggregated from SC tumors previously generated in a different cohort of NSG mice (SC + ORT models) as previously described (Alamo *et al*, 2014; Rueda *et al*, 2015). Briefly, when SC tumors reached a volume of 700 mm^3, mice were sacrificed by cervical dislocation and tumors were excised, discarding the necrotic areas, and 300 mg of viable tumor tissue was then cut into pieces and disaggregated in a mix of 0.05% trypsin (Invitrogen) and 100 mg/ml DNase (Sigma-Aldrich). The mix was pipetted 30 times, using a 10-ml pipette, and incubated for 10 min at 37°C with shaking. It was then re-pipetted 30 times, using 10-, 3-, and 1- pipettes, and re-incubated for 5 min at 37°C with shaking. The obtained SW1417 single-cell or M5 patient-derived cell suspensions were filtered through a cell strainer and centrifuged at 1,000 g for 10 min before counting the cells. We then microinjected 2×10^6 cells, previously grown in culture and re-suspended in 50 µl of media, in the cecum of each mouse. These models were used to evaluate the capacity of the T22-GFP-H6-FdU nanoconjugate to prevent metastasis development.

Evaluation of Spheroid formation capacity

To evaluate spheroid formation capacity after treatment, mice bearing SW1417 CXCR4$^+$ luciferase$^+$ or M5 patient-derived tumors were treated with 100 µg of T22-GFP-H6-FdU, the equimolar dose of free oligo-Fdu or vehicle for two consecutive days ($N = 2$ mouse/group). At 24 h post-treatment, tumors were excised and mechanically and enzymatically disaggregated with a mixture of collagenase IV (0.5 mg/ml) and DNAsa (0.1 mg/ml) in DMEM media at 37°C (Alamo *et al*, 2014). Isolated cells were cultured at 10^6 cells for 48 h in cancer stem cell media consisting in DMEM/F12, N2 supplement 1×, Hepes 1 M, L-glutamine, glucose 45% (Invitrogen, Carlsbad, CA, USA) Trace elements B and C (1/1,000×; VWR, Barcelona, Spain), 2 µg/ml heparine, 10 µg/ml insulin (Sigma-Aldrich), 0.02 µg/ml human EGF, 0.01 µg/ml human, and b-FGF (Peprotech, London, UK) and using T25 ultralow attachment surface coating flasks (Gibco) in order to minimize cell adherence. We measured spheroid formation by counting the number of spheroids generated from

isolated and cultured cells derived from treated tumors under a contrast phase microscope (200× of magnification) (N = 8; 2 mice/group; 4 plates/mice).

Evaluation of tumor re-initiation capacity

To assess tumor formation capacity after treatment, we inoculated 5 million cells per flank (right and left) in NSG mice that were obtained from the disaggregated M5 tumors generated in these mice after being treated with 100 μg T22-GFP-H6-FdU or the equimolar dose of FdU for two consecutive days (n = 4 tumors/group). We registered tumor burden at the point injection site every 2 days and tumor volume using a caliper, measuring the two perpendicular diameters [short diameter (S) and large diameter (L)] of each tumor and applying the following formula: Tumor volume = L*S^2/2.

T22-GFP-H6-FdU tumor uptake, tumor cell internalization, and induction of DNA damage and apoptosis *in vivo*

We used the SC CXCR4$^+$ SW1417 CRC model to assess the internalization of the T22-GFP-H6-FdU nanoconjugate into the cytosol of CXCR4$^+$ tumor cells after the administration of 100 μg T22-GFP-H6-FdU as an i.v. single bolus compared with Buffer, T22-GFP-H6 (untargeted nanoconjugate), and oligo-FdU (unconjugated free drug). Two, 5, and 24 h after the administration, we euthanized the mouse, resected the tumor, and registered *ex vivo* the intensity of the green fluorescence emitted by the nanoconjugate that had biodistributed to tumor tissue, using the IVIS® 200-Spectrum (PerkinElmer, Waltham, MA, USA). Following, we took tumor tissue samples and performed immunofluorescence (IF) and immunohistochemistry (IHC) to assess the presence or absence of the corresponding nanoconjugate in the membrane and/or cytosol of tumor cells using an anti-GFP antibody (1:300; Santa-Cruz Biotechnology, CA, USA). We also assess nanoconjugate CXCR4-dependence for internalization, as previously described for the T22-GFP-H6 nanoparticle in (Unzueta *et al*, 2012a).

The presence and localization of T22-GFP-H6-FdU nanoconjugate (detecting its GFP domain) were assessed by immunofluorescence labeling of formalin-fixed paraffin-embedded (FFPE) samples using standard protocols. Primary antibodies anti-CXCR4 (1:300, Abcam, Cambridge, UK) and anti-GFP (1:250, Abcam, UK) were incubated ON at 4°C. Then, we used the secondary antibodies: chicken IgG-Cy2 for GFP and rabbit IgG-Cy3 for CXCR4. Slides were then stained with DAPI (1:10,000 in TBS) for 10 min RT, rinsed with water, mounted, and analyzed under fluorescence microscope (405 nm, 488 Cy2 and 532/561 filters). Representative pictures were taken using confocal Leica TCS SPE at 200× or 600× magnifications. Immunofluorescence measurements were performed using the ImageJ software. Data were expressed as mean area ± s.e.m (μm^2) (N = 5 mice/group).

Once, we determined the specific internalization of T22-GFP-H6-FdU in CXCR4$^+$ cancer cells in tumor tissue, we assessed if this nanoconjugate also induced genotoxic damage and apoptosis in tumor tissue, before studying if both activities lead to CXCR4$^+$ cancer cell elimination. To that purpose, we treated the SC SW1417 mouse model, with a single 100 μg iv dose of T22-GFP-H6-FdU, or equimolar doses of T22-GFP-H6, free oligo-FdU, or Buffer. Five hours later, we sacrificed the mice and counted the number of cells containing double-strand breaks (DSBs) in tumor tissue, as assessed

by IHC using an anti-γ-H2AX mAb (1:400, Novus Biologicals, Cambridge, UK) as previously described (Kuo & Yang, 2008; Geng *et al*, 2010; Podhorecka *et al*, 2010). To that purpose, we counted the number of cells containing nuclei that stained positive for DSBs, using anti-γ-H2AX mAb IHC, in ten 400× magnification fields in one tumor section per mouse (N = 5 mice/group).

We also compared the capacity of T22-GFP-H6-FdU for apoptosis induction after the administration of an equimolecular dose of, T22-GF-H6, free oligo-FdU, or Buffer. Apoptotic signaling was assessed 5 h after treatment, by evaluation of cells positive for active cleaved caspase-3 as measured by IHC, whereas apoptotic induction was assessed 24 h after treatment, by counting the number of condensed or defragmented nuclei, after Hoechst staining. Both parameters were measured in ten 400× high-power magnification fields, in different sections from each tumor, using the Olympus DP73 digital camera.

Definition of the optimal dose interval by changes in CXCR4$^+$ tumor cell number after T22-GFP-H6-FdU administration

We also used the SC SW1417 mouse model, to determine the capacity of the nanoconjugate to induced DNA damage and apoptosis in tumor tissue, and its relationship with the kinetics of CXCR4 expression levels in the membrane of tumor cells after treatment, regarding the fraction of CXCR4 expressing tumor cells and their intensity, since CXCR4$^+$ are the target cells for the nanoconjugate. To that purpose 24, 48, and 72 h after the administration of a single i.v. bolus of 100 μg T22-GFP-H6-FdU, we euthanize the mice, took tumor samples, fix, and paraffin-embedded them to determine the levels and the percent of tumor cells expressing CXCR4 using IHC with an anti-CXCR4 antibody (1:300, Abcam, UK) as previously described (Céspedes *et al*, 2014). We used mice treated with equimolecular dosages of T22-GFP-H6, free oligo-FdU, or Buffer, in which we also determined the levels of CXCR4 expression in tumor tissue at the different times points. The results of the kinetics of CXCR4 expression in tumor cells were used to establish the optimal T22-GFP-H6-FdU nanoconjugate administration interval in the repeated dose schedule used to evaluate antimetastatic effect.

Evaluation of tumor emboli intravasation capacity in early metastatic experiment

We used the M5 patient-derived CRC model in *NSG* mice to evaluate the capacity of the nanoconjugate to block tumor emboli intravasation. NSG mice received an intracecal microinjection of M5 patient-derived CRC tumor cells (2 × 10^6) disaggregated from SC tumors as described in the above section. At day 7 post-inoculation, mice were treated with i.v. bolus of 100 μg T22-GFP-H6-FdU or the equimolar dose of free oligo-FdU or Buffer for two consecutive days and euthanized 24 h later (N = 5/group). The primary tumor was collected, fix, and paraffin-embedded for histopathology evaluation. Intravasated tumor emboli were determined by microscopic analysis under 200× magnification in H&E-stained primary tumor sections. We counted the vascular (blood or lymphatic) invasion by identifying tumor emboli that were invading an endothelium-lined vessel-like structure within the submucosa of the colonic wall, where a majority of vasa are located, and recording their number. Identification of

tumor emboli was done in H&E-stained tumor sections, under 200× magnification in each section, in five different mice per group. CXCR4 expression per tumor emboli was evaluated by using anti-CXCR4 IHC and calculating H-score (multiplying percent of CXCR4^{+} cells out of total cell number in the emboli area by their staining intensity), scoring each from 0 to 3 (where three is the maximal intensity) per tumor emboli area ($N = 5$ mice/group) using Cell^D Olympus software (v3.3.).

Treatment protocol for the evaluation of T22-GFP-H6-FdU induction of metastasis regression

We used the orthotopic and metastatic CRC model developed in *Swiss nude* mice to perform experiment of metastasis regression. We randomized 40 mice in a non-blinded manner into four groups: Buffer, T22-GFP-H6, T22-GFP-H6-FdU, and free oligo-FdU ($n = 10$/group) and administered repeated i.v. boluses at equimolecular doses, as follows: T22-GFP-H6-FdU: 20 µg, free oligo-FdU: 2.6 nmols, or Buffer, every 3 days (q3d) for a total of 10 doses. We initiated the T22-GFP-H6-FdU administration 2 months after tumor cell implantation, the time at which we determined, in previous experiments, that lymph node and lung metastases were present (see Appendix Fig S4). The experiment was finished when the first animal of the Buffer-treated group required to be euthanized. See below the studied parameters to evaluate the antimetastatic effect.

Treatment protocol for the evaluation of T22-GFP-H6-FdU metastasis prevention effect

We used the SC + ORT metastatic SW1417 CRC model developed in *NOD/SCID* or the M5 patient-derived CRC model in *NSG* mice to evaluate the capacity of the nanoconjugate for metastasis prevention. In each experiment, we non-blinded randomized mice into three groups: Buffer ($n = 7$–11), T22-GFP-H6-FdU ($n = 8$–12), and free oligo-FdU ($n = 7$–8) and administered repeated i.v. boluses at equimolecular doses, as follows: T22-GFP-H6-FdU: 20 µg; free oligo-FdU: 2.6 nmols; or Buffer), every 3 days (q3d) for a total of 12 doses in the SW1417 model or seven doses in M5 model. We initiated the T22-GFP-H6-FdU administration 1 week after tumor cell implantation before metastatic dissemination has occurred (see Appendix Fig S4). The experiment was finished when the first animal of the Buffer-treated-group required to be euthanized.

Evaluation of antimetastatic effect and determination of the CXCR4^{+} cancer cell fraction in tumor tissue at the end of treatment

At the end of both, the regression and the prevention of metastasis, experiments, we applied the same methodology to determine T22-GFP-H6-FdU antimetastatic effect. At necropsy, we recorded the number and size of visible metastasis in the organs where dissemination is expected in colorectal cancer (lymph nodes, liver, lung, and peritoneum) for each mouse in all compared groups. In the luciferase[+] SW1417-derived CRC model, we also counted *ex vivo* the number of metastatic foci that emitted bioluminescence in the target organs for metastasis, using the IVIS[®] 200-Spectrum (PerkinElmer).

We collected and processed samples for histopathological and immunohistochemical analyses. Two independent observers analyzed H&E-stained samples to count the number and measure the size of all observed metastatic foci in sections of each organ in each mouse. We used an Olympus microscope with the Cell^D Olympus software (v3.3) to take images and perform the measurements.

We determine CXCR4 expression in tumor tissue, using IHC with an anti-CXCR4 antibody, as described above, to determine the fraction of CXCR4^{+} cancer cells remaining in tumor tissue (CXCR4^{+} CCF) after treatment, including primary tumor and metastatic foci at the different organs affected by metastases (peritoneum, liver, lung, and lymph nodes). The obtained results were used to study a possible correlation between CXCR4^{+} CCF and antimetastatic effect at the different sites.

T22-GFP-H6-FdU biodistribution and toxicity in normal organs

We assessed T22-GFP-H6-FdU uptake measuring the green fluorescence emitted by the GFP domain of the nanoconjugate, as well as DNA DSBs and apoptotic induction in normal (non-tumor) tissues using the methodology described above. In addition, two independent observers evaluated the possible histopathological alterations observed in H&E-stained non-tumor tissue samples, searching for signs of toxicity. These tissues included CXCR4-expressing organs (despite expressing this receptor to a significantly lower level than in tumor tissue) where the nanoconjugate could accumulate such as the bone marrow and spleen and we also evaluated the toxicity in non-CXCR4 expressing organs, especially those in which the unconjugated oligo-FdU such as the liver.

Statistical analysis

Sample size was defined on the basis of previous preliminary experiments. Neither animals nor samples were excluded from the analyses. Randomization of animals into control and experimental groups was performed using the SPSS program. Histology and immunohistochemical samples were coded so that the researcher that analyzed them did not know to which group they belong to. Normal distribution of the data was tested using the Shapiro–Wilk test. The homogeneity of the variance between groups was tested using the Levene's test. We used the Fisher's exact test to analyze possible differences between control and experimental groups of affected mice regarding metastatic rates at the different organs. The nonparametric tests, Kruskal–Wallis, and *post hoc* pairwise Mann–Whitney U two-sided tests were used to compare number and size of metastatic foci in the affected organs among groups. All quantitative values were expressed as mean ± s.e.m. All statistical tests were performed using SPSS version 11.0 (IBM, New York, NY, USA). Differences among groups were considered significant at a $P < 0.05$.

Acknowledgements

MetSCs killing as antimetastatic therapy   *María Virtudes Céspedes et al*

The paper explained

Problem

In colorectal cancer (CRC), adjuvant therapy controls tumor progression and prolongs survival at the expense of high toxicity; however, metastases remain the primary cause of death. There is an urgent need to develop less toxic and more effective antimetastatic agents. CXCR4 receptor-overexpressing (CXCR4⁺) cells are metastatic stem cells (MetSCs) since they initiate metastases. Moreover, high CXCR4 tumor expression associates with metastatic dissemination and confers poor patient prognosis, a finding similar to other cancers. We hypothesized that a protein-based nanoconjugate (T22-GFP-H6-FdU) that selectively delivers the genotoxic drug Floxuridine (FdU) to CXCR4⁺ MetSCs will be antimetastatic.

Results

In contrast to free oligo-FdU, intravenous administration of T22-GFP-H6-FdU selectively accumulates and internalizes in CXCR4⁺ cancer cells, triggering DNA damage and apoptosis, which leads to the selective depletion of CXCR4⁺ MetSCs and to reduced tumor formation and spheroid formation. As compared to free oligo-FdU, repeated T22-GFP-H6-FdU administration, in cell line and patient-derived CRC mouse models, blocks CXCR4⁺ tumor emboli intravasation in colonic peritumoral vessels and completely prevents metastases development in a high percent of mice. In addition, this nanoconjugate induces CXCR4 expression-dependent and site-dependent reduction in foci number and size in liver, peritoneal, or lung metastases in the rest of mice. T22-GFP-H6-FdU induces also higher regression of established metastases than free oligo-FdU, with negligible biodistribution or toxicity in normal tissues, showing, therefore, a high therapeutic index.

Impact

The observation of a potent antimetastatic effect validates metastatic stem cells (MetSCs) as targets for clinical therapy. Moreover, to our knowledge, this protein-based nanoconjugate is the first compound that achieves a selective antimetastatic effect, which supports a change in drug development focus from primary tumor to metastasis control. This new approach is expected to highly enhance its clinical impact in CRC and other cancer types in which CXCR4 mediates metastasis development. Our results support the use of this nanomedicine in the neoadjuvant setting to achieve early-stage metastasis control in non-metastatic high-risk patients or in patients with limited disease as proposed. Its use could also increase therapeutic precision by selecting candidate patients with high CXCR4 overexpression, who are likely to be sensitive to the nanoconjugate, and determining CXCR4⁺ cancer cell fraction along time to monitor their response.

Author contributions

Conception and design: RM, AV, EV, MVC, and UU. Development of methodology: MVC, UU, AA, RE, AS-C, PA, RS, AG, IC, and MAM. Acquisition of data: MVC, UU, AA, EV, RS, PA, AG, and AS-C. Analysis and interpretation of data: RM, AV, RE, EV, MVC, UU, AA, IC, and AL-P. Writing of the manuscript: RM, AV, EV, RE, and MVC. Review and/or revision of the manuscript: UU, RE, IC, MAM, AS-C, PA, AG, RS, AA, and AL-P. Study supervision: RM, AV, and EV.

Conflict of interest

EV, UU, AV, MVC, IC, and RM are co-inventors of a patent (WO2012095527) covering the use of T22 as an intracellular targeting agent.

References

Alamo P, Gallardo A, Pavón MA, Casanova I, Trias M, Mangues MA, Vázquez E, Villaverde A, Mangues R, Céspedes MV (2014) Subcutaneous preconditioning increases invasion and metastatic dissemination in mouse colorectal cancer models. *Dis Model Mech* 7: 387–396

Balkwill F (2004) The significance of cancer cell expression of the chemokine receptor CXCR4. *Semin Cancer Biol* 14: 171–179

van den Berg NS, Buckle T, Kuil J, Wesseling J, van Leeuwen FW (2011) Immunohistochemical detection of the CXCR4 expression in tumor tissue using the fluorescent peptide antagonist Ac-TZ14011-FITC. *Transl Oncol* 4: 234–240

Brabletz T, Jung A, Spaderna S, Hlubek F, Kirchner T (2005) Migrating cancer stem cells-an integrated concept of malignant tumour progression. *Nat Rev Cancer* 5: 744–749

Céspedes MV, Espina C, García-Cabezas MA, Trias M, Boluda A, Gómez del Pulgar MT, Sancho FJ, Nistal M, Lacal JC, Mangues R (2007) Orthotopic microinjection of human colon cancer cells in nude mice induces tumor foci in all clinically relevant metastatic sites. *Am J Pathol* 170: 1077–1085

Céspedes MV, Unzueta U, Tatkiewicz W, Sánchez-Chardi A, Conchillo-Solé O, Álamo P, Xu Z, Casanova I, Corchero JL, Pesarrodona M *et al* (2014) *In vivo* architectonic stability of fully *de novo* designed protein-only nanoparticles. *ACS Nano* 8: 4166–4176

Céspedes MV, Unzueta U, Álamo P, Gallardo A, Sala R, Casanova S, Pavón MA, Mangues MA, Trías M, López-Pousa A *et al* (2016) Cancer-specific uptake of a liganded protein nanocarrier targeting aggressive CXCR4+ colorectal cancer models. *Nanomedicine* 12: 1987–1996

Chen F, Zhuang X, Lin L, Yu P, Wang Y, Shi Y, Hu G, Sun Y (2015) New horizons in tumor microenvironment biology: challenges and opportunities. *BMC Med* 13: 45

Croker AK, Allan AL (2008) Cancer stem cells: implications for the progression and treatment of metastatic disease. *J Cell Mol Med* 12: 374–390

Das M, Mohanty C, Sahoo SK (2009) Ligand-based targeted therapy for cancer tissue. *Expert Opin Drug Deliv* 6: 285–304

Fischer T, Nagel F, Jacobs S, Stumm R, Schulz S (2008) Reassessment of CXCR4 chemokine receptor expression in human normal and neoplastic tissues using the novel rabbit monoclonal antibody UMB-2. *PLoS One* 3: e4069

Gassmann P, Haier J, Schlüter K, Domikowsky B, Wendel C, Wiesner U, Kubitza R, Engers R, Schneider SW, Homey B *et al* (2009) CXCR4 regulates the early extravasation of metastatic tumor cells *in vivo*. *Neoplasia* 11: 651–661

Geng L, Huehls AM, Wagner JM, Huntoon CJ, Karnitz LM (2010) Checkpoint signaling, base excision repair, and PARP promote survival of colon cancer cells treated with 5-fluorodeoxyuridine but not 5-fluorouracil. *PLoS One* 6: e28862

Goswami S, Wang W, Arakawa T, Ohtake S (2013) Developments and challenges for mAb-based therapeutics. *Antibodies* 2: 452–500

Hermann PC, Huber SL, Herrler T, Aicher A, Ellwart JW, Guba M, Bruns CJ, Heeschen C (2007) Distinct populations of cancer stem cells determine tumor growth and metastatic activity in human pancreatic cancer. *Cell Stem Cell* 1: 313–323

Hermanson G (2013) *Bioconjugate techniques*, 3rd edn, pp 1200. London: Academic Press

Hernandez L, Magalhaes MA, Coniglio SJ, Condeelis JS, Segall JE (2011) Opposing roles of CXCR4 and CXCR7 in breast cancer metastasis. *Breast Cancer Res* 13: R128

Jin F, Brockmeier U, Otterbach F, Metzen E (2012a) New insight into the SDF-1/CXCR4 axis in a breast carcinoma model: hypoxia-induced endothelial SDF-1 and tumor cell CXCR4 are required for tumor cell intravasation. *Mol Cancer Res* 10: 1021–1031

Jin K, Gao W, Lu Y, Lan H, Teng L, Cao F (2012b) Mechanisms regulating colorectal cancer cell metastasis into liver. *Oncol Lett* 3: 11–15

Kim J, Takeuchi H, Lam ST, Turner RR, Wang HJ, Kuo C, Foshag L, Bilchik AJ, Hoon DS (2005) Chemokine receptor CXCR4 expression in colorectal cancer patients increases the risk for recurrence and for poor survival. *J Clin Oncol* 23: 2744–2753

Kim J, Mori T, Chen SL, Amersi FF, Martinez SR, Kuo C, Turner RR, Ye X, Bilchik AJ, Morton DL *et al* (2006) Chemokine receptor CXCR4 expression in patients with melanoma and colorectal cancer liver metastases and the association with disease outcome. *Ann Surg* 244: 113–120

Kreso A, van Galen P, Pedley NM, Lima-Fernandes E, Frelin C, Davis T, Cao L, Baiazitov R, Du W, Sydorenko N *et al* (2014) Self-renewal as a therapeutic target in human colorectal cancer. *Nat Med* 20: 29–35

Kucia M, Reca R, Miekus K, Wanzeck J, Wojakowski W, Janowska-Wieczorek A, Ratajczak J, Ratajczak MZ (2005) Trafficking of normal stem cells and metastasis of cancer stem cells involve similar mechanisms: pivotal role of the SDF-1-CXCR4 axis. *Stem Cells* 23: 879–894

Kuo LJ, Yang LX (2008) Gamma-H2AX. A novel biomarker for DNA double-strand breaks. *In Vivo* 22: 305–309

Longley DB, Harkin DP, Johnston PG (2003) 5-fluorouracil: mechanisms of action and clinical strategies. *Nat Rev Cancer* 5: 330–338

Mehlen P, Puisieux A (2006) Metastasis: a question of life or death. *Nat Rev Cancer* 6: 449–458

Müller A, Homey B, Soto H, Ge N, Catron D, Buchanan ME, McClanahan T, Murphy E, Yuan W, Wagner SN *et al* (2001) Involvement of chemokine receptors in breast cancer metastasis. *Nature* 410: 50–56

Murakami T, Kawada K, Iwamoto M, Akagami M, Hida K, Nakanishi Y, Kanda K, Kawada M, Seno H, Taketo MM *et al* (2013) The role of CXCR3 and CXCR4 in colorectal cancer metastasis. *Int J Cancer* 132: 276–287

Nair DP, Podgorski M, Chatani S, Gong T, Xi W, Fenoli CR, Bowman CN (2014) The Thiol-Michael addition click reaction: a powerful and widely used tool in materials chemistry. *Chem Mater* 26: 724–744

Nimmagadda S, Pullambhatla M, Pomper MG (2009) Immunoimaging of CXCR4 expression in brain tumor xenografts using SPECT/CT. *J Nucl Med* 50: 1124–1130

Oskarsson T, Batlle E, Massagué J (2014) Metastatic stem cells: sources, niches, and vital pathways. *Cell Stem Cell* 14: 306–321

Podhorecka M, Skladanowski A, Bozko P (2010) H2AX phosphorylation: its role in DNA damage response and cancer therapy. *J Nucleic Acids* 2010: 920161

Rhodes DR, Chinnaiyan AM (2005) Integrative analysis of the cancer transcriptome. *Nat Genet* 37(Suppl): S31–S37

Riihimäki M, Hemminki A, Sundquist J, Hemminki K (2016) Patterns of metastasis in colon and rectal cancer. *Sci Rep* 6: 29765

Rueda F, Céspedes MV, Conchillo-Solé O, Sánchez-Chardi A, Seras-Franzoso J, Cubarsi R, Gallardo A, Pesarrodona M, Ferrer-Miralles N, Daura X *et al* (2015) Bottom-up instructive quality control in the biofabrication of smart protein materials. *Adv Mater* 27: 7816–7822

Schimanski CC, Schwald S, Simiantonaki N, Jayasinghe C, Gönner U, Wilsberg V, Junginger T, Berger MR, Galle PR, Moehler M (2005) Effect of chemokine receptors CXCR4 and CCR7 on the metastatic behavior of human colorectal cancer. *Clin Cancer Res* 11: 1743–1750

Schimanski CC, Bahre R, Gockel I, Müller A, Frerichs K, Hörner V, Teufel A, Simiantonaki N, Biesterfeld S, Wehler T *et al* (2006) Dissemination of hepatocellular carcinoma is mediated via chemokine receptor CXCR4. *Br J Cancer* 95: 210–217

Schrag D (2004) The price tag on progress–chemotherapy for colorectal cancer. *N Engl J Med* 351: 317–319

Shi L, Zhao J, Lu Q, Chen X, Wang H, Jiang Y, Wu J, Ji M, Xu B, Chen L *et al* (2015) Initial hepatic artery infusion and systemic chemotherapy for asymptomatic colorectal cancer with un-resectable liver metastasis. *Int J Clin Exp Med* 8: 1000–1008

Sleeman J, Steeg PS (2010) Cancer metastasis as a therapeutic target. *Eur J Cancer* 46: 1177–1180

Spano D, Heck C, De Antonellis P, Christofori G, Zollo M (2012) Molecular networks that regulate cancer metastasis. *Semin Cancer Biol* 22: 234–249

Steeg PS, Theodorescu D (2008) Metastasis: a therapeutic target for cancer. *Nat Clin Pract Oncol* 5: 206–219

Steeg PS (2012) The right trials. *Nature* 485: S58–S59

Steeg PS (2016) Targeting metastasis. *Nat Rev Cancer* 4: 201–218

Sun X, Cheng G, Hao M, Zheng J, Zhou X, Zhang J, Taichman RS, Pienta KJ, Wang J (2010) CXCL12/CXCR4/CXCR7 chemokine axis. *Cancer Metastasis Rev* 29: 709–722

Takebayashi K, Mekata E, Sonoda H, Shimizu T, Shiomi H, Naka S, Endo Y, Tani T (2013) Differences in chemosensitivity between primary and metastatic tumors in colorectal cancer. *PLoS One* 8: e73215

Unzueta U, Ferrer-Miralles N, Cedano J, Zikung X, Pesarrodona M, Saccardo P, García-Fruitós E, Domingo-Espín J, Kumar P, Gupta KC *et al* (2012a) Non-amyloidogenic peptide tags for the regulatable self-assembling of protein-only nanoparticles. *Biomaterials* 33: 8714–8722

Unzueta U, Céspedes MV, Ferrer-Miralles N, Casanova I, Cedano J, Corchero JL, Domingo-Espín J, Villaverde A, Mangues R, Vázquez E (2012b) Intracellular CXCR4+ cell targeting with T22-empowered protein-only nanoparticles. *Int J Nanomedicine* 7: 4533–4554

Unzueta U, Céspedes MV, Vázquez E, Ferrer-Miralles N, Mangues R, Villaverde A (2015) Towards protein-based viral mimetics for cancer therapies. *Trends Biotechnol* 33: 253–258

Vignot S, Lefebvre C, Frampton GM, Meurice G, Yelensky R, Palmer G, Capron F, Lazar V, Hannoun L, Miller VA *et al* (2015) Comparative analysis of primary tumour and matched metastases in colorectal cancer patients: evaluation of concordance between genomic and transcriptional profiles. *Eur J Cancer* 51: 791–799

Wang TB, Hu BG, Liu DW, Shi HP, Dong WG (2014) The influence of lentivirus-mediated CXCR4 RNA interference on hepatic metastasis of colorectal cancer. *Int J Oncol* 44: 1861–1869

Weber GF (2013) Why does cancer therapy lack effective anti-metastasis drugs? *Cancer Lett* 2: 207–211

Wendel C, Hemping-Bovenkerk A, Krasnyanska J, Mees ST, Kochetkova M, Stoeppeler S, Haier J (2012) CXCR4/CXCL12 participate in extravasation of metastasizing breast cancer cells within the liver in a rat model. *PLoS One* 7: e30046

Zeelenberg IS, Ruuls-Van Stalle L, Roos E (2003) The chemokine receptor CXCR4 is required for outgrowth of colon carcinoma micrometastases. *Cancer Res* 63: 3833–3839

Zhang SS, Han ZP, Jing YY, Tao SF, Li TJ, Wang H, Wang Y, Li R, Yang Y, Zhao X *et al* (2012) CD133(+)CXCR4(+) colon cancer cells exhibit metastatic potential and predict poor prognosis of patients. *BMC Med* 10: 8

2) ANNEX 2: ARTICLE 2

FULL PAPER

Nanostructure Empowers Active Tumor Targeting in Ligand-Based Molecular Delivery

Hèctor López-Laguna, Rita Sala, Julieta M. Sánchez, Patricia Álamo, Ugutz Unzueta,* Alejandro Sánchez-Chardi, Naroa Serna, Laura Sánchez-García, Eric Voltà-Durán, Ramón Mangues,* Antonio Villaverde,* and Esther Vázquez

Cell-selective targeting is expected to enhance effectiveness and minimize side effects of cytotoxic agents. Functionalization of drugs or drug nano-conjugates with specific cell ligands allows receptor-mediated selective cell delivery. However, it is unclear whether the incorporation of an efficient ligand into a drug vehicle is sufficient to ensure proper biodistribution upon systemic administration, and also at which extent biophysical properties of the vehicle may contribute to the accumulation in target tissues during active targeting. To approach this issue, structural robustness of self-assembling, protein-only nanoparticles targeted to the tumoral marker CXCR4 is compromised by reducing the number of histidine residues (from six to five) in a histidine-based architectonic tag. Thus, the structure of the resulting nanoparticles, but not of building blocks, is weakened. Upon intravenous injection in animal models of human CXCR4⁺ colorectal cancer, the administered material loses the ability to accumulate in tumor tissue, where it is only transiently found. It instead deposits in kidney and liver. Therefore, precise cell-targeted delivery requires not only the incorporation of a proper ligand that promotes receptor-mediated internalization, but also, unexpectedly, its maintenance of a stable multimeric nanostructure that ensures high ligand exposure and long residence time in tumor tissue.

1. Introduction

Targeting of drugs for precision medicine is a widespread popular challenge, since proper drug biodistribution is expected to enhance effectiveness and minimize undesired side effects.[1] This is especially desirable regarding cytotoxic drugs, as those used in cancer, whose administration is associated to severe toxicities. It is assumed that functionalizing drugs or drug complexes with selective cell ligands would confer active targeting and ensure their accumulation in target cells and organs where such receptor is overexpressed. However, the biodistribution analyses of antibody drug conjugates and other similarly targeted drug constructs have repeatedly revealed that the fraction of administered agent reaching the target organ is limited to around 1%.[2] On the other hand, physical properties of drug vehicles such as surface charge, geometry, and size, among others, appear as key factors influencing the tissue accumulation

H. López-Laguna, Dr. J. M. Sánchez, Dr. N. Serna,
Dr. L. Sánchez-García, E. Voltà-Durán, Dr. A. Villaverde, Dr. E. Vázquez
Institut de Biotecnologia i de Biomedicina
Universitat Autònoma de Barcelona
Bellaterra, 08193 Barcelona, Spain
E-mail: antoni.villaverde@uab.cat

H. López-Laguna, Dr. J. M. Sánchez, Dr. N. Serna,
Dr. L. Sánchez-García, E. Voltà-Durán, Dr. A. Villaverde, Dr. E. Vázquez
Departament de Genètica i de Microbiologia
Universitat Autònoma de Barcelona
Bellaterra, 08193 Barcelona, Spain

H. López-Laguna, R. Sala, Dr. J. M. Sánchez, Dr. P. Álamo,
Dr. U. Unzueta, Dr. N. Serna, Dr. L. Sánchez-García, E. Voltà-Durán,
Dr. R. Mangues, Dr. A. Villaverde, Dr. E. Vázquez
CIBER de Bioingeniería
Biomateriales y Nanomedicina (CIBER-BBN)
C/ Monforte de Lemos 3–5, 28029 Madrid, Spain
E-mail: uunzueta@santpau.cat; rmangues@santpau.cat

The ORCID identification number(s) for the author(s) of this article can be found under https://doi.org/10.1002/ppsc.201900304.

R. Sala, Dr. P. Álamo, Dr. U. Unzueta, Dr. R. Mangues
Institut d'Investigacions Biomèdiques Sant Pau and Josep Carreras
Research Institute
Hospital de la Santa Creu i Sant Pau
08041 Barcelona, Spain

Dr. J. M. Sánchez
Universidad Nacional de Córdoba
Facultad de Ciencias Exactas
Físicas y Naturales. ICTA and Departamento de Química
Cátedra de Química Biológica. Córdoba. Argentina. CONICET
Instituto de Investigaciones Biológicas y Tecnológicas (IIBYT)
Córdoba, Argentina. Av. Velez Sarsfield 1611, X5016GCA
Córdoba, Argentina

Dr. A. Sánchez-Chardi
Departament de Biologia Evolutiva
Ecologia i Ciències Ambientals
Facultat de Biologia
Universitat de Barcelona
Av. Diagonal 643, 08028 Barcelona, Spain

ANNEXES

**ADVANCED
SCIENCE NEWS**
www.advancedsciencenews.com

Particle
& Particle Systems Characterization
www.particle-journal.com

pattern upon systemic administration when the delivery platform is based on passive targeting,[3,4] for instance by exploiting the enhanced permeability and retention (EPR) effect.[5] However, the weight of nanoscale properties of the material itself in determining biodistribution in presence of selective cell-ligands, that is, during active targeting, remains unsolved, despite its critical value in the design of new drug delivery systems. Combining efficient homing peptides with carrier materials in their optimal configuration might largely enhance the local accumulation in target tissues above the ≈1% threshold and thus increase precision and effectiveness in the delivery process.

To discriminate between the roles of the ligand and the architecture of the vehicle itself in the process of active tumor targeting, we have engineered the modular protein T22-GFP-H6 into related constructs and tracked selected resulting variants upon administration in animal models of human colorectal cancer. Such fusion protein is composed by T22, a potent ligand of the cell surface cytokine receptor CXCR4,[6] overexpressed in several metastatic human cancers,[7] a fully fluorescent GFP and a C-terminal polyhistidine tail. T22-GFP-H6 spontaneously self-assembles in physiological conditions as 12 nm nanoparticles, formed by around ten copies of the polypeptide, organized in a toroid architecture[8,9] and with some extent of structural flexibility.[9] The high selectivity of T22 for CXCR4 observed in cell culture[6] is fully kept in vivo.[10,11] When administered intravenously in orthotropic mice models of human CXCR4+ colorectal cancer the fluorescent nanoparticles accumulate in primary tumor and metastatic foci at unusually high levels, estimated to represent more than 85% of the whole-body detected fluorescence.[6] The accumulation of florescence in inhibited by SDF1-α, the natural ligand of CXCR4,[11] and it does not take place when T22 is absent in equivalent fusion proteins.[10] Used as a carrier of the cytotoxic drug floxuridine (FdU), the nanoconjugate T22-GFP-H6-FdU reduces the volume of primary tumor, prevents the development of metastasis, and precisely destroys already formed metastatic foci in absence of detectable systemic toxicity.[12] Similar antitumoral effectiveness has been observed when the nanoparticles deliver, accommodated in the building blocks by genetic fusion, proapoptotic factors, and other antitumoral peptides.[13]

Interestingly, the self-assembling of T22-GFP-H6 and related materials is driven by the overhanging polyhistidine tails that coordinate divalent cations from the media to promote stable cross-molecular protein interactions.[14] If the structure of the nanoparticle beyond the ligand itself, is relevant for precise targeting, destabilizing the supramolecular complex by modifying the histidine tail sequence would result in a potentially altered biodistribution map of the material, even if this material still contains the active CXCR4 ligand T22. The comparison of the fluorescence maps of T22-GFP-H6 and one of its less stable variants T22-GFP-H5T, once intravenously (iv) injected in colorectal cancer models, revealed that the presence of the targeting peptide T22 in the protein, although necessary for CXCR4-mediated cell binding,[6] is not sufficient for a proper tumor targeting. On the contrary, the nanoarchitecture of the material as an oligomeric supramolecular complex has a critical and unexpected impact on the fate, dynamics, and final accumulation of the material at the different organs, allowing the desired biodistribution upon administration. Therefore, nanoscale organization is an unexpected key determinant of not only passive but also active targeting.

2. Results

Being the H6 tail critical for nanoparticle formation,[15] this end-terminal peptide was replaced in T22-GFP-H6 by alternative histidine-rich peptides of similar length, with lower content of histidine (His) residues (**Table 1**). Since His residues promote the cross-molecular protein–protein interactions that sustain the architecture of the oligomers,[14] the reduction in the number of His residues was expected to generate less stable nanoparticles. Then, T22-GFP-H3A, T22-GFP-H5T, and T22-GFP-H5E fusions were designed, constructed, and expressed in bacteria as soluble protein versions, for comparison with the parental T22-GFP-H6. The alternative His-rich segments were selected according to previous reports indicating that His residues, intersected with hydrophobic or negatively charged residues, could be still retained in Ni^{+2}-based chromatography purification that uses His residues as binders.[16]

All proteins (the parental and the derived versions) were produced as proteolytically stable full-length forms of expected

Table 1. Main properties of T22-GFP His-rich protein nanoparticles carrying modified His tag sequences.

Protein[a]	Sequence[b,c,d]	M.M. [KDa]	S.F [units/mg] ± error	H.D. [nm]/PDI ± error	Z_p [mV] ± error	I.E. [× 10^{-3} M][e]	I.E. [%][f]
T22-GFP-H6	T22-*linker*-GFP-HHHHHH	30.69	9360.0 ± 198	11.7/0.361 ± 0.012	−17.2 ± 1.2	137.5 ± 2.5	100
T22-GFP-H3A	T22-*linker*-GFP-H<u>AA</u>H<u>A</u>H	30.49	12 003.9 ± 473	18.17/0.267 ± 0.006	−15.1 ± 0.59	84.2 ± 3.1	61.3
T22-GFP-H5T	T22-*linker*-GFP-H<u>T</u>H<u>T</u>H<u>T</u>H<u>T</u>H	30.96	15 121.8 ± 70	10.10/0.403 ± 0.010	−12.9 ± 0.32	119.2 ± 0.8	86.7
T22-GFP-H5E	T22-*linker*-GFP-H<u>E</u>H<u>E</u>H<u>E</u>H<u>E</u>H	31.07	10 920.2 ± 79	10.9/0.354 ± 0.043	−16.9 ± 2.1	94.0 ± 3.2	68.4

[a]The nomenclatures 6, 3, and 5 refer to the total number of His residues in the C-terminal tag and A, T, and E refer to alanine, threonine, and glutamic amino acids, respectively; [b]The sequence of T22 is MRRWCYRKCYKGYCYRKCR; [c]Underlined segments correspond to the amino acids introduced in the study; [d]The *linker* sequence is GGSSRSS; [e]The concentration (× 10^{-3} M) of imidazole needed to induce protein elution from immobilized metal ion affinity chromatography; [f]The above values (e) relative to that obtained when eluting T22-GFP-H6. M.M.: Molecular Mass | S.F.: Specific Fluorescence | H.D.: Hydrodynamic Diameter | PDI: Polydispersion Index | Z_p: Zeta Potential |, I.E.: Imidazole Elution.
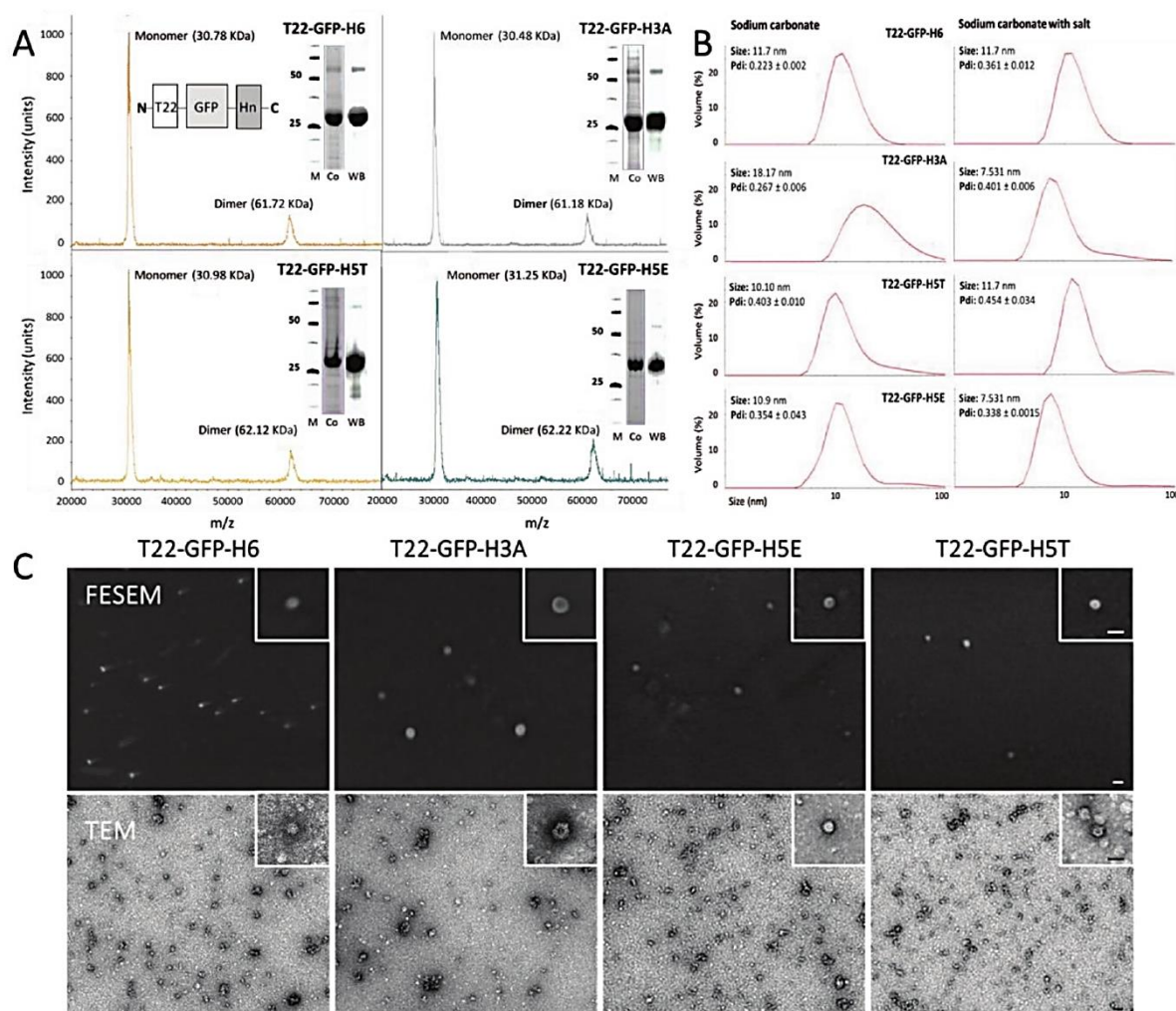
Figure 1. Physicochemical characterization of His-rich protein constructs. A) Mass spectrometry of purified samples indicating protein molecular weight of both monomeric and dimeric forms. Protein integrity was also assessed by Coomassie blue staining (Co) and anti-GFP Western Blot respectively. Numbers indicate molecular masses (in KDa) of markers. The inset illustrates the modular architecture of the polypeptides, Hn indicating tails with variable number of His residues. B) Size distribution of His-rich protein constructions dialyzed against standard sodium carbonate buffer with or without salt. Modal peak size (nm) and PDI (Polydispersity Index) mean ± standard error values are indicated. C) FESEM and TEM imaging of His-rich protein materials in sodium carbonate buffer. Representative images showing morphometry and architecture of the nanoparticles are displayed at two different magnifications for each technique. Scale bars represent 20 nm.

molecular masses (**Figure 1**A, Table 1), and the specific fluorescence emission values were of the same order of magnitude than that shown by T22-GFP-H6 (Table 1). This fact indicated that native-like conformation was reached in individual GFP-based building blocks. The purification by His-tag-based affinity chromatography was efficient in all cases, but the concentration of imidazole required to elute the proteins was different in each case (Table 1). It was lower, as expected, at lower His residue content. The H5T-tagged polypeptide was eluted at an imidazole concentration that represented 86% of that required by H6-tagged materials, indicating that the strength of His-divalent cation interactions was weakened down to this relative

level compared to the H6 tag. T22-GFP-H3A and T22-GFP-H5E required even less imidazole concentration for detachment from immobilized Ni^{+2}, representing 68% and 61% of that required for T22-GFP-H6, respectively (Table 1). This fact, and the resulting quantitative data about imidazole-mediated detachment, confirmed that the strength of His-based cross-molecular interactions can be regulated by the number of His residues in overhanging tags.

In this context, since the self-assembling of His-tagged T22-carrying nanoparticles is based on the ability of His residues to interact with each other's through divalent cations from the media, the quantitative reduction in the interactivity with Ni^{+2}

of the engineered proteins should be translated into nanoparticles less stable than T22-GFP-H6, if they were actually formed. When checking the self-assembling of the materials in the standard carbonate buffer, all proteins spontaneously formed nanoparticles (Figure 1B,C, Table 1), with hydrodynamic sizes and Z-potential values similar to those shown by the parental T22-GFP-H6 (Table 1). The microscopy scrutiny of all nanoparticles revealed a toroidal architecture (Figure 1C), compatible with the previously obtained molecular model of T22-GFP-H6.[8] However, when challenging the assembled materials with ionic strength, T22-GFP-H3A and T22-GFP-H5E, those with less molecular interactivity (Table 1), immediately disassembled into smaller materials with sizes compatibles with the dimeric form of GFP (around 7 nm, Figure 1B). This was indicative of weak cross-molecular interactions between building blocks. Instead, T22-GFP-H5T tolerated well the presence of salt in the media. However, this construct showed high instability during

freezing and thawing and it partially disassembled as structures smaller than 12 nm (**Figure 2**A), of size comparable to assembling intermediates described for T22-GFP-H6.[9] Some of these structures were also observed under transmission electron microscopy (TEM) (Figure 1C). These small forms appeared together with a minor occurrence of larger protein clusters, indicative of supramolecular instability (Figure 2A), and conformational impact linked to freezing and thawing-induced damage.[17] To further assess the differential stability between H6- and H5T-based nanoparticles, they were incubated for 24 h at 37 °C in human sera, to better reproduce the conditions of in vivo administration. As observed (Figure 2A), T22-GFP-H5T (but not T22-GFP-H6) nanoparticles dissociated under these conditions, confirming again the lower stability of the H5T material. Such weaker structural robustness was not due to defects in the folding of H5T building blocks, as thermal stability analysis indicated that both modular polypeptides were
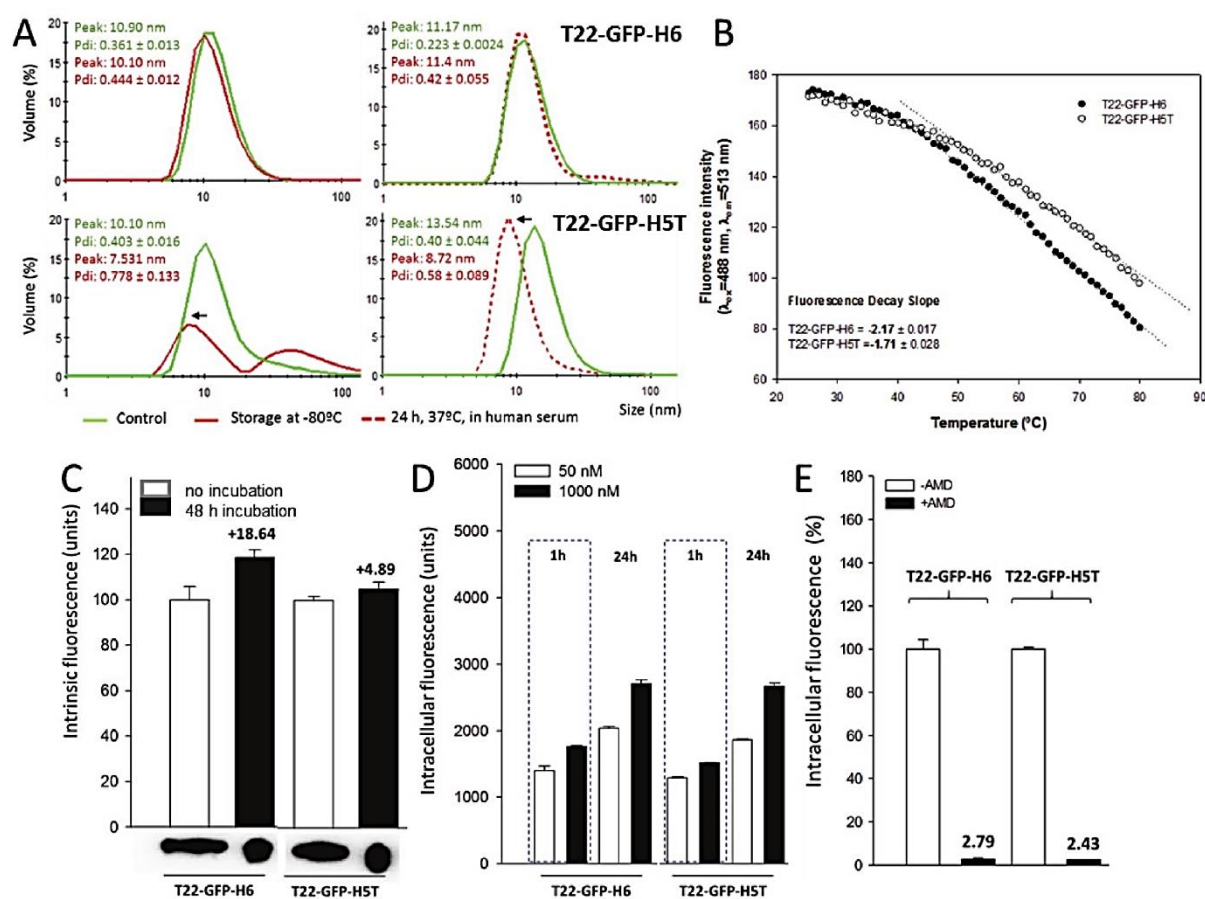

Figure 2. Structural and functional stability of protein nanoparticles. A) Size distribution of T22-GFP-H6 and T22-GFP-H5T nanoparticles upon purification and after storage at −80 °C, or upon incubation in human sera. Arrows indicate disassembling. Modal peak size (nm) and PDI (mean ± standard error) values are indicated. B) Decrease of chromophore fluorescence intensity (at 513 nm) of T22-GFP-H6 and T22-GFP-H5T versus temperature, measured at $\lambda_{ex} = 488$ nm. The slope decays from 50 to 80 °C was registered in the plot. C) Protein stability upon 48 h incubation in human serum at 37 °C. Fluorimetry (up) and western blot immunodetection (bottom) were used to determine protein integrity. Numbers indicated on top of plot bars represent variations of fluorescence intensity in percentage relative to original samples. D) Internalization of different amounts of protein nanoparticles in cultured HeLa cells, determined at 1 and 24 h postexposure. E) Inhibition of CXCR4+ cell binding mediated by the CXCR4 antagonist AMD3100.

equally stable (or even T22-GFP-H5T lightly more stable than T22-GFP-H6, Figure 2B). This was in agreement with the fluorescence data from Table 1.

In the light of these observations, we decided to comparatively determine the influence of nanoparticle stability on in vivo biodistribution by comparing T22-GFP-H6 and T22-GFP-H5T materials. Importantly, the modular polypeptides themselves, were both proteolytically resistant (Figure 1), structurally stable (Figure 2C), targeted to the tumoral marker CXCR4 through T22,[6,8,18] and only differ in a few structural amino acids at their C-termini. Also, the electrophoretic motility of these proteins did not change in serum, as well as their specific fluorescence (Figure 2C). All these data confirmed that despite the differences in the stability of the nanoparticles the building blocks were both structurally robust and competent. In addition, the interactivity between T22 and CXCR4

(Figure 2D) and the ability of the peptide to mediate receptor specific endosomal internalization of nanoparticles (Figure 2E) were fully confirmed in both constructs.

When both T22-GFP-H6 and T22-GFP-H5T were administered intravenously in mice bearing subcutaneous SP5 CXCR4$^+$ colorectal tumors, the accumulation pattern of both proteins in tumor was clearly divergent. While T22-GFP-H6 was progressively found in tumor (**Figure 3**A), with a plateau of fluorescence reached at 24 h, T22-GFP-H5T was only transiently found in tumoral tissues at 5 h postadministration, followed by a fast decline (Figure 3B). This might be indicative of lake or poor cell uptake in the tissue, through which the material appears to transiently pass by. Moreover, a background (off-target) fluorescence emission of T22-GFP-H5T was observed in liver and kidney, having an increase during the 24–48 h period postinjection, whereas T22-GFP-H6 emission during
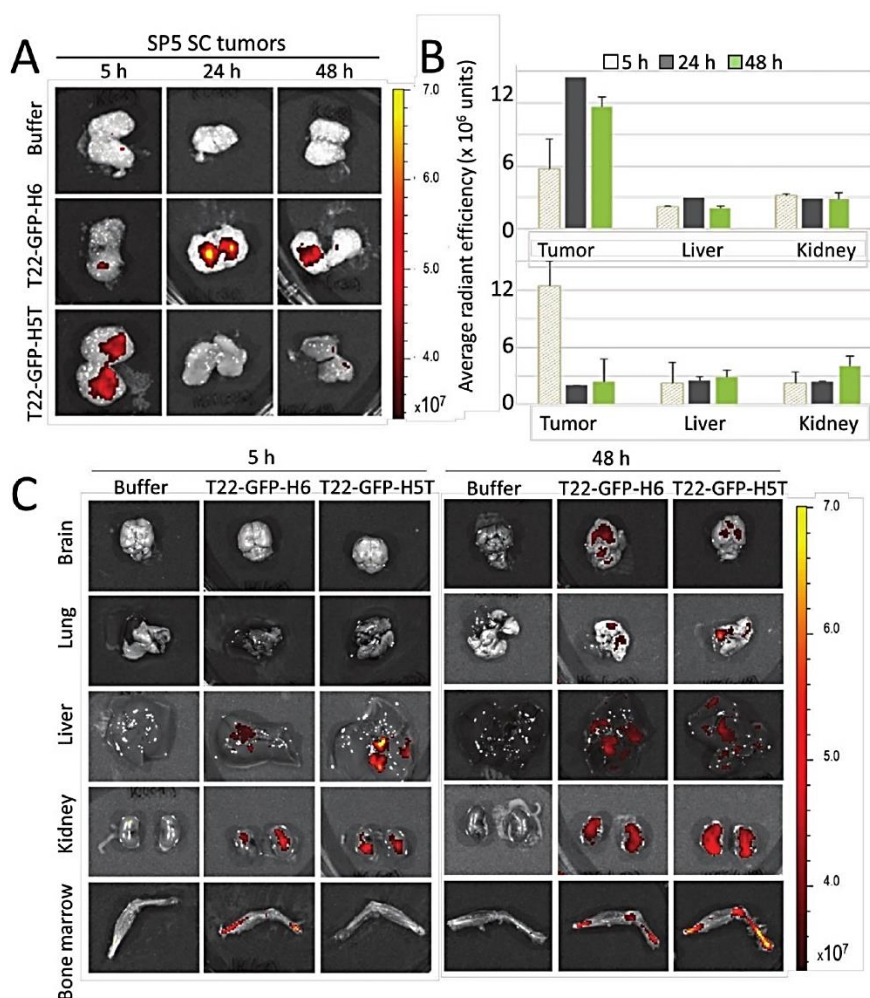

Figure 3. Tumor and nontumoral organ biodistribution of T22-GFP-H6 and T22-GFP-H5T. A) Representative ex vivo tumor fluorescence images (FLI) at 5, 24, and 48 h after iv administration of 100 µg dose of each protein nanoparticle in mice bearing subcutaneous SP5 CXCR4$^+$ colorectal tumors. B) Quantitation of GFP-emitted fluorescence in tumors, liver and kidney at 5, 24, and 48 h using the IVIS spectrum system. C) Representative ex vivo images of nanoparticle accumulation in normal mouse organs (brain, lung, liver, kidney, and bone marrow) at 5 and 48 h.
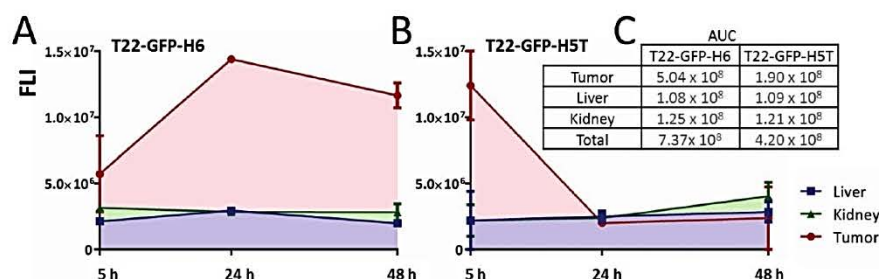
Figure 4. Comparison of tumor and nontumor exposure between T22-GFP-H6 and T22-GFP-H5T in tumor bearing mice. Representation of the area under the curve (AUC) of emitted fluorescence intensity (FLI) along time (5–48 h), as a measure of exposure, registered in tumors, liver, and kidney after 100 µg single dose injection of A) T22-GFP-H6 or B) T22-GFP-H5T proteins in CXCR4+ subcutaneous SP5 patient-derived mouse models. C) Percentage of protein accumulation (as measured by the AUC = FLI × hour) in tumor, liver, or kidney and total emission for both studied proteins. FLI signal from experimental mice was calculated subtracting the FLI auto-fluorescence of control buffer-treated mice. FLI, fluorescent intensity (expressed as average radiant efficiency).

this period was declining in these organs. The much more extensive and sustained T22-GFP-H6 tumor accumulation was clearly evidenced by the quantitative ex vivo analyses of relevant organs (Figure 3B). Thus, T22-GFP-H6 reached a tumor exposure (AUC = 5.04 × 10^8 emitted fluorescence intensity-FLI-units × hour) 2.7 fold higher than T22-GFP-H5T (AUC = 1.90 × 10^8) (**Figure 4**A,B, **Table 2**). Mostly, background signal was observed in other nontarget organs, except for T22-GFP-5HT in the 24–48 h period, which registered increases of 64% in the kidney and 14% in the liver (Figures 3C and 4B, Table 2). Consequently, T22-GFP-H6 had an AUC ratio tumor/(kidney+liver) of 2.2, while in T22-GFP-H5T this ratio was 0.8 (Figure 4C). Since the divergence in the biodistribution maps of the two tested related proteins is irrespective of the common N-terminal ligand (T22, binding CXCR4) but dependent on the amino acid sequence of the C-terminal architectonic peptide, we conclude that a multimeric organization of the modular proteins offers an appropriate nanoscale presentation of the ligand, with a geometry supporting its targeting function in the body.

3. Discussion

Two N-terminal homologous GFP modular proteins, namely T22-GFP-H6 and T22-GFP-H5T (Table 1), targeted to CXCR4

tumors, showed a very dissimilar biodistribution upon iv administration in mice models of human, CXCR4+ colorectal cancer (Figure 3). Both protein versions are proteolytically stable upon bacterial production (Figure 1) and upon incubation in human serum (Figure 2C), showing no loss, in any case, of relevant protein fragments that might abort the cell binding process. Both polypeptides are also highly fluorescent (Table 1), show robust structural stability (Figure 2B) and spontaneously assemble as regular nanoparticles of comparable size and physicochemical properties (Figure 1C, Table 1) that equally penetrate CXCR4+ cells in culture (Figure 2D). However, the minor sequence differences at the His-rich C-terminal peptide (Table 1), responsible for cross-molecular interactions and divalent cation-mediated nanoparticle formation[14] resulted weakened in T22-GFP-H5T relative to the parental T22-GFP-H6, to around 86% (Table 1). This is because of the reduction in the number of His residues in such architectonic peptide, from six to five, which minimizes the binding of the protein to divalent cations, including the Ni^{+2} of the purification columns (Table 1). Other two constructs with five and three His residues in the C-terminus, respectively, are not able to form nanoparticles in high salt buffer (Figure 1B), indicative of the inability of these agents to form stable interactions. Although in contrast, T22-GFP-H5T was stable in salt, long-term storage of this material at −80 °C and 24 h incubation in human serum

Table 2. Biodistribution kinetics of T22-GFP-H6 and T22-GFP-H5T proteins in tumor and nontumor organs.

Organs[a]	Groups					
	T22-GFP-H6			T22-GFP-H5T		
	5 h	24 h	48 h	5 h	24 h	48 h
Tumor	57.2 ± 28.7	144.3	116.5 ± 9.2	124.1 ± 26.2	20.1 ± 0.4	23.7 ± 23.7
Brain	26.5 ± 1.7	16.1	28.0 ± 1.7	21.8 ± 7.7	26.8 ± 5.6	23.9 ± 4.3
Lung and heart	5.6 ± 2.1	ND	10.9 ± 1.7	6.0 ± 0.9	5.0 ± 0.6	11.4 ± 1.5
Liver	21.2 ± 0.3	29.6	19.9 ± 2.0	22.1 ± 22.1	25.0 ± 4.1	28.6 ± 7.6
Kidney	31.6 ± 1.6	28.6	28.3 ± 6.3	22.1 ± 12.0	23.9 ± 0.7	40.4 ± 10.5
Bone marrow	10.9 ± 8.1	21.8	13.4 ± 0.9	2.5 ± 2.5	9.7 ± 6.7	17.4 ± 1.2

[a]Measures of ex vivo fluorescence emission by subcutaneous CXCR4+ SP5 patient-derived tumors and normal mouse organs, as measured by FLI (Protein-buffer Radiant Efficiency/10^5) at the indicated time after iv injection of the material, using the IVIS Spectrum equipment.

at 37 °C indicated structural instability of T22-GFP-H5T nanoparticles (Figure 2A) that was not apparent by the mere hydrodynamic size analysis upon biological fabrication (Figure 1B).

Such less stable T22-GFP-H5T nanoparticles reached the target tumor tissue at 5 h post iv administration (Figure 3). However, they failed to accumulate in the tumor (being undetectable at 24 h), while displaying a much lower tumor exposure than the parental H6-tagged protein (Figure 4). Moreover, the amounts of this protein were progressively fading in tumor tissue, while an increased in its fluorescence signal was observed, at later times and at important levels, in nontumor organs such as liver and kidney. Therefore, T22-GFP-H5T had a lower accumulation in tumor than in nontumor tissues (AUC ratio = 0.8). This was in sharp contrast with T22-GFP-H6, for which most of the injected dose accumulated in tumor rather than in nontumor tissues (AUC ratio = 2.2) (Figure 4, Table 2). Thus, despite T22-GFP-H6 started their tumor uptake at later times, it reached a total tumor exposure 2.7 fold higher than this achieved for T22-GFP-H5T, and also maintained a high fluorescence exposure in tumor tissue beyond 48 h. In addition to this, the injected equal dose and highly similar fluorescence emission of the two compared proteins lead to much higher tumor exposure for T22-GFP-H6 than in nontumor tissues, while the opposite happened for T22-GFP-H5T, suggesting a more intense and faster clearance from the body of T22-GFP-H5T, since its total (tumor + nontumor) fluorescence emission showed a 43% reduction as compared to total T22-GFP-H6 FLI emission (Figure 4). In this regard, the higher accumulation in kidney and liver at longer times (48 h) for T22-GFP-H5T, together with its lower nanostructure stability as determined in vitro (Figure 2A), strongly suggests the possible occurrence of a much higher renal excretion and/or hepatic metabolism than T22-GFP-H6. The tumor accumulation pattern followed by T22-GFP-H6 was in agreement with previous experiments in related mice models.[8] This was indicative of the robustness of the material regarding biodistribution to tumor, leading to high exposure in that tissue by achieving a high uptake peak and a long residence time, while displaying low uptake in off-target tissues.[6,8,10,19] In fact, the present data also suggested a lack of intracellular penetration of T22-GFP-H5T in tumor. When stable nanoparticles that effectively internalize in target CXCR4+ tumors cells are administered,[6] a residence time of around 48 h in tumor is consistently observed. During this time period, the nanocarrier is probably degraded within uptaking cells.[20] A 48 h residence time or longer, occurs also in therapeutic protein-only nanoparticles targeting CXCR4+ cancer cells.[21] The shorter tumor residence time of T22-GFP-H5T suggests that this protein carrier, despite interacting with the CXCR4 receptor through its T22 ligand, is not effectively internalized in target cells. Consistently, an early and short residence time of GFP-H6 (lacking the T22 ligand) in tumor has been also observed.[11] In summary, once rule out proteolytic degradation of both compared proteins for at least a 48 h period, equal to the biodistribution study time, it seems likely that having or lacking a nanostructure is a main driver for their biodistribution. Thus, T22-GFP-H5T lack of nanostructure and smaller size (6 nm) allows for early and rapid entrance in tumor extracellular space, despite precluding its internalization in target cancer cells, which is followed by an easy return to blood and renal clearance. In contrast, the higher size of the nanostructured T22-GFP-H6 particles slow their entrance in the tumor, but increases their recirculation in blood, because of lack of renal flirtation, and their internalization in CXCR4+ target cancer cells along time, significantly enhancing their whole exposure to the tumor.

These data were compatible with a robust structure of T22-GFP-H6 nanoparticles compared to a progressively disassembling T22-GFP-H5T materials, provided the nanostructure is assumed as a critical component of the active targeting process. While the role of nanostructure as an element influencing passive targeting has been largely discussed and recognized,[4,22] its potential impact on active targeting (that mediated by a cell-surface ligand) has been a rather neglected issue. Nanoscale organization of a targeted material might enhance its interaction with target cells by the multimeric binding of nanoparticles to cell surface receptor molecules.[23,24] Multivalent ligands generally show lower dissociation rates than individual versions ligands in the interaction with the receptor,[25] apart from a cooperative cell binding that promotes a more efficient early interaction and endosomal internalization.[26] Such cooperativity in both signaling and internalization of artificial constructs has been already described in different therapeutic platforms,[24,27] what could be specially efficient in the case of symmetrically ordered materials.[28] In the case of recombinant proteins, multivalent presentation of ligands in supramolecular constructs might be more efficient than monovalent versions,[29] what has been already discussed in the context of virus-like presentations of cell interactors and the consequent enhanced endosomal cell uptake.[26] In this regard, the results presented here support again the convenience of multivalent presentation, that also enhances the specificity in cell-receptor recognition. In this context, hybrid nanoparticles in which peptides R9 (an unspecific cell-penetrating peptide) and T22 (a specific CXCR4 ligand) are combined show lower CXCR4-specificity than T22 only-based nanoparticles.[15] Besides, the size increase derived from oligomerization, in the case of the modular proteins described here from ≈4 nm (the hydrodynamic size of a GFP monomer) to ≈12 nm, above the renal cut-off or ≈6–8 nm,[10] might also increase circulation time and in consequence opportunities for a tight interaction with target tissues, promoting the desired tumor accumulation of tumor-homing materials.

4. Conclusion

The occurrence of an effective ligand of a tumor cell marker is necessary but not sufficient to ensure a proper tumor biodistribution of functional proteins upon systemic administration, as proved here by using a model self-assembling protein. Contrarily, a supramolecular architecture of such targeted polypeptide, in form of multimeric nanoscale materials, enables the tumor homing peptide, here modeled by the CXCR4 ligand T22, to drive the accumulation of the material in the target tumor tissue. Several factors, including the multimeric regular presentation of the ligand and the nanoscale size of the complex are probably involved in the complex process of active targeting. In active targeting, the administered material

needs to overcome several biological barriers, including renal and hepatic clearance, to achieve higher exposure and residence time in tumor. The concept presented here might represent a convincing explanation of the poor biodistribution so far reached by tumor-targeted medicines, including antibody-drug conjugates. In addition to this, it is offering a potential developmental roadmap for the improvement of these drugs, of high intrinsic therapeutic potential, to reach satisfactory efficiencies in the clinical context.

5. Experimental Section

Genetic Design, Protein Production, and Purification: The genetic design of newly His-derived modular proteins was based on the parental T22-GFP-H6 construction. The C-terminal H6 poly-His tail was exchanged for alternative His-rich human peptides under specific criteria (explained during the work). The already displayed abbreviations -H6, -H3A, -H5T, and -H5E correspond to HHHHHH, HAAHAH, HTHTHTHTH, and HEHEHEHEH amino acid sequences respectively. Nomenclature has been established from N to C terminal according to their modular organization. All protein sequences were designed in house as codon-optimized genes, synthetized and inserted into pET22b plasmids using NdeI and HindIII restriction enzymes and provided by Geneart (ThermoFisher).

All fusion proteins were transformed by heat shock for 45 s at 42 °C in *Escherichia coli* Origami B (BL21, OmpT⁻, Lon⁻, TrxB, Gor⁻; Novagen). Transformed cells were then grown at 37 °C in LB (Lysogeny Broth) and encoding proteins produced at 20 °C overnight upon induction with 0.1×10^{-3} M of isopropyl-β-D-thiogalactopyronaside (IPTG) when the OD_{550} reached 0.5–0.7. Cells were then harvested by centrifugation for 15 min (5000 g at 4 °C) and stored at −80 °C until use. Pellets were then thawed and resuspended in Wash buffer (20×10^{-3} M Tris, 500×10^{-3} M NaCl, pH = 8) in presence of protease inhibitors (Complete EDTA-free; Roche Diagnostics). Cell disruption was subsequently performed by sonication (0.5-on, 0.5-off for 5 min) at 10% of amplitude (Branson Digital Sonifier), and the soluble fraction was separated by centrifugation for 45 min (15 000 g at 4 °C) and filtered using a pore diameter of 0.45 and 0.22 µm consecutively. Proteins were finally purified by immobilized metal affinity chromatography (IMAC) in an ÄKTA pure system (GE Healthcare) using HiTrap Chelating HP 5 mL columns (GE Healthcare). Protein elution was achieved by a linear gradient of Elution buffer (20×10^{-3} M Tris, 500×10^{-3} M NaCl, 500×10^{-3} M Imidazole, pH = 8) and rinsed protein dialyzed against sodium carbonate (166×10^{-3} M NaCO₃H, pH = 8) and sodium carbonate with salt (166×10^{-3} M NaCO₃H, 333×10^{-3} M NaCl, pH = 8) buffers.

Protein Purity, Integrity, and Concentration: Protein purity was determined by sodium dodecyl sulfate polyacrylamide gel electrophoresis (SDS-PAGE) and western blot (WB) immunoassay with an anti-GFP monoclonal antibody (Santa Cruz Biotechnology). Protein integrity was also analyzed by matrix-assisted laser desorption ionization time-of-flight (MALDI-TOF) mass spectrometry and concentration determined by Bradford's assay.

Volume Size Distribution, Z-Potential, and Fluorescence Emission: Volume size distribution (VSD) and protein surface charge (Z_p) of all proteins were determined by dynamic light scattering (DLS) and Z-potential measurements respectively at 633 nm and 25 °C in a Zetasizer Nano ZS (Malvern Instruments Limited) using ZEN2112 3 mm quartz batch cuvettes and DTS10170 capillary cells respectively. Measurements were performed in triplicate for error estimation and VSD peak values referred to the average mode of the populations with a rendered standard error lower than 0.01. Fluorescence emission of each GFP variant was determined at 513 nm using an excitation wavelength of 488 nm with a Varian Cary Eclipse Fluorescence Spectrophotometer (Agilent Technologies). For that, all the proteins were equally diluted in the corresponding sodium carbonate buffer w/o salt until 1 mg mL⁻¹ in a final volume of 100 µL.

Ultrastructural Morphometry: The nanoscale morphometry (size and shape) of self-assembled nanoparticles was determined at nearly native state, both by deposition on silicon wafers with field emission scanning electron microscopy (FESEM) and by negative staining with TEM. Drops of 3 µL of T22-GFP-H6, T22-GFP-H3A, T22-GFP-H5T, and T22-GFP-H5E samples diluted at 0.4 mg mL⁻¹ in sodium carbonate buffer were directly deposited on silicon wafers (Ted Pella Inc., Reading) for 30 s, excess of liquid was blotted with Whatman filter paper number 1 (GE Healthcare), air dried for few min, and immediately observed without coating with a FESEM Zeiss Merlin (Zeiss) operating at 0.8 kV and equipped with a high resolution in-lens secondary electron detector. Drops of 3 µL of the same four samples were directly deposited on 200 mesh carbon-coated copper grids (Electron Microscopy Sciences, Hatfield) for 30 s, excess blotted with Whatman filter paper, contrasted with 3 µL of 1% uranyl acetate (Polysciences Inc.) for 1 min, blotted again and observed in a TEM Jeol 1400 (Jeol Ltd.) operating at 80 kV and equipped with a Gatan Orius SC200 CCD camera (Gatan Inc.). For each sample and technique, representative images of a general field and a nanoparticle detail were captured at high magnifications (from 100 000× to 600 000×).

Determination of GFP Chromophore Fluorescence: The GFP chromophore fluorescence dependence on the temperature of each protein was also evaluated. Fluorescence spectra were recorded in a Varian Cary Eclipse spectrofluorimeter (Agilent Technologies). A quartz cell with 10 mm path length and a thermostated holder was used. The excitation slit was set at 2.5 nm and emission slit at 5 nm. λ_{ex} was 488 nm. Protein concentration was 0.2 mg mL⁻¹ in the corresponding buffer.

Structural Stability of Protein Constructs upon Human Serum Incubation: T22-GFP-H6 and T22-GFP-H5T protein nanoparticles were incubated at 37 °C with agitation (250 rpm) at proportion 1:1 in relation to human serum (Sigma-Aldrich) for 24 and 48 h. Protein VSD was determined at 24 h by a Zetasizer Nano ZS (Malvern Instruments Limited) and protein fluorescence and motility by a Varian Cary Eclipse spectrofluorometer (Agilent Technologies) and WB immunoassay respectively.

Protein Internalization: HeLa CXCR4⁺ cells (ATCC CCL-2) were cultured in 24-well plates (60 000 cells per well during 24 h for different time/concentration assays, in MEM Alpha 1× GlutaMAX medium (Gibco) supplemented with fetal bovine serum (FBS) at 37 °C in a 5% CO₂ humidified atmosphere, until reaching a confluence of 70%. Protein internalization was monitored at different concentrations (50 and 1000×10^{-9} M) and times (1 and 24 h). After protein exposure, cells were detached and external hooked protein removed by adding Trypsin-EDTA (Gibco) at 1 mg mL⁻¹ for 15 min and 37 °C. Intracellular protein fluorescence was determined by flow cytometry using a fluorescence assisted cell sorting (FACS)-Canto system (Becton Dickinson) at 15 mW with an air-cooled argon ion laser exciting at 488 nm. Measurements were performed in duplicate. Additionally, the specific protein CXCR4-mediated internalization was proved by the addition of the receptor antagonist AMD3100[30] that inhibits the interaction between T22 and CXCR4. This chemical compound was added at a final concentration of 500×10^{-9} M (ten times protein concentration) for 1 h prior to protein incubation at 50×10^{-9} M.

In Vivo Biodistribution Assays: All in vivo experiments were approved by the institutional animal Ethics Committee of Hospital Sant Pau. Five-week-old female Swiss nu/nu mice weighing between 18 and 20 g (Charles River, L-Abreslle) and maintained in specific-pathogen-free (SPF) conditions, were used for the in vivo biodistribution studies. A subcutaneous colorectal cancer mouse model, derived from the CXCR4⁺ patient sample SP5, was used. To generate this model, 10 mg of SP5 tumor tissue obtained from donor animals was implanted in the mouse subcutis. When tumors reached a volume of ≈500 mm³ biodistribution assays of T22-GFP-H6 and T22-GFP-H5T nanoparticles were performed at three different times after nanoparticle injection, namely 5, 24, and 48 h. Mice received 100 µg single iv bolus of T22-GFP-H6 ($n = 2$) or 100 µg single iv bolus of T22-GFP-H5T ($n = 2$) in sodium carbonate buffer with salt. Control animals ($n = 2$) were iv administered with 150 µL of the same buffer.

At 5, 24, and 48 h after the iv injection, mice were euthanized and subcutaneous tumors and normal organs, including lung and heart,

**ADVANCED
SCIENCE NEWS**
www.advancedsciencenews.com

Particle
& Particle Systems Characterization
www.particle-journal.com

kidney, liver, and bone marrow were collected. Biodistribution of GFP fluorescent nanoparticles was determined measuring ex vivo the fluorescence emitted by tumors and normal organs using the IVIS Spectrum equipment (PerkinElmer Inc, Waltham). The fluorescent signal (FLI) was first digitalized, displayed as a pseudocolor overlay, and expressed as radiant efficiency. FLI values were calculated subtracting the FLI signal from the protein-treated mice by the FLI auto-fluorescent signal of control mice.

Conflict of Interest

The authors declare no conflict of interest.

[1] a) R. V. Mangues, E. Vazquez, A. Villaverde, *Med. Sci.* **2016**, *4*, 6; b) V. J. Yao, S. D'Angelo, K. S. Butler, C. Theron, T. L. Smith, S. Marchio, J. G. Gelovani, R. L. Sidman, A. S. Dobroff, C. J. Brinker, A. R. Bradbury, W. Arap, R. Pasqualini, *J. Controlled Release* **2016**, *240*, 267; c) T. Lammers, F. Kiessling, M. Ashford, W. Hennink, D. Crommelin, G. Storm, *Nat. Rev. Mater.* **2016**, *1*, 16069; d) M. S. Lee, E. C. Dees, A. Z. Wang, *Oncology* **2017**, *31*, 198; e) A. David, *Adv. Drug Delivery Rev.* **2017**, *119*, 120; f) K. Ozturk-Atar, H. Eroglu, S. Calis, *J. Drug Targeting* **2018**, *26*, 633.

[2] a) R. Duncan, R. Gaspar, *Mol. Pharmaceutics* **2011**, *8*, 2101; b) S. Wilhelm, A. J. Tavares, Q. Dai, S. Ohta, J. Audet, H. F. Dvorak, W. C. W. Chan, *Nat. Rev. Mater.* **2016**, *1*, 16014.

[3] a) N. Bertrand, J. C. Leroux, *J. Controlled Release* **2012**, *161*, 152; b) S. D. Li, L. Huang, *Mol. Pharmaceutics* **2008**, *5*, 496.

[4] B. Mukherjee, *Curr. Pharm. Biotechnol.* **2013**, *14*, 1221.

[5] a) V. Torchilin, *Adv. Drug Delivery Rev.* **2011**, *63*, 131; b) J. Reineke, *J. Controlled Release* **2018**, *273*, 180.

[6] U. Unzueta, M. V. Cespedes, N. Ferrer-Miralles, I. Casanova, J. Cedano, J. L. Corchero, J. Domingo-Espin, A. Villaverde, R. Mangues, E. Vazquez, *Int. J. Nanomed.* **2012**, *7*, 4533.

[7] a) F. Balkwill, *Sem. Cancer Biol.* **2004**, *14*, 171; b) J. Kim, H. Takeuchi, S. T. Lam, R. R. Turner, H. J. Wang, C. Kuo, L. Foshag, A. J. Bilchik, D. S. Hoon, *Ann. Surg.* **2006**, *244*, 113; c) J. Kim, T. Mori, S. L. Chen, F. F. Amersi, S. R. Martinez, C. Kuo, R. R. Turner, X. Ye, A. J. Bilchik, D. L. Morton, D. S. Hoon, *Ann. Surg.* **2006**, *244*, 113.

[8] F. Rueda, M. V. Cespedes, O. Conchillo-Sole, A. Sanchez-Chardi, J. Seras-Franzoso, R. Cubarsi, A. Gallardo, M. Pesarrodona, N. Ferrer-Miralles, X. Daura, E. Vazquez, E. Garcia-Fruitos, R. Mangues, U. Unzueta, A. Villaverde, *Adv. Mater.* **2015**, *27*, 7816.

[9] M. Pesarrodona, E. Crosas, R. Cubarsi, A. Sanchez-Chardi, P. Saccardo, U. Unzueta, F. Rueda, L. Sanchez-Garcia, N. Serna, R. Mangues, N. Ferrer-Miralles, E. Vazquez, A. Villaverde, *Nanoscale* **2017**, *9*, 6427.

[10] M. V. Cespedes, U. Unzueta, W. Tatkiewicz, A. Sanchez-Chardi, O. Conchillo-Sole, P. Alamo, Z. Xu, I. Casanova, J. L. Corchero, M. Pesarrodona, J. Cedano, X. Daura, I. Ratera, J. Veciana, N. Ferrer-Miralles, E. Vazquez, A. Villaverde, R. Mangues, *ACS Nano* **2014**, *8*, 4166.

[11] M. V. Cespedes, U. Unzueta, P. Alamo, A. Gallardo, R. Sala, I. Casanova, M. A. Pavon, M. A. Mangues, M. Trias, A. Lopez-Pousa, A. Villaverde, E. Vazquez, R. Mangues, *Nanomed.: Nanotechnol., Biol. Med.* **2016**, *12*, 1987.

[12] M. V. Cespedes, U. Unzueta, A. Avino, A. Gallardo, P. Alamo, R. Sala, A. Sanchez-Chardi, I. Casanova, M. A. Mangues, A. Lopez-Pousa, R. Eritja, A. Villaverde, E. Vazquez, R. Mangues, *EMBO Mol. Med.* **2018**, *10*, e8772.

[13] N. Serna, M. V. Céspedes, L. Sánchez-García, U. Unzueta, R. Sala, A. Sánchez-Chardi, F. Cortés, N. Ferrer-Miralles, R. Mangues, E. Vázquez, A. Villaverde, *Adv. Funct. Mater.* **2017**, *27*, 1700919.

[14] H. Lopez-Laguna, U. Unzueta, O. Conchillo-Sole, A. Sanchez-Chardi, M. Pesarrodona, O. Cano-Garrido, E. Volta, L. Sanchez-Garcia, N. Serna, P. Saccardo, R. Mangues, A. Villaverde, E. Vazquez, *Acta Biomater.* **2019**, *83*, 257.

[15] U. Unzueta, N. Serna, L. Sanchez-Garcia, M. Roldan, A. Sanchez-Chardi, R. Mangues, A. Villaverde, E. Vazquez, *Nanotechnology* **2017**, *28*, 505102.

[16] a) S. Knecht, D. Ricklin, A. N. Eberle, B. Ernst, *J. Mol. Recognit.* **2009**, *22*, 270; b) V. Tolmachev, C. Hofstrom, J. Malmberg, S. Ahlgren, S. J. Hosseinimehr, M. Sandstrom, L. Abrahmsen, A. Orlova, T. Graslund, *Bioconjugate Chem.* **2010**, *21*, 2013.

[17] K. A. Pikal-Cleland, N. Rodriguez-Hornedo, G. L. Amidon, J. F. Carpenter, *Arch. Biochem. Biophys.* **2000**, *384*, 398.

[18] a) H. Tamamura, T. Imai, T. Ishihara, M. Masuda, H. Funakoshi, H. Oyake, T. Murakami, R. Arakaki, H. Nakashima, A. Otaka, T. Ibuka, M. Waki, A. Matsumoto, N. Yamamoto, N. Fujii, *Bioorg. Med. Chem.* **1998**, *6*, 1033; b) U. Unzueta, J. Seras-Franzoso, M. V. Cespedes, P. Saccardo, F. Cortes, F. Rueda, E. Garcia-Fruitos, N. Ferrer-Miralles, R. Mangues, E. Vazquez, A. Villaverde, *Nanotechnology* **2017**, *28*, 015102.

[19] P. Alamo, A. Gallardo, F. Di Nicolantonio, M. A. Pavon, I. Casanova, M. Trias, M. A. Mangues, A. Lopez-Pousa, A. Villaverde, E. Vazquez, A. Bardelli, M. V. Cespedes, R. Mangues, *FASEB J.* **2015**, *29*, 464.

**ADVANCED
SCIENCE NEWS**
www.advancedsciencenews.com

Particle
& Particle Systems Characterization
www.particle-journal.com

[20] A. Falgas, V. Pallares, U. Unzueta, M. V. Cespedes, I. Arroyo-Solera, M. J. Moreno, A. Gallardo, M. A. Mangues, J. Sierra, A. Villaverde, E. Vazquez, R. Mangues, I. Casanova, *Haematologica* **2019**, https://doi.org/10.3324/haematol.2018.211490.

[21] L. Sanchez-Garcia, N. Serna, P. Alamo, R. Sala, M. V. Cespedes, M. Roldan, A. Sanchez-Chardi, U. Unzueta, I. Casanova, R. Mangues, E. Vazquez, A. Villaverde, *J. Controlled Release* **2018**. *274*, 81.

[22] a) E. A. Sykes, J. Chen, G. Zheng, W. C. Chan, *ACS Nano* **2014**, *8*, 5696; b) D. Kalyane, N. Raval, R. Maheshwari, V. Tambe, K. Kalia, R. K. Tekade, *Mater. Sci. Eng., C* **2019**, *98*, 1252; c) E. Blanco, H. Shen, M. Ferrari, *Nat. Biotechnol.* **2015**, *33*, 941; d) M. Alavi, M. Hamidi, *Drug Metab. Pers. Ther.* **2019**, *34*, 20180032.

[23] S. Hong, P. R. Leroueil, I. J. Majoros, B. G. Orr, J. R. Baker Jr., M. M. Banaszak Holl, *Chem. Biol.* **2007**, *14*, 107.

[24] A. Arsiwala, A. Castro, S. Frey, M. Stathos, R. S. Kane, *Chem. - Asian J.* **2019**, *14*, 244.

[25] C. Chittasupho, *Ther. Delivery* **2012**, *3*, 1171.

[26] U. Unzueta, M. V. Cespedes, E. Vazquez, N. Ferrer-Miralles, R. Mangues, A. Villaverde, *Trends Biotechnol.* **2015**, *33*, 253.

[27] a) W. Song, Z. Tang, D. Zhang, M. Li, J. Gu, X. Chen, *Chem. Sci.* **2016**, *7*, 728; b) J. Reichenwallner, A. Thomas, T. Steinbach, J. Eisermann, C. E. H. Schmelzer, F. Wurm, D. Hinderberger, *Biomacromolecules* **2019**, *20*, 1118; c) A. Bekdemir, S. Liao, F. Stellacci, *Colloids Surf., B* **2019**, *174*, 367; d) J. F. Stefanick, D. T. Omstead, T. Kiziltepe, B. Bilgicer, *Nanoscale* **2019**, *11*, 4414.

[28] D. S. Goodsell, A. J. Olson, *Annu. Rev. Biophys. Biomol. Struct.* **2000**, *29*, 105.

[29] a) I. Cabrera, E. Elizondo, O. Esteban, J. L. Corchero, M. Melgarejo, D. Pulido, A. Cordoba, E. Moreno, U. Unzueta, E. Vazquez, I. Abasolo, S. Schwartz Jr., A. Villaverde, F. Albericio, M. Royo, M. F. Garcia-Parajo, N. Ventosa, J. Veciana, *Nano Lett.* **2013**, *13*, 3766; b) Z. Xu, U. , M. Roldán, R. Mangues, A. Sánchez-Chardi, N. Ferrer-Miralles, A. Villaverde, E. Vázquez, *Mater. Lett.* **2015**, *154*, 140.

[30] a) A. Kawaguchi, Y. Orba, T. Kimura, H. Iha, M. Ogata, T. Tsuji, A. Ainai, T. Sata, T. Okamoto, W. W. Hall, H. Sawa, H. Hasegawa, *Blood* **2009**, *114*, 2961; b) J. S. Song, C. M. Kang, H. H. Kang, H. K. Yoon, Y. K. Kim, K. H. Kim, H. S. Moon, S. H. Park, *Exp. Mol. Med.* **2010**, *42*, 465.

190

3) ANNEX 3: ARTICLE 3

A refined cocktailing of pro-apoptotic nanoparticles boosts anti-tumor activity

Laura Sánchez-García [1], Rita Sala [2], Naroa Serna [1], Patricia Álamo [2], Eloi Parladé [3], Lorena Alba-Castellón [4], Eric Voltà-Durán [1], Alejandro Sánchez-Chardi [5], Ugutz Unzueta [6], Esther Vázquez [1], Ramón Mangues [2], Antonio Villaverde [7]

Affiliations + expand

PMID: 32603867   DOI: 10.1016/j.actbio.2020.06.033

Abstract

A functional 29 amino acid-segment of the helix α5 from the human BAX protein has been engineered for production in recombinant bacteria as self-assembling, GFP-containing fluorescent nanoparticles, which are targeted to the tumoral marker CXCR4. These nanoparticles, of around 34 nm in diameter, show a moderate tumor biodistribution and limited antitumoral effect when systemically administered to mouse models of human CXCR4$^+$ colorectal cancer (at 300 μg dose). However, if such BAX nanoparticles are co-administered in cocktail with equivalent nanoparticulate versions of BAK and PUMA proteins at the same total protein dose (300 μg), protein biodistribution and stability in tumor is largely improved, as determined by fluorescence profiles. This fact leads to a potent and faster destruction of tumor tissues when compared to individual pro-apoptotic factors. The analysis and interpretation of the boosted effect, from both the structural and functional sides, offers clues for the design of more efficient nanomedicines and theragnostic agents in oncology based on precise cocktails of human proteins. STATEMENT OF SIGNIFICANCE: Several human pro-apoptotic peptides (namely BAK, BAX and PUMA) have been engineered as self-assembling protein nanoparticles targeted to the tumoral marker CXCR4. The systemic administration of the same final amounts of those materials as single drugs, or as combinations of two or three of them, shows disparate intensities of antitumoral effects in a mouse model of human colorectal cancer, which are boosted in the triple combination on a non-additive basis. The superiority of the combined administration of pro-apoptotic agents, acting at different levels of the apoptotic cascade, opens a

plethora of possibilities for the development of effective and selective cancer therapies based on the precise cocktailing of pro-apoptotic nanoparticulate agents.